A multiscale approach to understand and predict the effects of hydrothermal treatment on lignocellulosic biomass

Julia Parlatore Lancha

Thèse de doctorat

NNT : 2020UPASC023

université PARIS-SACLAY

A multiscale approach to understand and predict the effects of hydrothermal treatment on lignocellulosic biomass

Thèse de doctorat de l'université Paris-Saclay

École doctorale n°579 – Sciences mécaniques et énergétiques, matériaux et géosciences (SMEMAG)
Spécialité de doctorat : Génie des Procédés
Unité de recherche : Université Paris-Saclay, CentraleSupélec, Laboratoire de Génie des Procédés et Matériaux, 91190, Gif-sur-Yvette, France
Référent : CentraleSupélec

Thèse présentée et soutenue à Gif-sur-Yvette, le 8 juillet 2020, par

Julia PARLATORE LANCHA

Composition du Jury

Denis FLICK Professeur, AgroParisTech	Président
Gabriel PAËS Directeur de Recherche, INRAE	Rapporteur & examinateur
Vincent PLACET Maître de conférences HDR, Université Bourgogne Franche-Comté	Rapporteur& examinateur
Nicolas BROSSE Professeur, Université de Lorraine	Examinateur
Delphine JULLIEN Maître de conférences, Université de Montpellier	Examinatrice
Patrick PERRÉ Professeur, CentraleSupélec	Directeur de thèse
Giana ALMEIDA Maître de conférences, AgroParisTech	Co-Encadrante
Julien COLIN Maître de conférences, CentraleSupélec	Co-Encadrant

Remerciements

Quand j'ai commencé mon doctorat, j'étais sûre de m'embarquer dans une aventure intellectuelle. Trois ans, quelques mois et une pandémie plus tard, je vois que la thèse est avant tout une expérience humaine. Mes souvenirs le plus marquants de cette période concernent les personnes qui m'ont accompagnée le long de ce parcours, à qui je dois mes plus sincères remerciements.

Je tiens tout d'abord à remercier mon directeur de thèse, Patrick Perré, pour les moments consacrés à partager une partie de ses connaissances avec moi. Merci aussi (et surtout) pour la passion avec laquelle tu fais de la science. Elle est contagieuse et c'est ce qui m'a donné la motivation pour avancer même quand les résultats étaient, à première vue, peu réjouissants.

Je ne remercierai jamais assez Julien Colin pour son soutien quotidien au fil de ces années. Son aide est allée bien au-delà de la science. Elle était dans son attention aux petits détails, dans sa sensibilité de remarquer quand quelque chose n'allait pas, dans sa bonne humeur indéfectible même face à une bande de doctorants acharnés.

Mes remerciements viennent naturellement à Giana Almeida, sans qui je ne serais pas arrivée au LGPM. Merci pour ta délicatesse, ta force et pour m'avoir constamment apporté une touche de familiarité, notamment par ton optimisme typiquement brésilien.

Mes plus sincères remerciements à toute l'équipe qui a participé, directe ou indirectement, à ce projet. Je tiens à remercier plus particulièrement Joel Casalinho qui s'est énormément investi au développement de l'outil expérimental et qui est toujours venu au secours lors du moindre problème technique. Il sait être sérieux tout en gardant sa bonne humeur, et c'est pourquoi cela a toujours été un plaisir de travailler avec lui. Puisque je parle du dispositif, merci aussi à Mahamadou Mounkaila pour les discussions sur LabView et pour être intervenu en urgence quand j'en ai eu besoin. Je voudrais également remercier Cédric Guérin pour la mise en place des méthodes analytiques utilisées dans cette étude, pour sa patience et sa force de proposition. Ses nombreuses idées ont, à plusieurs reprises, failli orienter ma thèse vers la chimie analytique. Un grand merci à Pin Lu pour m'avoir formée au Raman et pour avoir réalisé les images au tomographe avec une minutie qui continue à m'impressionner. Merci également à Nathalie Ruscassier, pour l'acquisition d'images au microscope électronique, et à Fanny Duval pour avoir géré les commandes et pour son immense générosité. Enfin, merci à ma chère stagiaire Ana Milena Gómez qui m'a souvent poussée à aller plus loin grâce à son intérêt et sa curiosité.

Je tiens également à remercier l'ensemble des membres du jury de thèse pour leur présence et l'intérêt porté à mon travail. Merci à Denis Flick d'avoir accepté de présider cette assemblée, à Gabriel Paës et Vincent Placet pour le temps consacré à l'examen de ce manuscrit et Delphine Jullien et Nicolas Brosse pour leur implication en qualité d'examinateur.

Je remercie chaleureusement l'ensemble des membres du LGPM, de Pomacle et de Gif, pour tous les moments, les cafés et (forcément) les gâteaux partagés. Je pense, entre autres, à mes amis doctorants qui m'ont accompagnée dans ce périple et qui ont rendu cette aventure beaucoup plus légère et agréable. Une pensée également à Clarisse et Magali pour les conseils et les moments de

décontraction lors de la dernière ligne droite. Et puis, bien sûr, impossible d'oublier Catalina et Thuy, qui étaient toujours présentes pour m'encourager, pour m'alimenter et pour me gâter.

Un grand merci à tous les professeurs et chercheurs qui ont croisé mon chemin pendant ma scolarité et qui ont contribué à mon éveil scientifique. Je pense notamment à Silvia Germer, Pedro Augusto et Rosiane Lopes da Cunha, mais plein d'autres qui luttent pour faire de la recherche de qualité malgré le contexte brésilien actuel.

Enfin, je tiens à remercier mes amis et ma famille qui, de près ou de loin, m'ont toujours soutenue. Plus particulièrement, j'aimerais exprimer mon immense gratitude à mes parents et à mon frère pour leur soutien et leur amour inconditionnels. Tout ce que je fais par moi-même est aussi leur réussite. J'adresse mes derniers remerciements à John. Je n'aurais pas pu choisir un meilleur compagnon pour être confiné à mes côtés pendant la fin de la thèse. Ses conseils, son encouragement, sa patience et sa complicité m'ont été essentiels ces dernières années et m'ont souvent montré que je suis capable de bien plus que je ne le crois. Je suis extrêmement fière de la façon dont nous avons grandi et continuons à grandir ensemble.

General preamble

The work described in this thesis manuscript was carried out at the Chair of Biotechnology of CentraleSupélec (Université Paris-Saclay), part of the LGPM laboratory (Laboratoire de Génie des Procédés et Matériaux).

This manuscript is written in an article-based form. Three submitted publications constitute Chapters III, IV, and V. The content of publications has not been modified from the submitted versions, except for a layout homogenization to respect the general format of the manuscript.

The writing format chosen for this manuscript can lead to an apparent redundancy of some of the background information – mainly in the Introduction and Materials and Methods sections of the different articles – which is due to a need for self-sufficiency of the articles in their published or submitted form.

The references to the publications are as follows:

- **Multiscale investigation on the chemical and anatomical changes of lignocellulosic biomass for different severities of hydrothermal pre-treatment**
  Julia Parlatore Lancha, Patrick Perré, Julien Colin, Pin Lv, Nathalie Ruscassier, Giana Almeida
  To be submitted
- **In situ measurements of viscoelastic properties of biomass during hydrothermal treatment to assess the kinetics of chemical alterations**
  Julia Parlatore Lancha, Julien Colin, Giana Almeida, Patrick Perré
  Bioresource Technology
  Volume 315, November 2020, 123819
  DOI: https://doi.org/10.1016/j.biortech.2020.123819
- **A DAEM model based on in-situ shrinkage measurement of poplar wood during hydrothermal treatment as predictive indicator of chemical degradation**
  Julia Parlatore Lancha, Julien Colin, Giana Almeida, Joel Casalinho, Cédric Guerin, Patrick Perré
  To be submitted

This work was the subject of oral and poster communications at national and international scientific conferences, as follows:

Oral communications

- 27th European Biomass Conference and Exhibition (EUBCE) in Lisbon, Portugal, on May 27-30, 2019
  Imaging techniques for understanding physico-mechanical modifications of lignocellulosic biomass due to hydrothermal pretreatment
  Julia Parlatore Lancha, Julien Colin, Pin Lu, Giana Almeida, Patrick Perré
  DOI: https://doi.org/10.5071/27thEUBCE2019-3BO.3.4
- Exploring Lignocellulosic Biomass (ELB) in Reims, France, on June 26-29, 2018
  Lignocellulosic biomass subjected to hydrothermal pretreatment: highlighting

parietal modifications through imaging techniques
Julia Parlatore Lancha, Pin Lu, Julien Colin, Giana Almeida, Patrick Perré

Poster communications

- 6èmes Journées Annuelles du GDR 3544 « Sciences du Bois » in Nantes, France, on November 21-23, 2017
  Étude rhéologique des propriétés de la biomasse sous haute pression ? C'est possible !
  Julia Parlatore Lancha, Julien Colin, Giana Almeida, Patrick Perré
- 16th Conference of the French Society of Process Engineering (SFGP) in Nancy, France, on July 11-13, 2017
  Macroscopic shrinkage of poplar during hydrothermal pretreatment as a result of parietal degradation
  Julia Parlatore Lancha, Julien Colin, Pin Lu, Giana Almeida, Sidali Mokdad, Patrick Perré
  Récents Progrès en Génie des Procédés, Numéro 110, 2017
  ISBN: 978-2-910239-85-5

Résumé en français

Introduction

Il existe actuellement de nombreuses preuves des impacts humains sur le climat et la communauté scientifique semble s'accorder sur la nécessité d'une réponse urgente. Dans ce contexte, la biomasse fait l'objet d'une attention accrue en tant que ressource renouvelable. L'utilisation de carburants issus de la biomasse (biocarburants) est en effet une réponse technologique prometteuse pour atténuer les émissions nettes de CO_2 et réduire la dépendance vis-à-vis des matières premières fossiles. Un autre secteur qui présente un grand potentiel d'utilisation de la biomasse est celui des produits chimiques biosourcés, car les molécules extraites ou dérivées de la biomasse peuvent servir de plateformes pour de très nombreuses voies de valorisation.

Par rapport à la première génération, les biocarburants et les produits chimiques de deuxième génération – issus de la biomasse lignocellulosique – présentent l'avantage supplémentaire d'avoir une empreinte plus faible sur l'eau et la terre, et une concurrence directe moindre avec la production alimentaire. Cette dernière est associée au fait que les matières premières utilisées par cette technologie sont des parties non comestibles des plantes. Malgré ses nombreux avantages, la biomasse lignocellulosique présente un inconvénient majeur pour son utilisation industrielle : elle est extrêmement récalcitrante au fractionnement. Deux approches sont traditionnellement utilisées pour permettre sa valorisation : la voie thermochimique – basée sur des catalyseurs thermiques et métalliques – et la voie biochimique – impliquant des enzymes et des microorganismes, et à laquelle ce travail est consacré.

Dans la voie biochimique, le prétraitement est une étape clé pour résoudre l'écueil de la structure récalcitrante de la biomasse lignocellulosique, car il favorise l'accessibilité des polysaccharides à l'hydrolyse enzymatique. Parmi les méthodes de prétraitement disponibles, l'explosion à la vapeur est la plus employée et la plus efficiente d'un point de vue technico-économique. Elle comprend deux étapes, une cuisson acide et une étape de décompression explosive. Les changements subis par la biomasse au cours de la cuisson acide se produisent à de multiples échelles et ont un impact important sur l'efficacité de l'étape d'explosion. En outre, ces modifications déterminent la rentabilité de l'ensemble de la chaîne de production. Tout d'abord, parce que le prétraitement affecte de manière critique les rendements globaux de conversion. Deuxièmement, parce que le prétraitement lui-même est un processus coûteux et gourmand en énergie. L'optimisation de cette étape est donc cruciale.

En raison de la complexité de la biomasse lignocellulosique – et, en particulier, du bois – cette question ne peut être abordée d'un seul point de vue. En effet, les propriétés à différentes échelles s'influencent mutuellement et les propriétés macroscopiques peuvent avoir un impact aussi important que les propriétés chimiques sur le choix des conditions opératoires. Par ailleurs, bien qu'elles soient riches en informations sur les mécanismes de dégradation de la biomasse au cours du procédé, les analyses chimiques sont longues et impliquent des tests destructifs. Par conséquent, la possibilité d'effectuer d'autres mesures en continu est évidemment séduisante, permettant de réduire considérablement le nombre de tests requis.

Ce projet de doctorat a proposé une approche multi-échelle pour observer et comprendre les modifications subies par la biomasse lors de la cuisson acide. À cette fin, la combinaison de trois disciplines – mécanique, chimie et imagerie – peut aider à développer des outils de conception pour les systèmes industriels. Le but ultime était de fournir des indicateurs mécaniques macroscopiques de la cinétique de traitement permettant de faire émerger des règles pour optimiser le temps de séjour et la température de traitement lors de la cuisson acide.

Tout d'abord, d'un point de vue chimique, une approche analytique classique a permis de quantifier les réactions concomitantes d'hydrolyse et de dégradation des composants de la biomasse. La biomasse pouvant se comporter très différemment selon l'interaction entre ses différents composants et selon son organisation anatomique, la caractérisation par imagerie a également été nécessaire. En outre, d'un point de vue macroscopique, l'évaluation continue des propriétés mécaniques de la biomasse a pu fournir des informations sur l'effet de la sévérité du traitement (temps de séjour, température, pH). Enfin, le développement d'un modèle prédictif permet d'envisager l'application des indicateurs de la déconstruction de la biomasse, identifiés à partir de l'ensemble des données expérimentales, pour accompagner la conception ou l'optimisation des systèmes industriels.

Revue bibliographique

Alors qu'une grande partie de la littérature s'est consacrée aux modifications chimiques de la biomasse soumise à la cuisson acide, moins d'attention a été accordée aux modifications aux échelles pariétale, cellulaire et macroscopique.

D'un point de vue moléculaire, le principal phénomène impliqué lors de la cuisson acide est une hydrolyse partielle qui libère des mono- et oligosaccharides. Aux échelles pariétale et cellulaire, cette dégradation entraîne des changements de la structure anatomique de la biomasse. Puisque la structure de la biomasse a un rôle essentiel sur la performance de l'étape d'explosion et sur l'accessibilité des glucides pariétaux aux enzymes, la compréhension des changements auxquels elle est soumise pendant le prétraitement est particulièrement critique. Pour adresser cette question, la combinaison de différentes techniques d'imagerie peut être une approche intéressante.

L'évolution des propriétés macroscopiques lors de l'explosion à la vapeur est un sujet particulièrement peu exploré. Pourtant, quelques études ont démontré que les caractéristiques rhéologiques du bois ont une très bonne capacité à révéler les phénomènes chimiques ayant lieu au cours de la cuisson acide. Par ailleurs, à notre connaissance, aucune étude sur le retrait de la biomasse soumise à ce type de procédé n'a été réalisée. Lorsqu'il est mesuré lors d'une pyrolyse, le retrait du bois s'est avéré être un bon indicateur de la sévérité du traitement et représente donc une piste intéressante à explorer. On pourrait supposer que le même effet serait observé dans le cas d'un traitement hydrothermique. En effet, la réduction de l'hygroscopicité du bois observée après le prétraitement, ainsi que la perte de masse due à la dégradation chimique et des changements au niveau de l'ultrastructure du bois sont des facteurs qui modifient les dimensions du bois.

La rareté d'études concernant les changements macroscopiques (retrait et propriétés rhéologiques) subis par la biomasse au cours de la cuisson acide est certainement due à la

complexité de ce type de mesures en conditions sévères (température élevée et vapeur saturée), telles que ce type de traitement impose. Des recherches précédemment menées au sein du Laboratoire de Génie des Procédés et Matériaux portèrent sur le développement d'outils permettant de surmonter ce défi. Grâce à ces travaux, un dispositif de suivi rhéologique a été mis en place, pouvant travailler en vapeur saturante jusqu'à 190 °C, tout en assurant des mesures mécaniques très précises. La possibilité d'extraire des paramètres utiles à la conception ou à l'optimisation d'installations industrielles mérite une recherche approfondie.

Principaux résultats et conclusions

D'un point de vue chimique, les mécanismes déduits des résultats obtenus étaient conformes à ceux généralement décrits dans la littérature. L'autoprotolyse de l'eau forme des ions hydronium qui agissent comme catalyseurs pour une série de réactions d'hydrolyse, auxquelles les hémicelluloses se sont montrées particulièrement sensibles. Par ailleurs, l'hydrolyse des groupements acétyle a entraîné la production d'acide acétique – également observable par une diminution du pH du liquide de traitement. L'évolution de la dégradation de la biomasse a pu être suivie principalement par une augmentation de la quantité d'oligosaccharides dissous et, en outre, par leur conversion en monosaccharides. L'hydrolyse de la biomasse et, par conséquent, la solubilisation de ses composants dans la phase liquide ont entraîné une perte de masse de la fraction solide. La biomasse solide résiduelle a également été altérée. Des mesures de sorption ont révélé que l'hygroscopicité de la biomasse diminue avec l'augmentation de la sévérité du traitement, ce qui a été attribué à la perte de groupements hydroxyle, des groupements acétyles ou de monomères osidiques entiers.

L'hydrolyse des hémicelluloses a également pu être constatée par microscopie confocale Raman, qui a aussi révélé une migration de la lignine au sein de la paroi cellulaire. Ces changements ont ensuite pu être liés aux changements ultra-structuraux identifiés par nano-tomographie à rayons X et par microscopie électronique à balayage. L'analyse de ces images 3D a permis de mettre en évidence un amincissement des parois cellulaires des échantillons traités, cohérent avec la perte de masse produite par les réactions d'hydrolyse. Cette altération pariétale s'exprime au niveau macroscopique par un retrait du bois et indique également un affaiblissement des parois propice à l'efficacité de la décompression explosive qui suit la cuisson acide. Dans le cas de traitements plus sévères, une rupture et un détachement des cellules adjacentes ont également été observés.

Ces résultats ont confirmé la pertinence d'une approche multi-échelle pour l'étude du prétraitement de la biomasse lignocellulosique. Cependant, bien que riches en informations, les résultats obtenus par imagerie restent plutôt qualitatifs et ont été acquis de manière discontinue. Afin de trouver un indicateur macroscopique de la déconstruction de la biomasse, il était important de repérer des indicateurs quantitatifs. De plus, l'aspect continu de cet indicateur était un élément crucial, car il comble une information lacunaire des analyses chimiques classiques : la cinétique de la réaction.

D'un point de vue macroscopique, trois propriétés ont été suivies : la rigidité, la relaxation des contraintes et le retrait.

Trois principaux phénomènes ont pu être distingués grâce à l'évolution concomitante de la rigidité et de la relaxation : l'activation thermique du comportement viscoélastique, le clivage des

liaisons moléculaires et la re-condensation. Au début de la phase de chauffage, alors que la température reste assez basse, seule l'activation thermique viscoélasticité se produit. Nos résultats montrent que, ensuite, à partir d'une température relativement basse (60 °C), une dégradation chimique concomitante commence à être observée. Cet effet, probablement dû à l'hydrolyse des hémicelluloses, a été observé grâce aux tests de relaxation des contraintes. À ce stade, le comportement monotone des tests de rigidité empêche de distinguer les deux phénomènes.

Une fois le plateau de température atteint, on constate principalement deux phénomènes : des réactions de clivage et de re-condensation. La prédominance de l'un ou de l'autre dépend de la sévérité du traitement. Les réactions de clivage se sont révélées prédominantes au début du plateau quelle que soit la température du traitement, ce qui a été attribué à l'hydrolyse de l'hémicellulose et au clivage des liaisons β-O-4 des lignines. Une sévérité modérée – qu'il s'agisse de longues durées de traitement pour des températures de 150 et 160 °C ou de durées plus courtes pour une température plus élevée (180 °C) – a favorisé les réactions de condensation de la lignine. La condition la plus sévère testée (long temps de séjour à 180 °C) a favorisé de nouvelles réactions de clivage, qui sont probablement liées à la réduction du dégrée de polymérisation de la cellulose. La saturation préalable de la biomasse lignocellulosique par une solution aqueuse acide semble également favoriser l'hydrolyse, tandis que l'utilisation d'un liquide alcalin semble provoquer l'extraction des lignines et des hémicelluloses à basse température mais limite les altérations ultérieures pendant le plateau de température. Contrairement à la phase de chauffage, les différents phénomènes se produisant pendant le plateau de température n'ont pu être mis en évidence que grâce à la rigidité, qui présente un comportement non monotone lors de cette phase.

Ces deux propriétés mécaniques se sont donc révélées complémentaires et ont fourni des indications précieuses sur les mécanismes chimiques impliqués dans la cuisson acide.

Le même dispositif utilisé pour mesurer les propriétés rhéologiques a servi au suivi de l'évolution de la taille de l'échantillon pendant le traitement.

Au cours des essais préliminaires, deux phénomènes (hydro)mécaniques se sont avérées avoir un impact sur les dimensions des échantillons et ont dû être pris en compte lors de l'élaboration de la méthodologie et du traitement de données : la récupération hygrothermique des contraintes de croissance de la paroi cellulaire et la modification du point de saturation des fibres.

Le retrait a augmenté de façon monotone avec l'augmentation de la température et du temps de séjour. Les résultats obtenus ont été utilisés pour alimenter un modèle d'énergie d'activation distribuée (*Distributed Activation Energy Model*, DAEM), dont les paramètres ont été identifiés en utilisant simultanément les données de tous les tests. La capacité du modèle DAEM ainsi alimenté à prédire les propriétés chimiques de la biomasse (mesurées par des analyses chimiques classiques) en fonction de la température de traitement et du temps de séjour a été évaluée. Le degré de conversion, tel que calculé par le modèle DEAM et ajusté à partir de la mesure du retrait *in situ*, s'est révélé être un indicateur synthétique des altérations chimiques. Cet excellent résultat a ensuite servi à l'ajustement d'expressions simples pour relier les mesures physiques et chimiques au modèle identifié. Le retrait ressort donc comme un bon indicateur de la dégradation chimique de la biomasse pendant la cuisson acide. Il peut être considéré comme un outil précieux pour choisir les conditions optimales de cuisson acide.

Dans une optique plus large, ces résultats peuvent aider à comprendre les effets du traitement hydrothermique sur les étapes ultérieures de la chaîne de production du biocarburant. Ils apportent des informations précieuses pour une meilleure modélisation, simulation et optimisation de l'explosion vapeur. Enfin, en ce qui concerne l'hydrolyse enzymatique, les modifications structurelles de la biomasse sont susceptibles d'améliorer l'accessibilité de la cellulose aux enzymes. La rupture de certaines cellules et le détachement entre cellules voisines augmentent la surface exposée, tandis que la dépolymérisation des hémicelluloses et la délocalisation de la lignine modifient l'accessibilité de la cellulose.

Perspectives

De ce travail émergent une variété de perspectives et de pistes pour la recherche et les applications futures. Elles peuvent être résumées comme suit :

- Les modifications chimiques des lignines, en particulier la re-condensation, ont fait l'objet de nombreuses discussions dans le cadre de ce projet. Une étude complémentaire de ces changements à l'aide de méthodes de chimie analytique pourrait alors grandement enrichir ce travail. Elle permettrait à la fois de mieux comprendre les modifications auxquelles sont soumises les lignines, comme la condensation, et d'identifier les molécules d'intérêt solubilisées dans la phase liquide.
- Le modèle DAEM développé au cours de cette étude pourrait être validé avec d'autres types de biomasses lignocellulosiques. Il serait également intéressant d'inclure la concentration en acide comme paramètre dans le modèle.
- La spectroscopie confocale Raman a prouvé son intérêt pour l'étude concomitante des changements chimiques et anatomiques de la biomasse. Cependant, de nombreux défis ont été rencontrés au cours de cette étude, ce qui a limité les analyses à des températures de traitement douces. Il reste donc beaucoup de travail à fournir pour surmonter les limitations imposées par la fluorescence. L'exploration d'autres techniques de topochimie pourrait être une réponse aux problèmes rencontrés. L'une des options consiste à tirer parti de cette caractéristique plutôt que d'essayer de la surmonter, car certaines études ont démontré que la fluorescence est liée aux types de liaisons présentes dans la structure des lignines.
- La phase de décompression explosive qui suit la cuisson acide est une étape importante dans le processus d'explosion vapeur. Cette phase, qui bénéficie de l'expansion brutale de la phase gazeuse et de vaporisation de l'eau liquide contenue dans les pores de la biomasse, est responsable de la fragmentation des particules et, par conséquent, de l'accessibilité de la paroi cellulaire à une attaque enzymatique ultérieure. Il serait donc intéressant d'améliorer la prédiction de TransPore – un modèle de calcul complet simulant les transferts de chaleur et de masse dans un milieu poreux – pour la fragmentation de la biomasse pendant l'explosion, en prenant en compte l'effet de la forme représentative des cellules et de l'épaisseur moyenne de la paroi cellulaire sur le module de rupture. Le présent travail fournit des informations précieuses sur la manière dont ces deux caractéristiques changent pendant la cuisson acide. La réduction de l'épaisseur de la paroi cellulaire a été démontrée avec succès par nano-tomographie à rayons X et quantifiée par analyse d'images. La même technique a illustré les changements de forme

des cellules, entraînant une réduction de la circularité moyenne de celle-ci. En outre, le modèle DAEM identifié a pu prédire les changements chimiques subis par la biomasse pour différentes températures et durées de traitement. Ces résultats pourraient alors être combinés dans une nouvelle étude qui comprenant également l'étape d'explosion.

- Plus globalement, et en termes d'applications futures, nos résultats montrent deux approches antagonistes. La biomasse prétraitée peut être utilisée soit dans des processus de fermentation – auquel cas une dégradation minimale des monosaccharides qui la composent est nécessaire – soit dans l'obtention de molécules plateforme résultant de la dégradation des sucres. La première approche nécessite de traitements plus doux, tandis que la seconde implique une augmentation de la sévérité du traitement.
- Si appliquées aux processus de fermentation, ces études devraient être analysées sous l'angle de l'hydrolyse enzymatique. Il s'agit, en effet, du seul moyen permettant de valider les éventuels résultats d'optimisation du prétraitement.
- Enfin, les aspects économiques et environnementaux de ce procédé devraient être pris en compte lors de son optimisation afin de trouver le juste équilibre entre l'augmentation de l'efficacité et la consommation énergétique du prétraitement. Cela permettrait également de valider les intérêts de cette technologie en tant qu'alternative aux combustibles et aux produits chimiques issus des ressources fossiles.

Table of contents

List of figures

List of tables

Abbreviations

1G	First Generation
2G	Second Generation
2D	Two-dimensional
3D	Three-dimensional
AA	Acetic Acid
AFEX	Ammonia Fiber Explosion
C5O	C5 Oligosaccharides
C6O	C6 Oligosaccharides
CAD	Computer Aided Design
CCD	Charge-Coupled Devices
CML	Compound Middle Lamella
DAEM	Distributed Activation Energy Model
DP	Degree of Polymerization
EMC	Equilibrium Moisture Content
EU	European Union
FEG-SEM	Field Emission Gun Scanning Electron Microscopy
FSP	Fiber-Saturation Point
FUR	Furfural
G	Guaiacyl
GHG	Greenhouse Gas
H	*p*-Hydroxyphenyl
HMF	5-Hydroxymethylfurfural
ILs	Ionic Liquids
IPCC	Intergovernmental Panel on Climate Change
IR	Infra-Red
L	Longitudinal
LASIRE	Laboratoire de Spectroscopie pour les Interactions, la Réactivité et l'Environnement
LCC	Lignin-Carbohydrate Complexes
LIF	Laser Induced Fluorescence
LMOPS	Laboratoire Matériaux Optiques, Photonique Et Systèmes
LODP	Level-Off Degree of Polymerization
MC	Moisture Content
ML	Middle Lamella
NREL	National Renewable Energy Laboratory
P or PCW	Primary Cell Wall
R	Radial
S	Syringyl or Secondary Cell Wall
SEM	Scanning Electron Microscopy
T	Tangential

TDS	Total Dissolved Sugars
TEM	Transmission Electron Microscopy
UV	Ultraviolet
WAVE^{T}	Environmental Vibration Analyzer for Wood
XYL	Xylose

Symbols

		Unit
A	Area	m^2
A	Pre-exponential factor	min^{-1}
a_B	Slope of the force-displacement curve in the blank test from linear regression	N/mm
a_R	Slope of the force-displacement curve for wood in the radial direction from linear regression	N/mm
a_T	Slope of the force-displacement curve for wood in the tangential direction from linear regression	N/mm
a'_i	Slope of the force-displacement curve for wood in the *i* direction after correction	N/mm
D	Measured displacement	mm
D_B	Part of the displacement due to the device	mm
D_S	Part of the displacement strictly related to the sample	mm
E	Modulus of elasticity	Pa
E_0	Mean activation energy	$J.mol^{-1}$
E_i	Activation energy of the reaction *i*	$J.mol^{-1}$
E_L	Longitudinal modulus of elasticity	Pa
E_R	Radial modulus of elasticity	Pa
E_T	Tangential modulus of elasticity	Pa
F	Force	N
L	Length	mm
L_0	Initial sample length	mm
L_C	Length correction	mm
MFA	microfibril angle	Degrees
ML	Mass loss	%
MOE	Modulus of elasticity	Pa
P	Perimeter	m
R	Universal gas constant	8.314 $J.(mol.K)^{-1}$
R_{30}	Dimensionless stress at the end of the relaxation interval (t = 30 s)	-
RH	Relative humidity	%
S	Shrinkage	%
S_0	Initial cross-sectional area	mm^2
T_0	Initial temperature	°C
T_g	Glass transition temperature	°C
Tm	Melting temperature	°C
T_t	Temperature at time t	°C
V_i	Hydrolyzed mass fraction of the reaction *i*	-
V_i^{∞}	Total mass fraction that can be hydrolyzed	-

Greek letters

		Unit
α	Thermal expansion coefficient	K^{-1}
α	Degree of conversion	-
α	Asymptotic value	-
β	Shrinkage coefficient	-
ε	strain	-
ε_d	Densification strain	-
λ	Wavelength	nm
σ	Stress	Pa
σ	Standard deviation of the energy distribution	$J.mol^{-1}$
σ_e	Equilibrium stress	Pa
τ	Characteristic time of relaxation	s

General Introduction

There is currently much evidence of the human impacts on climate and the scientific community seems to agree on the need of an urgent response. In this context, biomass has gained increased attention as a renewable resource. The use of biomass-based fuels (biofuels) is indeed a very promising technological response towards mitigating the CO_2 emissions and reducing the dependency on fossil feedstocks. Another sector with great potential for biomass utilization is that of organic chemicals, as the building blocks extracted or derived from biomass serve as monomers or platform molecules with countless options of production pathways and final products.

In comparison with the first generation, second-generation biofuels and bio-based chemicals offer the additional advantages of having a lower water and land footprints and a lower direct competition with food production. The latter is associated to the fact that the feedstocks used by this technology (lignocellulosic biomass) may be inedible part of plants. Despite its numerous advantages, lignocellulosic biomass presents a major drawback for its industrial utilization: it is extremely recalcitrant to fractionation. Two approaches are traditionally used to enable lignocellulosic biomass valorization: the thermochemical pathway – based on heat and metal catalysts – and the biochemical pathway – involving enzymes and microorganisms, and to which this work is devoted.

In the biochemical pathway, pretreatment is a key step in overcoming the recalcitrant structure of lignocellulosic biomass, as it promotes the accessibility of polysaccharides to enzymatic hydrolysis. Among the available pretreatment methods, steam explosion is the most employed and cost-effective. It consists of two steps, a hydrothermal treatment and an explosion step. The changes suffered by biomass during hydrothermal treatment take place at multiple scales and have a great impact on the explosion step efficiency. Furthermore, these modifications dictate the profitability of the entire production chain. Firstly, because pretreatment critically affects the overall conversion yields. Secondly because pretreatment itself is an expensive and energy-demanding process. Optimizing this step is therefore crucial.

Due to the complexity of lignocellulosic biomass – and, particularly, wood – this question cannot be addressed from a single point of view. Indeed, the properties at different scales influence one another and macroscopic properties can have as important an impact as chemical ones on the choice of a pretreatment method and its conditions. Additionally, although rich in information about the mechanisms of biomass degradation during the process, chemical analyses are time-consuming and involve destructive tests. Therefore, the possibility of carrying out continuous measurements is certainly attractive, greatly reducing the number of tests required.

This doctoral project proposes a multiscale approach to observe and understand the modifications suffered by biomass during hydrothermal treatment. Within this aim, the combination of three disciplines—mechanics, chemistry and imaging—can help developing tools to the design of industrial systems. The ultimate goal is to provide macroscopic mechanical indicators of the treatment kinetics likely to give rules to optimize the residence time and treatment temperature during hydrothermal treatment.

First, from a chemical perspective, classical wet chemistry analyses allow the quantification of concomitant hydrolysis and degradation of biomass. As biomass can behave very differently depending on the interaction of its different components and on the morphological organization, imaging characterization is also necessary. Finally, from a macroscopic point of view, the continuous assessment of biomass mechanical properties can provide insight on the effect of residence time. Additionally, the development of a predictive model, which is always desired and sought, can reinforce their value as an indicator of biomass deconstruction.

Manuscript outline

The overall objective of this research was achieved in the various phases of this work, presented as distinct chapters.

Chapter I provides the necessary and useful notions for understanding the study. In a first stage, these notions are mainly related to the use of lignocellulosic biomass as a feedstock for the production of biofuels and bio-based chemicals: the interests and challenges involved, the productions pathways and the characteristics of this material influencing its suitability with processes. A second part focusses on the hydrothermal treatment and the changes it causes on biomass.

Chapter II covers the description of the methodology developed throughout this work, from sampling to imaging techniques and the mechanical tests. All the actions taken during methodology development aimed at improving the quality and reliability of the results and include some preliminary results.

Chapter III corresponds to the experimental study of the influence of hydrothermal treatment on the anatomical and topochemical properties of biomass. These features were evaluated using imaging techniques, namely: confocal Raman microscopy, X-ray nano-tomography and electronic microscopy. The influence of the location of different components through the cell wall on the chemical changes undergone by biomass is discussed. Anatomical parameters such as cell wall thickness and cell circularity are also evaluated and their potential as indicators of the treatment severity is highlighted.

In the search of a good macroscopic indicator of biomass deconstruction, **Chapter IV** explores two mechanical properties of wood: the apparent modulus of elasticity and the viscoelastic relaxation. Through these means, different treatment conditions are compared (temperature and acidity). Their capacity of reflecting different phenomena taking place during hydrothermal pretreatment is demonstrated and their relevance as macroscopic indicators is discussed.

Chapter V looks at the changes suffered by biomass during hydrothermal treatment from both chemical and dimensional perspectives. From continuous shrinkage measurement, a Distributed Activation Energy Model (DAEM) is identified and its ability to predict biomass chemical degradation is highlighted.

A general conclusion, as well as suggestions for future work and possible applications of the innovative outcomes of this work to the design or optimization of industrial plants conclude this manuscript.

CHAPTER I. Literature review

A. Lignocellulosic biomass as a feedstock for biofuels and bio-based chemicals

1. General context

Global warming is one of the contemporary society's primary concerns. There is currently much scientific evidence of the human impacts on climate and of the need of an urgent response. In its most recent report [1], the Intergovernmental Panel on Climate Change (IPCC) highlighted the importance of keeping warming within 1.5 °C above pre-industrial levels (data relative to 1850-1900). This value was stablished in order to limit several impacts concerning human welfare, water supply, biodiversity and so on. To do so, unprecedent efforts are required. They estimate that current net CO_2 emissions should decrease by 45 % until 2030 and should reach net zero by 2050 (Figure 1).

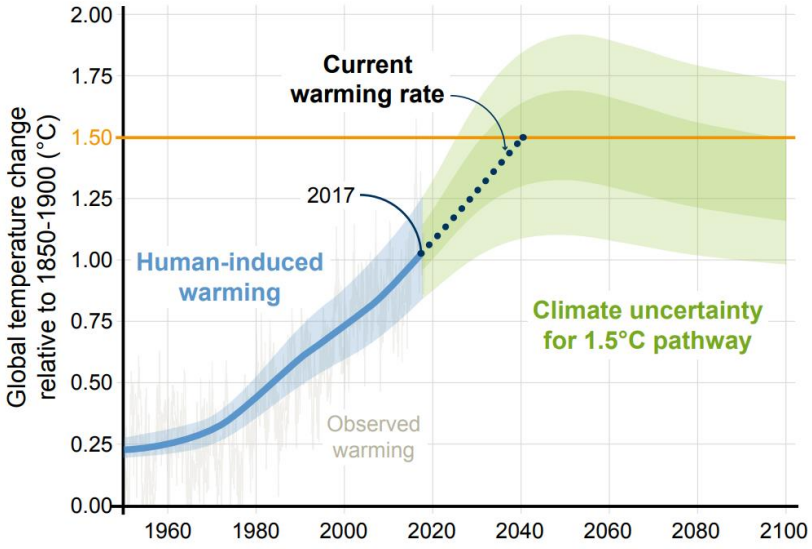

Figure 1. Human-induced global warming. The blue curb shows the current level (ca. 1 °C) and the green curb shows the pathway to limiting global warming to 1.5 °C. It requires immediate reductions of greenhouse gas emissions, reaching a net zero by 2050 [1].

As the world's primary energy source, fossil fuels are a central issue, representing approximately 82 % of the net greenhouse gas (GHG) emissions in the world [2]. In addition to the environmental impact, the fluctuation of crude oil prices and fuel policy changes also encourage the switch from a fossil fuel based economy to a carbon-neutral bio-economy [3,4].

In the search for sustainable alternatives, biomass has gained increased attention. Beyond heat and power generation, two sectors could particularly benefit from the advantages of this type of feedstock: transportation and chemicals.

The transport sector was responsible for 25 % of the European GHG emissions in 2017 [5], with 92 % of its final energy demand consisting of oil products [1]. Most of the advances towards

renewables in this sector still rely on public policies. In its revised Renewable Energy Directive for 2020-2030, the European Union (EU) has set that renewable energy must account for at least 14 % of the energy consumed by road and rail transport by 2030 and that second generation (2G) biofuels should represent at least 3.5 % of the total. Concerned with the possible land-use change impacts and food security, EU also stablished a maximum of 7 % first generation (1G) biofuels [6].

Even though there is an agreement about the importance of biofuels in limiting the global warming to 1.5 °C, they seem to be a rather temporary solution. In the long term, some countries are favoring electric vehicles over internal combustion engine vehicles, the main reason probably being the land limitation in order to respond to such a large market. Of course, some exceptions exist, such is the case of Brazilian ethanol and the aviation market [1,6].

Another sector that represents great potential for biomass is that of organic chemicals, which has been historically constructed around fossil resources. Indeed, while there is a large variety of renewable energy sources (wind, solar, hydroelectricity), the production of bio-based materials and chemicals largely depends on biomass [7]. Today, around 92 % of organic chemical products come from petroleum, not to mention the fossil fuels needed for providing the large amount of heat and power needed by this industry [8]. The building blocks contained in biomass could be an answer for a more sustainable chemical sector, with countless options of production pathways and final products [9] (Figure 2).

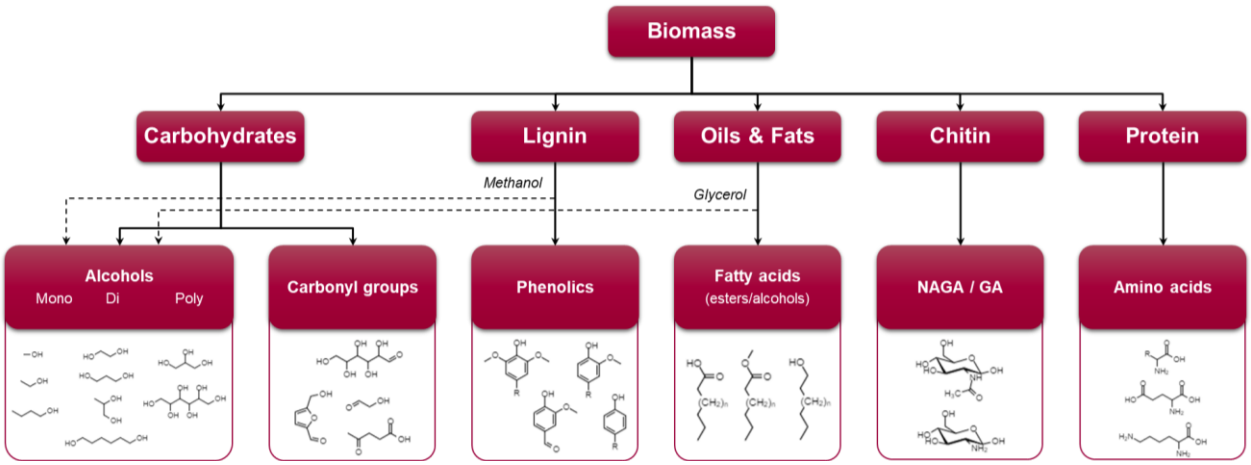

Figure 2. Examples of platform molecules obtained from biomass. GA: glucosamine; NAGA: N-acetyl-D-glucosamine. Adapted from [10].

Even though mitigating the CO_2 emissions and reducing the dependency on fossil feedstocks might seem a good argument for the use of renewable feedstocks, converting the fossil-based into a bio-based chemical industry requires other driving forces. As an example, it could be said that there is a market potential for bio-based products to respond to the increasing demand from consumers and that biomass opens up the possibility of creating a whole new product portfolio, instead of just finding equivalents to the fossil-based ones [11].

However, competing with petroleum-based products is not easy since a lot of effort has been put in the past century to optimize their production. In order to meet the demand of the consumers,

cost effective technologies must be developed for eliminating the bottlenecks of biomass valorization.

2. The specifics of lignocellulosic biomass

The upcoming importance of lignocellulosic biomass as a renewable resource is obvious. As is the case of the first-generation (1G, based on sugar or starch crops), the second-generation (2G) biofuels and biochemicals can offer a mitigation of CO_2 emissions and improve domestic energy security. Furthermore, 2G products present additional advantages, namely a lower water and land footprints, and a lack of direct competition with food production [12]. The latter is associated to the fact that the feedstocks used by this technology (lignocellulosic biomass) are inedible. As for their sources, they can be either specifically grown for a biorefinery purpose or come from forestry, agricultural and agro-industrial residues [9].

Despite its numerous advantages, the application of lignocellulosic biomass to produce biofuels and biochemicals also presents some challenges. The major part of them originate from its recalcitrance. Indeed, plants have gone through millions of years of evolution to resist to biological and chemical attacks, as well as to have mechanical resistance. Overcoming those obstacles requires reducing the complexity of lignocellulosic structure (CHAPTER I.B). Traditionally, two approaches can be used: the biochemical pathway – involving enzymes and microorganisms - or the thermochemical pathway – that uses heat and metal catalysts. Whether one is preferable to the other has been subject to considerable discussions. The answer to this question depends on many factors, such as the feedstock and the desired final product, and should consider socioeconomical and environmental aspects [13,14]. Both of them have their advantages. The biochemical conversion is often viewed as highly selective, while the thermochemical one is more robust and more adaptable to a wide range of feedstocks [14]. The research questions in this study focused on the biochemical pathway, which is going to be detailed in the following section. For the sake of simplicity and because it is the most common product of this conversion method, ethanol is often going to be explored as molecule of interest.

3. The biochemical pathway

The biochemical production of ethanol is not an innovation made by modern biotechnology. Humankind has actually been using alcoholic fermentation in its daily life for at least 300 centuries [15]. The alcoholic fermentation consists on the conversion of hexoses (C6 sugars) into ethanol by the metabolism of microorganisms according to the following equation [16]:

$$C_6H_{12}O_6 \rightarrow 2\ CH_3CH_2OH + 2\ CO_2$$

Feedstocks like sugarcane or sugar beet (1G) contain sucrose, a disaccharide composed of two C6 sugars, glucose and fructose, linked by a α-1,2-β bond. This linkage can easily be broken by invertase, an enzyme produced by yeast and therefore making direct fermentation of sugarcane and sugar beet possible. Ethanol production is also possible using starch – e.g. from maize crops (also from 1G). In this case, a prehydrolysis step is needed to breakdown the chains of starch obtaining glucose that will later be fermented. This step is usually performed by starch-hydrolyzing enzymes [16].

Regarding lignocellulosic biomass, not only sugar molecules are present in the form of polysaccharides (cellulose and hemicelluloses) but they also form a strongly bonded and highly recalcitrant matrix, together with lignins (CHAPTER I.B). Thus, the main challenge of 2G bioethanol production is to obtain simple sugars from this complex structure, so that they can be used during fermentation. In addition to the enzymatic hydrolysis, another step (Figure 3) becomes necessary and is called pretreatment.

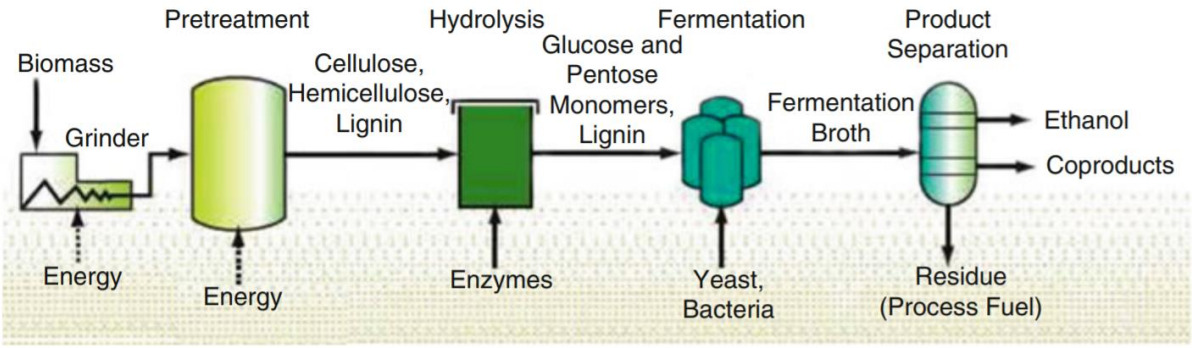

Figure 3. The different steps of lignocellulosic biomass conversion into ethanol [17]

4. Pretreatment: an essential step towards lignocellulosic ethanol

As previously mentioned, in lignocellulosic biomass, sugars are present in the form of cellulose and hemicelluloses, which are both polysaccharides. Polysaccharides are not directly available for fermentation, requiring thus an enzymatic hydrolysis. In the case of cellulose, the enzymatic hydrolysis is carried out by cellulases. Cellulases constitute the class of enzymes able to hydrolyze β-1,4 linkages in cellulose chains, releasing oligosaccharides, cellobiose, and glucose [18]. Due to its high crystallinity and to the protection provided by lignins, however, cellulose is hardly accessible to enzymes. Therefore, a pretreatment is needed prior to the enzymatic hydrolysis (Figure 4) [19].

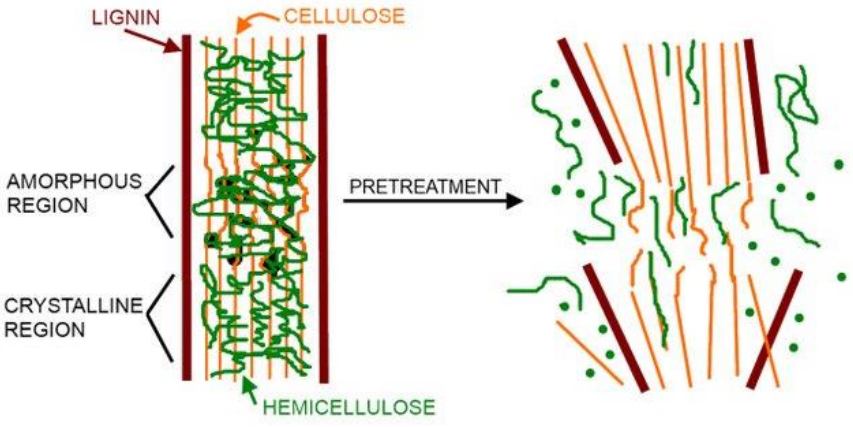

Figure 4. Schematic representation of the effect of pretreatment on lignocellulosic biomass [20]

Optimizing the pretreatment step is crucial for ensuring the rentability of the whole production chain because of a double effect. Firstly, the pretreatment is itself an expensive and energy-demanding process. Secondly, because the effectiveness of pretreatment will critically affect the overall conversion process. It explains the importance of this step and the importance of studying this subject. To ensure a cost-effective and environmental friendly process, an ideal pretreatment should meet the following requirements [21–26]:

- Separate biomass components (cellulose, hemicelluloses and lignins), with high recovery of all of them in usable forms;
- Reduce cellulose crystallinity;
- Increase cellulose surface area;
- Efficient to a large range of feedstocks;
- Minimize the use of water and chemicals. When applied, they should have a low cost and be noncorrosive;
- Minimize the production of waste;
- Be able to handle large size particles (biomass milling is energy-intensive and expensive);
- Fast reactions;
- Products formed should not have processing or disposal challenges;
- Promote high enzymatic hydrolysis or fermentation yields with minimal operational costs.

When ethanol is the desired end product, promoting high fermentation yields means that there is little or no production of fermentation inhibitors. Since most of the known inhibitors come from sugar degradation products, it implies that sugars should be preserved.

Trying to meet most of these requirements, many pretreatments have been proposed. They can be classified into physical, chemical, physico-chemical, biological and even a combination of these approaches (Figure 5).

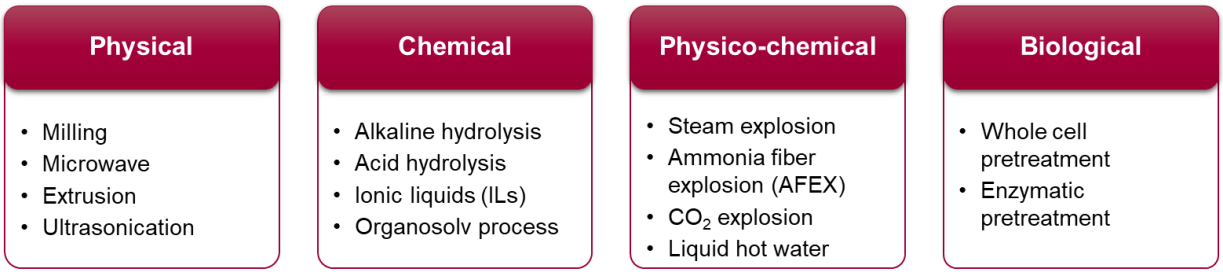

Figure 5. Diversity of existing pretreatment processes. Adapted from [19].

To date, none of these options can provide all the desired outcomes in all types of lignocellulosics [24]. The advantages and disadvantages of the leading pretreatment methods are summarized in Table 1.

Table 1. Features of leading pretreatment methods [19,23,26,27]

Pretreatment method	Advantage	Disadvantadges
Liquid hot water	• No catalysts or chemicals • Low formation of toxic materials • Low-cost reactor construction due to low-corrosion potential	• Energy intensive • Large amount of water needed
Dilute acid pretreatment	• Accelerated sugar conversion rate (especially hemicelluloses) • Lignin removal after hemicellulose removal	• Undesired sugar degradation into inhibitory products • Need of neutralization of the pretreated slurry • Corrosion of the equipments
Steam explosion	• Causes lignin trasformation and hemicellulose solubilization • Cost-effective • Low environmental effect • Limited chemicals use • High energy efficiency • High sugar recovery • Reduction in particle size and increased pore volume	• Generation of inhibitory compounds • Partial hemicellulose degradation
Alkali pretreatment	• Lignin removal • Increased carbohydrate exposure • Lower temperature than the other pretreatments	• Technique of alkali recovery yet to be improved • Long pretreatment time • Salt production • Less effective for high lignin content biomass
Ionic liquids (ILs) pretreatment	• High cellulose and lignin solubilization • Most of the ILs are recoverable and reusable • Safe and environmental friendly	• Expensive • Toxic to microorganisms and enzymes.
AFEX	• Increases accessible surface area • Reduction of cellulose cristallynity • Negligible formation of inhybitors	• Not efficient for materials with high lignin content • Large amount of ammonia and the high cost that it implies
Organosolv	• Relatively pure cellulose residue • Increased volume and surface area • Easy recovery of the solvents by distillation • Obtention of high quality isolated lignins	• Cost of the organic solvents • Energy-intense process to recover solvents • Operation under controlled conditions due to high flammability and volatility of the solvents

4.1. Steam explosion

From the existing methods, steam explosion is the most employed and cost-effective option [19]. Even though many variants to this process have been proposed, it generally does not require adding any chemicals, which is an advantage. Aditionally, it was demonstrated that it requires

almost 70 % less energy than traditional mechanical methods to attain the same particle size [19,23,26].

It consists of two steps, a hydrothermal treatment and an explosion step. The hydrothermal treatment can also be applied alone and, in this case, it is comonly called autohydrolysis or liquid hot water. During this phase the biomass is submitted to high temperatures (between 160 and 260 °C) under saturated steam conditions (which implies pressures from 0.69 to 4.83 MPa) during several seconds to a few minutes, which leads to several chemical and structural modifications of the biomass (CHAPTER I.D). This is followed by a sudden release of the pressure. Under lower pressure, part of the water that was present in a liquid state revaporizes. The resulting shear forces cause a mechanical breakage of the biomass structure [19,23,24,28].

Residence time, temperature, particle size, and moisture content are the factors that most affect steam explosion [25]. It has been found that under severe conditions, the production of inhibitors becomes drastically important [19] and that temperatures higher than 250 °C should be avoided due to the unwanted pyrolysis of hemicelluloses [29–31]. Indeed, the optimum temperature for most of lignocellulosic materials seems to be between 160 and 200 °C [23].

From a structural point of view, process temperatures of up to 200 °C are largely sufficient for water saturated lignins to go past their glass transition temperature [32]. As a result, cells separate at the middle lamella and allow for single free cells to be obtained, whereas higher temperatures can cause fiber damage [24].

4.2. Biomass mechanical properties during steam explosion

Up to now, literature on steam explosion has been paying far too little attention to the mechanical properties of biomass. Yet, studies have shown that the continuous measurement of the mechanical behavior of wood provides precious information on the chemical degradations during hydrothermal pretreatment [33,34]. More than an indicator, some authors affirm that the mechanical properties of biomass at the end of hydrothermal pretreatment can dictate its response to the explosion step [35,36]. However, they only took into consideration the plasticizing action of water adsorption (CHAPTER I.C.3.3.2) – making biomass sufficiently soft to enable a tearing effect during decompression – and not the possible mechanical changes suffered during treatment.

The extent to which the mechanical properties change during hydrothermal treatment and, consequently, affect steam explosion is still poorly understood. Studies correlating chemical and mechanical properties are also required. This information would contribute to a better understanding of the mechanisms involved in the steam explosion pretreatment towards its optimization.

B. Wood structure and composition

Knowing the characteristics of lignocellulosic biomass is an imperative for the optimization of the different steps in the production chain. It is important to note that although there are common characteristics to all lignocellulosic biomasses, each raw material has its own specificities. Because it represents one of the major sources of lignocellulosic biomass [37], wood was chosen as a model biomass in this research. Throughout this dissertation, the terms "lignocellulosic biomass" and "wood" will be used indiscriminately.

Wood as it is known today is a result of millions of years of evolution. In the living tree, it evolved to ensure essential roles, such as mechanical support and nutrients transportation. As many other biological materials, it presents a high level of organization, in different scales. The interest, but also the complexity of this material come from its hierarchical structure. The response of wood to different treatments depends not only on its chemical composition but also on how the components interact with each other, on their localization within the cell wall and the structures at the upper scales. The effect at a molecular level is reflected in all other scales of the material. It is therefore necessary to have some knowledge on wood structure and properties, before starting to study the effects of hydrothermal pretreatment.

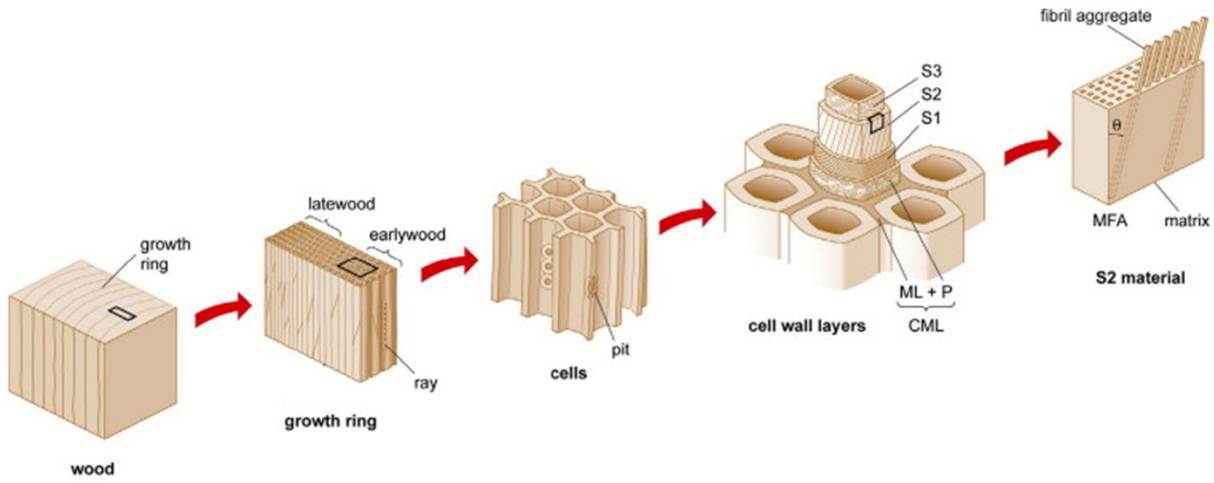

Figure 6. Hierarchical structure of wood. Adapted from [38]. ML: middle lamella; P: primary wall; S: secondary wall (with its sub-layers: S1, S2 and S3); CML: compound middle lamella; MFA: microfibril angle.

Figure 6 presents the different hierarchical structures of wood. From a macroscopic point of view, wood is a multilayered orthotropic material. Microscopically, it is possible to see the different types of cells and their morphology. The different cell wall layers and the organization of the different components within these layers are called the ultrastructure of wood [39]. In this study, the effects of hydrothermal pretreatment are studied (with different depth levels) at all these scales, which are presented in greater detail in the next sections.

1. Sub-parietal properties

Wood is mainly composed of three polymers: cellulose, hemicelluloses and lignins. Other substances with lower molecular weight, like pectin, ashes and extractives, can also be found but they are more specific to each species and will generally be present in lower quantities.

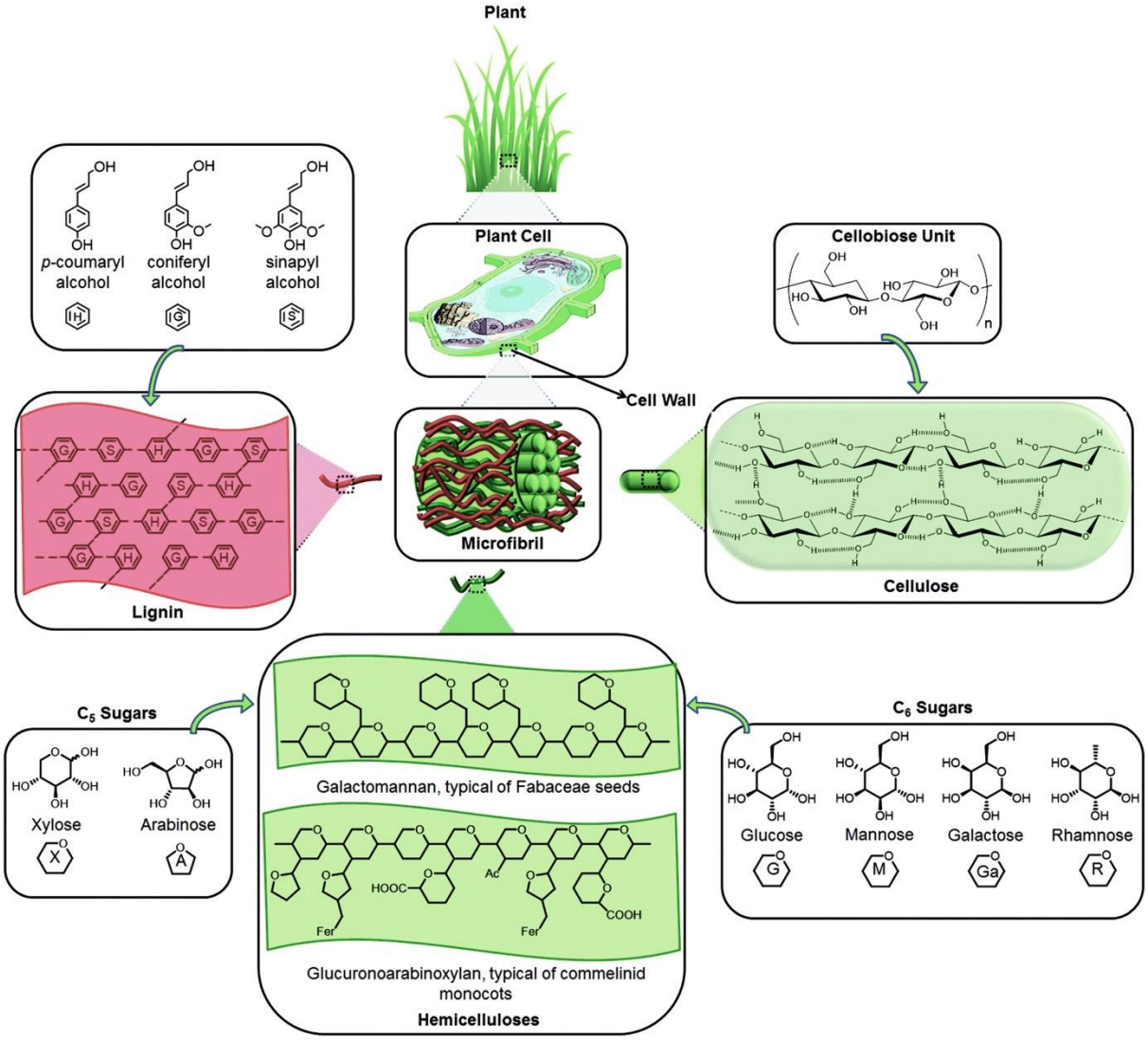

Figure 7 Composition of lignocellulosic biomass [40]

1.1. Cellulose

Being synthesised by many different species, from bacteria to plants, cellulose is the most abundant biopolymer on earth [41]. In wood, it corresponds to approximately 40-45 % of its dry weight [42]. It is a linear polymer containing around 9 and 10 thousand units of β-D-glucopyranose bond together by glycosidic linkages (C-O-C) at the C1 and C4 positions [43]. The stabilization of these long molecular chains in ordered systems is ensured by the presence of hydroxyl functional groups, capable of interacting with each other to form intra- and intermolecular hydrogen bonds. Cellulose chains alternate crystalline and amorphous regions

(Figure 8). They end up by packing together alongside one another in a highly ordered manner forming microfibrils which, in turn, form microfibril bundles or aggregates (Figure 8). This crystalline nature is what gives cellulose its main properties as a material: insolubility in water and most organic solvents and high tensile strength [44]. The insoluble character of cellulose, together with the poor accessibility of its crystalline region, make it very recalcitrant.

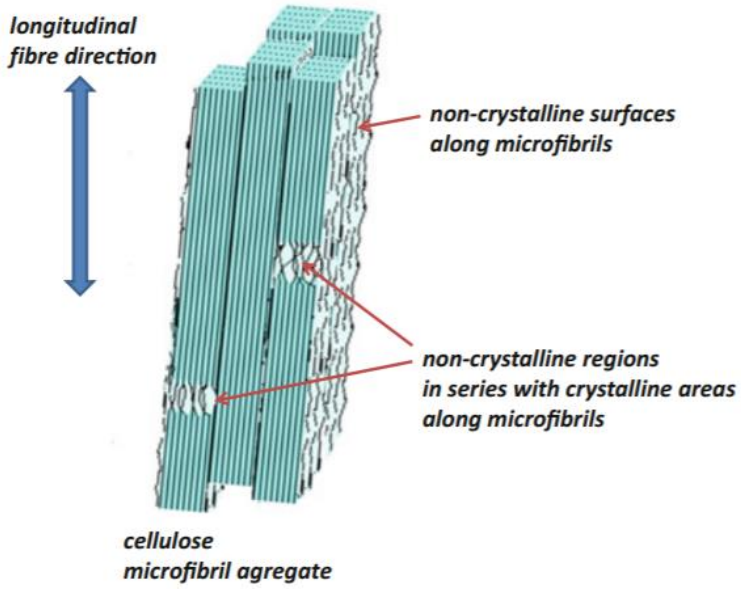

Figure 8. Schematic representation of the organization of non-crystalline cellulose areas in a cellulose microfibril aggregate [45].

1.2. Hemicelluloses

Hemicelluloses are heteropolymers whose main constituents are pentose sugars (L-arabinose and D-xylose), hexose sugars (D-glucose, D-mannose and D-galactose) and uronic acids (β-D-glucuronic acid, α-D-4-O-methylglucuronic acid and α-D-galacturonic acid). Unlike cellulose, hemicelluloses are branched polymers and have much shorter molecular chains (degree of polymerization, DP, of 50–200). Large substitute groups replace sugars hydroxyls, which makes a crystalline structure very unlikely. This difference on the physical structure is responsible for important differences in the chemical reactivity of hemicelluloses when compared to cellulose. For example, a more branched polymer is more soluble and more accessible to chemical and enzymatic attacks [43,46].

A large variety of hemicelluloses can be found in nature. They are classified according to the main sugar residue in the backbone. The two main types in wood are xylans and glucomannans (Table 2).

Table 2. Main wood hemicelluloses, expressed as a percentage of the dry weight ([10] cited by [11]).

Hemicellulose	Occurrence	Percentage in wood (%)
Galactoglucomannan	Softwood	5-8
Glucomannan	Softwood	10-15
Arabinoglucuronoxylan	Softwood	7-10
Glucuronoxylan	Hardwood	15-30
Glucomannan	Hardwood	2-5

In the case of xylans, the main chain is composed by xylose units linked together by β(1→4) glycosidic bonds. The specific characteristics of the side groups attached to this backbone depend on the species. In general, hardwoods have one 4-O-methyl-glucuronic acid unit attached every 10 units of xylose. Of these xylose units, 3 to 7 are acetylated at C3 and C2 (less common) positions (Figure 9). Given this proportion, xylose is by far the major hemicellulose monomer in hardwoods. As for softwoods, the ratio of 4-O-methyl-glucuronic acid is one for every 6 units of xylose and some arabinose side groups can eventually be found [43,46,49].

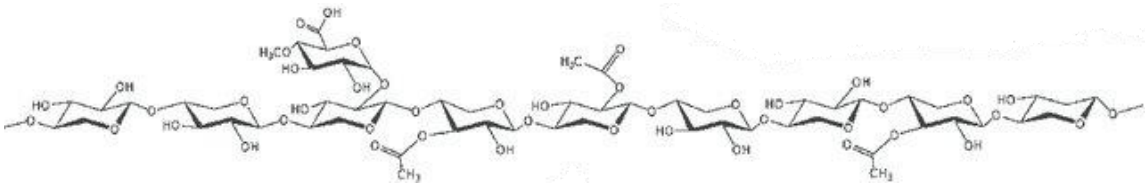

Figure 9. Chemical structure of O-acetyl-4-O-methyl glucuronoxylan, a typical hardwood xylan. Adapted from [50].

Glucomannans, as the name says, are heteropolymers of glucose and mannose. Table 3 presents the typical composition of hardwoods and softwoods glucomannans. In hardwoods, it corresponds to 3 to 5 % of the dry weight and is usually found at a mannose to glucose ratio of 2:1, with no side chains. Glucomannans are more abundant in softwoods and can represent up to 25 % of their dry weight. The backbone often presents a mannose to glucose ratio of 3:1, 25 % acetylated, and a galactose side chain attached to the C6 of every 15 or 30 units of mannose [43,46,49].

Table 3. Ratio between sugar and acetyl units in wood glucomannans. Adapted from [46].

	Mannose	Glucose	Galactose	Acetyl
Hardwoods	1-2[a]	1	-	-
Softwoods	3[a]-4	1	0.1-0.2	1

a More common

1.3. Lignins

Lignins are the second most abundant polymer in lignocellulosic biomass, after cellulose. In hardwoods they account for 18-25 % of wood dry mass, whereas in softwoods they represent

from 25 to 35 % of the dry mass of wood [42]. Lignin is the term used to describe a family of amorphous aromatic polymers of high molecular weight present in plant cell walls. They are often referred to in plural due to the high variability of their structure, presenting no regular structure. Despite this complexity, they can be defined as polymers resulting from the oxidative polymerization of three main hydroxycinnamyl alcohols (monolignols), that differ from each other in the degree of methoxylation: sinapyl alcohol, coniferyl alcohol and p-coumaryl alcohol (Figure 10). They are also called syringyl (S), guaiacyl (G) and *p*-hydroxyphenyl (H) units when polymerized in lignin [43,51].

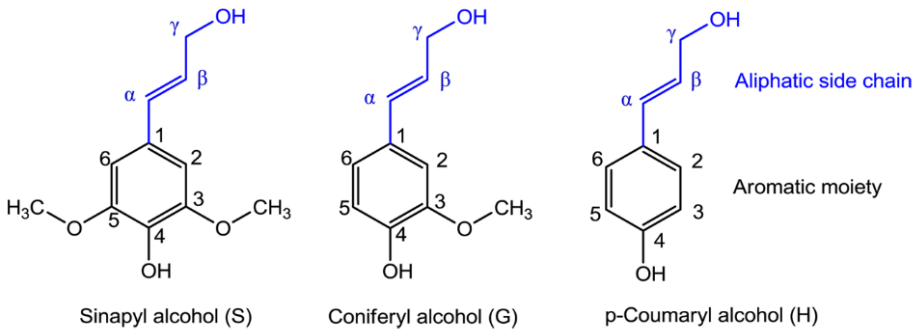

Figure 10. Three main lignin precursors: sinapyl alcohol, coniferyl alcohol, and p-coumaryl alcohol [52].

The proportion of each unit depends on many factors, such as the source of biomass, the part of the plant and even the location of lignins within the cell wall. A global comparison between the percentage of each unit in hardwoods and softwoods can be found in CHAPTER I.D.1.3. Softwood lignins are mainly composed of G units and present a rather low variability between species [53,54]. Hardwood lignins are composed of S and G units. The ratio between these two units (S/G ratio) depends largely on the species – between 0.5 and 4 [42] – and determines important structural features of lignins, such as the degree of condensation and the quantity of β-O-4 linkages [53]. Some authors have also reported that a higher S/G ratio resulted in an increased degradability of lignins [55]. That is because the steric repulsion caused by the presence of an extra methoxyl group in the C5 position keeps it from cross linking, resulting in a less condensed, more linear structure and in a lower molecular weight [43,52].

The linkages between the primary units is another source of variability on the structure of lignins. β-O-4 are the most abundant linkages. In poplar, for example, they account for 69 % of the total inter-unit linkages, while β-β and β-5 represent only 28 % and 3 %, respectively [56]. They are also the weakest ones and, thus, the main target during biomass pretreatments [57]. Figure 11 shows a lignin model, with the main interunit linkages usually found.

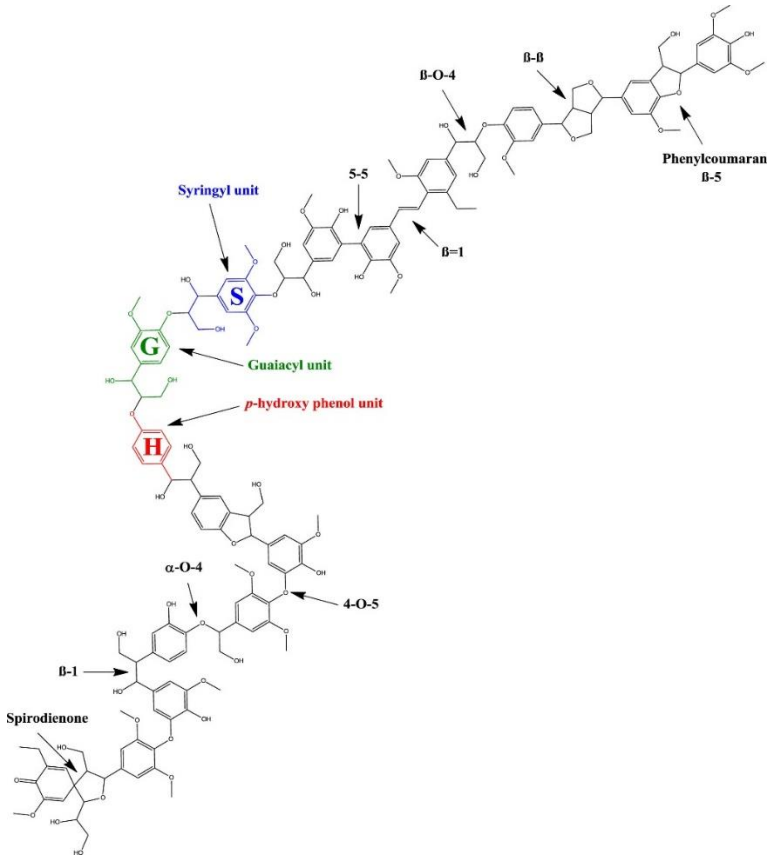

Figure 11. Schematic representation of a lignin fraction and its interunit linkages [58]

It is generally accepted that lignins are not simply deposited between the polysaccharides of cell walls but are bound with them through covalent and non-covalent bonding (Figure 12) [59]. The structures thus formed are called lignin-carbohydrate complexes (LCC) [49,59,60]. This intimate association between lignins and polysaccharide fractions constitutes a major challenge of biomass pretreatment due to the difficulty in separating them [49,60].

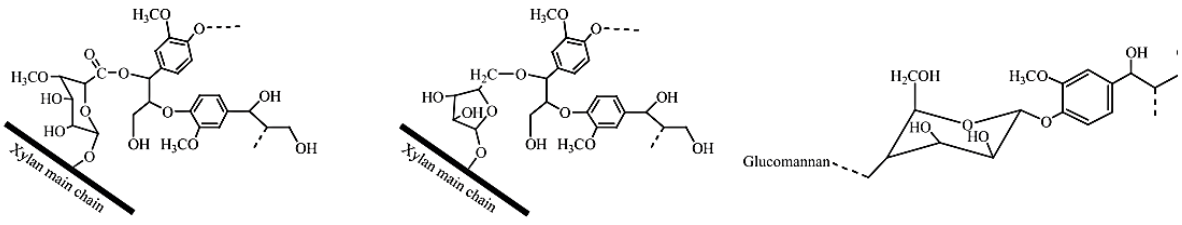

(a) (b) (c)

Figure 12. Examples of covalent bonds between lignins and carbohydrates: (a) ester bond to xylan; (b) ether bond to xylan; (c) phenyl glucoside bond to the reducing end of glucomannan [61].

Due to the aforementioned properties, lignins have three main functions on plants: providing compression strength to the cell wall, increasing its hydrophobicity (which is useful for water transportation) and acting as a barrier for chemical and biological attacks [43,51,61].

1.4. Ultrastructure

As previously mentioned, wood cell wall is a multilayered structure formed from inside to outside the cell by successive deposition of materials. As the result of the growing of a living cell, the cell wall responds to cell's specific needs during its development and to those of the plant once the maturity has been achieved. The cell wall is composed of three main regions, namely: the intercellular layer or middle lamella (ML), the primary cell wall and the secondary cell wall (Figure 13) [43].

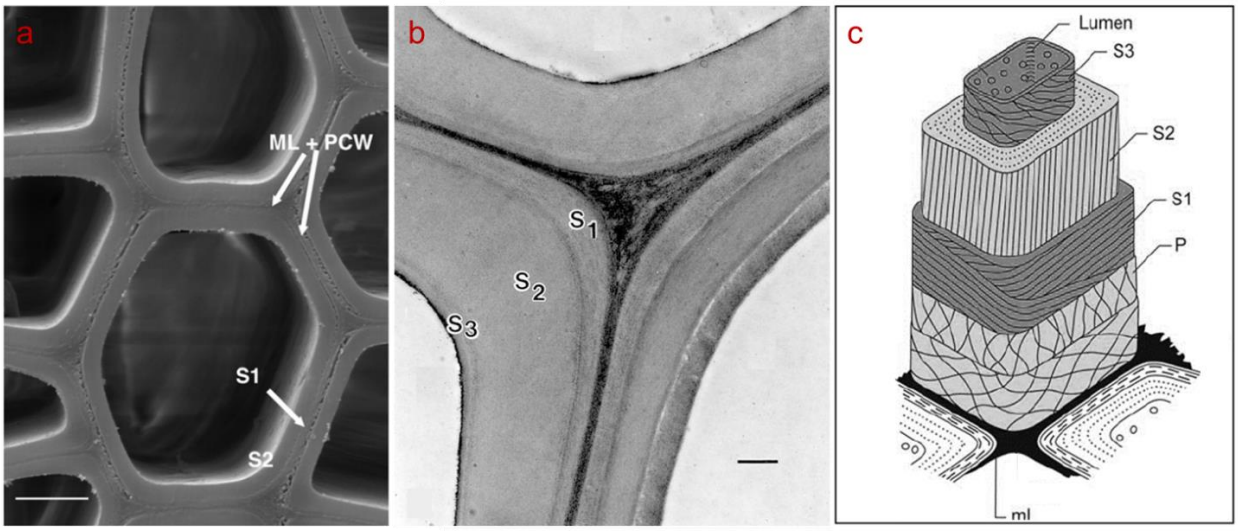

Figure 13. (a) Scanning electron microscopy (SEM) and (b) transmission electron microscopy (TEM) images of a poplar fiber in which the different layers of the cell wall can be identified and (c) a schematic representation of these layers with the preferred microfibril orientation. Adapted from [62], [63] and [47]. The scale bars correspond to 5 µm (a) and 0.5 µm (b).

The intercellular layer is responsible for connecting each cell with its neighbors. No cellulose microfibrils are observed in this region, whose composition evolves during cell development. In its early stages, it is mainly pectic, becoming posteriorly highly lignified.

The primary cell wall (P or PCW) is a thin membrane (0.1-1 µm) [64] composed of cellulose, pectin and hemicelluloses that appears just after the duplication. At this moment, cell requires an expansible membrane, allowing it to grow longitudinally and radially. Due to a reorganization during cell enlargement, this layer presents roughly organized cellulose microfibrils. The primary cell walls of two adjacent cells and the intercellular region between them is called compound middle lamella (CML).

Once the cell has achieved its maximum size, the secondary (S) cell wall begins to be formed. Cellulose is the main constituent of the S layer. It is the first macromolecule to be deposited, in the form of highly organized microfibrils, oriented parallelly. Hemicelluloses are aggregated just after, with the main chains being placed around cellulose microfibrils and the whole structure being reinforced by the addition of branching chains. Finally, lignin precursors are spread throughout the cell wall and polymerize *in situ* from the cell corner towards the center of the cell, filling the voids of the saccharide matrix. Consequently, the cell wall thickens and the fiber shrinks longitudinally, provoking growth stresses in wood [65]. The characteristics of lignins highly

depend on its location. In the intercellular region, it has enough space to freely polymerize, forming preferentially spherical structures of more condensed lignins. In the S region, however, due to the presence of polysaccharides, it presents more elongated forms (following microfibril orientation) and forms LCCs, where lignins are less concentrated and more loosely packed [65,66].

The secondary cell wall is the thickest layer and is composed of three sub-layers, called S1 (the outer one), S2 and S3 (the inner one). Each sub-layer differs from the others in terms of chemical composition, thickness (Figure 14) and microfibril angle (MFA - Figure 6). The S1 layer is 0.1 to 0.2 µm thick and presents a roughly perpendicular microfibril orientation related to the longitudinal direction [67]. The thickest sub-layer is S2, reaching up to 5 µm thick in latewood [67]. The presence of long microfibrils, oriented almost parallelly to the fiber axis (MFA of 5 to 30° in the case of normal wood [68]), is considered as the main cause of the anisotropic behavior of wood [48]. This behavior is reflected in almost all wood properties, from shrinkage to strength. S3 has the same thickness as S1, with MFA from 30 to 90°. From a mechanic point of view, the variation of MFA between secondary wall sub-layers is very important, increasing the rigidity and the strength of wood [64].

The distribution of the main cell wall components throughout the different layers of hardwood and softwood is summarized in Figure 14.

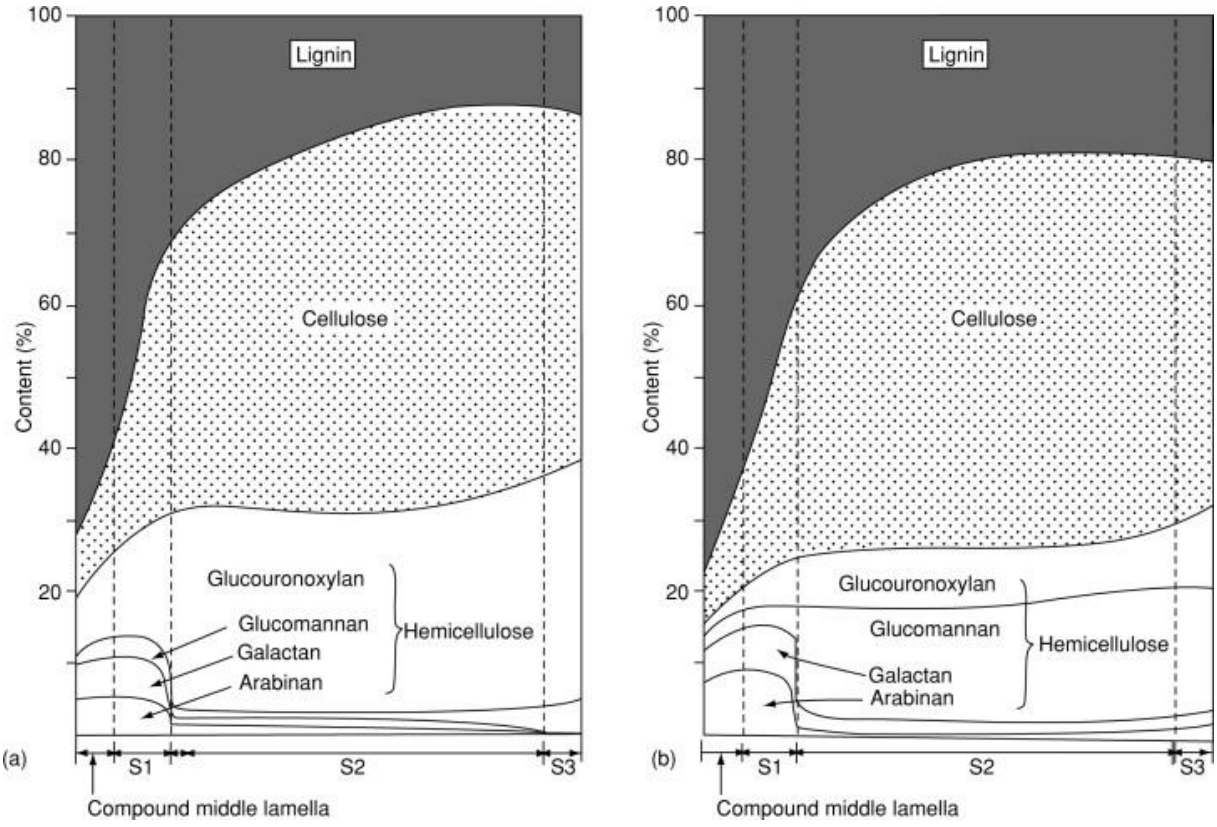

Figure 14. Distribution of the main constituents in (a) hardwood and (b) softwood cell walls [46]

For many years, assessing wood properties and composition at the parietal scale was almost impossible. The former available techniques would either provide information on the chemical composition, as is the case of classical wet chemistry techniques, or allow the visualization of cell

wall morphology (e.g., by electron microscopy), without further information on the molecules present. Some methods existed to obtain parietal organization of wood components, but they could drastically change the native state of the sample, as they required either the isolation of each morphological region, embedding the samples or chemical treatments [69].

Even tough fully understanding cell wall structure and composition remains a great challenge, a lot of progress has been done on this field, thanks to *in situ* techniques such as Raman micro spectroscopy. It is a powerful tool for this purpose and deserves a parenthetical comment (CHAPTER I.B.3).

2. Micro and macroscopic structures of wood (supra parietal levels)

So far, this chapter has focused on the components of wood and on the structure of a single cell. Wood is, however, a complex tissue resulting from the assembly of different cells [62], most of which are dead and hollow.

The cell arrangement depends largely on the species of the tree, but they can generally be divided into two groups: softwoods (gymnosperms) and hardwoods (angiosperms). Their typical tridimensional organizations are shown in Figure 15. When compared to hardwoods, softwoods have a simpler structure, with fewer cell types. In these trees, tracheids exert both structural and conducting functions. On the other side, hardwoods present more cell types and each of these functions is carried out by highly specialized cells. Vessels are responsible for conducting the sap, while fibers provide mechanical support [48]. These are just the main examples of cell types. Of course, there are many other elements in wood, whose presence depends on the species.

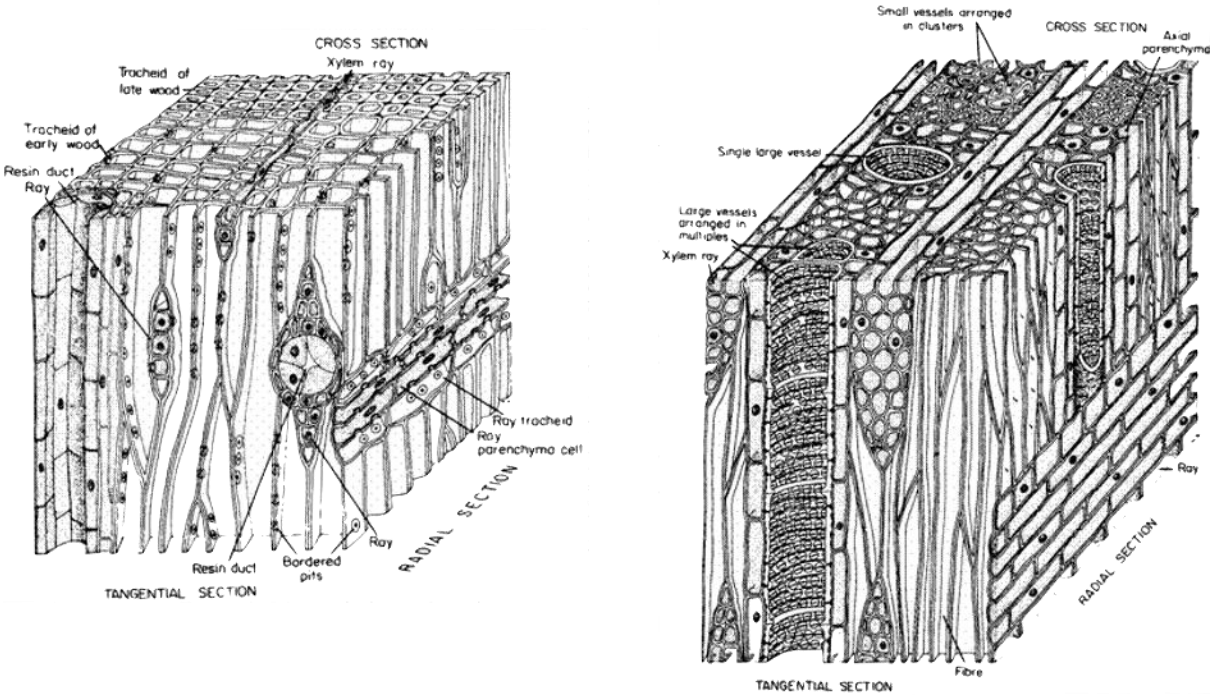

Figure 15. Tridimensional cell arrangement of softwoods (left) and hardwoods (right) [70]

From Figure 15, wood is clearly an oriented material. Most of the cells are oriented vertically, which favorizes conducting functions. From this oriented nature, one can easily guess that wood presents an anisotropic behavior. Indeed, almost all of its properties – physical, mechanical and even the way it is attacked by plagues [71] – depend strongly on the direction considered. Thus, mutually perpendicular directions are defined (Figure 16): the longitudinal direction, along the trunk axis; the radial direction, normal to the growth rings; and tangential direction, perpendicular to the grain but tangent to the growth rings [72].

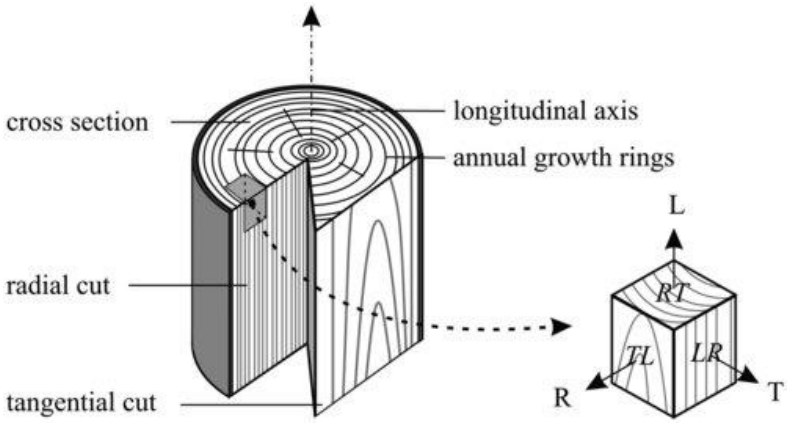

Figure 16. The three directions (L. Longitudinal, T. Tangential, R. Radial) and three main planes of wood [73]

3. Raman micro-spectroscopy as a powerful tool for the study of wood cell wall

When it comes to the application of Raman spectroscopy to the study of lignocellulosics, it is hard to miss out the works of Agarwal, Atalla and Gierlinger.

Pioneers of this field in the mid-1980s, Atalla and Agarwal [74–76] proved the capacity of Raman spectroscopy of generating valuable information on chemical and structural aspects of wood tissues. Their work allowed the first direct evidences of the orientation of cellulose [74] and lignins [74,75] on wood cell walls to be found. By this time, studies were made with Raman probes and it was not until the end of the 1990s that the first Raman imaging studies in plant research came out [77].

However, early Raman spectroscopy of lignocellulosics was confronted with two major problems: laser induced fluorescence (LIF) and large acquisition time. Indeed, LIF can be a serious drawback when using Raman spectroscopy. It is particularly true for lignocellulosic materials due to presence of lignins, which emit a considerable amount of fluorescence when excited by visible lasers. Over the past decades, the availability of longer laser wavelengths (785 and 1064 nm) and confocal microscope configurations allowed to overcome this problem, at least when it comes to native wood samples [64,78]. Another important improvement on commercially available Raman was the use of charge-coupled devices (CCD), allowing the acquisition time to be substantially reduced [64,78].

Since then, a considerable amount of literature on Raman spectroscopy of lignocellulosic biomass has been published. A first effort was put on identifying the relevant bands of the Raman spectra. At first, the contributions of wood's different components were studied separately or by means of model compounds [79,80]. When analyzing lignocellulosic biomass in its entirety, Raman spectra become as complex as the structure of this material. A summary of the main Raman bands used for the analysis of lignocellulosic materials and their respective assignment is given on Table 4. Due to the chemical resemblance of cellulose and hemicelluloses, for example, their bands are often overlapped and, thus, hard to be distinguished from each other [81]. However, the highly organized structure of cellulose results in more intense and sharper bands, as opposed to the non-crystalline structure of hemicelluloses [79].

Table 4. Main Raman bands used for the analysis of lignocellulosic materials and their respective assignments. Adapted from [81].

Wavenumber (cm^{-1})	Component	Assignment
903	Cellulose	Heavy atom (CC and CO) stretching
1096	Cellulose, Xylan and Glucomannan	Heavy atom (CC and CO) stretching
1122	Cellulose, Xylan and Glucomannan	Heavy atom (CC and CO) stretching
1150	Cellulose	Heavy atom (CC and CO) stretching; HCC and HCO bending
1274	Lignins	Aryl-O of aryl OH and aryl O-CH_3; guaiacyl ring (with C=O group) mode
1333	Cellulose	HCC HCO bending
1376	Cellulose	HCC, HCO and HOC bending
1423	Lignins	O-CH_3 deformation; CH_2 scissoring; guaiacyl ring vibration
1462	Lignins, Cellulose	HCH and HOC bending
1508	Lignins	Aryl ring stretching, asymmetric
1601	Lignins	Aryl ring stretching, symmetric
1620	Lignins	Ring conjugated C=C stretching of coniferaldehyde
1660	Lignins	Ring conjugated C=C stretching of coniferyl alcohol; C=O stretching of coniferaldehyde
2897	Cellulose, Xylan	CH and CH_2 stretching
2938	Lignins, Glucomannan	CH stretching in OCH_3 asymmetric

The reduction in the acquisition time, promoted by improvements in the Raman technology, allowed a large number of data to be collected in a shorter time. At the same time, the increasing knowledge of Raman spectra of lignocellulosics proved its interest in the study of wood cells. The combination of these factors, allied with the high resolution of Raman micro-spectroscopy, opened a new field of application: the chemical mapping of wood cell walls. It allowed information on both morphology and chemical composition to be obtained at the same time and has been widely used to the study of ultrastructural features of wood cell wall. Some relevant works on this field are the study of polymer distribution throughout the cell wall of black spruce [69] and poplar [81], to name but a few.

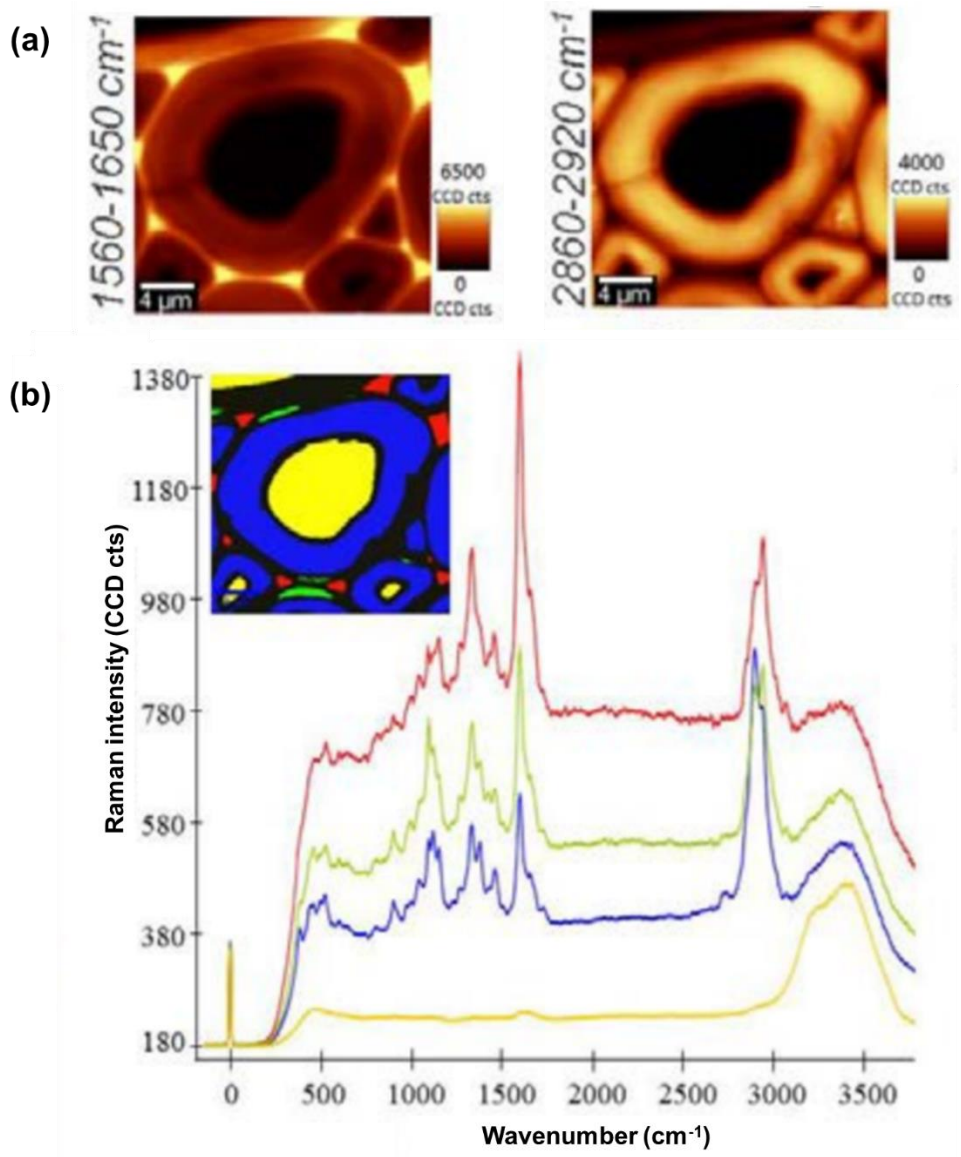

Figure 17. (a) Raman chemical mapping of a beech cell obtained by integrating over defined wavenumber areas. (b) Mean spectra of the area corresponding to different morphological regions of the cell. Adapted from [82].

Figure 17 shows examples of results that can be obtained by Raman micro-spectroscopy [82]. After scanning the sample, one obtains as much spectra as the number of pixels previously defined. One possible way to represent the collected data is to integrate over selected wavenumber areas. Each pixel of the image represents then the intensity of the selected band (Figure 17a). In wood, the band from 1560 to 1650 cm^{-1} is typically attributed to the lignin aromatic band and is stronger in the cell corners. The band from 2860 to 2920 cm^{-1} is attributed to the C-H stretching and is more intense in the zones corresponding to the secondary cell wall. It is also possible to group different regions of the image by their spectra resemblance. Figure 17b shows an example where different morphological regions of a beech cell could be identified by multivariate analysis thanks to their spectral signature.

C. How wood structure and composition impact its properties

The basis of wood structure was presented in the previous section. Every macroscopic property of wood is a reflect of its composition and architecture. The main properties regarding biomass pretreatment will be presented next.

1. Wood-water relationship

It is impossible to talk about wood without mentioning hygroscopicity, as it affects almost every single one of its properties, from the dimensions to the mechanical behavior. Indeed, wood is a highly hygroscopic material, adsorbing or desorbing water, in a search for equilibrium with the surrounding environment.

From a chemical point of view, lignocellulosic materials owe their hygroscopicity to the capacity of some groups of forming hydrogen bonds with water. These groups are mainly represented by hydroxyls and other polar groups (such as O-acetyl groups) of the polymers that constitute cell walls, more importantly the carbohydrate fraction [83–85]. Indeed, both cellulose and hemicelluloses present highly hydroxylated structures [85]. Previous works have shown that cellulose has 18.5 mmol of hydroxyl groups per gram, while 14.4 mmol/g are found in xylans [85]. However, only the OH-groups present on the surface of the microfibrils – i.e. 33 % of the total amount – are accessible to water, making it far less hygroscopic than hemicelluloses and their short, branched, open structure [83].

1.1. The different states of water in wood

Due wood's composition and structure, water can be present under three forms, represented in Figure 18:

- Liquid free water filling up the cavities of wood (such as cell lumens) by capillary or tension forces;
- Water vapor that can be found in those spaces as well;
- Bound (or adsorbed) water attached to the cell wall by hydrogen or Van der Waals bonds.

The fiber-saturation point (FSP) is the moisture content (MC) at which the cell wall is fully saturated, but no liquid water is observed at the lumen. Above FSP, wood has its lumens (fully or partially) filled with water, but no additive quantity of water is adsorbed by the cell wall. The range of MC comprised between the anhydrous state (relative humidity = 0 %) and the FSP is called hygroscopic range [86]. While in the hygroscopic range, wood physical and mechanical properties change according to the RH, which is going to be presented in the next sections.

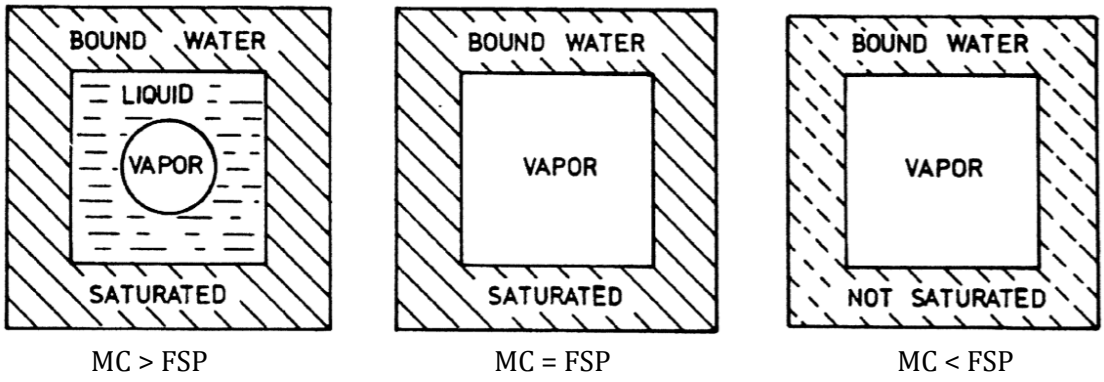

Figure 18. Schematic representation of the moisture distribution in a wood cell cross-section [87]

1.2. Equilibrium moisture content

Macroscopically, when exposed for a sufficiently long time to a given relative humidity (RH), wood stabilizes at a MC that assures its equilibrium with the ambient atmosphere. This MC is called equilibrium moisture content (EMC). Many are the factors that can influence the EMC. They can be intrinsic, such as the chemical composition of wood, or extrinsic (RH, temperature, etc.) [87].

A typical way of representing this phenomenon is a sorption isotherm. It shows a discrete representation of the EMC attained under constant temperature and RH. The typical sorption isotherm of lignocellulosic materials is presented in Figure 19.

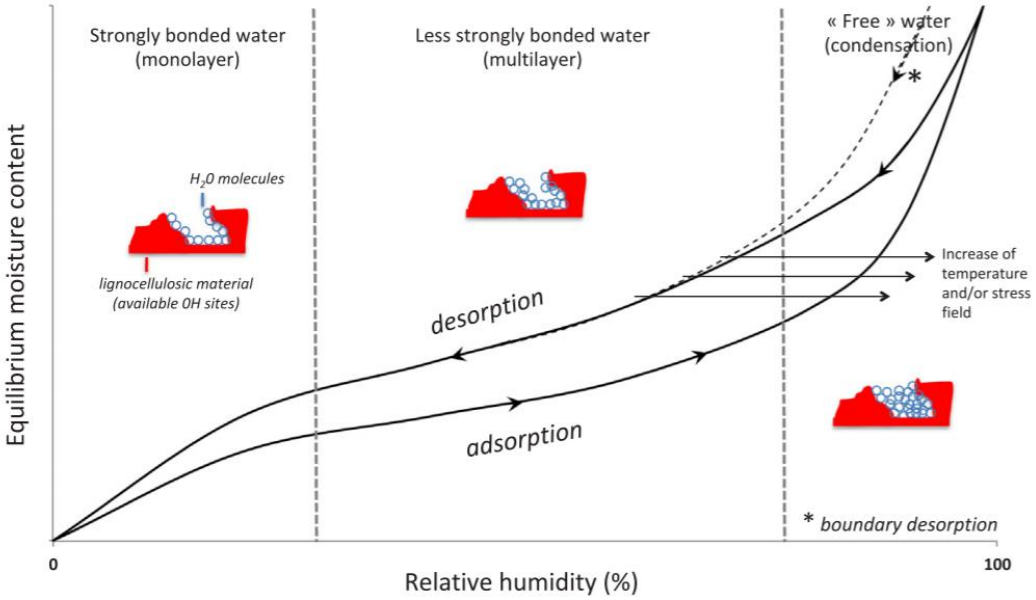

Figure 19. Typical sorption isotherm of lignocellulosic materials [88]

This sigmoidal shaped sorption isotherm presents three distinct zones (identified in Figure 19), which can be described as follows [88]:

- At low RH values, the first layer of water molecules fixates to the sorption sites of cellular wall. The binding energy is high and water molecules have low mobility;

- At intermediate RH, the water molecules attach themselves to the first layer already adsorbed. The binding energy decreases with the number of layers;
- At high values of RH, the molecules adsorbed on the different sites interact and form a continuous liquid film on the pores surface (capillary condensation).

As shown in Figure 19, increasing the temperature results in a lower EMC for a given RH. Which means that FSP is reduced as well. Indeed, with the increase of temperature, molecules intensify their state of excitation, increasing the distance and decreasing the attraction forces between molecules [89,90].

2. Shrinkage and swelling of wood

In a microscopic scale, the adsorption of water molecules to the cell wall matrix – only possible under the FSP – sunders the hydrophilic polymers and results in swelling [84]. The reflect of this behavior at a mesoscopic level depends on the architecture of the wood cell as well.

Because it is the thickest layer, S2 responds for most of these dimensional changes. In this layer, MFA is very low, which implies that microfibrils are oriented almost parallelly to the longitudinal axis of the cell. For this reason, macroscopic swelling is observed mainly in the transverse directions of wood, and almost no dimensional change can be seen along the fibers [84].

The microfibril orientation is also responsible for an anisotropic behavior between radial and tangential directions, with the tangential swelling usually being greater than radial swelling. [85].

3. Mechanical properties

Before talking about the mechanical behavior of wood two concepts must be defined: stress (σ) and strain (ε).

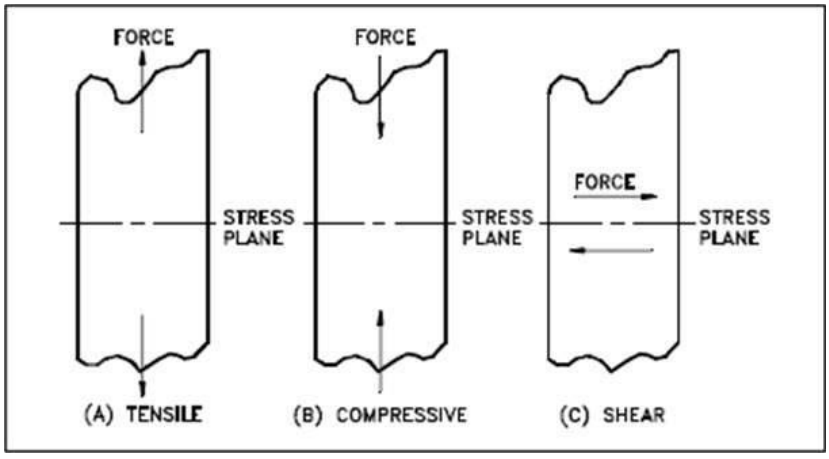

Figure 20. Primary stress types [91]

Stress is the measure of the internal forces per surface unit exerted in a material as a result of the application of an external load. Stresses can be classified in three types: tensile, compressive and

shearing stresses (Figure 20). Tensile and compressive stresses have a stress plane perpendicular to the axis of the applied force – they are called normal stresses. In the case of shear stresses, however, the stress plane is parallel to the forces from which it originates [91,92]. In this thesis we will focus on normal stresses and, more precisely, compression tests.

Stress (σ) can, thus, be equated as the force (F) applied per cross-sectional area (A):

$$\sigma = \frac{F}{A} \quad (1)$$

When subjected to an external load, a solid body deforms. Strain (ε) is the relative deformation suffered by this material as a result of the applied force:

$$\varepsilon = \frac{\Delta L}{L_0} \quad (2)$$

Where L_0 is the initial length of the material and ΔL is the difference in length caused by the application of a force.

The mechanical properties of a material reflect its behavior in the face of loads. In response to external loads, wood presents a viscoelastic response, combining both instantaneous and time-dependent strain components [93–95].

3.1. Instantaneous deformations

When analyzing instantaneous deformations, stress is usually plotted against strain, resulting in a stress-strain diagram. A typical stress-strain diagram for wood is presented in Figure 21.

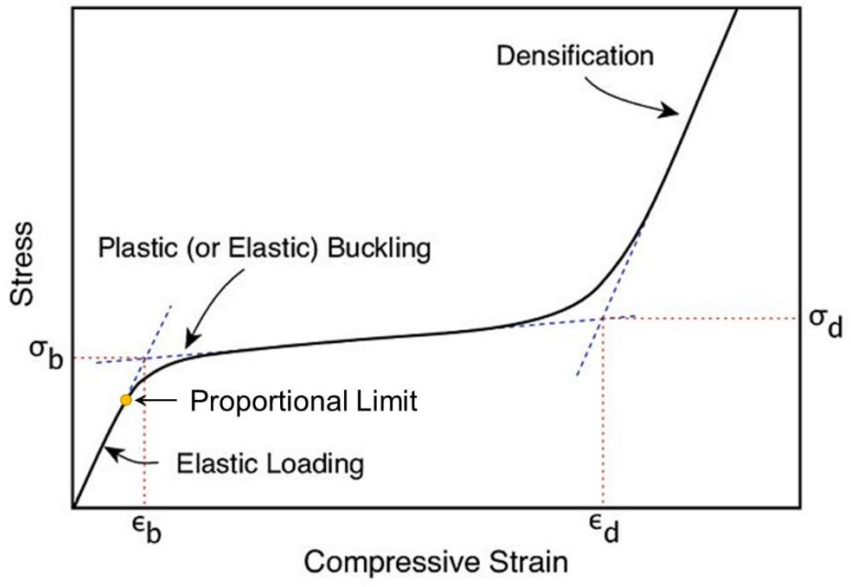

Figure 21. Typical compressive stress-strain diagram for wood. Adapted from [94].

Under low stress levels, the deformations are completely recoverable once the loads are removed. This region, comprised between the origin and the proportional limit (Figure 21), is known as the elastic range [96]. In this range, stress and strain correlate linearly according to the Hooke's law [92], which can be expressed by the equation:

$$\sigma = E \,.\, \varepsilon \qquad (3)$$

It means that stress and strain are directly proportional by a constant E, called elastic modulus, modulus of elasticity (MOE) or Young's modulus [92]. The MOE reflects the stiffness of a material [97] – or its resistance to deformation under an applied force – and can be experimentally determined by a compression test. Due to the orthotropic nature of wood, three MOE can be identified according to the three axes of wood: longitudinal (E_L), radial (E_R) and tangential (E_T) [96]. Wood typically presents a ratio E_L/E_R of 10 and a ratio E_R/E_T of 2 [98].

Over the proportional limit (Figure 21), the material enters the plastic zone, where a linear relation between stress and strain is no longer observed and the material does not regain its original dimensions, even after the stress is removed [99]. In the case of wood, it leads to cell wall collapse. Firstly, plastic or elastic buckling of cell walls take place, with little stress variation. Ultimately, under high strains ($\varepsilon > \varepsilon_d$ - Figure 21), cell walls touch one another and the stress increases rapidly during a phase called wood densification [94].

3.2. Viscoelastic time-dependent deformations

As discussed in the previous section, when subjected to an instant load, wood deforms elastically. If, the load is maintained, an additional time-dependent deformation occurs. It is the case of creep tests. On the other hand, if the strain is held constant, the initial stress decreases with time. It is the case of stress relaxation tests [96,100].

Stress relaxation tests are very important to determine the viscoelastic properties of materials, including wood. They may be conducted in shear, uniaxial tension, or uniaxial compression [100]. During this test, a strain is applied and kept constant. As a response to stress relaxation tests, a wide range of behavior may be observed (Figure 22). For ideal elastic materials, no relaxation is observed – meaning that the stress level remains constant – whereas ideal viscous materials relax instantaneously. Viscoelastic materials have an intermediate behavior, progressively relaxing until reaching certain level. This level depends on the molecular structure of the material being tested. Viscoelastic liquids reach a residual stress of zero, while viscoelastic solids – which is the case of wood – reach an equilibrium stress (σ_e) superior to zero [100].

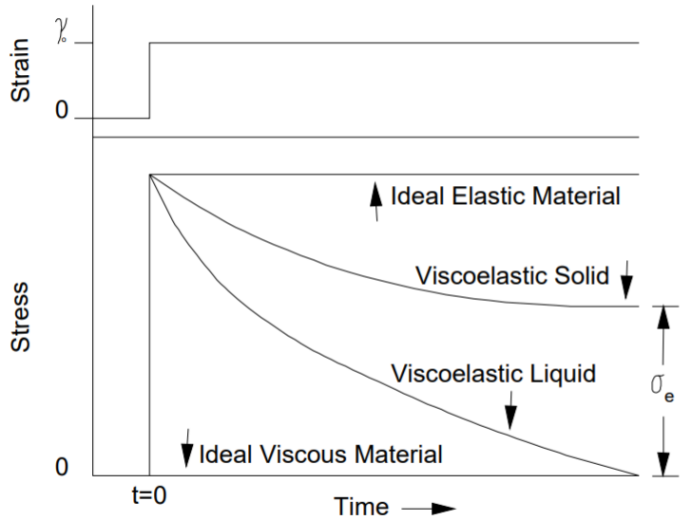

Figure 22. Stress relaxation curves [100].

3.3. Factors affecting the mechanical properties of wood

In such a hierarchically organized material as wood, understanding its features requires a multiscale approach. The mechanical properties of wood are no exception: the behavior observed macroscopically is a result of wood properties coming from many different scales. They are mainly attributed to the structure of the cell wall which, in turn, depends on its chemical composition. In addition to inherent characteristics of the material, environmental factors, such as temperature and relative humidity, play an equally important role. In this section the main factors affecting wood mechanical properties are addressed.

3.3.1. Factors inherent to wood

When it comes to the wood structure, three factors seem to have a major influence on its mechanical properties: the polymer composition and their interactions, the cellulose microfibril angle, and the density.

Cellulose is considered to dictate most of the mechanical properties of wood, due to its high DP and linear orientation [99,101]. The S2 layer of the cell wall, responsible for 75-85 % of the fiber volume and rich in cellulose, is particularly important for this matter [68,102].

Lignins act as stiffening agents for the cellulose molecules and are also responsible for holding fibers together [45,99]. Although the mechanisms relating lignins to wood's mechanical behavior are yet to be fully understood, researchers seem to agree on the importance of this component [39,95,103,104]. Indirectly, its hydrophobic nature prevents water uptake, which could have a plasticizing effect (more information about the influence of water is given in the next section) [39]. However, a more active role of lignins in mechanical properties of wood has recently been explored, especially in the case of transverse loading or longitudinal loading for cells with MFAs superior to 15° [103,104]. Lignin content was shown to positively correlate to cell wall elastic modulus [103], probably because, in room conditions (temperature and relative humidity), lignins are in a vitreous state. It limits the mobility of the cell wall, contributing to wood stiffness [39,95].

More recently, a model to evaluate the effect of cell wall features on the mechanical properties of wood fibers has been developed [105]. It highlighted that transverse cell wall elastic modulus is also highly influenced by hemicelluloses. This finding is consistent with other studies demonstrating that hemicelluloses affect the creep response of fibers due to their important viscoelastic behavior [106,107].

More than the polymers themselves, it is the interaction between them that allows a fully understanding of the mechanisms involved in the mechanical behavior of wood. The hydrogen bonds between cellulose and hemicelluloses provide at the same time strength and flexibility, due to their capacity to break and reform. Hemicelluloses also form covalent bonds with lignins and, thus, help assembling the whole structure [106].

The relation between cellulose and the mechanical properties of wood has been largely studied and the influence of the MFA has been unquestionably highlighted. In the longitudinal direction, cellulose microfibrils act as load-bearing elements due to their very high axial stiffness in comparison to other cell wall polymers [103] and are responsible for controlling the MOE of wood in this direction [95,106,108]. Figure 23 was obtained from axial tension tests of wood fibers with low (earlywood) and high (compression wood) MFA. It shows that a lower MFA results in a higher modulus of elasticity [108]. Microfibrils with larger MFAs are off the longitudinal axis, inducing shear stresses in the matrix [103]. Once the shear strength of the matrix is surpassed, cellulose microfibrils can glide past one another without further damaging the matrix, hence the large plastic deformation observed in Figure 23 [108].

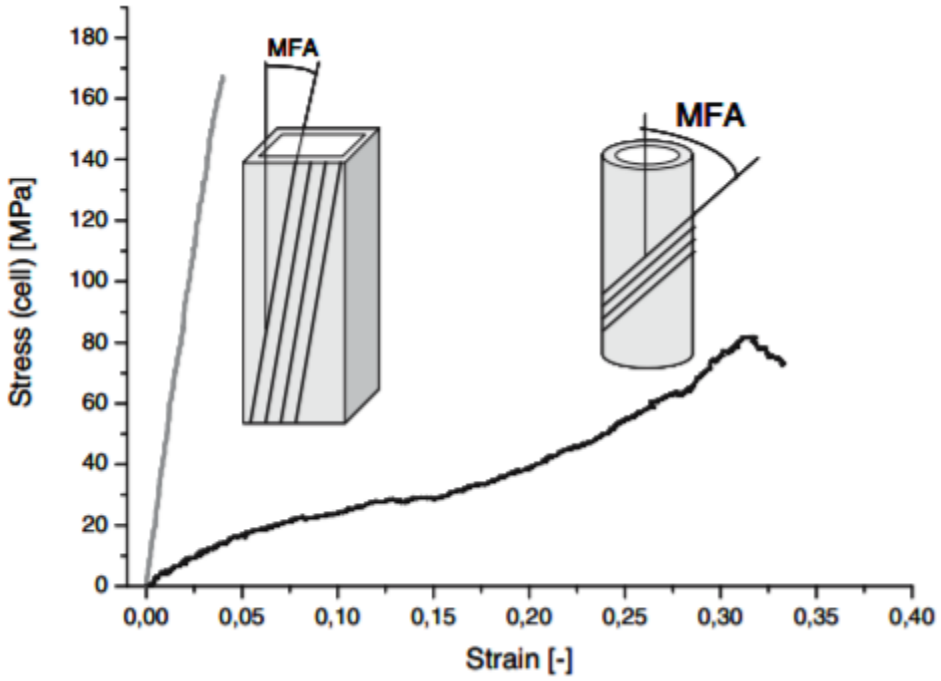

Figure 23. Stress-strain curves of low (grey) and high (black) MFA wood cells in the longitudinal direction [108]

For fibers with high MFAs and for transversal loading, however, the contribution of polymers other than cellulose becomes important [103,104,109]. In this case, the orientation as well as the

viscoelastic properties of lignins and hemicelluloses must thus be considered for a complete appreciation of cell wall mechanics.

In higher scales, wood density has a major influence on the MOE [95], as showed in Figure 24. It can also be related to the cell wall thickness, which was proven to greatly affect the MOE in radial compression [110]. An increase in either wood density or cell wall thickness results in an increase of the elastic modulus, which can be attributed to the fact that internal stresses have more molecular material to be distributed to [99].

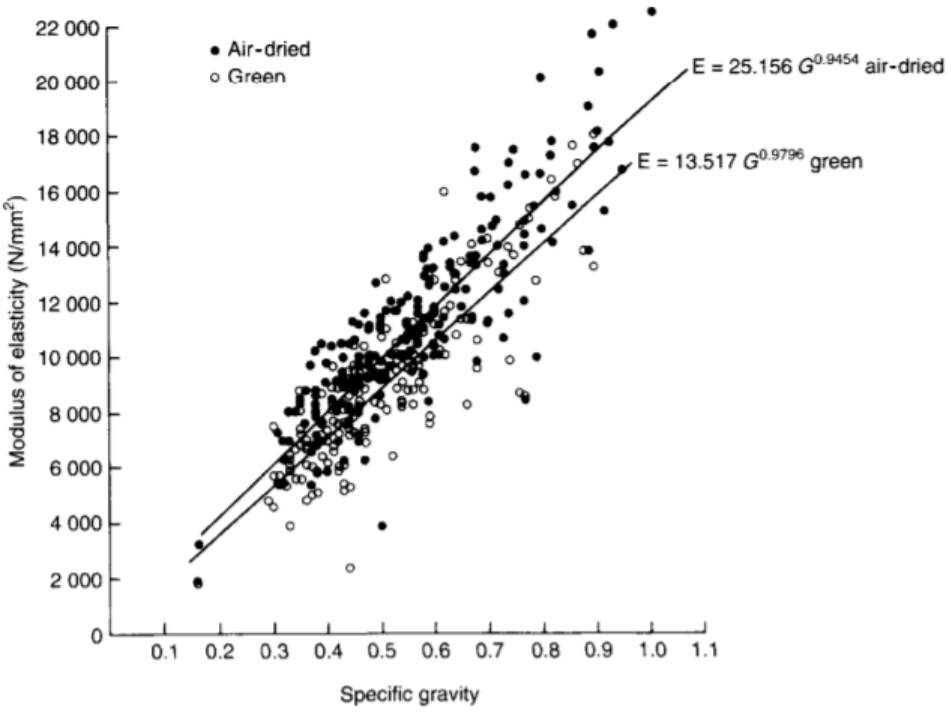

Figure 24. Effect of the specific gravity on the longitudinal modulus of elasticity of green and air-dried wood [95]

3.3.2. Influence of temperature and water

The influence of temperature is mostly related to the glass transition temperature (T_g), a characteristic of the viscoelastic behavior of amorphous polymers. Below T_g materials are in a glassy state, which is also observed by a high modulus of elasticity. Once temperature exceeds its T_g, the stiffness of a material decreases drastically and begins to present a rubbery-like aspect [32]. From this point, many of materials properties change drastically.

Softening depends directly on the rotational or translational mobility of molecule segments. At low temperature, this mobility is minimal. When heated, materials suffer a thermal expansion, which provides the necessary space for the motion of molecules to occur [32].

Some of the main molecule properties affecting the T_g are [39]:

- Size of side groups: For rigid side groups, the larger the side group, the higher the glass transition temperature. For flexible groups, however, the mobility of the lateral sequences

brings an additional free volume. Therefore, the increase in size of the lateral groups results in lower T_g values.

- Polarity of side groups: T_g increases with the polarity of the lateral groups. Indeed, interactions such as hydrogen bonds strongly increase the cohesion energy, having an important impact in the T_g.
- Molecular mass: T_g increases with average molecular mass, which is related to the concentration of chain ends. Indeed, the greater the number of chain ends (low molecular weight), the greater the free volume and the lower the T_g.

As it is composed of three different polymers, wood presents a softening range rather than one specific glass transition temperature [32,39]. It is, however, impossible to talk about the T_g of wood polymers without mentioning the effect of water. As previously mentioned, the adsorption of water by wood sunders the polymer chains, increasing the volume and creating free spaces between molecules. As a consequence, wood macromolecules see their mobility increase and can slide past each other more easily, lowering the T_g [111].

Table 5. Tg values of wood polymers in water-saturated and anhydrous states [39].

	T_g (°C)		
	Cellulose	**Hemicelluloses**	**Lignins**
Water-saturated		0 – 60	60 – 100
Anhydrous	220	150 – 220	130 – 195

Hemicelluloses are particularly affected by this phenomenon. Their structure is rich in hydroxyl and carboxyl groups, to which water has a strong affinity [112]. Due to this fact, the T_g of hemicelluloses exhibits a broad range of values (Figure 25) [113]. In the anhydrous state, the T_g of hemicelluloses is superior to 100 °C (Table 5), while, for water contents near the FSP, it can approach 0 °C (Table 5) [39,113]. In the normal ambient conditions to which wood is exposed, temperature is superior to the T_g of hemicelluloses and, it is, thus, in the rubbery state. The same cannot be said for cellulose. Its crystalline structure makes it almost insensitive to the effects of water adsorption and gives it a very high T_g (Table 5) [39].

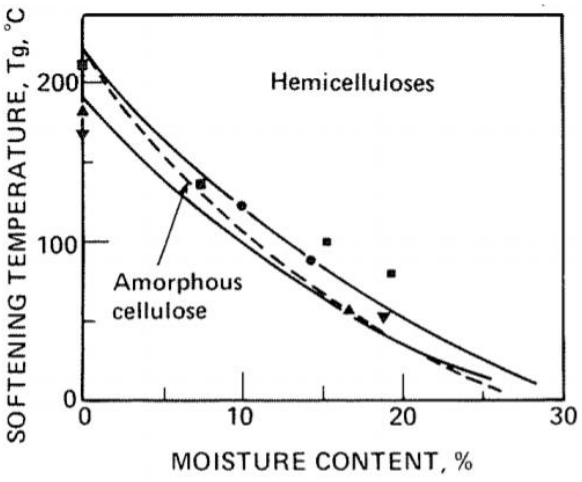

Figure 25. Influence of the moisture content on the glass transition temperature of hemicelluloses [113]

In usual ambient conditions, considering the very low T_g of hemicelluloses and the very high T_g of cellulose, the softening temperature of wood is thus mostly influenced by that of lignins (Table 5), occurring in the same range as wood's (50 °C to 100 °C) [39,112]. Lignins T_g is related to the presence of large methoxyl side groups, preventing covalent cross-linking and entanglement of the structure. A similar effect is caused by free phenolic hydroxyl groups [112].

If the quantity of methoxyl groups is an important factor to the T_g of lignins, the proportion of different units is obviously something to be considered. G units, that constitute the major part of softwood's lignins, have only one methoxyl unit. Whereas S units, major units of hardwood's lignins, have two methoxyl units (Section B.1.3). It explains why hardwoods have a lower T_g when compared to softwoods [39,112].

The increase of moisture content, for the reasons mentioned above, causes the modulus of elasticity to decrease steadily up to the FSP (Figure 26) [95]. For moisture contents under 8%, however, the molecular rearrangements caused by water adsorption seem to increase the stiffness of wood [114].

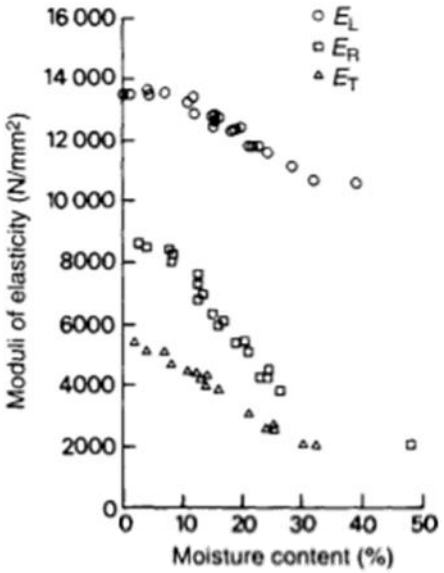

Figure 26. Effect of the moisture content on the modulus of elasticity of spruce. Adapted from [95].

D. How hydrothermal pretreatment affects lignocellulosic biomass

As previously mentioned, the goal of pretreatment in the production chain of second-generation bioethanol is to facilitate the access of enzymes to the carbohydrates without prejudice to the fermentation step. From a chemical point of view, hydrothermal pretreatment has been extensively studied in literature. The changes induced on carbohydrates are particularly well documented. Due to the greater complexity of their structures, lignins changes are less understood. The consequences of the chemical changes suffered by biomass during hydrothermal pretreatment can be observed in a wide range of scales. Some of them have been widely studied, others remain as hypothesis. This section aims to review the work done on hydrothermally pretreated biomass at different scales.

1. Biochemical changes

1.1. Hemicelluloses

During hydrothermal pretreatment, hydronium ions (H_3O^+) from water are responsible for starting the hydrolysis process [115,116]. Hemicelluloses are the most thermosensitive components of wood cell walls and represent, thus, the major part of the mass loss [117]. This is attributed to their low degree of polymerization when compared to cellulose [118] and to their branched, amorphous structure, making them more sensitive to chemical attack [43].

The first hemicellulose structures to be attacked are their side chains, mainly acetyl groups (Figure 27). The acetic acid produced by acetyl groups hydrolysis and other *in situ*-generated compounds (such as uronic and phenolic acids) then behave as catalysts themselves [115], promoting the breakage of glycosidic linkages [119]. Due to the presence of more acetyl groups in their hemicelluloses, hardwoods are more susceptible to this treatment than softwoods [117]. The lack of enough acetyl groups in softwoods to promote autohydrolysis may require the addition of an acid catalyst prior to treatment [24].

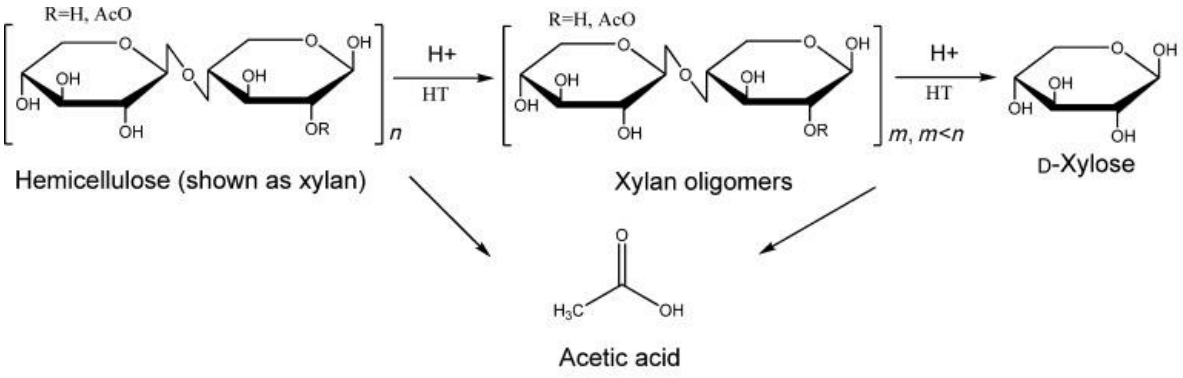

Figure 27. Hydrolysis reactions of hemicelluloses taking place during hydrothermal pretreatment, with xylan as model compound [22].

Xylan, the most important component of hardwood hemicelluloses, can be present in wood under three forms [119]: free xylan, glucuronoxylans bound to the surface of cellulose microfibrils or forming lignin-carbohydrate complex (LCC) bonds. Free xylan is the easiest fraction to be removed [50], whereas the xylan fraction associated with the crystalline cellulose microfibrils is seldom removed during hydrothermal treatment [119].

At the end of the treatment, up to 85 % of hemicelluloses original amount is released [119], generating oligosaccharides. These oligosaccharides are later hydrolyzed into monomers and may be partially degraded into other degradation products, such as furfural and formic acid (CHAPTER I.D.1.4) [119].

1.2. Cellulose

As hemicelluloses, cellulose can also undergo hydrolysis reactions, producing oligomers and monomeric glucose (Figure 28). However, the conditions applied to biomass during hydrothermal pretreatment favorize cellulose depolymerization reactions rather than solubilization [120].

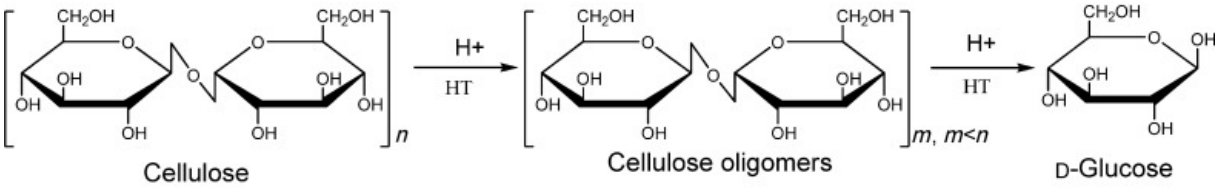

Figure 28. Hydrolysis reactions of cellulose taking place during hydrothermal pretreatment [22].

A study on the hydrolysis behavior of cellulose showed that the amorphous fraction needs at least 150 °C to start breaking glycosidic bonds. This minimal temperature rises to 180 °C in the case of crystalline cellulose [121]. Thus, the initial rapid decrease in cellulose degree of polymerization (DP) is mainly due to the hydrolysis of amorphous cellulose [43], especially once the protective barrier of hemicelluloses has been solubilized [24]. DP then stabilizes at a level-off degree of polymerization (LODP) [122] of around 200 units. Indeed, amorphous regions occur in series with crystalline areas along cellulose microfibrils approximately every 150 to 250 units of anhydrous glucose [23,24] as presented in Figure 8 (CHAPTER I.B.1.1).

Structurally, cellulose also follows significant changes during hydrothermal pretreatment, such as the separation into single microfibrils or small bundles of fibrils, resulting in less packed structures with increased surface area [123,124]. Indeed, some authors believe that hemicellulose solubilization and lignin reorganization partially release molecular tensions holding crystalline cellulose together, which allows amorphous cellulose to be incorporated into the crystalline structure [24]. Contrastingly, previous works have observed an increased crystallinity index of lignocellulosic material after hydrothermal pretreatments. It was attributed to a loss of amorphous components (hemicelluloses, lignins and amorphous cellulose) and, thus, a concentration of crystalline cellulose [22,122].

1.3. Lignins

Reactions involving lignins during hydrothermal pretreatment are less elucidated than the ones acting on carbohydrates, probably due to the structural complexity of this component [58]. However, a lot of effort has been made recently to better understand its behavior [125].

Hydrothermal treatments have been proven to significantly promote the cleavage of β-O-4 aryl ether linkages [125–127], even at temperatures as low as 150°C [128–130]. Two different mechanisms leading to this cleavage have been described in literature (Figure 29): the heterolytic and the homolytic pathways [126]. In the acid-catalyzed heterolytic path, the cleavage of the β-O-4 linkages is a result of the formation of a carbonium ion on the α position of the lateral chain. The homolytic mechanism, on the other hand, results from a β-O-4 radical cleavage and its subsequent coupling [126].

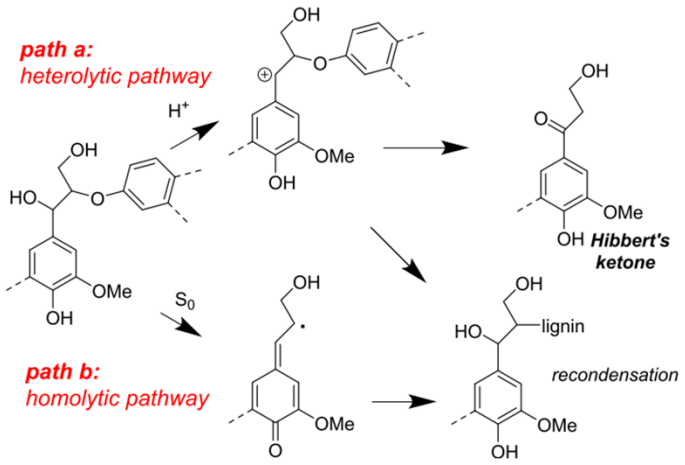

Figure 29. Cleavage mechanisms of the β-O-4 aryl ether linkages. Adapted from [126].

At 200 °C for 30 minutes, previous studies observed that 90 % of β-O-4 linkages were removed [128]. It resulted in an initial decrease of lignin molecular weight [127] and a generation of aromatic monomers in the liquid phase [122]. However, as the duration of the treatment increased, the molecular weight was again shifted to higher values, which suggests that lignin depolymerization was also accompanied by condensation reactions [127,131]. The concomitant increase in C-C bonds [33,126,131] supports these observations. The resulting structure, rich in strong inter-unit linkages such as β-5', β-β' and 5-5' [33,131], is much more stable and less likely to form lignin monomers [131].

The balance between these two contrasting reactions – depolymerization and re-condensation – and, thus, the extent of lignin structural changes depend largely on the type of biomass and the process conditions. Lignins monomeric composition, for example, can impact their susceptibility to depolymerization. The monomeric composition can in turn be influenced by many factors, such as the species and the location within a cell [66]. S-units are methoxylated at the C-5 position (section B.1.3). As a consequence, S-rich lignins present a more linear structure than G-rich lignins, with fewer inter-unit cross-links [132,133]. Additionally, since the C-5 position is taken by

a methoxyl group, S-units are less likely to form highly stable 5-5 and β-5 linkages [133]. Therefore, the predominance of S units make lignins more susceptible to thermal degradation [115,132,133]. As mentioned in section B.1.3, hardwoods have more S units in their structure than softwoods. Poplar lignins, for example, are composed by 61.9 % of S-units, 37.8 % of G-units and 0.3 % of H-units [56]. Within the cell wall, the secondary layer is also known to be richer in S-units than the others [132,134]. It is therefore reasonable to imagine that lignin degradation during pretreatment depends on its location through the cell wall thickness. Previous studies on the chemical pulping of spruce have indeed reported that lignins present in the middle lamella are less reactive than those within the cell wall, which was attributed to their higher C-C bond content [43].

Another possibility is that lignins undergo a migration process. Donohoe et al. [135] suggested a mechanism (Figure 30) in which, once treatment exceeds lignin melting temperature (Tm), lignins expand and become mobile. Due to their hydrophobic nature, when in aqueous environment they coalesce into spheres to minimize their surface of contact. These spheres can migrate within the biomass sample. Even though thermal expansion and diffusion may force lignin spheres to be expelled from the cell wall matrix, according to the proposed mechanism, the main cause to lignin extrusion is the approach of adjacent cellulose microfibrils. This extrusion process could also apply to pseudo-lignin droplets [24], presented in more detail in CHAPTER I.D.1.4.

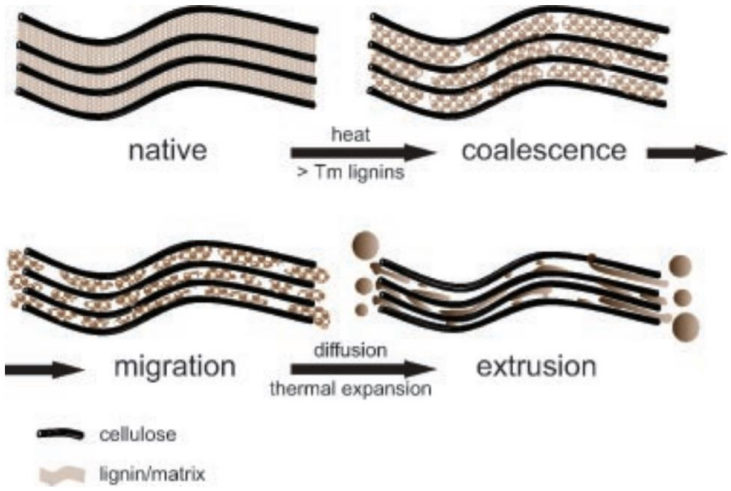

Figure 30. Possible mechanism for lignin migration [135].

The effect of lignin relocation in enzymatic hydrolysis is rather controversial. Some authors claim that the removal of lignins creates an opened-up cell wall structure, improving the accessibility to the cellulose microfibrils [135]. Indeed, lignins are important to cell wall integrity and delignification is likely to alter 3D ultra-structural network [119]. Others suggest that the redeposit of this material on the biomass surface during the cooling phase may have a coating effect, negatively impacting the enzymatic attack [136].

Moreover, it has been shown that the redeposition of droplets is not limited to the outer surfaces of biomass. Clusters of spherical droplets have also been found in inner anatomical regions such as cell corners [122,135]. The composition of these droplets may however change according to

the anatomical region in which they are found. According to Zeng et al. [137] the droplets formed in the cell corners tend to be composed of dense (or concentrated) lignins (Figure 31a), while the droplets formed in the secondary cell wall consist of loosely packed lignins (Figure 31b), structures of carbohydrate cross-linked with relatively low amounts of lignins.

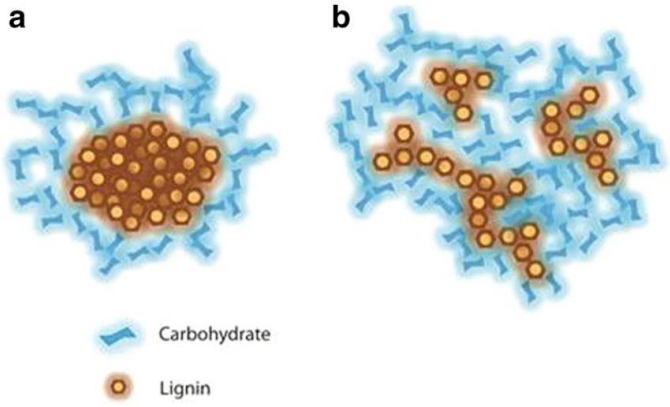

Figure 31. Hypothetic representation of (a) dense and (b) loosely packed lignin structures [137].

1.4. Degradation products and their inhibition power

Under high temperature and acidic conditions, the monosaccharides released during hydrothermal pretreatment are unstable and tend to dehydrate. C6 monosaccharides form 5-hydroxymethylfurfural (HMF) and C5 monosaccharides form furfural (Figure 32) [24,25]. When high severity pretreatments are applied, these components can be further degraded into products such as levulinic acid and formic acid [122].

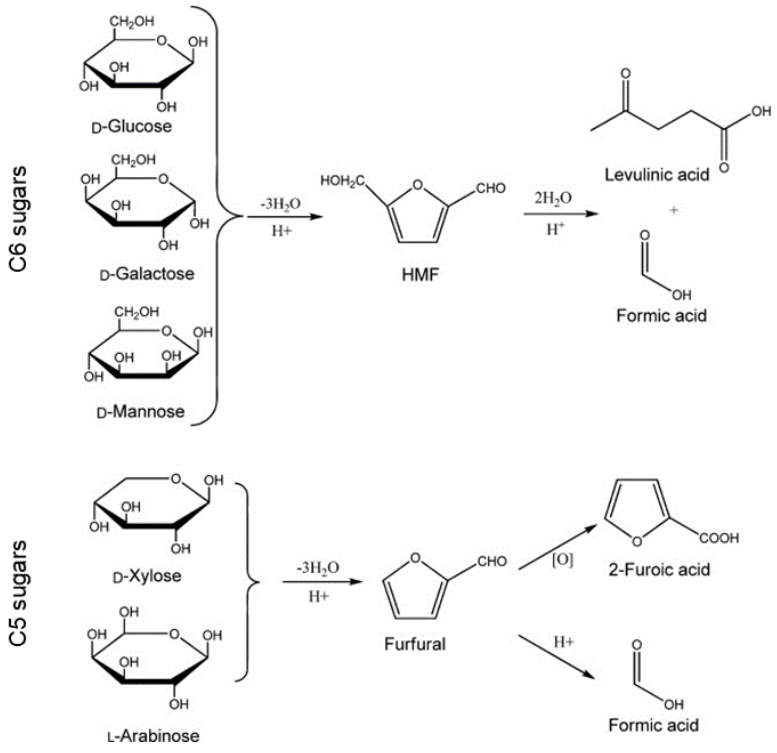

Figure 32. C6 and C5 sugar degradation reactions taking place during hydrothermal pretreatment. Adapted from [22]

When a further fermentation step is foreseen, care must be taken to minimize the formation of these molecules, as they have a highly inhibitory effect on microorganisms [24]. Furfural, for example, starts to inhibit ethanol production by *Saccharomyces cerevisiae* from 0.5 g/L and presents a complete inhibitory effect at 4 g/L [138].

Furthermore, carbohydrate degradation products can be converted into key aromatic intermediates that, through polymerization and polycondensation reactions, form lignin-like compounds [116]. These compounds are insoluble in sulfuric acid and are often accounted for as lignins in classical wet chemistry analyses. A possible pathway to the formation of this pseudo-lignins is shown in Figure 33. Two problems originate from their formation. Firstly, it represents a reduction in sugar yields. Secondly, like lignins, they tend to form spherical structures that adhere to the cell wall surface during the cooling phase [139]. The presence of such structures on the cell wall may be prejudicial to enzymatic hydrolysis by reducing cellulose accessibility and by unproductively binding to the enzymes [116,140].

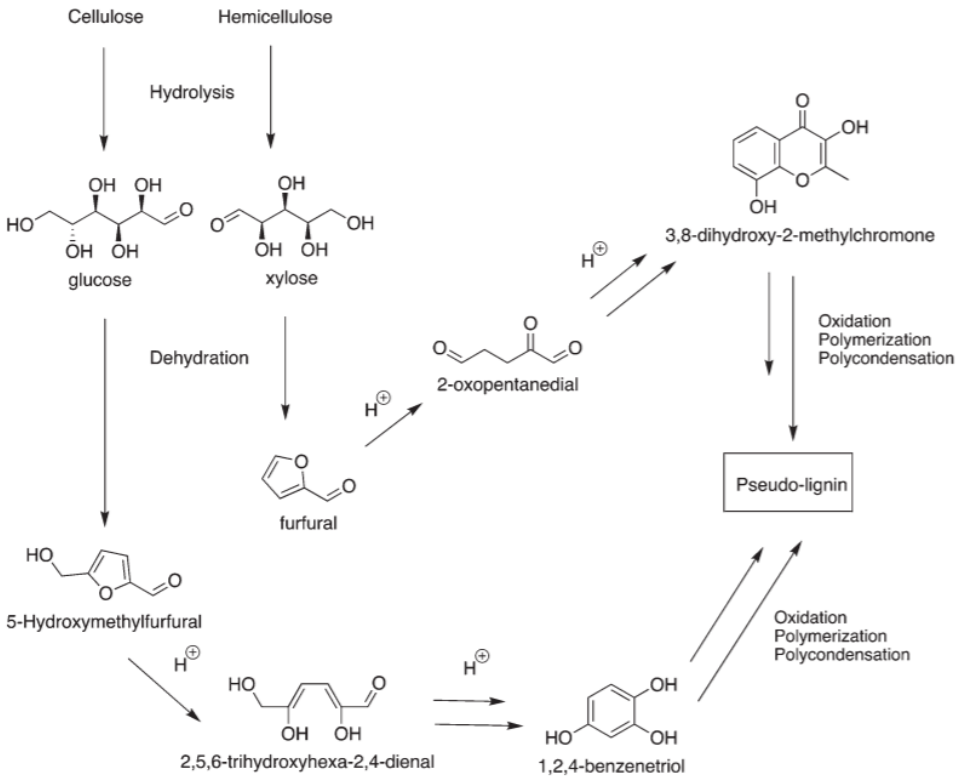

Figure 33. Possible reaction pathways for the formation of pseudo-lignins [139]

The pretreatment conception must take these aspects into account. Optimized time-temperature couples should allow oligomeric sugars to be preserved. Hydrothermal pretreatment has been shown to be particularly good at limiting oligomers degradation, as the pH is maintained around 4. Another option is to continuously remove the released sugars, which is possible when flow-through or countercurrent processes are applied [24].

2. Hygroscopicity

Hygroscopicity is a macroscopic property directly affected by biomass chemical characteristics. Previous studies on heat treatment of eucalyptus [141] and hydrothermal treatment of spruce [142] have shown that increasing the treatment temperature would significantly reduce wood hygroscopicity. Both works attributed this phenomenon to a reduction in the number of accessible hydroxyl groups caused by the hydrolysis reactions suffered by hemicelluloses (CHAPTER I.D.1.1) [141,142].

3. Shrinkage

To the best of our knowledge, no previous study on the shrinkage of biomass subjected to hydrothermal pretreatment has been made, probably due to the severe conditions (high temperature and steam saturated conditions) that it requires. However, wood shrinkage has already been measured for both hardwoods and softwoods in the case of mild pyrolysis and has been proven to be a good indicator of the treatment severity [143], increasing both with treatment time and temperature.

It is reasonable to presume that the same effect would be observed in the case of hydrothermal treatment. Indeed, the reduction of wood hygroscopicity observed after pretreatment naturally results in a lower FSP [141]. A lower hygroscopic swelling power results in an overall smaller scaled cell wall structure [144]. Moreover, shrinkage can reflect a reduction in the cell wall thickness as a result of the mass loss due to molecular degradation [143].

Beyond the chemical influence, shrinkage could equally inform on the ultrastructure of wood. For example, electron microscopy has shown that mild pyrolysis can induce changes in the cellular shape, such as vessels flattened along the tangential direction [143].

4. Rheological changes

Despite the relevance of this subject in many fields, relatively few papers are devoted to the simultaneous effect of temperature and time in wood's rheological properties under saturated conditions. Most of the research has been carried out in temperatures no higher than 140 °C [33,145–148]. This is probably due to the severe conditions involved in higher temperatures, requiring special experimental set-ups to be designed. Two papers describe especially conceived apparatus allowing the application of temperatures relevant to the pretreatment of biomass [34,149].

Mokdad et al. highlighted the existence of two mechanisms as being responsible for the changes in wood mechanical properties: thermal activation and thermal degradation [34].

Increasing the temperature up to 100 °C favorizes thermal activation over thermal degradation [33,145]. Under these conditions, enough energy is provided to allow macromolecules to slide past each other due to the breakage of weak or even covalent intermolecular bonds [33]. As explained in section C.3.3.2, in the case of saturated wood, hemicelluloses are in a softened state

even at room temperature. Consequently, the thermal activation of hydrothermally treated wood is mostly related to the softening of lignins [148], which happens between 50 and 100 °C [32,33,148]. It can be observed by a substantial decrease of the elastic modulus, especially in the transversal direction [148].

When treatment temperature exceeds 100 °C or when treatment times are sufficiently long, the effects of thermal degradation on water saturated samples can no longer be neglected, as it has been shown by several works. Placet et al. [145] used dynamic mechanical tests to assess the viscoelastic properties of hardwood and softwood under water-saturated conditions during several hours. They noted a loss of beech samples rigidity of up to 17.2 % in tangential and 14.7 % in radial directions, respectively, after 8h at 93 °C. This fact was related to the degradation of hemicelluloses (section 1.1). Similar results were found in other studies [34,147,150].

However, for treatments above 100 °C and long residence times, the tendency was not the same. After 3h at 135 °C, for example, samples storage modulus had experienced a reduction of around 50 %, in both tangential and radial directions. During the following hours, samples regained rigidity until reaching their original storage modulus values after 24h of treatment. This rather surprising result was attributed to the condensation generated by the formation of strong links between lignin units.

To better understand the mechanisms leading to this behavior, Assor et al. [33] studied the concomitant changes in chemical and mechanical properties of wood. This study showed that hardwood lignins were more susceptible to hydrothermal treatment than softwood lignins. Indeed, according to the authors, oak lignins (hardwood) initially contained 66 % of non-condensed units only involved in β-O-4 bonds, which are the most susceptible ones to hydrothermal treatment. The cleavage of these bonds could be responsible for a loss of rigidity even before hydrolysis of hemicelluloses takes place, as it requires milder conditions. At 135 °C, for treatments longer than 4h, the loss of non-condensed lignins gave rise to condensed structures to which has been attributed the increase in rigidity.

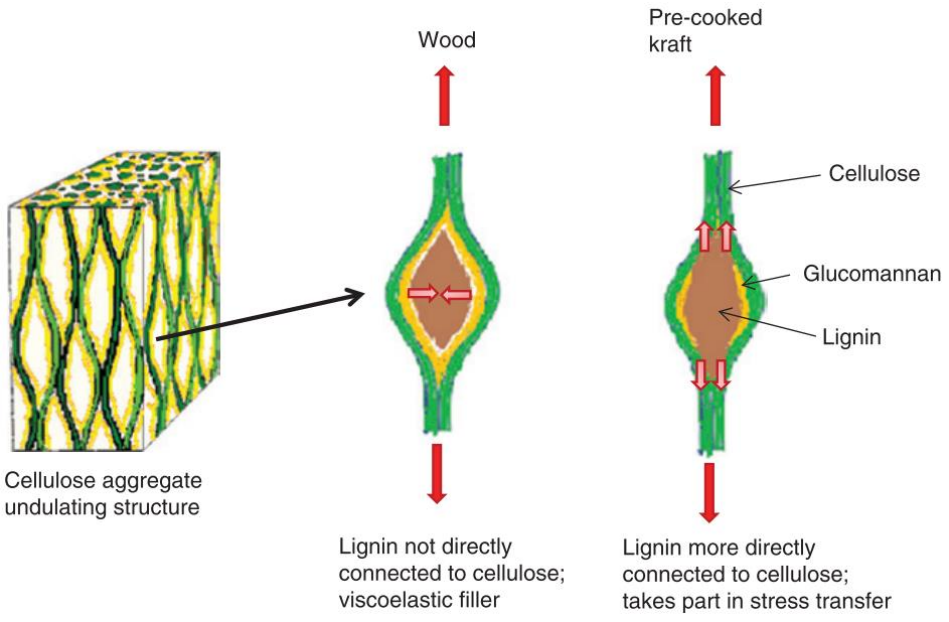

Figure 34. Schematic picture of the lignin matrix material within undulating spaces of secondary cell wall cellulose aggregates [151].

Hemicelluloses may also take part on the mechanical properties of wood. In native wood, lignins are placed within the undulating cellulose aggregates, recovered by hemicelluloses. Stress is thus indirectly transferred between cellulose and lignins. Under longitudinal tensile loads, it results in transverse compressive forces on the lignin-hemicellulose complex, to which it responds with viscoelastic relaxation. After kraft pre-cooking, when hemicelluloses have been partially removed, lignins participate more actively in the stress transfers because they have a more direct contact with cellulose [151].

E. Conclusion

It is clear that industrialization of lignocellulosic ethanol cannot be made without an optimization of the pretreatment step. Ultimately, it is the overall amount of recovered sugars and inhibitors – and therefore a chemical aspect – that will dictate the choice of a pretreatment method and its conditions. However, this question cannot be addressed from a single point of view since properties at different scales influence each other. A comprehensive study of the effects of pretreatment on biomass requires, thus, looking at its multiple scales.

While much of the literature has focused on the chemical changes of biomass subjected to hydrothermal treatment, less focus has been given to larger length scales. Although rich in information about the mechanisms of biomass degradation, chemical analyses are time-consuming and involve destructive tests.

The possibility of carrying out continuous measurements is certainly attractive. It greatly reduces the number of tests required to describe the evolution of certain properties during pretreatment. Based on previous studies, continuous assessment of biomass rheological properties has been chosen as a macroscopic indicator of the pretreatment extension and lies in the heart of this thesis. The interest of continuous rheological monitoring is to use the mechanical signature of the chemical modifications to assess the degradation kinetics and the effects of time and temperature. Several measurements will be explored throughout this study: the apparent modulus of elasticity, the viscoelastic relaxation and the variation of the sample dimensions.

Rheological results are further related to useful data for pretreatment, such as chemical and morphological modifications at chosen treatment durations. This allows a broad overview of the modifications taking place during the process. Ultimately, this multiscale study aims at obtaining a model able to predict lignocellulosic chemical degradation.

CHAPTER II. Material and methods

A. Poplar: a promising feedstock

Samples used in this work were obtained from a 25-year-old poplar tree (*Populus euro-americana* 'Koster') that grew in Auménancourt-le-Petit (Marne, North-East of France). It was chopped and sawn into boards that were subsequently dried before sample preparation.

The choice of poplar (*Populus* spp.) as model biomass in this study was motivated by its great potential as feedstock for the production of 2G biofuels [152]. Because of its relatively compact genetic complement, poplar was one of the first trees to have its DNA sequenced [153]. This knowledge accelerated the development of new poplar hybrids and clones, optimized for the biofuel production. Hybrid poplar now figures among the fastest-growing trees (from 3.2 to 21.5 dry tons per hectare and per year), thanks to which it can be farmed as short rotation woody crops [154]. Other important characteristics include a wide site adaptability, low need of fertilizers input and aptitude to be harvested in different seasons [154].

B. WAVE^{T} 2: general principle and accuracy

As previously stated, the ultimate goal of this study was to provide macroscopic indicators of the treatment kinetics during hydrothermal treatment. To explore the macroscopic changes suffered by biomass during hydrothermal treatment, two approaches were used: monitoring the dimensions of wood samples (strain measurement at almost zero stress level) and their rheological properties (strain and stress measurements).

Such measurements were only possible thanks to an in-house developed device, lying at the heart of this work. It allows rheological measurements to be performed under the severe conditions imposed by hydrothermal pretreatment (high temperature and saturated steam pressure). The rheological results obtained with this device are presented in Chapters IV and V, where a brief description of its principle is presented. The aim of this section is to give details about its functioning and development. Several blank and preliminary tests, specially designed to increase the accuracy of the system and reliability of the results, will also be presented in this section.

1. General principle

The bases of this equipment were inspired by a previous device (named WAVE^{T}, for Environmental Vibration Analyzer for Wood) [39,145,155], able to perform harmonic tests on a water-saturated sample under pressure. Even though perfectly functional, this first device was limited to 130 °C, which does not cover the ranges of temperature usually applied to biomass during hydrothermal treatment. This is the reason why a second device (WAVE^{T} 2) was designed and built prior to this research, as a part of Futurol project led by Procethol 2G, allowing uniaxial compression tests to be performed under saturated steam conditions and temperatures of up to

190 °C (which implies more than 12 bar of pressure) [34]. WAVE^{T} 2 consists of two separate parts: a reactor and a controlling system.

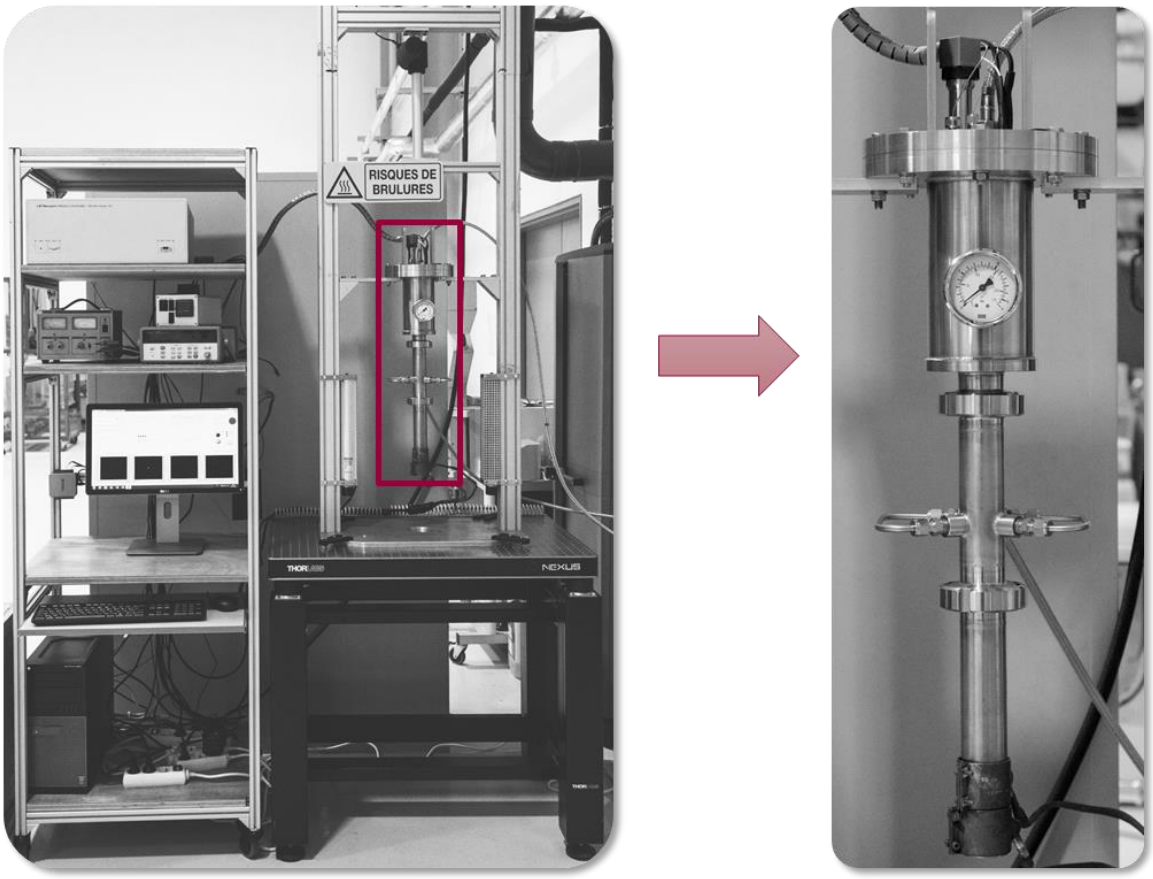

Figure 35. The WAVE^{T} 2 device (left) and a zoom on the reactor (right).

1.1. The reactor

The reactor (Figure 36) is where the samples are treated under controlled conditions and where rheological measurements are made. It is composed of two chambers. The bottom one (Figure 36 (b)) is where the treatment takes place. With treatment temperatures reaching up to 190 °C under steam saturated conditions, the instrumentation system (CHAPTER II.B.1.2) must be kept in a separate chamber (Figure 36 (a)), where a cold and dry environment is maintained (T < 30 °C and RH < 50 %).

The key feature of this device is its aptitude to maintain two extremely distinct conditions in one single frame, enabling a physical communication without friction between them – a prerequisite for reliable force measurements. Due to its huge partial pressure gradient, water vapor tends to diffuse from the lower chamber towards the upper chamber, which could degrade electrical components. To prevent the water vapor from reaching instrumentation, a patented system [156] was used. On top of the device, a flow of cold dry air (T < 30 °C and RH < 50 %) is injected. This air flow (with a pressure 1.5 bar higher than saturated water vapor pressure) acts as a counter-pressure to the water vapor. Both flows meet at the center of the reactor (Figure 36 (e)), where a controlled leakage (Figure 36 (3)) and a set of successive fins (Figure 36 (1)) are present. They

ensure a downwards convective flux of cold dry air that progressively limits the upwards convective-diffusion flux of warm water vapor in each volume between two successive fins, and eventually stops any flow to the upper chamber. The leakage is controlled through a flowmeter and set at 40 L/min.

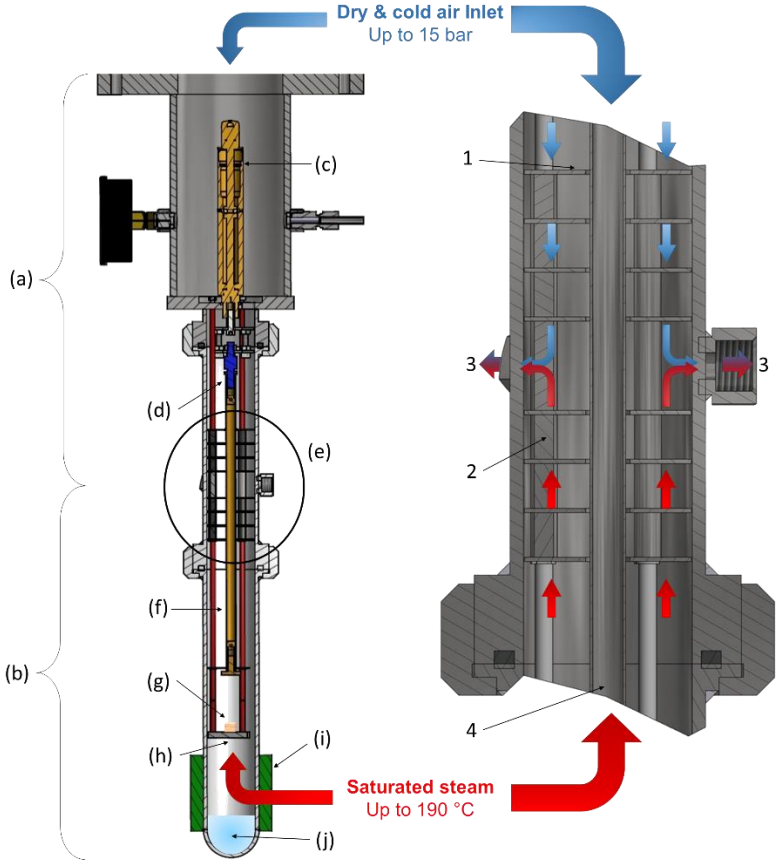

Figure 36. Scheme of the device. Left: (a) instrumentation zone; (b) reaction chamber; (c) actuator; (d) load cell; (e) frame for zoom; (f) compression rod; (g) sample; (h) sample holder; (i) electric heater; (j) liquid water. Zoom in the device (right): 1 - fin set (4 on each zone - cold/hot); 2 - fins and sample holder support rods; 3 - controlled leakage (3 symmetric outlets); 4 - compression rod.

The sample (Figure 36 (g)) is placed on the sample holder (Figure 36 (h) and Figure 37). To limit the effects of differential thermal expansion, all the elements present in this zone are made of the same material (stainless steel 316). At the bottom of the reactor, near the sample holder, 100 mL of distilled water (Figure 36 (j)) ensure a vapor saturated atmosphere and, thus, a good heat transfer inside the chamber while avoiding drying. Two electric heating collars (total of 370 W) placed at the outer surface of the chamber (Figure 36 (i)) are responsible for reaching the treatment temperature, while two external fans cool-down the reaction chamber at the end of the treatment. The temperature is measured by a K-thermocouple near the sample and controlled by a PID system (EUROTHERM 3216).

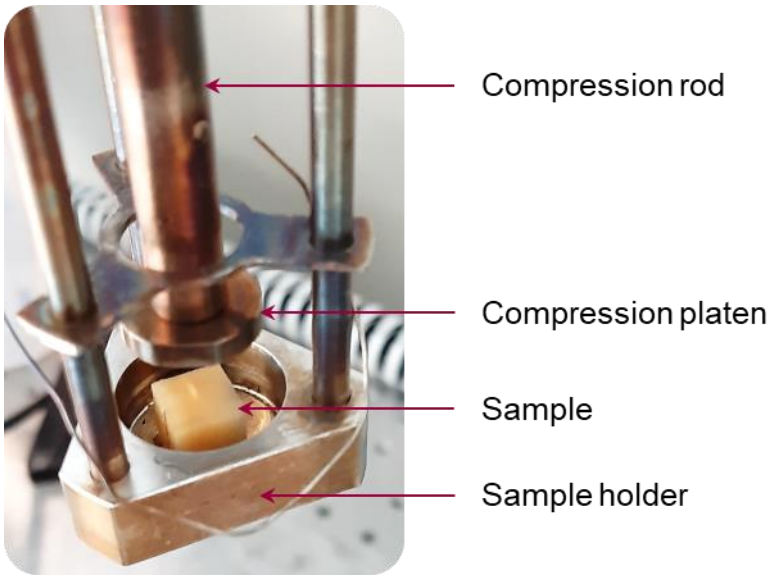

Figure 37. Sample on the sample holder and the compression system, including the compression rod and the compression platen.

1.2. The mechanical testing system

The sample is subjected to compression loading by a Newport LTA-HL actuator (Figure 36 (c)) – travel range of 25 mm, minimum incremental motion of 0.05 µm and accuracy of 3 µm – equipped with a displacement sensor. The actuator is controlled by a Newport XPS Q8 universal controller. The force applied to the sample is independently measured by a load cell (Figure 36 (d)) – MEASUREMENT SPECIALTIES XFTC 310, full range of 100 N and 10^{-5} N precision. The transmission of the load from the actuator (located in the upper chamber) to the sample (located in the lower chamber) is ensured by a rod (Figure 36 (f)), with a load platen at its extremity (both visible in Figure 37). The whole system is placed on an anti-vibration table (Nexus, THORLABS) to prevent any external interference on the measurements.

1.3. Data acquisition

The data emitted by the actuator and the load cell are transmitted to a USB-6002 NI card (NATIONAL INSTRUMENTS), allowing a sampling rate of 50 kHz. The signal from the thermocouple is transmitted to an acquisition unit (AGILENT HP 34970A) which directly provides the temperature in degrees Celsius.

2. Improving the reliability of the results

Throughout this work, a significant amount of time was dedicated to improving the accuracy of the results. The series of actions taken in this regard – which included developing a new control software (and, consequently, a new user interface) as well as testing protocols – are going to be presented hereafter.

2.1. Development of a new control software

A LabVIEW application has been developed as a part of this thesis in order to control the experimental set-up (Figure 38). It allows the previously mentioned testing system to be controlled from a PC: Newport XPS Q8 universal controller, NI acquisition card and Agilent data acquisition unit. The communication between the PC and these devices is done via RS232 ports, USB ports and using 10/100 Base-T Ethernet communication with a TCP/IP Ethernet protocol. This LabVIEW interface allows an almost completely automatic piloting of the experimental set-up during the entire experiment. Nevertheless, for safety reasons, the pressurized air inlet (1.5 bar higher than the saturated steam pressure at maximum plateau temperature) and the leakage are manually controlled. The acquired data is saved in its raw format for posterior processing. Security of the equipment is also a crucial point of this application. Indeed, the maximum force exerted at the force sensor should never exceed 100 N, which could otherwise damage it. For this reason, a data acquisition rate of 300 Hz was stablished in order to have a quick response in the event of exceeding a force threshold (set at 70 % of the maximum limit).

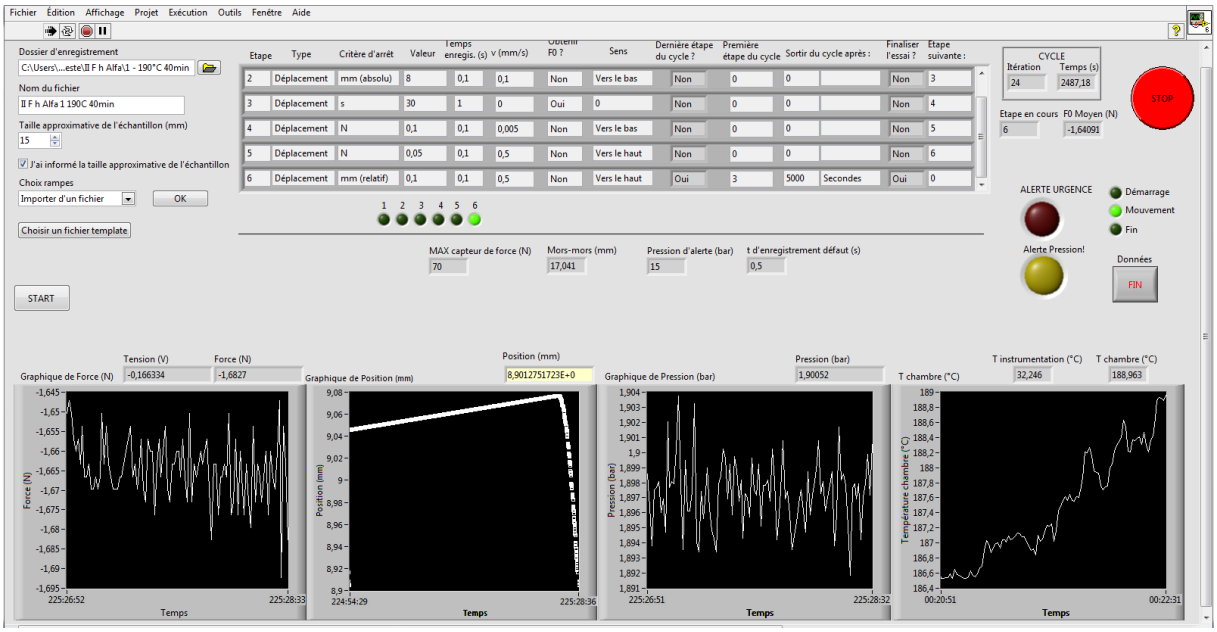

Figure 38. Overview of the control software (user interface).

At the beginning of the experiment, the operator enters the desired experimental protocol, which can be done manually or by importing a previously created protocol template. The protocol consists of a sequence of steps and each step represents a motion command whose characteristics are the following:

- The direction of the motion: upward or downward;
- Speed of motion: Maximum of 1 mm/s. A speed of 0 mm/s should be selected if no motion is desired;
- The stopping criterium: dictates the end of a step. It is composed of:
    - A type of criterium: a force, an elapsed time, a total displacement or a relative displacement;

    - A value;
- The frequency of data recording;
- Whether or not the force scale should be set to zero during this step.

The protocols can also include cycles, during which certain steps are repeated in loop. To create a cycle, the user should indicate its first and last steps, its stopping criterium (elapsed time, number of repetitions or reaching a certain temperature) and which step to go to at the end of the cycle.

Each data point is recorded in a text file and contains the following information:

- Elapsed time since the beginning of the experiment;
- Position;
- Force;
- Pressure;
- Temperature of the upper chamber;
- Temperature of the bottom chamber;
- Current step;
- Current repetition (in the case of a cycle);
- Date and time.

2.2. Contact detection: defining a force threshold

When executing mechanical tests, an important step consists in detecting the contact of the compression platen with the sample. In the case of this device, the contact is detected when the measured force exceeds a predefined threshold. This threshold must be, at the same time, sufficiently small not to crush the sample and sufficiently larger than the sensor noise (which would otherwise result in false positives). In order to find an acceptable compromise between these constraints, preliminary tests were made.

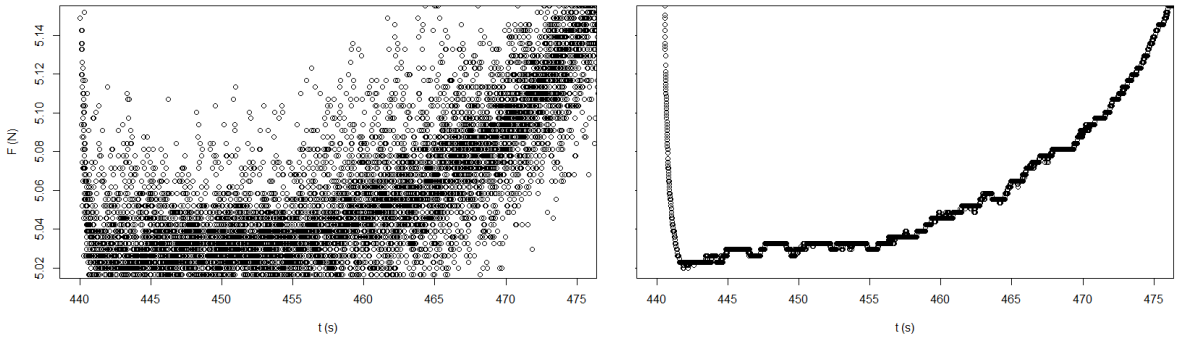

(a) (b)

Figure 39. (a) Unfiltered and (b) median filtered (200-points sliding window) force values during time.

The first step was to look at the force sensor noise. Figure 39a, shows raw force values measured in a blank test during a few seconds as the compression platen approaches contact with the sample holder. In this case, noise can reach up to 0.1 N. In post-processing, the effect of applying a 200-points sliding window median filter to these values was evaluated (Figure 39b). The increase in

the signal quality is clear and motivated the adoption of this filter directly in the LabVIEW application.

The second step involved finding an adequate threshold value for the contact detection. With this purpose in mind, four different force thresholds were tested. For each one of these values, ten attempts of detecting the contact with a sample were made and the position of contact detection was recorded. The results are presented in Figure 40.

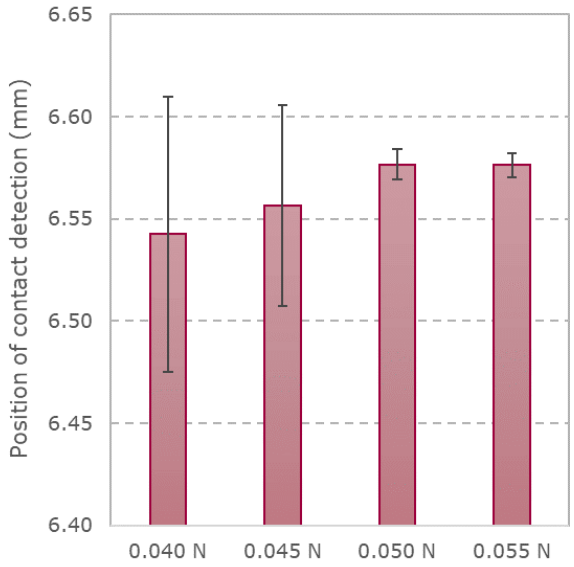

Figure 40. Position of contact detection as a function of force threshold (n=10 for each tested force threshold)

The reduction of standard deviation between 0.045 and 0.050 N is drastic (from ±0.049 mm to ±0.007 mm), whereas there is only a small change between 0.050 N and 0.055 N (from ±0.007 mm to ±0.006 mm). These results encouraged the use of 0.05 N as force threshold for detecting the contact between the compression platen and the sample.

2.3. Blank tests

Measuring the size of the sample with this device requires knowing the distance between the zero position of the actuator and the sample holder, as shown in Figure 41.

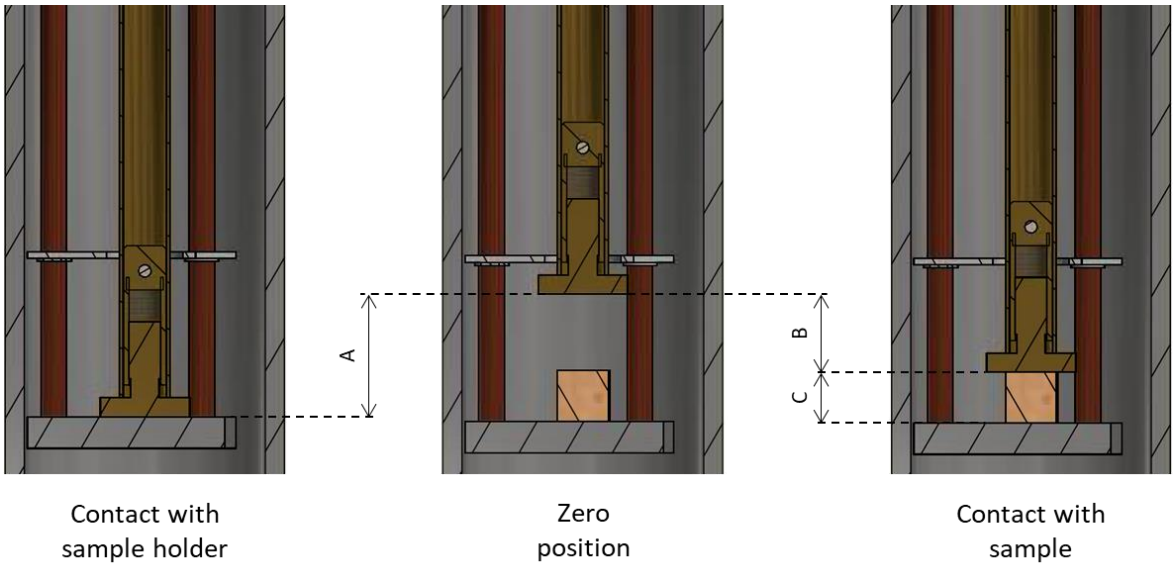

Figure 41. Schematic representation of the load platen in different positions. The size of the sample (C) is calculated by subtracting the position of contact with the sample (B) from the position of contact with the sample holder (A).

For this reason, a series of blank tests was made. The blank test consisted in detecting the position of the sample holder during time using the same protocol applied for the samples (threshold of 0.05 N, as described in the previous section). Three temperature plateaus were applied for each blank test: an initial plateau at room temperature, followed by a plateau at the temperature levels used during treatment (160 or 180 °C) and finally a second plateau at room temperature. A typical blank test result is showed in Figure 42.

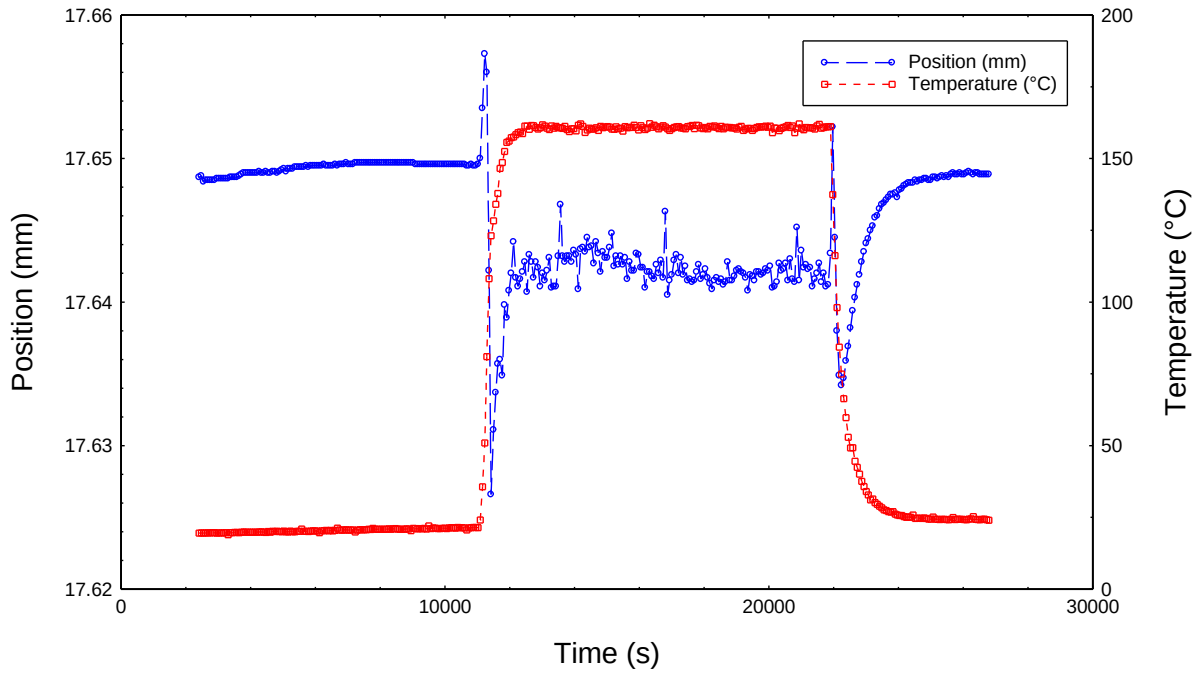

Figure 42. Typical blank test result (160 °C).

The results obtained at room temperature show a stability of 0.5 µm in the measured position of the sample holder throughout time, which is remarkable. The results obtained at higher temperatures might, however, seem disappointing at a first glance. Immediately after the heating system is turned on and temperature begins to rise, an overshoot in the measured position is observed, followed by an undershoot. The same phenomenon happens at the end of the temperature plateau, when the heating system is turned off and the fans are turned on. During the temperature plateau, even though it presents a higher noise than under room temperature, the position reaches stability. The values measured at this moment are clearly smaller than the ones measured at room temperature. From this fact, it becomes evident that temperature must be accounted for when defining the total distance used for the sample size calculation.

Several repetitions were made in order to assess the effect of temperature on sample holder position (Figure 43). The position measurements respond equally to the increase of temperature in each repetition, with overshoots and undershoots of similar magnitudes. Such comparable behaviors happening during heating could be explained by a response of the device frame to a different thermal expansion in different parts of the device. Indeed, during this phase, temperature is probably not equal throughout the device.

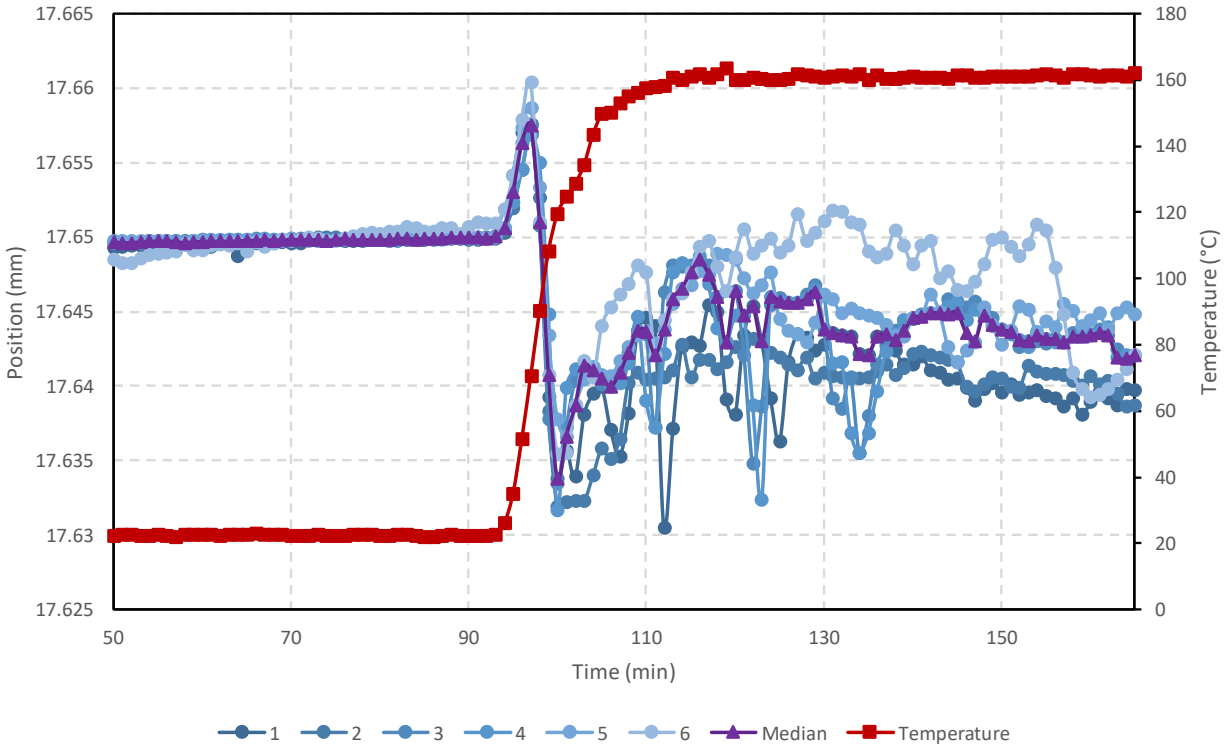

Figure 43. Series of blank tests performed at 160 °C. The measured values of the sample holder position are shown in blue, the temperature in red and the median between the tests is shown in purple.

This dynamic behavior of the device, with deviations of the order of a few tens of micrometers, cannot be neglected when following the size of the samples during treatment. The approach chosen for correcting the measured values was based on the median of all the blank tests (Figure 43, in purple). During the temperature plateau, however, the noise in the measured values is high,

compared to data obtained at room temperature. For this reason, a 5-point sliding window median filter was applied for the values within temperature plateau.

The length of the samples was then calculated as the difference between the median blank test results (as a function of both time and temperature) and the position measured during treatment:

$$\Delta L = L_B(t,T) - L(t,T) \quad (4)$$

In which ΔL is the length difference between the compression platen and the sample holder (equal to the size of the sample), L_B is the median blank test value (as a function of time and temperature) and L is the position measured during treatment (as a function of time and temperature).

Additionally, during the heating phase, the rod and the sample holder dilate differentially due to their difference in length (which corresponds to the size of the sample). It results, thus, in an artificial effect of elongation of the sample. To correct this effect, each measurement was corrected using the following equation:

$$L_C = \Delta L \,.\, \alpha \,.\, (T_t - T_0) \quad (5)$$

In which L_C is the length correction, α is the thermal expansion coefficient of stainless steel (14.10^{-6} K^{-1} [157]), T_t is the temperature at time t and T_0 is the initial temperature.

2.4. Mechanical tests

Uniaxial compression tests are often expressed in terms of stress versus strain. The data obtained from this device contains information on force and displacement, from which the modulus of elasticity (MOE) of a sample can be calculated.

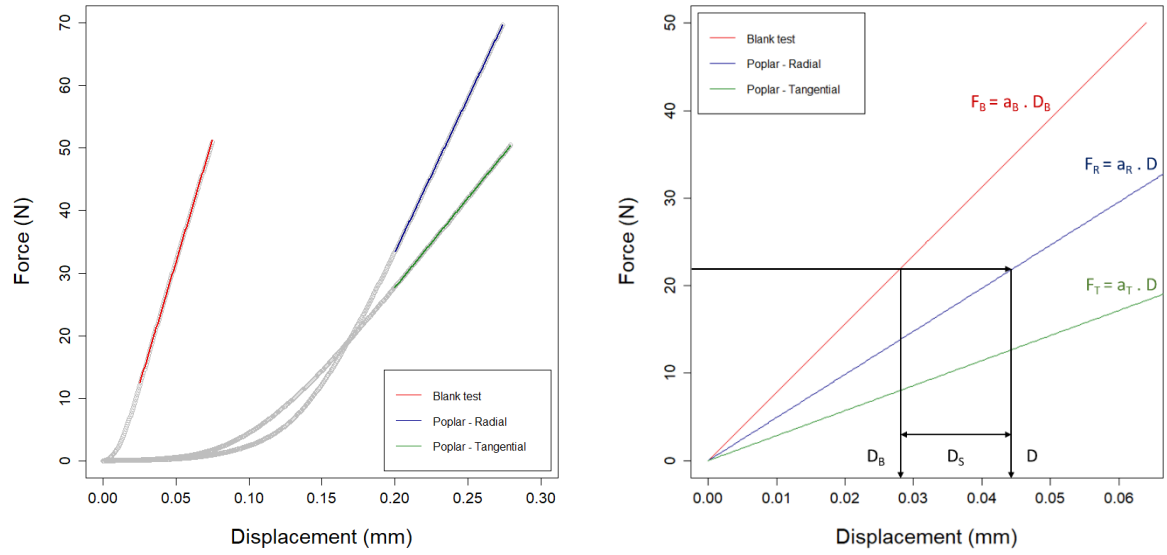

(a) (b)

Figure 44. (a) Measured displacement as a function of the imposed force (F – in grey) and the regression of the linear region for the blank test (red) and a native water-saturated poplar sample in the radial (blue) and tangential directions (green); (b) Displacement as a function of the imposed force after correction of the toe region. For a poplar sample, D is the total measured displacement, D_B is the part of the displacement due to the device and measured during the blank test and D_S is the part of the displacement strictly related to the sample. a represents the slope of the linear regression obtained for the blank test (B) and the poplar sample in the radial (R) and tangential (T) directions.

It is clear that, since the device itself is also subjected to loading, a correction must be made in order to subtract this effect. The first step was, thus, to perform a blank test in which the displacement undergone by the sample holder as a function of the applied force was identified and whose result is shown in Figure 44a. Figure 44a also shows the results of preliminary tests made with native water-saturated poplar samples in both radial and tangential directions. In each case, a linear domain can be identified, within which a linear regression was calculated (colored lines). As explained in Figure 44b, for a given force, the total displacement measured during the test with a poplar sample (D) has two components: a component is tied to the deformation suffered by the device (D_B) and the other is the real deformation suffered by the sample (D_S). The effect of the equipment can then be subtracted using a simple correction of the slope of the curbs, as shown in Equation 6:

$$a'_i = \frac{a_i}{1 - \frac{a_i}{a_B}} \qquad (6)$$

In which a_i is the slope of the curb in the direction i (either R or T) and a'_i is the corrected slope of the curb in the direction i.

An example of the obtained results can be observed in Figure 45:

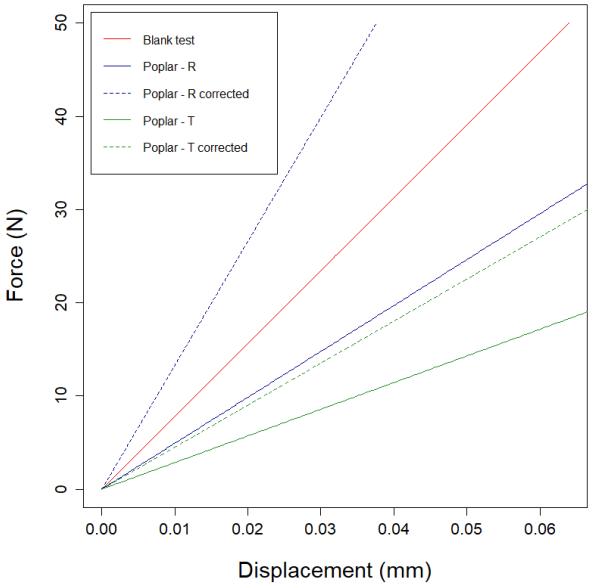

Figure 45. Measured displacement as a function of the imposed force and the respective corrected values.

The corrected slope of the curb is later used for calculating the MOE of the biomass according to the following relation:

$$E = a' \frac{L_0}{S_0} 10^{-3} \qquad (7)$$

Where E is the MOE of the material (in MPa), L_0 is the original length of the sample (in mm) and S_0 its cross-sectional area (in mm^2).

In Figure 44a, under low stress and strain, poplar presents a region where the relation between stress and strain is nonlinear and the slope increases with increasing loading. In a smaller scale, the same behavior result is obtained in the blank test. This is a very common behavior during mechanical testing, known as the toe region. International norms for the determination of mechanical properties of materials preconize the correction of this artifact, either by applying a preload (or prestress) before the beginning of the test (ISO 527 for tensile tests [158] and ISO 604 for compression tests [159]) or by mathematically removing the toe region by extrapolating the measured MOE to zero stress and setting strain equal to zero at that point (ASTM D638 [160]). Commercially available mechanical testing machines provide and recommend the use of a preloading feature, which can also help to ensure that the sample is correctly aligned and that its surface is uniformly in contact with the compression platen. Failure to do so may result in incorrect determination of a material's properties [45,97,161–163]. An aggravating factor in this study is that samples are submitted to a wide range of temperature levels, under which the mechanical behavior of wood can drastically change, as exemplified in Figure 46.

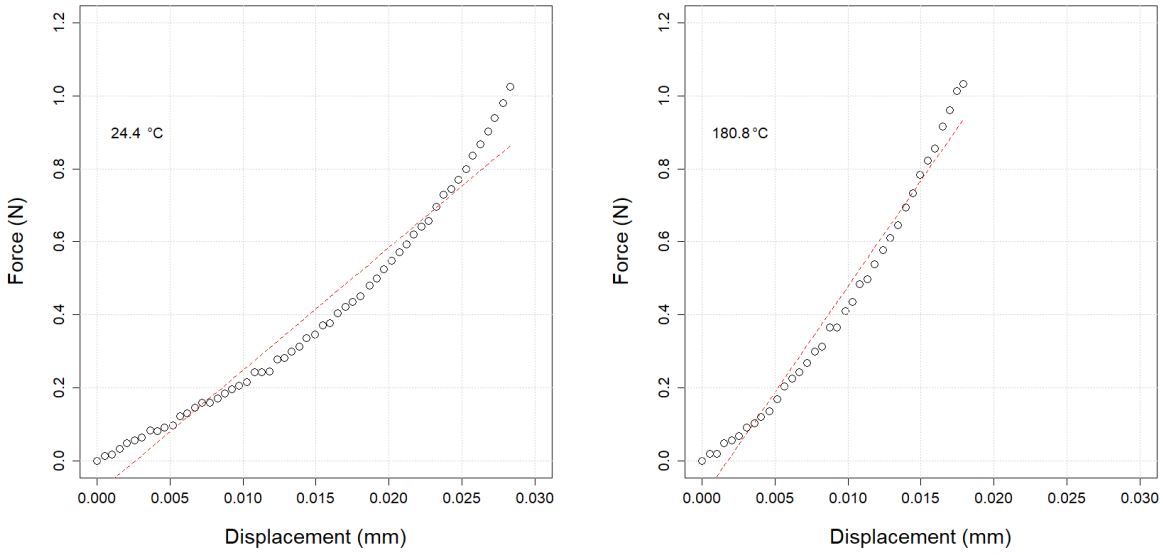

(a) (b)

Figure 46. Measured displacement (points) as a function of the imposed force (1 N) and the calculated linear regression (red line) for a poplar sample submitted to (a) room temperature and (b) 180 °C.

These results clearly demonstrate the need of a preload phase in the mechanical test protocol. Under room temperature (Figure 46a), the applied force is not sufficiently high to reach the linear region, making a post-treatment correction useless. At a higher temperature (Figure 46b), the linear region is reached under a lower force. Considering the fragility of wood materials after pretreatment, excessively high preload forces could result in damages to the samples. From these observations, a preload step in which the applied force decreases with the temperature was adopted (Figure 47).

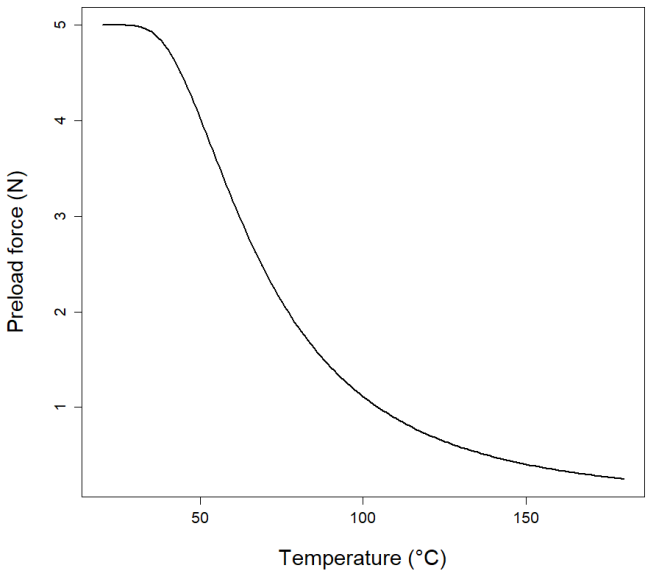

Figure 47. Adopted values of preload as a function of temperature

C. Chemical analyses

Giving a sense to the mechanical properties measured macroscopically required them to be accompanied by information on the chemical changes suffered by biomass. Chemical analyses were performed according to the National Renewable Energy Laboratory's (NREL) analytical procedures [164–166], as depicted in Figure 48.

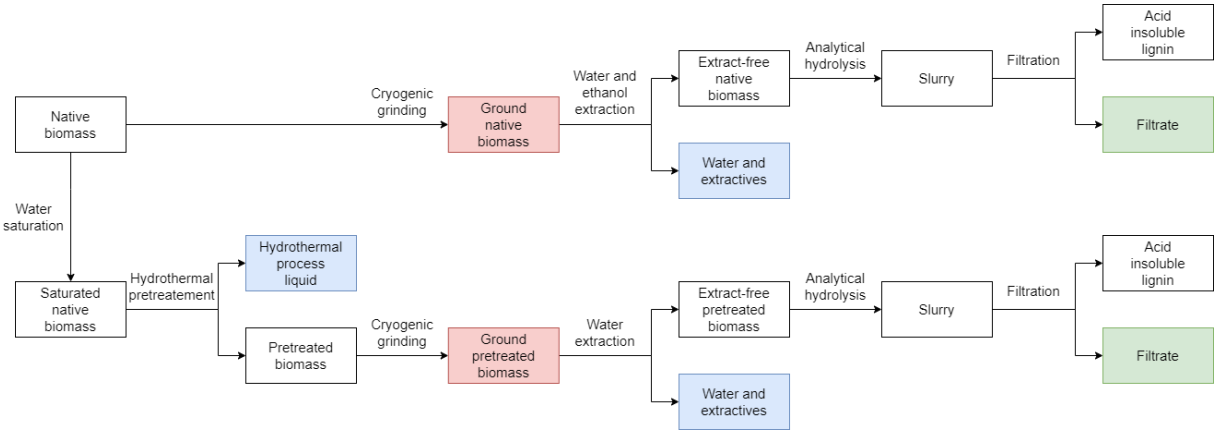

Figure 48. Flow chart of analysis. Fractions in blue were analyzed for monosaccharides, oligosaccharides, organic acids and degradation products; fractions in green were analyzed for monosaccharides and acid soluble lignin; and fractions in red were analyzed for isotherm sorption

It is important to note that, in the experimental set-up used in this study, biomass is not directly in contact with the hydrothermal process liquid. As a result, the hydrolyzed fraction present in the solid pretreated biomass – attached to its surface or in the liquid phase of internal pores – may have a higher concentration than the liquid fraction and, thus, must not be neglected. This is why, instead of just washing the treated biomass, as proposed by NREL method, a supplementary extraction step was performed and taken into account in the final result. To prevent any additional thermal degradation of chemical compounds, a three-step cold extraction was chosen. An aliquot of the solid sample was put in contact with distilled water in a 20:1 (m/m) water/biomass ratio. The mixture was submitted to an ultrasound bath for five minutes and then separated with a centrifuge. The supernatant was collected, and the pellet was submitted to two additional extractions according to the same protocol. The pellet was then oven dried at 40 °C, as recommended by NREL's analytical procedure.

D. Imaging techniques

Imaging techniques played an important role during this study, providing the connection between chemical and macroscopic scale. A total of four techniques were chosen: confocal Raman microscopy, X-ray nano-tomography, scanning electron microscopy (SEM) and field emission gun

scanning electron microscopy (FEG-SEM). This choice was made in order to cover different structural levels, but also to obtain information on both anatomical and topochemical aspects. In this chapter, only confocal Raman microscopy and X-ray nano-tomography are highlighted, as they required special methodology development. For their part, SEM and FEG-SEM were performed according to standard protocols and will be mentioned later on this manuscript.

1. Confocal Raman microscopy

As stated in Chapter I, Raman spectroscopy is a powerful technique for the study of wood, providing a chemical fingerprint of the material. When combined to confocal microscopy, it allows the obtention of topochemical information on the sub-parietal level, which is particularly interesting for highly organized materials such as wood. In this study, confocal Raman microscopy was used to assess, at the cell wall scale, the modifications suffered by lignocellulosic biomass after hydrothermal treatment.

Raman imaging involves three main steps, all of them equally important for obtaining good quality results [167]:

- Sample preparation;
- Spectra acquisition;
- Data treatment.

Each of these steps must be adapted to address the needs of a specific sample and according to the equipment available. The following sub-sections describe the methodology developed for our samples, with special attention to hydrothermally treated samples [167].

1.1. Sample preparation

In this study, confocal Raman microscopy is used to obtain a chemical map of wood cells before and after hydrothermal treatment. During sample preparation for confocal Raman microscopy, it implies finding a balance between keeping the material as close as possible to its original state and improving the quality of the signal.

Ideally, massive samples (whose thickness are greater than 1 mm) allow the observation of cells at their most unaltered state. In practice, however, it proves to be very complicated. Air-dried massive samples are likely to burn due to the overheating caused by the concentration of the laser at a single point [64,167,168]. To prevent samples from burning, a solution would be to immerse them in water. Nevertheless, the excess of fluorescence emanating from wet thick samples compromises the quality of the signal. For these reasons, the use of massive plant samples has quickly been discarded by confocal Raman microscopy users. Instead, they turned into typical transmission light microscopy sample preparation, very well described in previous works [82,167]. This configuration involves placing a thin section of the sample between a glass slide and a coverslip, with a few drops of distilled water. The coverslip is sealed with nail polish to keep water from evaporating during the tests (Figure 49d).

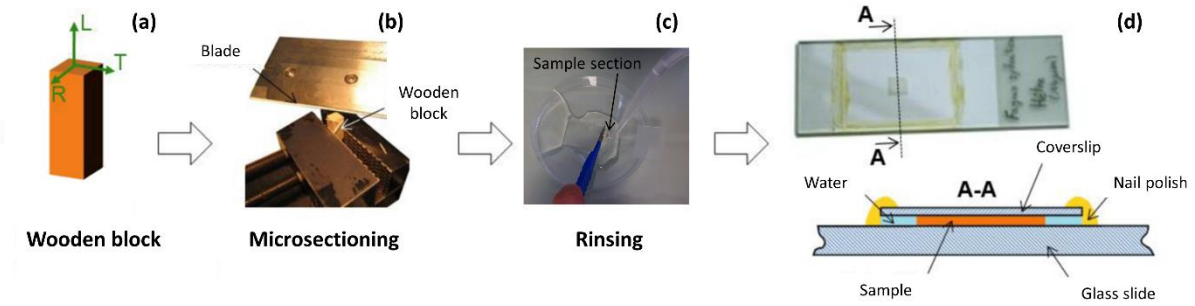

Figure 49. Sample preparation steps for confocal Raman microscopy. Adapted from [82].

The first step consists of sectioning the sample (Figure 49b) out of a wooden block (Figure 49a). The cross-sectional plane was chosen in this work for a better assessment of the different cell wall layers. Sectioning was performed with a sliding microtome (HM 450, ThermoFisher Scientific). Needless to say, new microtome blades are essential for obtaining good quality cuts. A sample thickness between 8 and 25 µm is recommended in the literature [82,167], which can easily be achieved in the case of native samples. For treated samples, the fragility of the vegetal tissue and the lack of cohesion between the cells made this step much more challenging and imposed a rather high thickness bracket (the precise parameters are given in Chapter IV). Another difference between native and treated samples lies in the technique used for sectioning. For native samples, it is customary to humidify the wooden block with distilled water prior to the sectioning, which eases the cut and increases the quality of the sections. In the case of treated samples, this intensified the fragility of the tissue and hindered the obtention of a slice. Thus, sectioning had to be performed in air-dried samples. The conditions found optimal for treated samples (in terms of thickness and cutting method) were also applied for native samples.

Sample sections were then sequentially rinsed with distilled water, a diluted sodium hypochlorite solution (0.02 % m/v) and distilled water. Rinsing has two objectives. Firstly, to remove low molecular weight components that do not participate on the structure of the cell wall. Secondly, to reduce laser-induced fluorescence. This is achieved by the oxidation of the chromophoric groups of lignins and wood extractives, which tend to fluoresce in their natural state reducing signal quality. Sodium hypochlorite solutions at concentrations lower than 5 % (m/v) seem to provide the above mentioned benefits without prejudice to the wood structure nor to the ratios between different peaks of the spectra [82].

After rinsing, samples were thoroughly placed on a glass slide, to which a few drops of water were added. A clean coverslip was placed on top, whose borders were then dried and sealed with nail polish.

1.2. Spectra acquisition

The measures taken during sample preparation to avoid laser-induced fluorescence were effective and allowed good results to be obtained for native samples under the usually applied conditions (most importantly for this part, a laser wavelength of 532 nm). However, preliminary tests of treated samples presented a high baseline, which was increasingly important with the augmentation of treatment severity (Figure 50a,b). Cell corners (Figure 50a,c,d) were particularly

affected by fluorescence. This led to a poor signal-to-noise ratio and, in some cases, even spectra saturation (Figure 50c,d). Two approaches can be found in literature to deal with highly fluorescent samples: the use of different laser wavelengths (especially those located either in the UV or the infrared (IR) / near-IR regions) [169–171] or the application of photobleaching [171–177]. These approaches will be discussed hereafter.

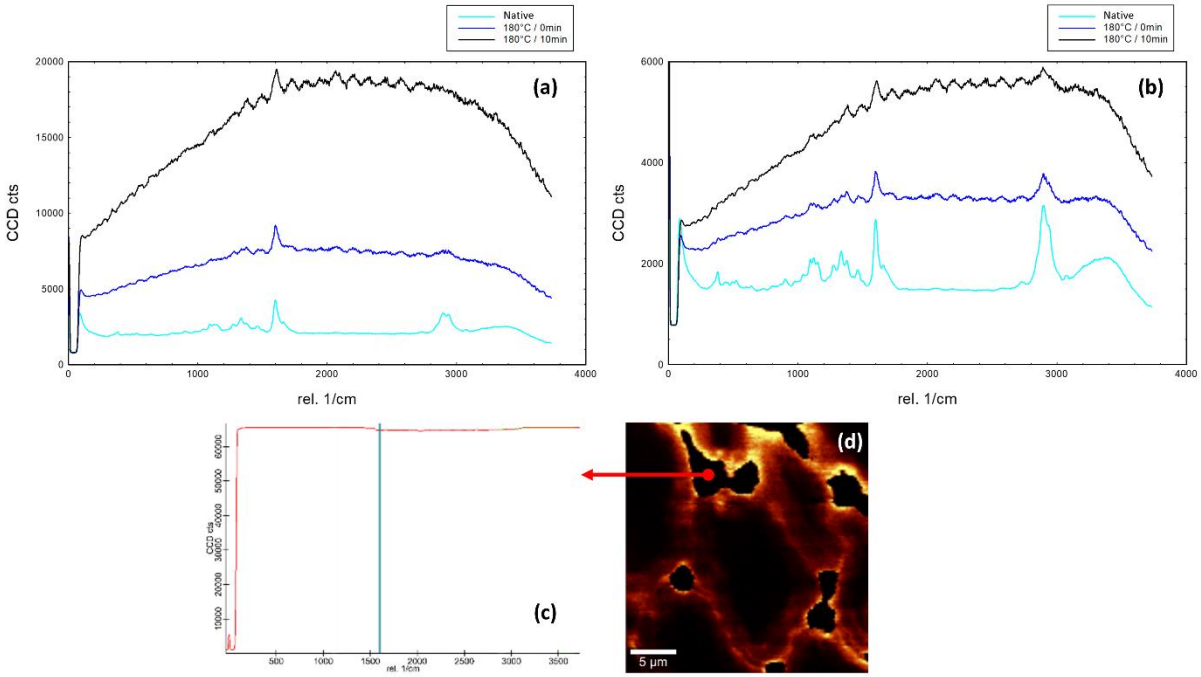

Figure 50 . Spectra of native and treated samples from points located at (a) the cell corner and (b) the S2 layer. Example of a saturated Raman spectrum (c) obtained from the cell corner of a treated sample (180 °C / 40 minutes) - point highlighted in (d). Image obtained by integrating the 1600 cm^{-1} band (d). Different regions of spectra saturation can be distinguished.

1.2.1. Laser wavelength

Given the very encouraging results obtained in previous papers, the first approach was to evaluate the effect of the laser wavelength. Increasing the laser wavelength (λ) implies a reduction in the energy supplied to the sample, which can prevent fluorescence. On the other hand, the intensity of the Raman scattering is proportional to $1/\lambda^4$ [64], therefore longer wavelengths result in less Raman scattering. The quality of a Raman spectrum depends, thus, on finding a good compromise between signal intensity and minimum fluorescence. Typical laser wavelengths used in Raman spectroscopy are: 364 nm (ultra-violet), 532 nm, 633 nm (visible), 785 nm and 1064 nm (near infra-red). The Alpha 300R+ confocal Raman microscope (Witec), available in the laboratory is equipped with a 532 nm (green) and a 785 nm laser (near-IR). To test other wavelengths, we benefitted from the help and the devices of the LMOPS (Laboratoire Matériaux Optiques, Photonique et Systèmes – CentraleSupélec/Université de Lorraine) and the LASIRE (Laboratoire de Spectroscopie pour les Interactions, la Réactivité et l'Environnement – Université de Lille). A summary of the tested conditions is given on Table 6. It is important to notice that operating under UV or near-IR lasers required the use of quartz coverslips [167].

Table 6. Summary of the different laser tested, and the respective device used

Wavelength (nm)	Region	Device	Objective
266	UV	LabRam HR Evolution UV (Horiba)	x80
473	Visible	LabRam HR Evolution visible (Horiba)	x100
532	Visible	Alpha 300R+ (Witec)	x60
532	Visible	LabRam HR Evolution visible (Horiba)	x100 Fluo
532	Visible	LabRam HR Evolution visible (Horiba)	x100
633	Visible	LabRam HR Evolution visible (Horiba)	x100
785	Near-IR	Alpha 300R+ (Witec)	x60

Compared with the previously mentioned results (532 nm), 266 nm (UV) seemed to be the most promising laser wavelength. It provided low baseline spectra (Figure 51a), which is a sign of low fluorescing.

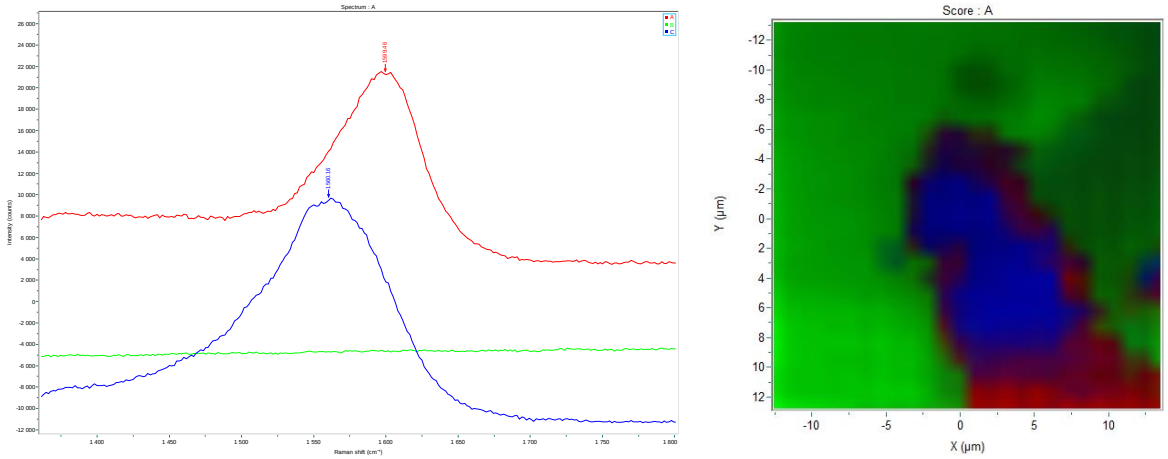

(a) (b)

Figure 51 . Mean Raman spectra (a) obtained for different zones (b) of a sample treated at 180 °C for 10 minutes using a 266 nm (UV) laser.

However, the use of UV Raman only allowed good results for a limited range of the spectra, around 1600 cm^{-1}. The peaks relative to carbohydrates could not be identified, which, allied with the low image resolution obtained with this equipment (Figure 51b), made us chose to continue with our device, despite the higher fluorescence.

1.2.2. Photobleaching

The second approach considered was photobleaching. Even though no reports of the application of photobleaching in treated wood samples has been found, it has been largely used for biological applications, such as *in vivo* measurements of carotenoid concentration in human skin [174] or the study of bone tissues [177]. Photobleaching – as far as the Raman technique is concerned – consists in irradiating the sample with the laser during a certain time before acquiring a spectrum [176], which converts the fluorophore into a non-fluorescent species [178]. The interest of applying photobleaching to hydrothermally treated samples was quickly confirmed by

preliminary tests. By performing two successive measurements, spectra had their baselines greatly reduced (Figure 52a,b), which made the Raman peaks stand out (Figure 52c,d).

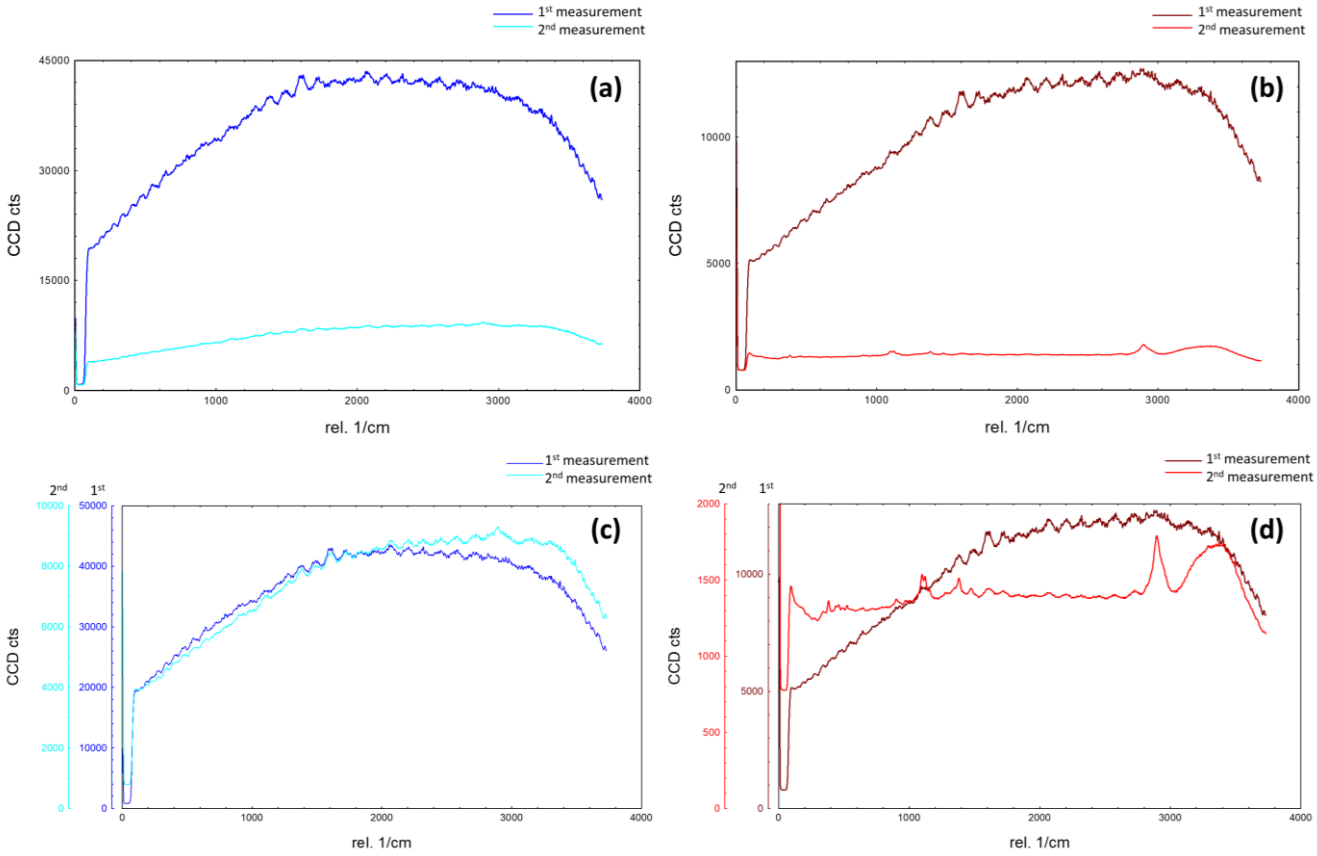

Figure 52 . Effect of photobleaching (2nd measurement) on the Raman spectra of hydrothermally treated (180 °C / 10 minutes) samples compared with the same samples before photobleaching (1st measurement). Spectra were obtained from a cell corner (a, c) and the S2 layer (b, d). For a better visualization of the results, a zoom is presented (c-d).

The ideal conditions (laser power and bleaching duration) that promote a successful removal of photoluminescence background without altering or degrading the sample can only be found empirically [178]. With this goal in mind, three different values of laser power (10, 20 and 30 mW) and four different exposure times (0.05, 0.1, 0.2 and 0.5 s) were evaluated by applying 60 successive measurements (with a 1-second gap between each measurement) on a severely treated sample (160 °C / 40 minutes). Spectra obtained from these measurements were then used to calculate noise-to-signal ratios, whose results are depicted in Figure 53. "Noise" was defined as the maximum peak height within the 2000-2500 cm^{-1} region, where no peak from the sample is expected. The height of the peak of interest (1600 or 2984 cm^{-1}) was considered as the "signal".

From Figure 53, it is possible to see that noise-to-signal ratio decreased exponentially with the number of acquisitions whichever the condition applied. In the case of the 2894 cm^{-1} band (Figure 53b), increasing the laser power resulted in a faster decrease of the noise-to-signal ratio. However, higher laser powers also resulted in a higher initial noise-to-signal ratio. Therefore, regardless the laser power used, the same ratios were obtained after 60 measurements.

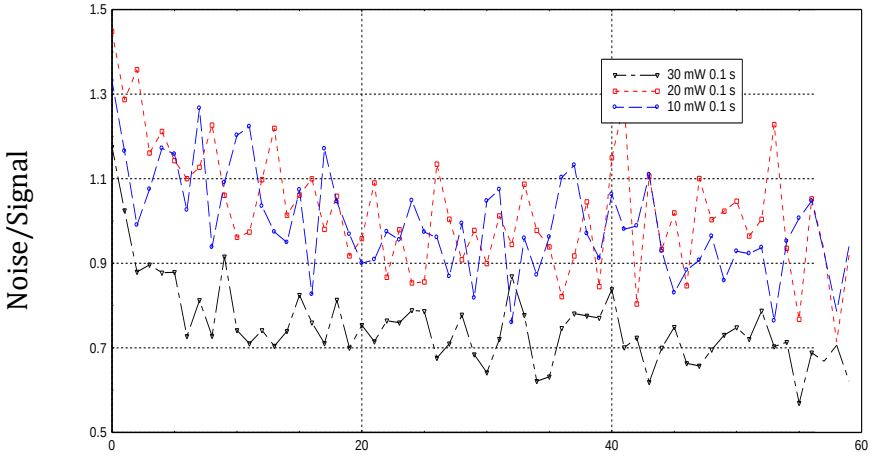

(a)

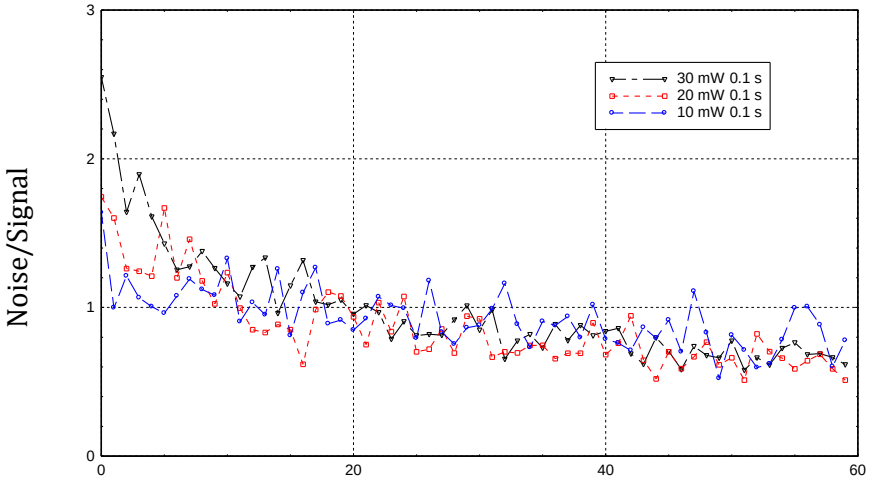

(b)

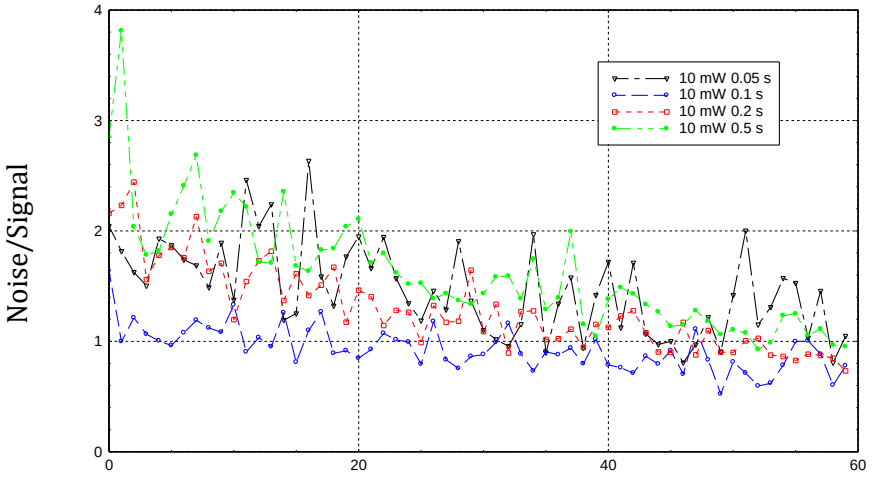

(c)

Figure 53 . Effect of successive measurements on the noise-to-signal ratio of Raman spectra of a hydrothermally treated (160 °C / 40 minutes) sample regarding the 1600 cm^{-1} band (a) and the 2894 cm^{-1} band (b, c).

Regarding the band at 1600 cm^{-1} (Figure 53a), a slightly better signal was obtained using 30 mW of laser power rather than 10 or 20 mW. However, previous studies [179] have reported that a laser power superior to 10 mW could cause significant chemical changes to the cell wall components. This is the reason why we chose to continue with 10 mW of laser power. Using this laser power, an exposure time of 0.1 s seemed to provide the better noise-to-signal ratio (Figure 53c). Moreover, according to works on native wood [179] no molecular change is observed with an exposure time inferior to 0.13 s.

Finally, the choice of the number of preliminary exposures prior to the image acquisition was based on the total acquisition time. Indeed, with each repetition taking approximately two hours for the scan of one cell and considering the time for sample preparation and calibration of the device, no more than four measurements could be made per day, which limited our protocol to three preliminary exposures, followed by one final measurement.

Despite all the actions taken to limit samples fluorescence, it remained a major drawback for the most severely treated samples (180 °C), affecting the quality of the results. Consequently, only the Raman images from samples treated at 160 °C are presented in Chapter III.

1.3. Data treatment

All the data treatment performed during this work was based on built-in functions of the Witec PROJECT FOUR software. Spectra were treated for cosmic ray removal and background subtraction. They were then used for image generation. The data generated by confocal Raman microscopy is composed of multiple dimensions. Each pixel contains (at least) information on its coordinates (x and y), wavenumber and intensity of the signal. To display this information using a Raman image two approaches can be used: univariate or multivariate analysis. In univariate analysis, each spectrum provides information to its corresponding pixel in the image, whose values are generally determined using filters. In the present work, integrated intensity (sum) filters were used. The resulting images present different colors depending on the signal intensity of the selected peak. Contrarily, multivariate analysis uses the entire data set for defining the value (color) of each pixel. In this work, the cluster analysis method was used. It automatically sorts the acquired spectra by similarity and provides an image showing the location of each cluster and its mean spectrum [180].

2. X-ray nano-tomography

X-ray nano-tomography was another important imaging technique during this study. The objective was to develop a non-destructive method, so that the same sample can be analyzed before and after treatment, constituting a powerful tool for the assessment of anatomical changes.

For this purpose, 3D scans of samples are obtained using a nano-tomograph EasyTomXL Ultra 150-160, RX Solutions. In X-ray nano-tomography, 2D projections are generated by measuring the X-ray attenuation caused by the sample. Because the sample is positioned on a rotating support between a nano-focus vacuum tube for X-ray emission and a CCD detector of 2,016 x 1,344 pixels, projections can be obtained under different angles and are posteriorly used for generating cross-

sectional slices – treated with ImageJ software, version v1.52i – and reconstructing 3D volumes – using Avizo 2019.2 software (Thermo Scientific™).

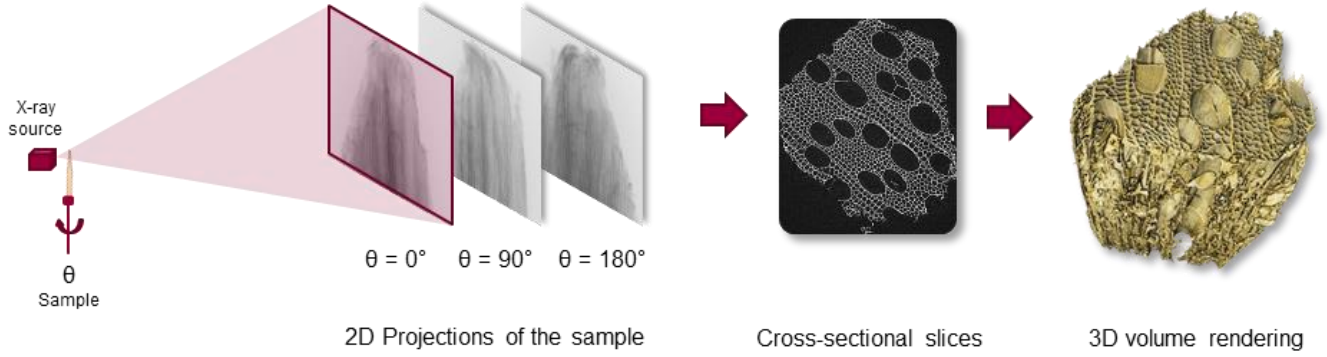

Figure 54 . Principle of X-ray nano-tomography.

2.1. Sample preparation

Sample strain during scanning would generate noise and, even, make the 3D reconstruction impossible. Thus, samples are usually analyzed in the dry state (in equilibrium with the relative humidity of air) to prevent shrinkage. Treated samples must also be dried. Due to the fragility of the cell wall, however, air drying is likely to alter the morphology of the treated sample and even causing the collapse of the cells. For this reason, a method to dry the treated samples without altering their morphology had to be developed. Two drying methods were tested: *i)* natural air drying under room conditions for 48 h; and *ii)* freeze-drying (or lyophilization) – at -55 °C using an Alpha 1-2 LD (Martin Christ) laboratory freeze-dryer – commonly used prior to imaging as a preparation method for highly shrinkable samples [135].

For image acquisition, a scan was made in a native wood sample, which was posteriorly water-saturated for 12 h and hydrothermally treated. After treatment, the two drying methods were applied to different samples and a new scan was performed. The obtained results are shown in Figure 55.

When compared to its native state, the air-dried treated sample (Figure 55a) revealed a great extent of deformation throughout the sample and of shrinkage in the tangential direction, as expected. Freeze-drying (Figure 55b) clearly prevented the deformation and shrinkage promoted by air drying (Figure 55a). Nevertheless, some extent of anatomical modification can be observed in the freeze-dried treated sample, which is most likely due to the treatment.

To validate freeze-drying as a drying method, it was also necessary to verify if it could alter the anatomy of native wood samples. A native sample was therefore scanned, water-saturated, freeze-dried and then re-scanned. The comparison between the cross-sectional images obtained before and after freeze-drying (Figure 55c) revealed no influence of this technique on the morphology, which validates the method.

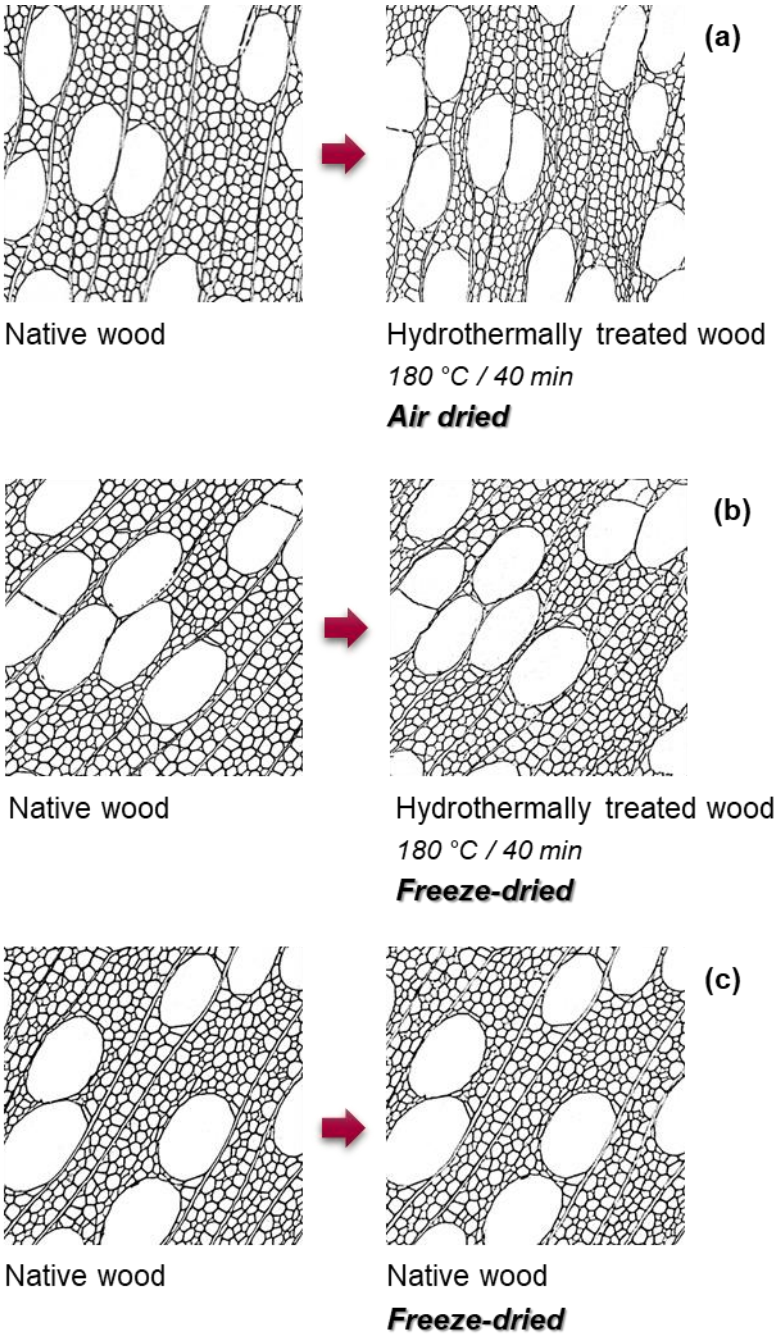

Figure 55 . Comparison between air drying and freeze drying as methods to prepare samples for X-ray nano-tomography (voxel size = 1x1x1 µm³). Segmented X-ray cross-sectional images of native (left column) and treated (right column) samples using different preparation methods: (a) hydrothermal treatment followed by air drying; (b) saturation and freeze drying; (c) hydrothermal treatment and freeze drying.

2.2. Image analysis

One of the main anatomical changes qualitatively observed on hydrothermally treated samples was the reduction of cell wall thickness. To quantitatively assess this shrinkage, an image analysis method was developed using the Local Thickness plugin of ImageJ software. It is mainly based on the Saito-Toriwaki euclidean distance transformation algorithm [181,182]. Since this plugin requires segmented images, a segmentation method had to be implemented. It involved three

steps, all based in ready-to-use functions from ImageJ. The raw image (Figure 56a) was firstly segmented using the "Auto Threshold" function with the "Moments" method (for dark background). Auto thresholding is important to remove all bias related to the user. More particularly, the "Moments" method was chosen for its good suitability to the cross-sectional slices from different samples and because it preserved the dimensions of the cell wall. The resulting image (Figure 56b) was then submitted to the "Particle analysis" (minimum particle size was set to 5000 pixel^2) and the resulting mask (Figure 56c) was finally input into the "Local thickness" function.

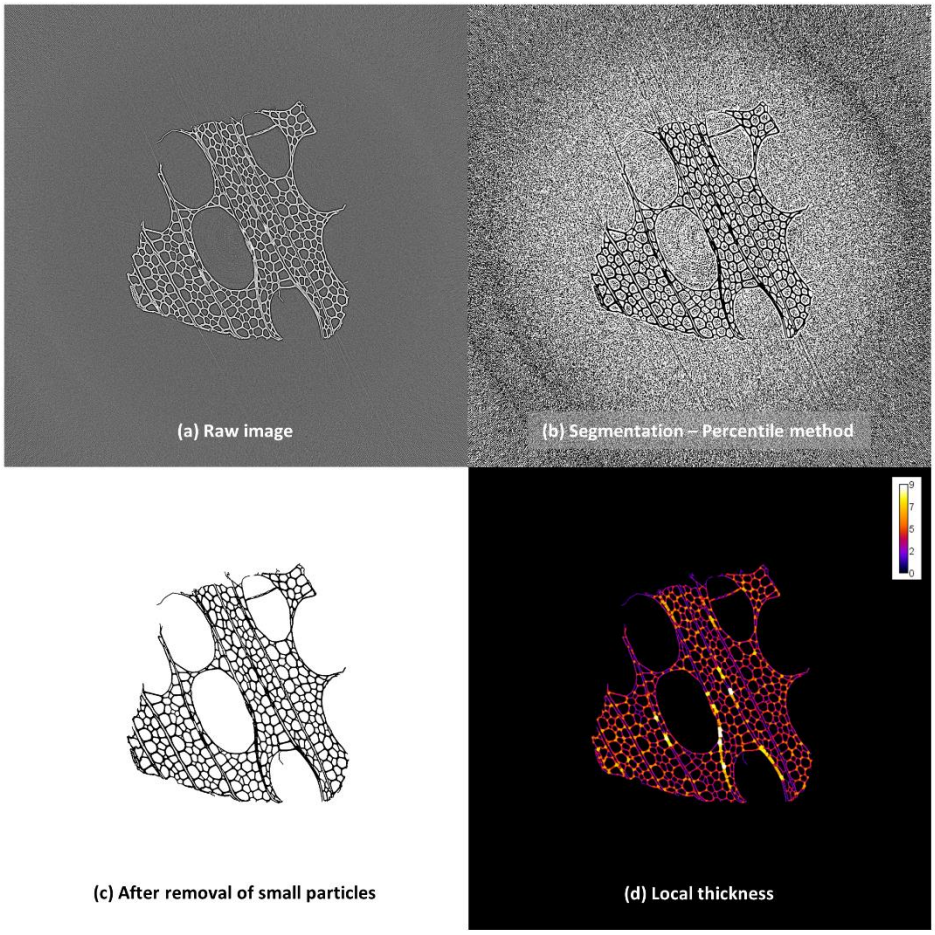

Figure 56 . Chain of image treatments from raw image (a) to local thickness (d) using ImageJ software.

E. Sampling

Like other biological materials, wood presents a high variability. For example, the mechanical properties of wood can vary by a factor 10 between the longitudinal direction and the other two directions [98]. The sampling protocol is therefore crucial to prevent measurement errors by ensuring the obtention of twin samples. Sufficiently small wood specimens – in comparison to the

radial distance to the pith – can be considered as orthotropic materials and this orthogonality must be respected during sample preparation.

The final size of the specimens was chosen to fulfil the constraints from different protocols (sample size for mechanical and shrinkage tests and amount of biomass required for chemical tests). These constraints impose sample sizes of 8^3 mm^3 (radial - R, tangential - T, longitudinal - L) for mechanical and shrinkage tests, and 40 x 8 x 8 mm^3 (R x T x L) for chemical tests. The greatest challenge of the sampling step was, therefore, to obtain small samples from large wood boards, always respecting the orthogonality of the material.

A defect-free core board (Figure 57a) was chosen for this work due to its correct orientation with respect to the three reference planes (LT, LR and TR). The longest dimension of the board corresponded to the L direction. The first step was to cut the board into five pieces (Figure 57a), with cross-sections corresponding to the TR plane (Figure 57b), using a miter saw. The small boards were then cut into bars along the longitudinal direction (Figure 57c).To orientate the subsequent cuttings, a line was drawn in each bar to guarantee than all samples were aligned according to the longitudinal direction following the same annual rings. Indeed, among the three orientations, wood presents less variability in the longitudinal direction. Each bar was then divided into 7 blocks of ca. 5 cm (L) x 3 cm (T) x 1.5 cm (R) (Figure 57d). These blocks were sufficiently small to be cut by a precision cutting machine (Secotom-60, Struers). Always following the drawn line, a smaller bar was extracted, from which 8 x 8 x 8 mm cubes were cut. For a better visualization of the successive cuts made, the LR plane is highlighted in green in Figure 57. It does not mean, however, that the highlighted pieces are exactly the ones used in the following steps.

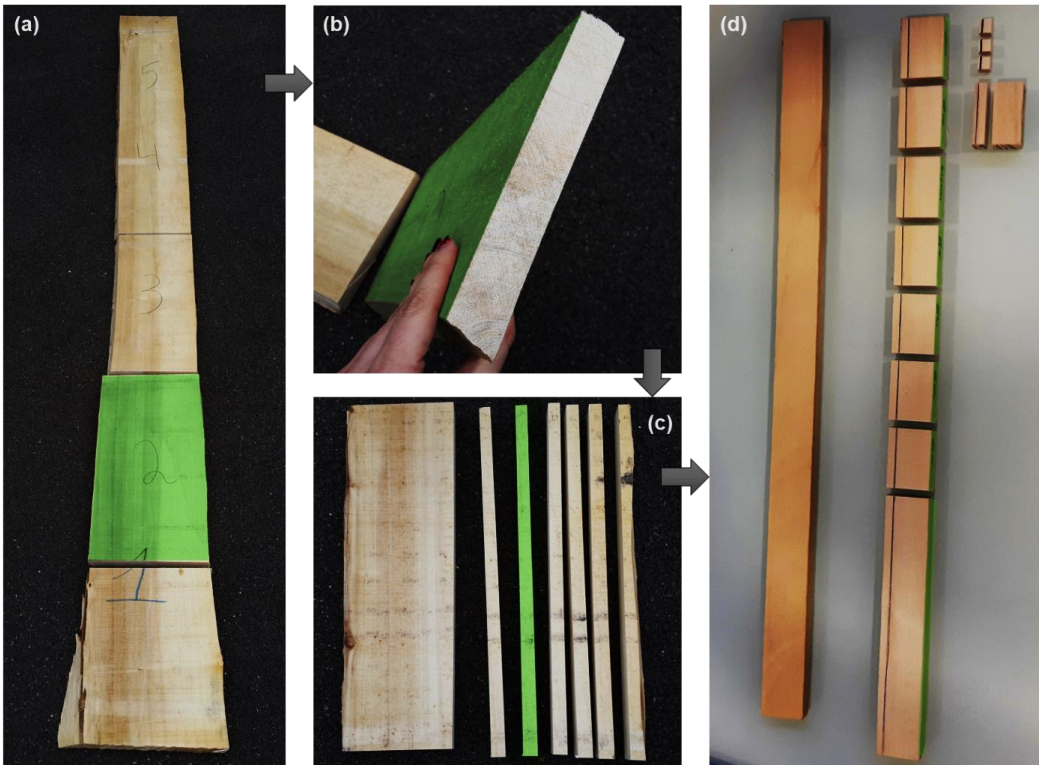

Figure 57. Sampling protocol from wood board (a) to small cubic samples (d). The green color highlights the LR plane.

In most cases, due to the large amount of data, the results obtained are presented for one sample. However, each test has been performed at least in duplicate. It is important to highlight that care has been taken so that all measurements were made on twin samples and that the repeatability of these measurements has been ensured.

When a concomitant evaluation of the chemical composition had to be performed (Chapter V), the sampling protocol was slightly changed. In this case, the L direction was purposely chosen as the smallest dimension (8 mm) to ease mass transfer and, thus, ensure a good homogeneity of the hydrothermal treatment. From the small boards (Figure 57a), the first cut was made according to TR plane (Figure 58). Small bars (40 x 8 x 8 mm^3 - R x T x L) were then cut, all aligned along the longitudinal direction.

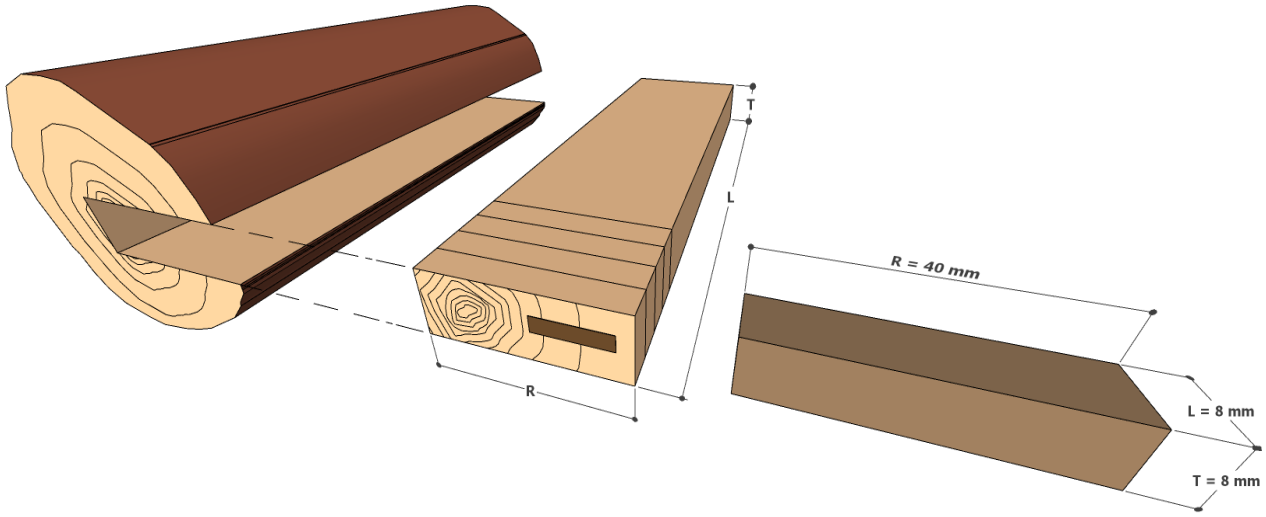

Figure 58. Schematic representation of the sampling process

When applied to imaging, samples needed a special geometry as a function of the constraints of each specific technique. The 8 x 8 x 8 mm wooden cubes previously mentioned were then used to produce adapted samples, as summarized in Figure 60.

For confocal Raman microscopy, 3 x 3 x 8 mm (R x T x L) blocks were split from the original cubes along the grain and 16 µm thick cross-sectional slices were cut from these blocks using a sliding microtome (Microm HM 450 – Thermo Fisher Scientific).

Samples for nano-tomography analysis should be very small to ensure good resolution. However, after pretreatment, samples are fragile, making sample manipulation challenging. Small samples are also difficult to attach to the sample holder. For these reasons, untreated samples were carved out of wood blocks in a conical shape. The smaller portion (with a diameter of about 1 mm) was scanned while the larger one was used to hold the sample.

After submitted to nano-tomography, samples were cross-sectioned using a microtome blade and then observed using an environmental scanning electron microscope (ESEM, FEI Quanta 200).

To examine the structure of cell walls to a greater depth, a field emission gun scanning electron microscope (FEG-SEM) Model LEO 1530 (Leo Electron Microscopy Ltd, Zeiss, Oberkochem,

Germany) was used. In this case, the 8 x 8 x 8 mm wooden cubes were split along the longitudinal-radial plane.

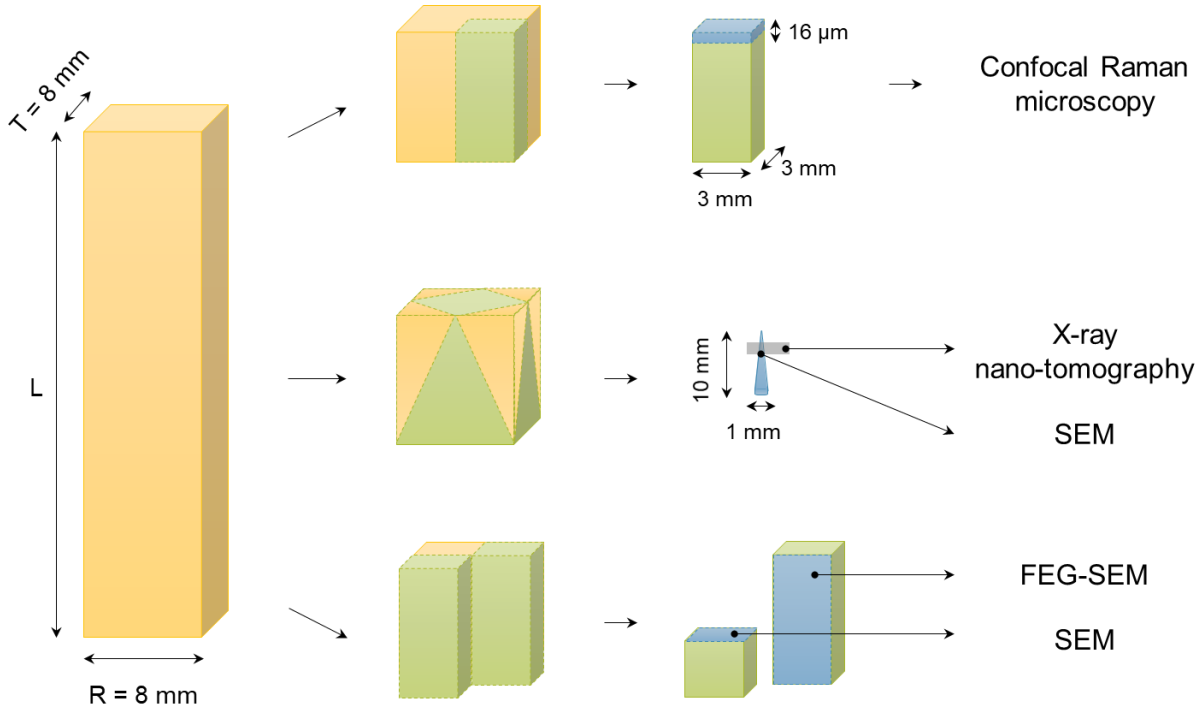

Figure 59. Summary of the sampling methods used for different imaging techniques.

CHAPTER III. Multiscale investigation on the chemical and anatomical changes

A. Preamble

As stated in the literature review, structural and anatomical aspects of biomass can be as important for its valorization as its chemical composition. Despite the major influence of these properties on the steps that follow pretreatment, there is still a lack of knowledge regarding the effects of pretreatment on the morphology of biomass, especially at the cell and cell wall scales. Imaging techniques constitute a powerful tool to explore this subject. The large range of available techniques can cover most of the relevant scales. Furthermore, some of them allow the obtention of both anatomical and chemical information. It is therefore interesting to combine different techniques in order to obtain a global vision of the changes on the cell wall structure through qualitative and semi-quantitative data.

The purpose of this chapter is to investigate the concomitant anatomical and chemical changes of lignocellulosic biomass submitted to hydrothermal treatment. Within this aim, four imaging techniques were deployed – confocal Raman micro-spectroscopy, X-ray nano-tomography, scanning electron microscopy (SEM) and field emission gun SEM – achieving spatial dimensions from a few tenths of micrometers to a few nanometers. This rather unique combination also has the advantage of combining the strengths of each of the used techniques: chemical information (through Raman spectroscopy), non-destructive analysis, 3D anatomy (X-ray tomography) and good spatial resolution (SEM). The methods developed during this thesis to ensure the quality and reliability of the results have been described in Chapter II and are briefly covered in Chapter III.

From a chemical point of view, the main observed changes were hemicellulose hydrolysis and lignin migration. These changes could later be linked to ultrastructural changes. The shrinkage coupled with thinner cell walls of treated samples clearly reflected a mass loss which is, probably, related to the hydrolysis reactions. As a consequence, cell walls were likely weakened, resulting in the observed reduction of cell circularity. In the case of more severe treatments, rupture and detachment of adjacent cells were also observed.

From a broader perspective, these results can help understand the effects of hydrothermal treatment on the subsequent stages of the bioethanol production chain. The observed detachment of adjacent cells and the thinning of the cell wall are likely to increase biomass susceptibility to the explosion step. It represents valuable information towards better modelling, simulation and optimization of steam explosions. Finally, regarding the enzymatic hydrolysis, the changes in biomass structure are likely to improve the accessibility of cellulose to enzymes. The disruption of certain cells and the detachment between neighbor cells increases the exposed area, whereas, depolymerization of hemicelluloses and lignin delocalization change cellulose exposition.

B. Multiscale investigation on the chemical and anatomical changes of lignocellulosic biomass for different severities of hydrothermal treatment

Julia P. Lancha[1], Patrick Perré[1,2], Julien Colin[1,2], Pin Lv[1], Nathalie Ruscassier[2], Giana Almeida[3]

[1] Université Paris-Saclay, CentraleSupélec, Laboratoire de Génie des Procédés et Matériaux, SFR Condorcet FR CNRS 3417, Centre Européen de Biotechnologie et de Bioéconomie (CEBB), 51110 Pomacle, France

[2] Université Paris-Saclay, CentraleSupélec, Laboratoire de Génie des Procédés et Matériaux, 8-10 rue Joliot-Curie, 91190 Gif-sur-Yvette, France

[3] Université Paris-Saclay, INRAE, AgroParisTech, UMR SayFood, 91300 Massy, France

To be submitted

Abstract

The changes sustained by lignocellulosic biomass during hydrothermal treatment have a chemical origin and are reflected at multiple scales. This study proposes the use of multiple imaging techniques—confocal Raman microscopy and X-ray nano-tomography—to obtain a multiscale understanding of biomass alterations during hydrothermal treatment. This unique combination of analyses provided valuable information on topochemical and morphological changes of poplar samples. Holocellulose hydrolysis and lignin modifications were observed and the chemical changes detected at the cell wall level corresponded to microscopic modifications. Overall, after treatment, samples shrank and had thinner cell walls. Subject to more severe pretreatments, cells were disrupted and detached from adjacent cells. Our results demonstrate that these specific techniques have proven utility in providing a multiscale assessment of the cell wall degradation after hydrothermal treatment.

Keywords: Imaging techniques; Poplar; Pretreatment; Confocal Raman microscopy; X-ray nano-tomography

1. Introduction

Most biological materials have hierarchically organized structures whose properties are affected by their chemical composition, the interactions between components, and by their spatial distribution and organization. These relationships between properties are observed for lignocellulosic biomass and, particularly, wood.

Wood cell walls are composed of layers that differ in their structure, thickness and composition. The main layers are the primary cell wall and the secondary cell wall, which is composed of three layers (S1, S2 and S3). The structure between two adjacent cells is called the middle lamella, but

due to the difficulty in distinguishing the primary cell wall from the middle lamella, they are often analyzed together as the compound middle lamella [43]. In this study, we focus on two of these layers: the secondary cell wall, easier to observe because of its large thickness; and the compound middle lamella, because it ensures bonding between neighbor cells. Even though each layer has distinct characteristics, they are all composed primarily of three polymers: cellulose, hemicellulose and lignin.

Cellulose is the main component of wood, accounting for 45–47% and 40–45% of hardwood and softwood weight, respectively [37]. It is a polymer of β-D-glucopyranose [43] linked by 1,4-glycosidic bonds [122]. Its linear nature and the presence of multiple hydroxyl groups [122] make it likely to form intra- and intermolecular hydrogen bonds. This chemical feature has structural consequences: cellulose is highly organized into microfibrils [22], forming a crystalline core with a semi-crystalline shell. This structure gives wood its strength. Moreover, the crystalline nature of cellulose also makes it resistant to chemical attack [43].

Unlike cellulose, hemicellulose is a type of polymer composed of different pentose and hexose monosaccharides [119]. In hardwoods, hemicelluloses constitute 25–40% of wood by weight [37] and are mainly composed of glucuronoxylans, which consist of a xylose unit backbone with 4-O-methylglucoronic acid and O-acetyl side groups. In softwoods, they can constitute 25–29% of wood by weight [37] and have glucomannan as their main constituent [47]. Their lower degree of polymerization and branched structure make them more sensitive to temperature and chemical attacks than cellulose [43].

Lignins are heterogeneous, high molecular weight phenolic compounds that constitute 20–25% and 30–60% of hardwoods and softwoods, respectively [37]. They are composed of three basic units: syringyl (S), guaiacyl (G) and p-hydroxyphenol (H) phenylpropanoid moieties. Lignins frequently form covalent bonds with surrounding carbohydrates, especially hemicelluloses [122]. Softwood lignins are almost entirely composed of G units, while hardwoods have both S and G units [183].

These three components form an extremely recalcitrant matrix, requiring pretreatment when lignocellulosic biomass is utilized in the production of second-generation biofuels. Among the vast range of pretreatments available, steam explosion is notable as it requires no additional solvent and can be applied to a variety of raw materials. It consists of two steps, the first of which is hydrothermal treatment, during which biomass is subjected to temperatures up to 230 °C under steam-saturated pressure for several minutes [44]. The pressure is then rapidly released in the explosion step. The changes experienced by biomass during hydrothermal treatment greatly influence the explosion and the subsequent bioethanol production steps and impact the efficiency of the entire production chain.

A full understanding of the effects of pretreatment on lignocellulosic biomass, including both chemical and structural aspects, can only be achieved through a multiscale approach. From a molecular point of view, partial hydrolysis releases mono- and oligosaccharides, which has been extensively demonstrated in literature [22,115]. At larger scales, cell wall breakdown can alter mechanical and anatomical biomass properties. Despite the effect of structural changes on the subsequent enzyme accessibility, very little attention has been paid to the cell wall and cell scales. Combining several imaging techniques can be a powerful tool in addressing this issue. Raman spectroscopy is of particular interest because it provides a chemical fingerprint of the material

and combined with microscopy, allows the assessment of sub-parietal composition. It has proven useful mainly in the study of lignocellulosics [69,184]. One disadvantage of using confocal Raman microscopy is that sample preparation requires cutting the sample into thin layers, which can alter its morphology. In contrast, X-ray nano-tomography is non-destructive, allowing morphological assessment of the same sample before and after treatment without the artifacts of sample preparation. The results obtained from this technique provide morphological information on the tissue scale with a sub-micrometric resolution. For the first time in this field, we combine these two imaging techniques to characterize hydrothermal treatment by providing a global, multiscale view of biomass changes during the process.

2. Material and methods

2.1. Biomass

A 25-year-old poplar tree (*Populus euroamericana* 'Koster') from a forest in Auménancourt-le-Petit (France) was used as a source of biomass. It was chopped and cut into boards that were subsequently air-dried. All samples were obtained from a single defect-free board with a straight grain angle and carefully cut along the longitudinal direction, in which the natural variability of wood is the lowest. The sample size and preparation method depended on the constraints of each imaging technique, as presented in the next sections and summarized in Figure 60.

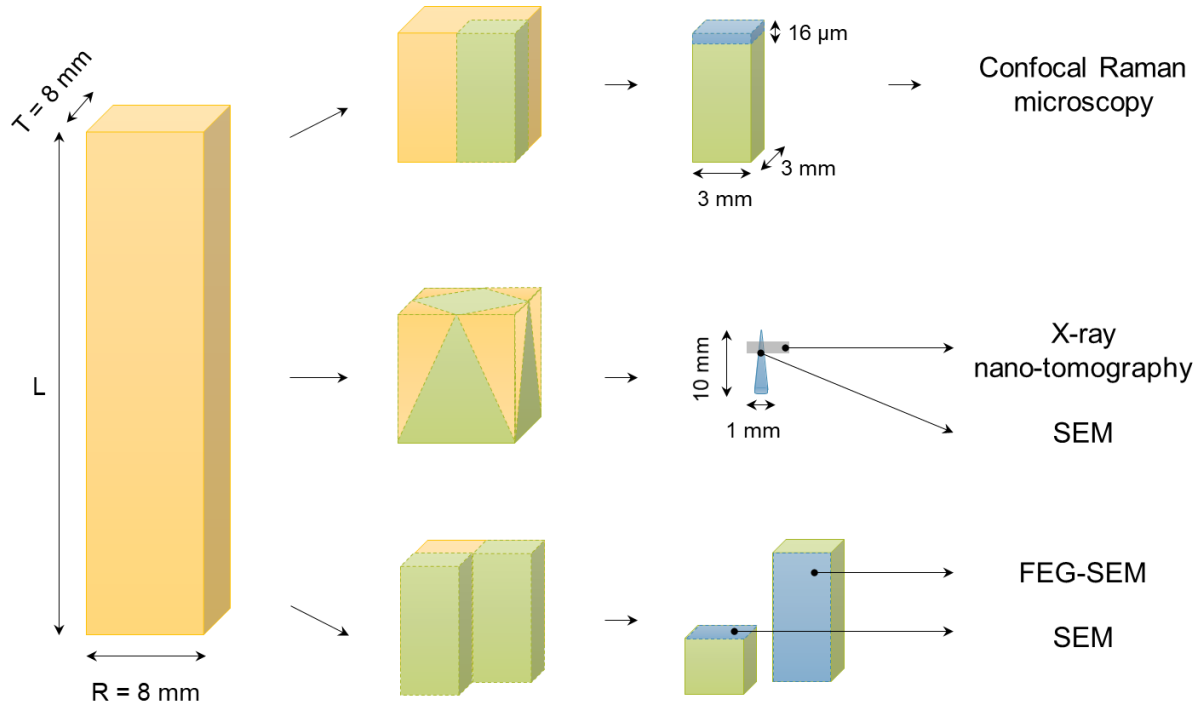

Figure 60. Summary of the different sampling methods

2.2. Hydrothermal treatment

Hydrothermal treatment was conducted in an in-house developed device, described in previous works [34,185]. This device allows temperature to be perfectly controlled by two electric heating collars (370 W) placed at the outer surface of the chamber and a PID device (Eurotherm 3216) equipped with a K-thermocouple.

The hydrothermal treatment requires samples to be saturated in water to allow a good heat transfer and reproduce the industrial process, where water vaporization is essential for the explosion step. Samples were saturated in distilled water for 12 h using vacuum-pressure cycles. To avoid any deformation from sudden contact with liquid water, all samples were previously submitted to a pre-saturation step, during which they were kept at 75 % relative humidity (RH) conditions overnight.

Treatments were performed at 160 and 180 °C under saturated water vapor conditions for 0, 10, 20 and 40 minutes (plateau duration). The reaction chamber was heated from room temperature to the treatment temperature (around 8 °C/min). Chamber was kept at a constant temperature for the desired time and then cooled down (approximately 9 °C/min) to room temperature by two external fans. After treatment, samples were subjected to different protocols described in the following sections.

Paired samples were used for chemical analysis of untreated and hydrothermally treated samples and for the calculation of mass loss during the treatment, as described by [186].

2.3. Confocal Raman microscopy

2.3.1. Sample preparation

Poplar cubes (8^3 mm^3) were hydrothermally treated according to the previously described protocol. Treated water-saturated samples were stored in a closed chamber at 75% relative humidity for two days to allow slow drying and to minimize deformation and cell wall collapse. Samples were then dried in ambient air for two more days. Control and hydrothermally treated 3 x 3 x 8 mm poplar blocks were then split from original cubes along the grain (respectively in radial, tangential and longitudinal directions) and 16 µm thick cross-sectional slices were cut from these blocks using a sliding microtome (Microm HM 450 – Thermo Fisher Scientific). Slices were sequentially washed with distilled water, a diluted NaClO solution (0.02% m/v) and distilled water. Washed samples were placed between a microscope slide and a coverslip with a drop of water, to prevent the sample from burning. The set was sealed with nail polish to avoid water evaporation [167].

2.3.2. Image acquisition

Chemical maps of wood fibers were obtained using an Alpha 300R+ confocal Raman microscope (Witec), equipped with an objective from Nikon (Plan Apo VC 60x NA=1.40 Oil), a piezoelectric x-y stage and a CCD detector. Scans were run at least in triplicate for each combination of treatment temperature and residence time. For each analyzed point of the sample (every 0.2 µm), a spectrum was acquired with a 532 nm laser at 10 mW and an integration time of 0.1 seconds per pixel. Laser-induced fluorescence (LIF) is a known challenge when dealing with Raman spectroscopy of

lignocellulosic materials, especially in highly lignified or treated samples [78]. Even though there are no studies showing the application of photobleaching to treated wood, it has been largely used to reduce fluorescence of biological samples, e. g. carotenoids in human skin [174]. At the same time, studies of untreated wood show that Raman bands were not significantly affected by a 10 mW green laser exposure (532 nm), even after repeated measurements, when integration time was less than 0.13 s [179]. In the present study, the application of a photobleaching before spectra acquisition allowed for an increase in the signal-to-noise ratio, as a consequence of fluorescence reduction.

Spectra were treated for cosmic ray removal and baseline correction using WITec's software PROJECT FOUR. The same software was used for generating chemical maps with a univariate approach, by integration over selected wavenumber bands; and with a multivariate approach, by cluster analysis.

2.4. X-ray nano-tomography

2.4.1. Sample preparation

Samples for nano-tomography analysis should be very small to ensure good resolution. However, after pretreatment, samples are fragile, making sample manipulation challenging. Small samples are also difficult to attach to the sample holder. For these reasons, untreated samples were carved out of wood blocks in a conical shape. The smaller portion (with a diameter of about 1 mm) was scanned while the larger one was used to hold the sample.

To study the effect of hydrothermal treatment on the anatomical structure of biomass, the same samples were scanned before and after treatment. Thus, untreated samples were scanned, then submitted to hydrothermal treatment according to the protocol previously described, and finally re-scanned. To prevent the collapse of treated water-saturated samples, after treatment, these samples were immediately frozen at -80 °C and later freeze-dried (Alpha 1-2 LD, Martin Christ). Preliminary tests were made on untreated samples to evaluate the effect of freeze-drying on anatomical structure. It proved that this methodology does not affect samples morphology.

2.4.2. Image acquisition and treatment

Samples were scanned (EasyTomXL Ultra 150-160, RX Solutions) with a voxel size of 500 nm^3 using a nano-focus vacuum tube for X-ray emission at a working voltage of 100 kV and working current of 170 µA. A total of 1,440 radiographs were obtained, each with an exposure time of 2 s and an average of 5 frames, using a CCD detector of 2,016 x 1,344 pixels. Avizo 2019.2 software (Thermo Scientific™) was used to generate 3D volumes. 2D cross-sectional slices were treated with ImageJ software (version v1.52i) to remove the background and were later analyzed for cell wall thickness using the Local Thickness plugin and for circularity using the particle analysis plugin, according to the following equation:

$$Circularity = \frac{4\pi A}{P^2} \quad (8)$$

In which A is the area and P is the perimeter of the identified cell lumens.

2.5. Scanning electron microscopy

After submitted to nano-tomography, the nanostructure of treated samples was observed using scanning electron microscopes. To observe the effect of hydrothermal treatment on the anatomical structure, untreated control samples were also observed. In both cases, the samples were preliminarily freeze-dried.

To study the middle lamella of cells, samples were cross-sectioned using a microtome blade. Because wood is non-conductive, samples were first coated with gold. Observation was made using an environmental scanning electron microscope (ESEM, FEI Quanta 200) using the following conditions: secondary electron detector, high vacuum mode, an accelerating voltage of 10 kV (control sample) and 12 kV (treated sample), a spot size of 3 and a work distance of approximately 9 mm.

To examine the structure of cell walls to a greater depth, a field emission gun scanning electron microscope (FEG-SEM) Model LEO 1530 (Leo Electron Microscopy Ltd, Zeiss, Oberkochem, Germany) was used. Samples were first split along the longitudinal-radial plane. Then, the non-conductive samples were coated with tungsten (Q150TS, Quorum Technologies). The operating conditions of FEG-SEM were an accelerating voltage of 2 kV, a diaphragm of 30 µm and a work distance of 2 mm.

3. Results and discussion

3.1. Chemical modifications

Figure 61 presents the results obtained by confocal Raman microscopy after univariate analysis for samples treated at 160 °C for 0, 10, 20 and 40 minutes as well as a native sample. The same samples had their data submitted to a cluster analysis. Only the most severely treated samples (20 and 40 minutes) were chosen to be represented in Figure 62, due to their higher contrast with the native sample. Figure 62 also provides the respective average spectra of the clusters, normalized with the maximum value.

In Raman spectroscopy, lignins are expected to exhibit an intense peak at a 1,600 cm^{-1}, attributable to phenyl groups of lignins [79] and a second peak at approximately 1,650 cm^{-1}, that corresponds to the ring conjugated C=C stretching of the coniferaldehyde and coniferyl alcohol units. It is less intense and usually observed as a shoulder of the first one [69,81].

Analyzing hemicelluloses and cellulose through this technique is more challenging than lignins. Due to their similar structure, several bands appear at the same wavenumber [79], making it impossible to distinguish hemicelluloses from cellulose. They are thus analyzed together, as holocellulose. The band at approximately 2,894 cm^{-1} corresponds to the aliphatic C-H and C-H_2 stretch from carbohydrates [79,81] and is commonly used for the study of wood carbohydrates due to a good signal-to-noise ratio [69].

3.1.1. Lignins

To obtain chemical maps for lignins, peaks at 1,600 cm^{-1} and 1,650 cm^{-1} were integrated together as it resulted in a better signal-to-noise ratio and did not alter the determination of lignins

distribution [69]. Figure 61a shows the intensity of this broad band in an untreated wood cell. It can be seen that, even though lignins are present in all regions of the cell wall, signal intensity is higher (seen in yellow and orange) in regions corresponding to the cell corner and the middle lamella. These results are consistent with those of previous studies [69,81].

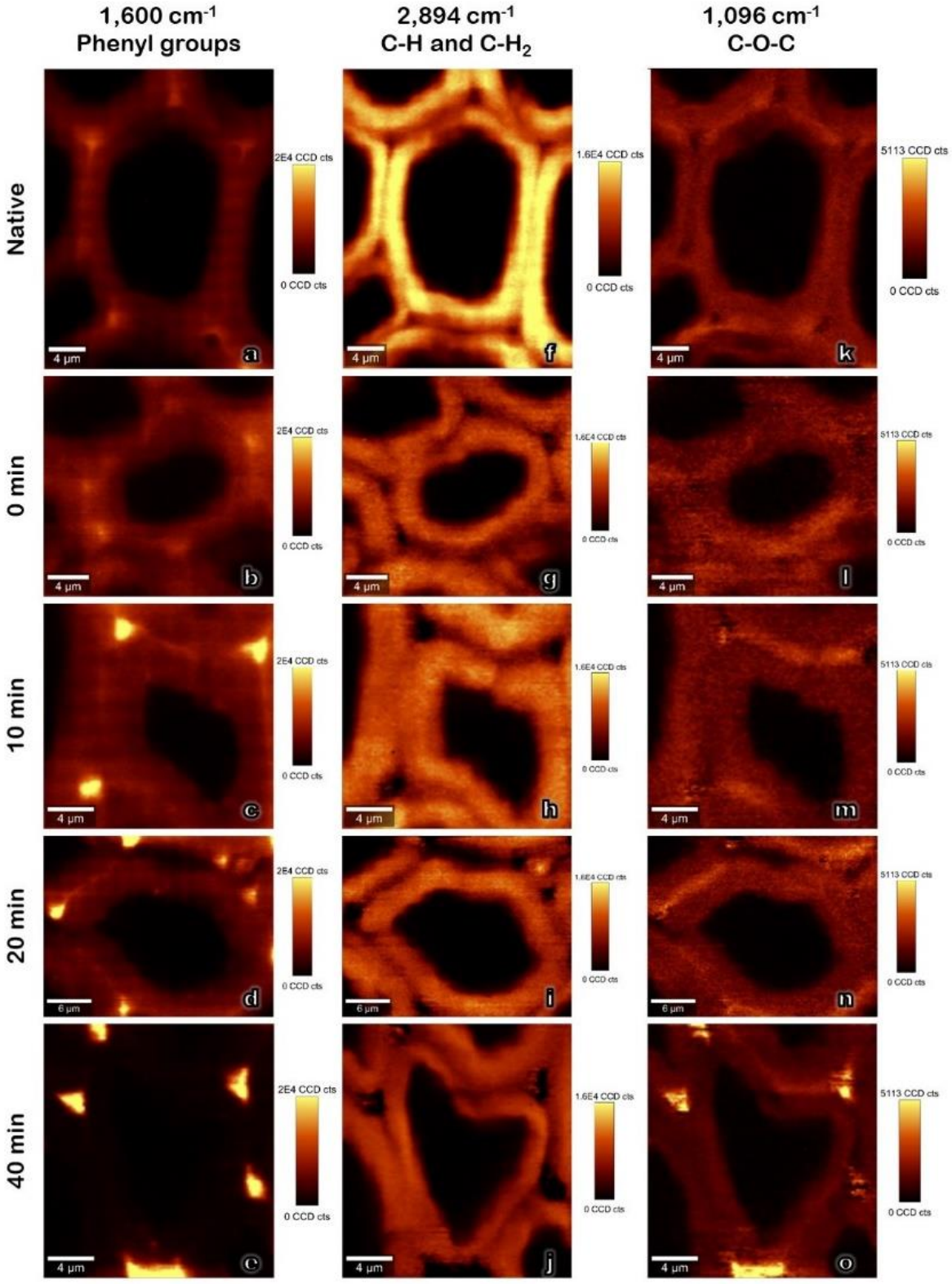

Figure 61. Raman images obtained by integration at different wavenumbers of untreated and hydrothermally treated poplar samples (160 °C).

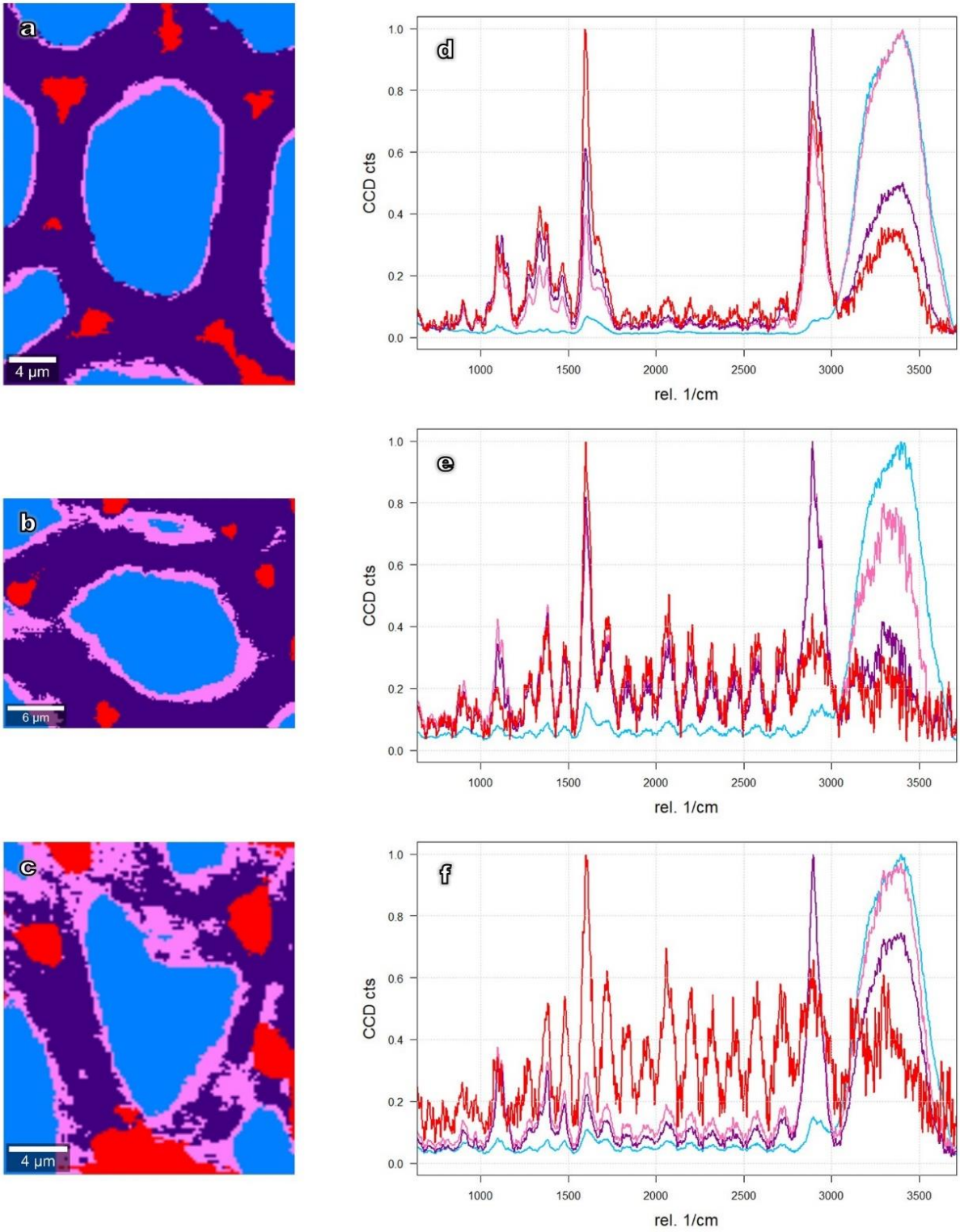

Figure 62. Raman images of untreated (a) and pre-treated samples (b-c) based on hierarchical cluster analysis and the average spectra of respective clusters (normalized) (d-f). Samples were treated at 160 °C for 20 (b,e) and 40 (c,f) minutes.

After treatment (Figure 61 b-e), it was possible to observe a reduction of signal intensity in zones corresponding to the secondary cell wall. At the same time, the signal seemed to intensify in the

intercellular regions, such as the triple points and middle lamella. This effect intensified with increasing treatment time and became particularly evident in the spectra obtained by cluster analysis (Figure 62). In the untreated sample, regions corresponding to cell corners (red) presented a clear predominance of the lignins band (1,600 cm^{-1}). After 20 and 40 minutes at the temperature plateau, holocellulose signal intensity (2,894 cm^{-1}) decreased in comparison with lignins in the cell corners. On the other hand, the contribution of lignins to the spectra of the secondary cell wall (purple) became weaker as the treatment time increased.

Based on these results, it is possible to assume that different cell wall regions responded differently to hydrothermal treatment. An increase in lignin signal intensity in high lignified cell wall regions has also been observed during dilute acid pretreatment of *Pinus bungeana* Zucc. [187]. A few hypotheses may explain mechanisms behind the observed changes, likely the result of a combination of different factors.

Some authors consider solubilization one of the modifications experienced by lignins in hydrothermal treatments [115]. The acidic condition leads to the breaking of lignin – carbohydrate bonds and later, to depolymerization of lignins [139]. Solid biomass would then suffer a loss of lignins to the treatment liquid, which could explain the reduction of signal intensity observed on the secondary cell wall. Additionally, the monomeric composition of lignins influences its susceptibility to hydrothermal degradation. Syringil (S) units present fewer cross-links, which makes it more susceptible to hydrothermal treatment [115,132]. The predominance of S units in the secondary cell wall [132] is one possible cause of the differential attack observed in Raman images. However, it only explains the decrease in the signal intensity in the secondary cell wall, but not its increase in other regions.

Another possible explanation is the migration of the lignins. The treatment temperatures largely exceeded lignin's glass transition temperature (T_g), of 50 and 100 °C for water-saturated wood [33]. These temperatures allow lignins to melt and coalesce. They are then forced out of the cell wall matrix and form droplets during the cooling phase [135]. To verify if this hypothesis applies to the samples analyzed here, further observations were made by electron microscopy, the results of which are presented in Figure 63 (obtained by SEM and FEG-SEM). It is possible to observe the formation of round droplets in the inner surface of the cell (Figure 63e-f) and in the intercellular region (Figure 63b-c), which is consistent with previous results [135]. The observed droplets had a maximum diameter of 0.35 µm (measured with the help of the ImageJ software), which is large enough for their chemical composition to influence the Raman spectra of the region in which they are deposited. However, they might not be seen as single droplets since their size is close to the lateral diffraction limit of the confocal Raman microscope. It is then conceivable to assume that the intense lignin signal observed at triple points of pre-treated samples originate from these lignin droplets. This effect is, however, only observed at the intercellular region and not at the inner surface of the cell, where lignin droplets are also found in large quantities. This suggests that droplets found in different anatomic regions of the cell wall have different compositions and thus different contributions to the Raman spectra.

A previous study [188] used fluorescence lifetime imaging microscopy and stimulated Raman scattering microscopy to evaluate the effect of low concentration maleic acid pretreatment on poplar. Based on the fluorescence lifetime, they were able to distinguish two types of lignin: dense lignins and loosely packed lignins. In the untreated sample, loosely packed lignins were mainly

present in the secondary wall. Dense lignins, on the other hand, were present all over the cell wall. After pretreatment, lignins present in the cell corner formed dense lignin droplets, while lignins present in the secondary cell wall were released with hemicelluloses and end up forming loosely packed lignin droplets [188,189]. These loosely packed lignin droplets are composed of lignin-carbohydrate complexes and contain a low lignin concentration, undetectable when analyzed through stimulated Raman scattering microscopy at the lignin resonance frequency (1,600 cm^{-1}). Therefore, our results are consistent with previous findings, showing that droplet composition depends on the anatomic region in which they are formed. This fact reinforces the importance of imaging techniques in providing a better understanding of cell wall degradation during hydrothermal treatment.

The effect of droplet formation on subsequent steps, such as enzymatic hydrolysis, remains uncertain. Lignin migration could result in higher accessibility of cellulose inside the cell wall to enzymes, but on the other hand, the presence of droplets attached to the cell wall surface could physically limit the access of enzymes or result in non-productive binding with lignins or lignin-carbohydrate complexes [116].

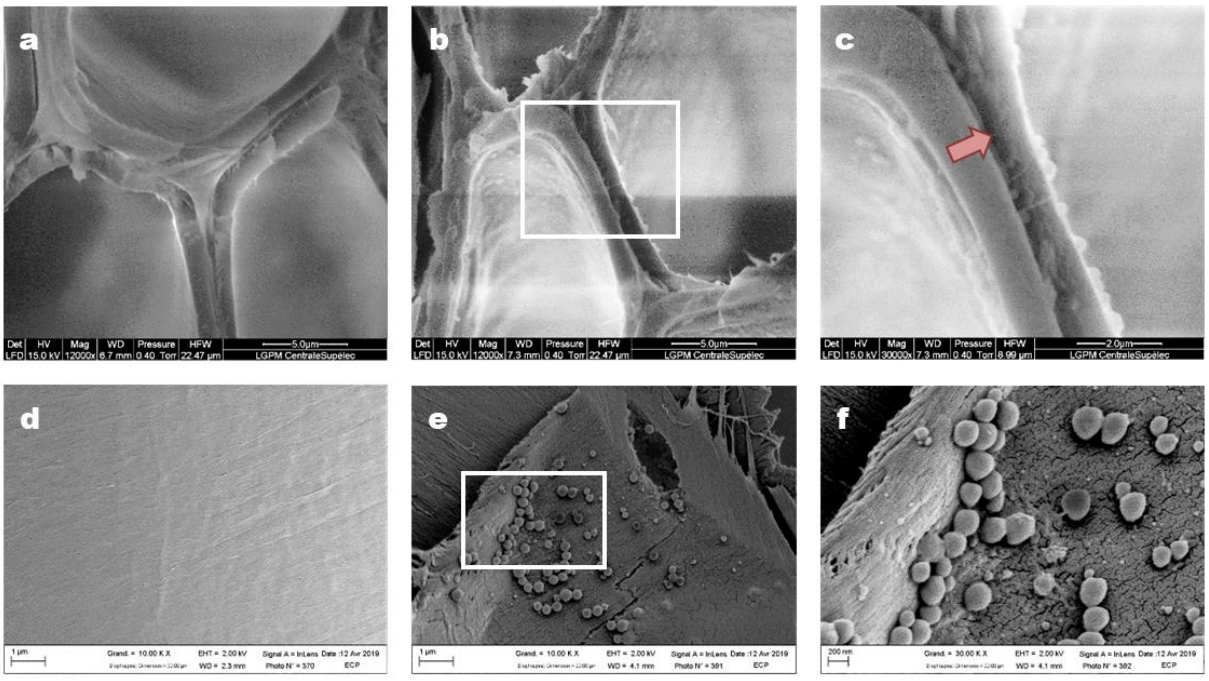

Figure 63. SEM (a-c) and FEG-SEM (d-f) images of poplar cell wall before (a, d) and after (b, e) 40 minutes of hydrothermal treatment at 180 °C. The regions within the white rectangles are shown in (c, f) at increased magnification. It is possible to observe cell wall layer detachment and the formation of round droplets.

Laser-induced fluorescence considerably increased with pretreatment severity. Despite the application of photobleaching prior to the Raman analysis, a maximum was reached after 40 minutes of treatment (Figure 61e). For this sample, the quality of Raman spectra (observed by the signal-to-noise ratio) was reduced (Figure 62f). These results thus need to be interpreted with caution, as the high signal intensity in cell corners could be overshadowing less concentrated areas. For the same reason, results obtained for more severely treated samples (such as those treated to 180 °C) through confocal Raman microscopy could not be explored and, therefore, were

not presented in this study. Despite the limitations of this method, an increase in laser-induced fluorescence is also an indicator of biomass chemical modifications, as shown previously [190]. When studying lignins and lignin-derived model compounds using Raman spectroscopy, they demonstrated that freely-rotating 5-5' linkages were a precondition for laser-induced fluorescence in wood. During treatment, more sensitive linkages (such as α- and β-aryl ether) were broken, allowing 5-5' linkages to rotate without restrictions. These results are consistent with those of the current study and suggest a modification of lignin mobility and degree of condensation. Future studies could provide a greater understanding of the mechanisms leading to laser-induced fluorescence in treated wood and utilize it for analytical purposes.

3.1.2. Holocelluloses

Figure 61f shows the image obtained by integration over the 2,894 cm^{-1} band of the Raman spectrum (corresponding to holocellulose) of an untreated poplar sample. As expected, the highest holocellulose concentration is observed in the secondary layer of the cell wall. Regions of weaker signal in this band correspond to the middle lamella and cell wall corners, which are known to have lower holocellulose concentrations [69,81]. Small intensity variations throughout the S2 region can be observed and, in addition to differences in concentration, can also be attributed to the microfibril angle of cellulose [69]. Because the chemical bonds represented by this band (C-H and $C-H_2$) are perpendicular to the axis of microfibrils, the intensity of the Raman signal is maximized when microfibrils are aligned with the laser axis, orthogonal to the electric field vector.

Treated samples (Figure 61g-j) showed a decrease in the signal intensity with an increase in treatment time. From the beginning of the temperature plateau (0 minutes of treatment - Figure 61g), no influence of this band is observed in the spectra of cell corners and compound middle lamella, which appear in black. At the same time, the secondary cell wall signal intensity decreased from yellow to dark orange or red. Considering the treatment conditions, the loss of signal intensity can be explained by the hydrolysis of hemicelluloses to oligosaccharides and monomeric sugars such as xylose, glucose and arabinose [186]. Previous studies have shown that hemicelluloses constitute the major source of biomass loss during pretreatment [117,186]. In poplar samples hydrothermally treated for 20 minutes at 180 °C [186], these components released 33.1% of their initial content in the treatment water, and experience up to 85% loss depending on pretreatment conditions [119]. Due to a lower degree of polymerization [118] and to a branched, non-crystalline structure, hemicelluloses are much easier to degrade than cellulose [43]. Thus, they constitute the main target of lignocellulosics pretreatment prior to the production of second-generation biofuels. The most susceptible bonds of hemicelluloses are those of heterocyclic ether bonds [115]. Their breakage generates hemicellulose oligosaccharides and acetic acid that acts as a catalyst [115]. Hardwood hemicelluloses contain more acetyl groups than softwood, which contributes to greater hydrolysis [117]. Therefore, the signal that can still be observed even during the most severe treatment (Figure 61j) would mainly be cellulose. Approximately one-third of the hemicelluloses, however, associate with the crystalline microfibrils of cellulose [43] and are harder to hydrolyze, another possible contributor to the signal intensity.

Depending on the severity of the pretreatment, monomeric sugars released from hemicelluloses and (to a lesser degree) cellulose can undergo further dehydration, producing furfural and 5-hydroxymethylfurfural, respectively. These degradation products can later be converted into aromatic intermediates and then form pseudo-lignin [139] through polymerization and polycondensation reactions. During the cooling process, these compounds are susceptible to production of spherical structures similar to lignin droplets, which also tend to adhere to cell wall surfaces [139]. The decrease in holocellulose concentration beginning in the early stages of the hydrothermal treatment meets the necessary conditions for the production of pseudo-lignin, reinforcing the previous hypothesis that the droplets observed in Figure 63 may not all have the same composition.

3.1.3. Cellulose

As previously stated, cellulose can roughly be distinguished from hemicelluloses in the Raman spectra of lignocellulosics. The 2,894 cm^{-1} is used for the analysis of both cellulose and hemicelluloses [79,81]. However, given the crystallinity of cellulose and the temperature levels applied in this study, it is unlikely that the loss of intensity previously observed in this band was due to a loss of cellulose. Previous works have shown that cellulose remains essentially unaffected during hydrothermal treatment, even at higher temperature levels [22,186], which confirms the initial hypothesis that a reduction of the signal of 2,894 cm^{-1} band mainly represents a loss of hemicelluloses or, on a much smaller scale, loss of amorphous cellulose [43,117].

Another band located near 1,096 cm^{-1}, can be used to analyze cellulose. It corresponds to the asymmetric C-O-C linkages, generally aligned with the microfibril axis [81,191]. This band is thus sensitive to cellulose orientation and can provide an idea of its supramolecular structure [191]. In the untreated sample (Figure 61k), the intensity is evenly distributed throughout the secondary layer, with a slightly higher intensity in the S1 layer due to microfibril orientation. As expected, no signal is observed for this band in the cell corners and compound middle lamella, since these regions are essentially composed of lignin. As the treatment time increases (Figure 61l-o), the intensity of this band increases, especially in the S1 layer. The same observation was made in a previous study [191], in which two possible reasons to explain this signal increase were provided. Firstly, molecules may be more parallel to the beam polarization. Indeed, even though it is not completely hydrolyzed during pretreatment, cellulose undergoes a significant reduction in the degree of polymerization [123,192]. The presence of shorter polymer chains provides enhanced mobility to the cell wall, perhaps allowing more molecules to align with the laser beam. The second explanation was an increase in cellulose crystallinity, which would result either from the loss of amorphous components (hemicelluloses and amorphous cellulose)—i.e. increasing the relative amount of crystalline cellulose—or come from a genuine rearrangement of cellulose organization.

3.2. Consequences on macroscopic properties of biomass

The previous results showed the effect of hydrothermal treatment on the chemical structure of biomass cell walls. It is reasonable to presume that the changes observed at the cell wall level have an impact on the macroscopic structure of biomass. To examine this further, the anatomical structure of the samples was observed using X-ray nano-tomography. After data processing, each

analysis resulted in a set of cross-sectional slices. Five cross-sectional slices of each sample (100 µm apart from each other) were used to assess the cell wall thickness and no significant difference was found between different slices of the same sample. Figure 64 and Figure 65 show untreated and hydrothermally treated samples at 160 °C/40 minutes and 180 °C/40 minutes, respectively. Because X-ray nano-tomography analyses are time-consuming, only the most severely treated samples (40 minutes) for each temperature—and, therefore, those with the most significant morphological changes—were analyzed.

There was obvious shrinkage on both radial and tangential directions of wood, especially for the sample treated at 180 °C (Figure 65a-b). Shrinkage has been observed in a previous work [186], that used it as a macroscopic indicator of biomass degradation during hydrothermal treatment. For both treatment temperatures, a reduction of cell wall thickness when the treatment duration increased can also be observed. In Figure 64c-d and Figure 65c-d the cell wall thickness was calculated by image processing and is represented according to the color scale. The results also show that in untreated samples (Figure 64c and Figure 65c), cell wall thickness can reach up to 7 µm depending on the anatomical structure (orange-yellow color). For pre-treated samples, it barely exceeds 5 µm in the mildest pretreatment (red-orange color) and 3 µm for the most severe one (pink-purple color). The mean calculated cell wall thickness shrank from 3.8±1.0 µm to 2.7±0.7 µm and from 3.5±0.9 µm to 2.2±0.6 µm for 160 and 180 °C pretreatments, respectively. It corresponded to a reduction of 29 and 36 % on the cell wall thickness (for temperatures of 160 and 180 °C, respectively). A similar observation was made by electron tomography in the case of mild pyrolysis of wood [143].

Shrinkage and decrease in cell wall thickness are connected phenomena and can both be linked to mass loss. Our previous study [186], using the same poplar samples, reported up to 27.3% mass loss after 40 minutes of hydrothermal treatment at 180 °C. This significant loss is logically reflected in sample dimensions. As previously stated, hemicelluloses are the most sensitive components of wood to this kind of treatment, representing the most significant source of mass loss [117,186].

For the most severe pretreatment (180 °C / 40 min), shrinkage may also be a result of drastic changes in the biomass anatomy. As shown in Figure 65a-b, vessels and rays are likely the most fragile to this kind of treatment of all anatomical elements of biomass structure. Cell walls of vessels and rays parenchyma are thinner than those of fibers, which explains their fragility. Vessels have been completely disrupted, as shown by the blue narrows (Figure 65e-f) and collapsed. It is also possible to see (Figure 65e-f) that at this intensity level many fibers start to detach from adjacent cells (a few examples are highlighted by the red arrows), seldom seen in the treatment at 160 °C (Figure 64e-f). The same process can be observed in the SEM images previously shown (Figure 63c, highlighted by the red arrow). Figure 62b reinforces these observations. Even for milder treatment conditions (160 °C / 20 min), it is possible to observe a void between two cells, a region whose spectrum has been found similar to that of the lumen by cluster analysis (in blue) – i.e. it is filled with water. These observations are consistent with those of previous studies [123,130].

The hydrolysis of hemicelluloses and the modifications experienced by lignins are likely the main cause of all these structural changes. In untreated wood, hemicelluloses and lignins are responsible for bonding the structure together within the layers of one cell or between neighbor

cells [118]. Previous works have found that the hydrolysis of hemicelluloses and the loss or migration of lignins can induce substantial ultra-structural changes on the biomass network [119,132,144], owing to a loss of mechanical properties and a fragilization of middle lamella. The loss of cohesion between cells and cell wall layers weakens biomass structure and is likely to make it more susceptible to the shearing forces arising during the explosion step. This effect is realized when neighbor cells detach from each other. In this case, the double cell wall of adjacent cells is split in half, meaning that the explosion faces less resistance than from that of the original cell wall.

To further explore the obtained results, X-ray nano-tomography slices were also used to calculate the circularity of the cells (Figure 66). As expected, no significant difference (p-value = 0.21) was found between the two samples before treatment. For the sample treated at 160 °C for 40 minutes, the mean cell circularity decreased from 0.71±0.18 before treatment to 0.67±0.16 after treatment (p-value < 0.001). This effect was even more evident for the sample treated at 180 °C (40 minutes), in which case the mean cell circularity decreased from 0.69±0.19 before treatment to 0.57±0.21 after treatment (p-value < 0.001). These results support our previous observations. The mass loss suffered by biomass during treatment and the re-organization of cell wall components are likely to induce a fragilization of the cell wall. This loss of mechanical resistance would therefore allow the cells to acquire more elongated forms. Consistently, Zoghlami et al. [193] demonstrated a reduction in the sphericity of poplar cells with the increase of treatment severity. In the same study, cell sphericity was also found to negatively correlate with the yields obtained after enzymatic hydrolysis. It suggests that, after treatment, samples are more susceptible to the enzymatic attack, probably due the increased accessibility of the cellulosic fraction.

Finally, 3D reconstruction of samples (Figure 64e-h and Figure 65e-f) allowed for exploration of the structure before and after treatment and provided an overall picture of the modifications taking place inside the sample, without any particular sample preparation. Therefore, different directions of the same wood sample can be visualized with a single analysis.

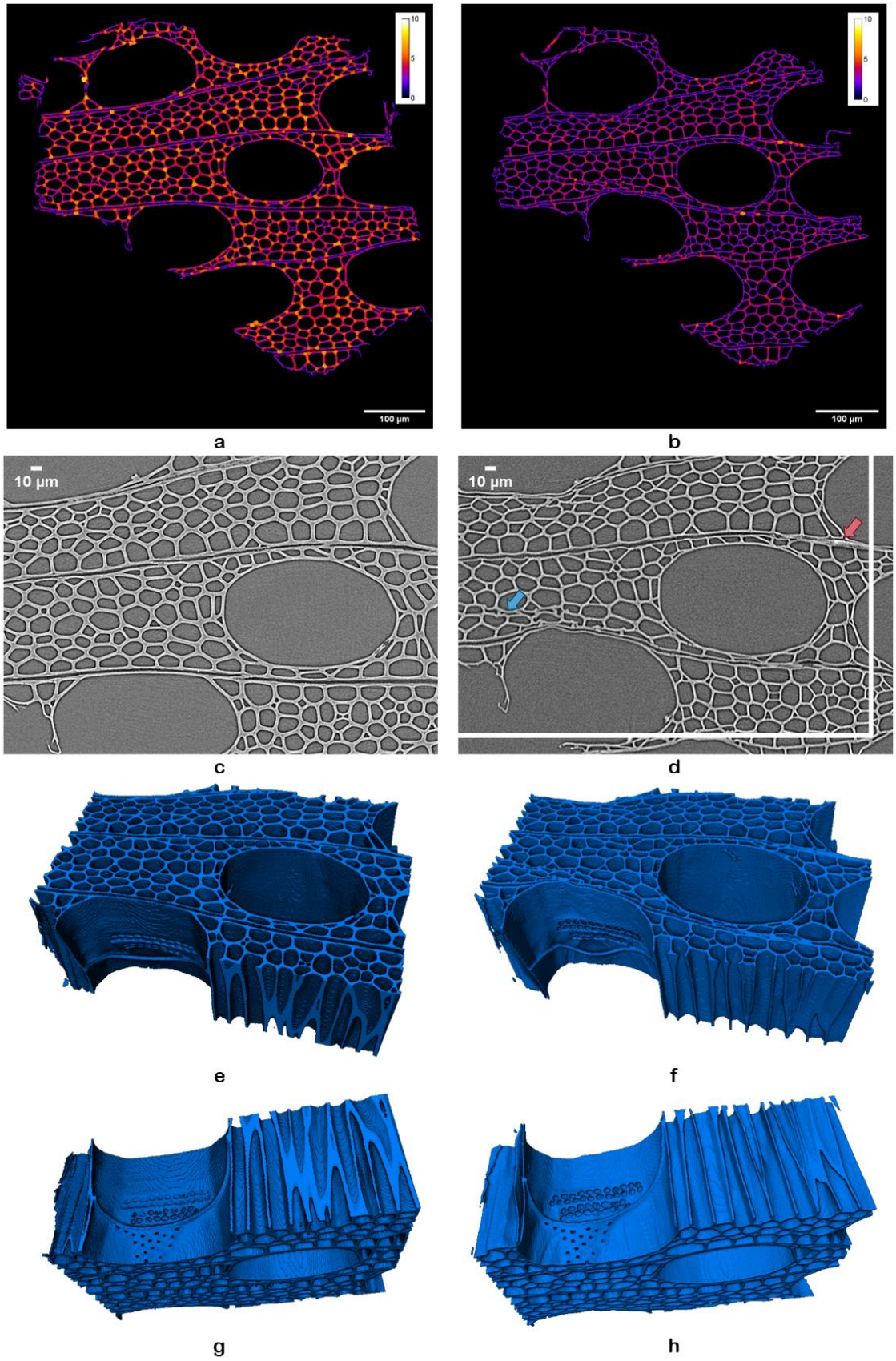

Figure 64. X-ray nano-tomography images of the same sample in its untreated state (a, c, e and g) and after 40 minutes (b, d, f and h) at 160 °C. The images show (a-b) the calculated thickness of cell walls throughout the slices (in µm); (c-d) highlights of cell wall collapse (blue) and cell detachment (red). The white rectangle (d) highlights the changes in sample dimensions due to shrinkage; (e-h) 3-D reconstructions of the sample.

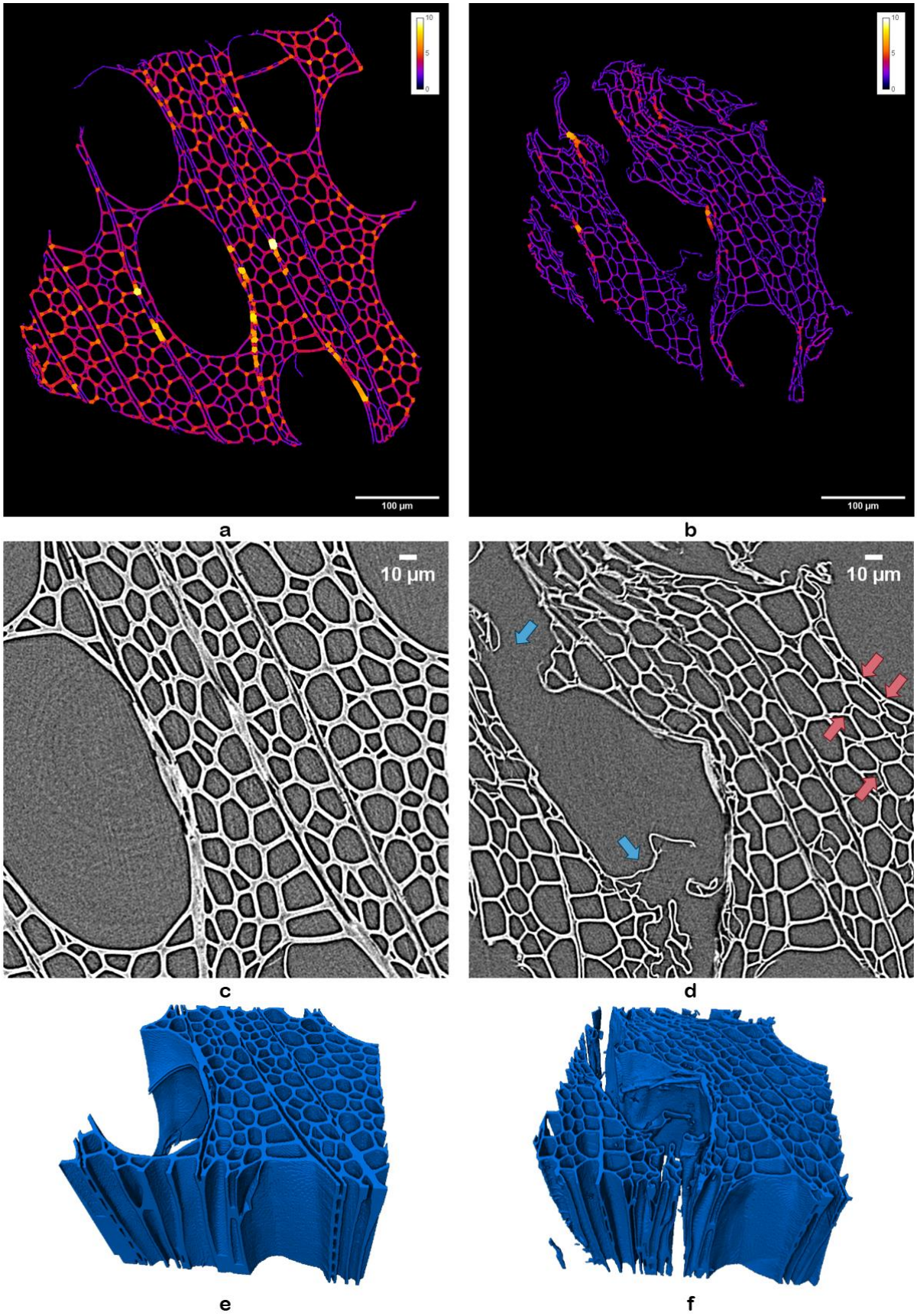

Figure 65. X-ray nano-tomography images of the same sample in its untreated state (a, c, e) and after 40 minutes (b, d, f) at 180 °C. The images show (a-b) the calculated thickness of cell walls throughout the slices (in µm); (c-d) highlighted vessel disruption (blue) and cell detachment (red); (e-f) 3-D reconstructions of the sample.

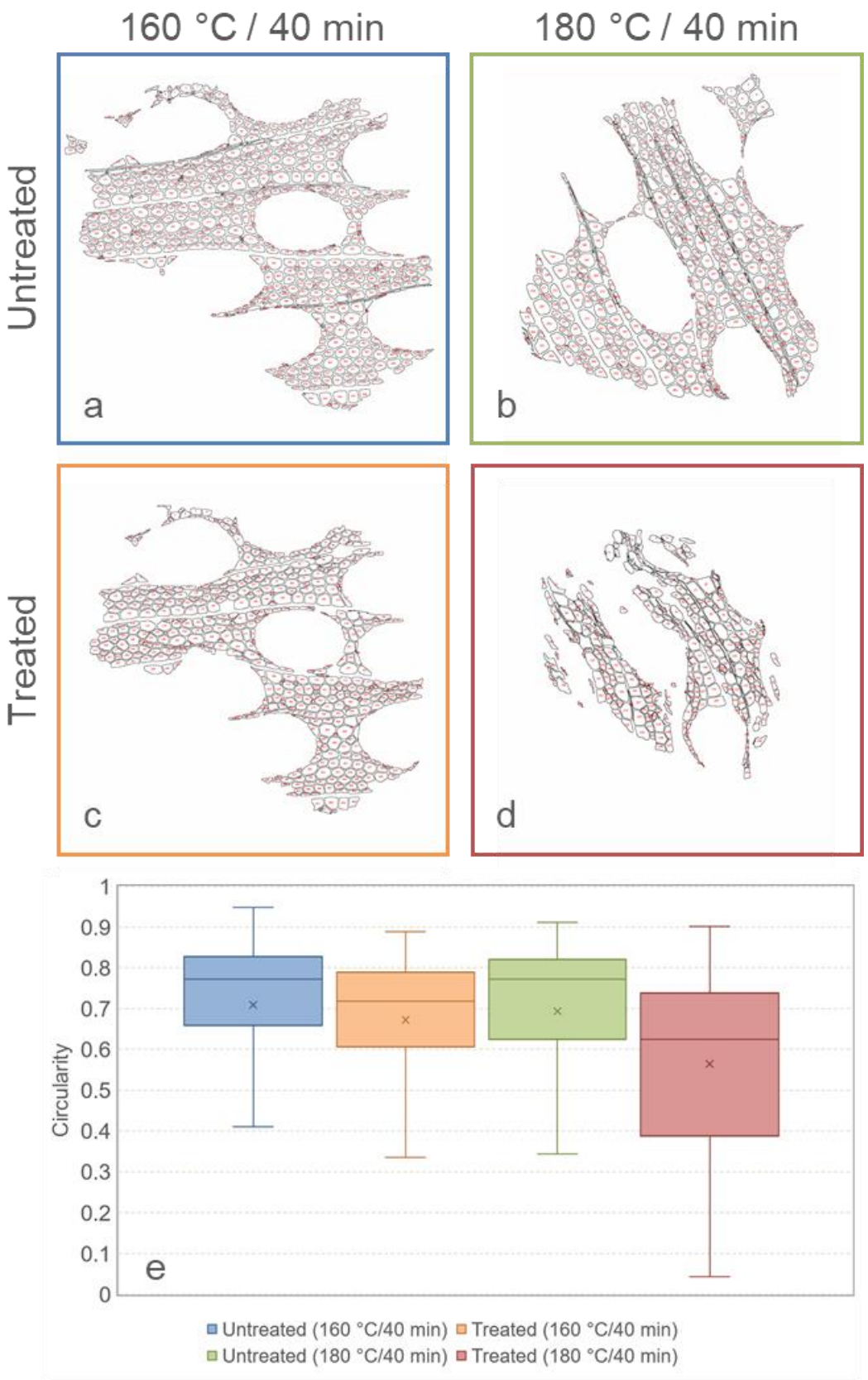

Figure 66. Effect of hydrothermal treatment on the circularity of poplar cells. (a-d) Automatically identified cell lumens for untreated (a-b) and pre-treated (c-d) samples. (e) Distribution of cell circularity (vessels excluded) of the different samples. The boxes represent the interquartile ranges. Medians and means are represented by the lines inside the boxes and by the markers, respectively. The number of analyzed cells was 548 (a), 473 (b), 408 (c) and 254 (d).

4. Conclusions

This study investigated the multiscale effect of hydrothermal treatment of poplar on its chemical composition and structure. It was made possible by a unique combination of several imaging techniques. Hemicellulose hydrolysis and lignin migration were observed by confocal Raman microscopy. The chemical changes observed at the cell wall level have later been connected to ultrastructural modifications. Overall, after treatment, samples presented thinner cell walls and shrinkage. In more severe treatments, cell disruption and detachment from adjacent cells were also observed. Imaging techniques provided an overall (3D) vision of the degradation of cell walls after hydrothermal treatment.

Finally, regarding later steps in the bioethanol production chain, the detachment of neighbor cells and the reduction of cell wall thickness increased susceptibility to the subsequent explosion phase. It provides knowledge for improved steam explosion modelling, simulation and optimization. The hydrolysis of hemicelluloses and the delocalization of lignins may contribute to the accessibility of cellulose by exposing it to enzymes, as reflected by a reduction of the cell circularity. The access of enzymes is also facilitated by disruption of some cells, exposing inner portions of biomass.

5. Acknowledgements

The authors would like to thank Région Grand Est, Département de la Marne, Grand Reims and the European Union for supporting the Centre Européen de Biotechnologie et de Bioéconomie (CEBB 51110 Pomacle, France), where this study was conducted. In particular, the authors would like to thank Département de la Marne for its financial support and the French Council for Poplar as well as Huberlant sawmill (Cormicy, France) for providing the wood used in this study.

For four years (from 01/05/2016 to 31/07/2020) and with a total budget of 965,000€, 3D-BioMat is co-financed by the Grand Reims (31%) and the European Union by 48.7% (i.e. 50% of eligible expenditure). Europe is committed to the Grand Est with the European Regional Development Fund.

CHAPTER IV. *In situ* measurements of viscoelastic properties of biomass during hydrothermal treatment to assess the kinetics of chemical alterations

A. Preamble

Chapter III confirmed the relevance of a multiscale approach on the study of lignocellulosic biomass pretreatment. Even though rich in information, especially concerning the following enzymatic hydrolysis step, the results obtained from imaging techniques remain rather qualitative and discontinuous. In our search for a macroscopic indicator of biomass deconstruction, it was important to find quantitative parameters. Furthermore, the continuous aspect of this indicator was an important feature, as it provides a lacking information of classical chemical analysis: the reaction kinetics.

As stated in literature review, previous works have demonstrated the ability of rheological properties to reflect structural rearrangements of the cell wall components as well as changes in their molecular and supramolecular structure. However, most of these studies were performed at lower temperatures than those industrially applied for hydrothermal treatment. More recently, a study was dedicated to the development of a device capable of performing this type of test under the severe conditions required by hydrothermal treatments [34]. The present study used this device to further explore its potential.

Two viscoelastic properties were continuously measured perpendicular to the grain and under uniaxial compression: the apparent modulus of elasticity and the stress relaxation. The pertinence of these properties as indicators of biomass deconstruction was assessed. The testing protocol is described throughout the present chapter, but complementary information on preliminary tests and on the implementation of this protocol was given in Chapter II. In addition to the evaluation of the two viscoelastic properties, this study also aimed at assessing the effects of operating conditions — including the temperature (150, 160, and 180 °C) and the soaking liquid (distilled water, acidic solution, or alkaline solution) — on such properties.

Three main phenomena could be distinguished through the concomitant evolution of stiffness and relaxation: thermal activation of the viscoelastic behavior, cleavage of molecular linkages, and re-condensation. At the beginning of the heating period, while the temperature remains quite low, thermal activation occurs solely. Our results show that at relatively low temperature (60 °C) concomitant chemical degradation begins to be noticed. This effect, probably due to the hydrolysis of hemicelluloses, was observed thanks to the stress relaxation tests. However, the monotonous behavior of rigidity tests during the heating phase prevents the distinction between both phenomena.

Once the temperature plateau is reached, the two main phenomena become cleavage and re-condensation reactions. The dominance of either one or the other depended on the treatment severity. Cleavage reactions were predominant at the beginning of the treatment plateau, which was attributed to hemicellulose hydrolysis and cleavage of lignin β-O-4 linkages. Moderate severity favored lignin condensation reactions, whether it was long treatment durations for temperatures of 150 and 160 °C or shorter times for a higher temperature (180 °C). The most severe condition tested (long residence time at 180 °C) promoted new cleavage reactions, which must probably be related to the reduction of the DP of cellulose. The use of an acidic pre-soaking medium also seemed to promote the hydrolysis of lignocellulosic biomass, whereas, the use of

alkaline pre-soaking medium seemed to provoke lignin and hemicellulose extraction at low temperatures but limited further alterations during the temperature plateau. Contrary to the heating up phase, the different phenomena taking place during the temperature plateau could only be highlighted thanks to the MOE and its non-monotonous behavior at this stage.

The two mechanical properties studied in Chapter IV, therefore, proved to be complementary and provided meaningful insights regarding the chemical mechanisms involved in hydrothermal treatment. The conclusion extracted from this data can be resumed by the image below.

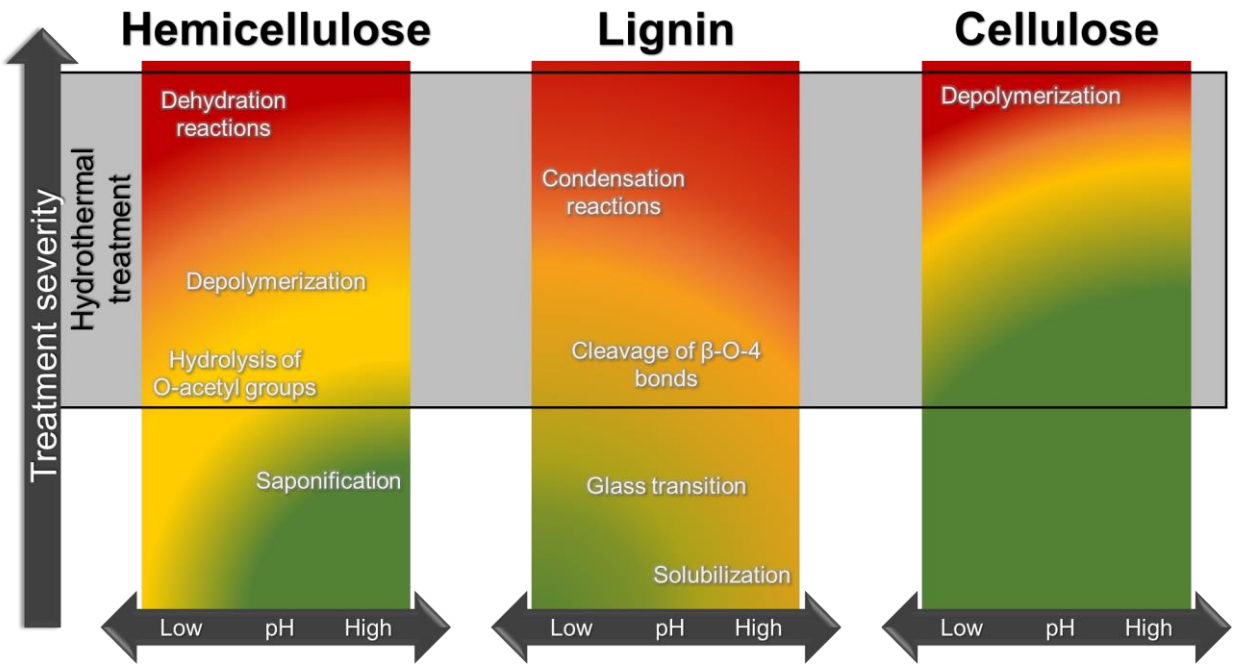

Figure 67. Graphical abstract of Chapter IV

B. *In situ* measurements of viscoelastic properties of biomass during hydrothermal treatment to assess the kinetics of chemical alterations

Julia P. Lancha[1], Julien Colin[1,2], Giana Almeida[3], Patrick Perré[1,2]

[1] Université Paris-Saclay, CentraleSupélec, Laboratoire de Génie des Procédés et Matériaux, SFR Condorcet FR CNRS 3417, Centre Européen de Biotechnologie et de Bioéconomie (CEBB), 51110 Pomacle, France

[2] Université Paris-Saclay, CentraleSupélec, Laboratoire de Génie des Procédés et Matériaux, 8-10 rue Joliot-Curie, 91190 Gif-sur-Yvette, France

[3] Université Paris-Saclay, INRAE, AgroParisTech, UMR SayFood, 91300 Massy, France

Bioresource Technology 315 (2020) 123819

Abstract

This work aimed to use continuous measurements of viscoelastic properties to evaluate the effect of hydrothermal treatment on poplar samples. Different conditions (temperature and pre-soaking liquid) were tested on wood in both tangential and radial directions. Two viscoelastic properties were determined: the modulus of elasticity and the stress relaxation. The applicability of these properties as indicators of the kinetics of biomass deconstruction was also evaluated. The ultimate goal is to build a macroscopic indicator capable of establishing rules to optimize the hydrothermal treatment before the explosion stage. The joint use of the two parameters succeeded in revealing the effects of chemical degradation, including the coexistence of cleavage and re-condensation and the impact of process conditions (temperature, residence time, and pre-soaking liquid). The monotonous behavior of stress relaxation is a major asset as a possible macroscopic indicator of biomass deconstruction.

Keywords: Lignocellulosic biomass, Steam explosion; Modulus of elasticity; Viscoelasticity; Poplar

1. Introduction

Lignocellulosic biomass constitutes one of the most abundant renewable sources of carbon [194]. It has received increased attention in recent years as an alternative feedstock for industries such as biofuel and bio-based chemical production. However, as a result of evolution, lignocellulosic components—and especially wood—play the role of mechanical support in plants and help them withstand biological degradation. This natural recalcitrance, therefore, presents a significant challenge for industrialization. Regardless of the application, a pretreatment step is necessary to promote subsequent enzymatic hydrolysis by increasing the accessibility of polysaccharides [24].

Several pretreatment methods have been proposed. Among them, steam explosion seems to be best suited to meet industrial needs, for example, the efficient treatment of a wide variety of biomass sources [37,44]. It involves a hydrothermal step—during which biomass is subjected to high temperature under saturated steam conditions—followed by explosive decompression. Ideally, hydrothermal treatment should promote the separation of the three main components of lignocellulosic biomass (cellulose, hemicellulose, and lignin) with limited changes to their molecular structures. An increase in the porosity, as well as the reduction of cellulose crystallinity, are also expected for enhanced accessibility. At the same time, an ideal pretreatment should limit the formation of sugar degradation products (such as furfural and 5-hydroxymethylfurfural) and other inhibitory compounds [22].

The chemical degradation mechanisms occurring during hydrothermal treatment, especially those involving the hydrolysis of polysaccharides, are well documented in the literature. Under high temperatures, water autoionizes and forms hydronium ions that act as catalyzers for a series of hydrolysis reactions [115]. Hemicelluloses are the most susceptible components of the cell wall to this kind of reaction, probably due to their amorphous structure [117,186,195]. The first hydrolysis reaction is a split of the acetyl side groups, resulting in the production of acetic acid. The formation of this organic acid has a catalyzing effect and promotes the hydrolysis of hemicelluloses into oligo- and monosaccharides [115,117]. To a lesser extent, lignin is also affected by hydrolysis. Cleavage of β-O-4' aryl ether linkages has been observed to a significant extent even at 150 °C, due to their low thermal stability [127,128]. Poplar can be particularly affected by this mechanism, as its lignins are predominantly composed of β-O-4' bonds [56,196–198]. Lignin depolymerization is, however, often accompanied by condensation reactions. The cleavage of the most thermolabile linkages (β-O-4') gives rise to a rearranged lignin structure, rich in resistant bonds, such as β-β', β-5', and 5-5' [33,126,131,199]. Additionally, polysaccharide degradation products are also susceptible to polymerization and condensation reactions, forming aromatic lignin-like structures [139].

The pretreatment conditions greatly affect the outcomes of the entire production chain and, thus, must be optimized. Depending on the planned application and the desired physico-chemical characteristics, acidic or alkaline pre-soaking media can also be deployed [28,126]. Diluted sulfuric acid has been widely used in biomass pretreatment to increase sugar yields [122,200]. Alkaline pretreatments, on the other hand, enhance lignin solubilization and require milder treatment conditions, limiting the formation of inhibitory products [201,202].

Mechanical tests can be used to assess the properties of a material. Young's modulus, for example, has long been used as a measure of polymer degradation [150,203]. More specifically, previous works have proven that viscoelastic properties are good indicators of biomass degradation during hydrothermal treatment [33,34], reflecting structural rearrangements of the cell wall components as well as changes in their molecular and supramolecular structure. In this case, the evolution of creep in time is likely to be due to the additive effects of treatment duration that alters the macromolecular structure and the effect of time on the viscoelastic behavior [204]. To address this confusion, cyclic protocols, such as harmonic tests, are needed to decouple the effects of treatment duration with the effect of time on the viscoelastic creep [145,155].

The present work aims to use in-line measurements during hydrothermal treatment to assess the effects of operating conditions (temperature, pre-soaking liquid) on viscoelastic properties. For

this purpose, poplar (*Populus euro-americana* 'Koster') tested across the grain was used as a biomass model. Two viscoelastic properties, tested under uniaxial compression, were measured: the apparent modulus of elasticity and the stress relaxation. Performing rheological tests under the severe conditions imposed by hydrothermal treatments (high temperature and saturated steam) was possible because of an original device conceived and built by our team [34]. The pertinence of these properties as indicators of biomass deconstruction was assessed, with the ultimate goal of finding a macroscopic indicator likely to provide guidelines to optimize the hydrothermal treatment prior to the explosion step.

2. Material and methods

2.1. Poplar samples

The samples were collected from a 25-year-old poplar tree (*Populus euro-americana* 'Koster') cultivated in Auménancourt-le-Petit (Marne, northeastern France). Green logs were cut in boards that were subsequently dried and stored before sample preparation. A defect-free board was selected, from which 8 x 8 x 8 mm^3 (radial - R, tangential - T, longitudinal - L) cubes were cut. To minimize the natural variability of wood, all samples were taken from the same straight line parallel to the longitudinal direction.

Approximately 12 hours before hydrothermal treatment, the samples were pre-soaked in the desired medium by subjecting them to vacuum cycles until saturation. Different pre-soaking liquids were chosen to assess the effects of acid concentration (distilled water, H_2SO_4 0.3 % m/m, and H_2SO_4 0.6 % m/m). As an alternative to standard acidic conditions, an alkaline medium (NaOH 0.6 % m/m) was also tested. The conditions of each test are summarized in Table 7. The saturated dimensions of the samples before the test were measured using a laser sensor (Bullier Automation M5L/4). There were three main reasons for using saturated samples: assurance of good heat transfer throughout the samples and prevention of changes in the viscoelastic properties and, more importantly, any mechanosorptive effects of wood due to changes in moisture content during the test.

2.2. Rheological measurements

The viscoelastic properties were measured using an in-house developed device, whose features and working principles have been presented in previous papers [34,186]. It has a dual-chamber reactor which allows mechanical tests to be accurately performed under high temperature and water-saturated conditions. The upper chamber is kept at room temperature to house the instrumentation system: i) a Newport LTA-HL actuator (travel range of 25 mm, a minimum incremental motion of 0.05 µm and accuracy of 3 µm) equipped with a displacement sensor; and ii) a load cell (MEASUREMENT SPECIALTIES XFTC 310). The sample is treated in the bottom chamber, which is, therefore, subjected to high temperatures and saturated steam conditions. The chambers are connected by a patented system [156], enabling a mechanical link between the two chambers without friction, a prerequisite for reliable force measurements. The transmission of the load from the actuator (located in the cold chamber) to the sample (located in the hot chamber) is ensured by a vertical moving rod. A plate, lying at the end of this rod, subjects the

sample to compressive stress. Prior to each test, 100 mL of liquid water were added to the bottom of the chamber. During the heating-up phase, water vaporization ensured a water saturated atmosphere and condensation at the surface of the sample ensured its full saturation during the test.

Different continuous mechanical tests on biomass under compression can be performed with this device. This study focuses on the evolution of two parameters during the hydrothermal treatment: i) apparent modulus of elasticity (MOE) and ii) stress relaxation measured under compression.

At the beginning of the experiment, the sample is placed on the sample holder, and the reaction chamber is closed. The software is then launched for the experimental assay. Each test is composed of the following phases:

1. Heating (8 °C/min) from room temperature to the desired temperature using two electric heating collars (total of 370 W) placed at the outer surface of the chamber. The temperature was measured by a K-thermocouple near the sample and controlled by a PID system (Eurotherm 3216).
2. Maintaining the treatment temperature for 150 minutes
3. Cooling to room temperature by two external fans at approximately 9 °C/min

The mechanical properties of the samples were measured throughout the test according to the following cyclic protocol, repeated every 75 seconds:

1. **Offset of the load cell** in the absence of contact, allowing the sensor drift to be corrected, which is important as the applied force decreases at high temperature;
2. Slow (0.005 mm/s) displacement of the rod towards the sample;
3. **Contact detection** when the measured force reaches 0.05 N;
4. **Preload of the sample,** using compression until the preload force is reached (the targeted force depends on the temperature, and was determined during preliminary tests);
5. **MOE stage**, consisting of compression up to 0.5 % of deformation of the sample based on its initial water-saturated length;
6. **Viscoelastic stage**, relaxation for 30 seconds under constant deformation; and
7. Backward translation to release the contact and wait until the next cycle.

The stress levels applied in this protocol are intended to load the samples within the linear elasticity and viscoelastic ranges. The raw data obtained included the temperature of the chamber and the force and position of the actuator. The latter includes the additional deformations of the sample and the testing bench. To extract the sample deformation only, a series of blank tests were performed to quantify the deformation of the bench (without sample) as a function of the applied force. For a given force, it is then possible to calculate the portion of the deformation strictly related to the sample.

After blank correction and knowing the original sample dimensions, the stress and strain values are calculated:

$$\sigma = \frac{F}{S} \quad (9)$$

in which σ is the stress level (in Pa), F is the force measured by the load cell (in N), and S is the initial cross-sectional area of the sample (in m^2).

$$\varepsilon = \frac{\Delta L}{L_0} \quad (10)$$

In which the strain (ε) is the dimensionless ratio between the sample deformation (ΔL) and the initial sample length (L_0).

The MOE is then determined by linear regression between the values of calculated stress and blank-corrected strain during the linear phase:

$$MOE = \frac{\Delta\sigma}{\Delta\varepsilon} = \frac{\Delta F}{\Delta L}\frac{L_0}{S} \quad (11)$$

Concerning the stress relaxation phase, results are expressed in terms of normalized stress levels (Eq. 12) as a function of relaxation time, in which σ_0 is the stress level at the beginning of relaxation. To express the temporal evolution of normalized stress, the following expression is proposed, from which two parameters can be obtained: the recoverable part of the asymptotic value (α) and the characteristic time of relaxation (τ) [34].

$$\frac{\sigma_{(t)}}{\sigma_0} = 1 - \alpha\left(1 - e^{\frac{-t}{\tau}}\right) \quad (12)$$

For each repetition, α and τ were fit to the data using the Nelder-Mead method. Equation 13 was then used to calculate the dimensionless stress at the end of the relaxation interval (t = 30 s), R_{30}.

$$R_{30} = \frac{\Delta\sigma}{\sigma_0} = \frac{\sigma_0 - \sigma_{(t=30\,s)\,calculated}}{\sigma_0} = 1 - \frac{\sigma_{(30)}}{\sigma_0} \quad (13)$$

This data analysis allows the signal noise to be averaged at best over the 30-second interval.

2.3. Treatment conditions

Treatments were performed at 150, 160, and 180 °C, and the mechanical properties of wood were measured in the radial (R) and tangential (T) directions. All treatment conditions are summarized in Table 7. Sodium hydroxide and sulfuric acid concentrations were chosen based on previous studies [202,205].

Table 7. Summary of the treatment conditions of all tests performed on poplar samples

Temperature (°C)	Direction	Reagent	Concentration (% m/m)	pH
150	T	Water	-	-
160	T	Water	-	-
180	T	Water	-	-
150	R	Water	-	-
160	R	Water	-	-
180	R	Water	-	-
160	R	NaOH	0.6	12.57
160	R	H_2SO_4	0.3	1.51
160	R	H_2SO_4	0.6	1.29
180	R	NaOH	0.6	12.57
180	R	H_2SO_4	0.3	1.51
180	R	H_2SO_4	0.6	1.29

3. Results

3.1. MOE

3.1.1. Effect of temperature and wood direction

Figure 68 reports typical apparent MOE results obtained with distilled water in the radial (left column) and tangential (right column) directions for the three plateau temperatures (150, 160, and 180 °C). At the beginning of each test, the MOE was measured at room temperature. The mean MOE value was 843 ± 13 MPa in the radial direction and 335 ± 97 MPa in the tangential direction. All results are presented as the dimensionless ratio between the MOE measured at a given time and the mean MOE value at room temperature. The evolution of the dimensionless MOE is plotted as a function of time (Figure 68a-d) and as a function of temperature (Figure 68 e-f).

During the heating phase, a strong MOE decrease was observed until the treatment temperature was reached (Figure 68a-b). Consistently during this phase, the tests conducted at different temperatures superpose, as the heating rate is the same for all tests. The same trend is observed for either radial or tangential directions: regardless of the direction, approximately 97 % of the MOE initial value is lost at 150 °C. These observations take place during ca. the first 20 minutes of treatment (heating-up phase), highlighted by vertical solid lines in Figure 68a-b. This phase is, therefore, better observed when the apparent MOE is plotted against temperature (Figure 68e-f). In these plots, a difference between directions is observed in the shape of the curves. The MOE of samples loaded in the tangential direction decreased somewhat linearly with temperature, whereas radial tests demonstrated linear behavior only over a limited range of temperatures.

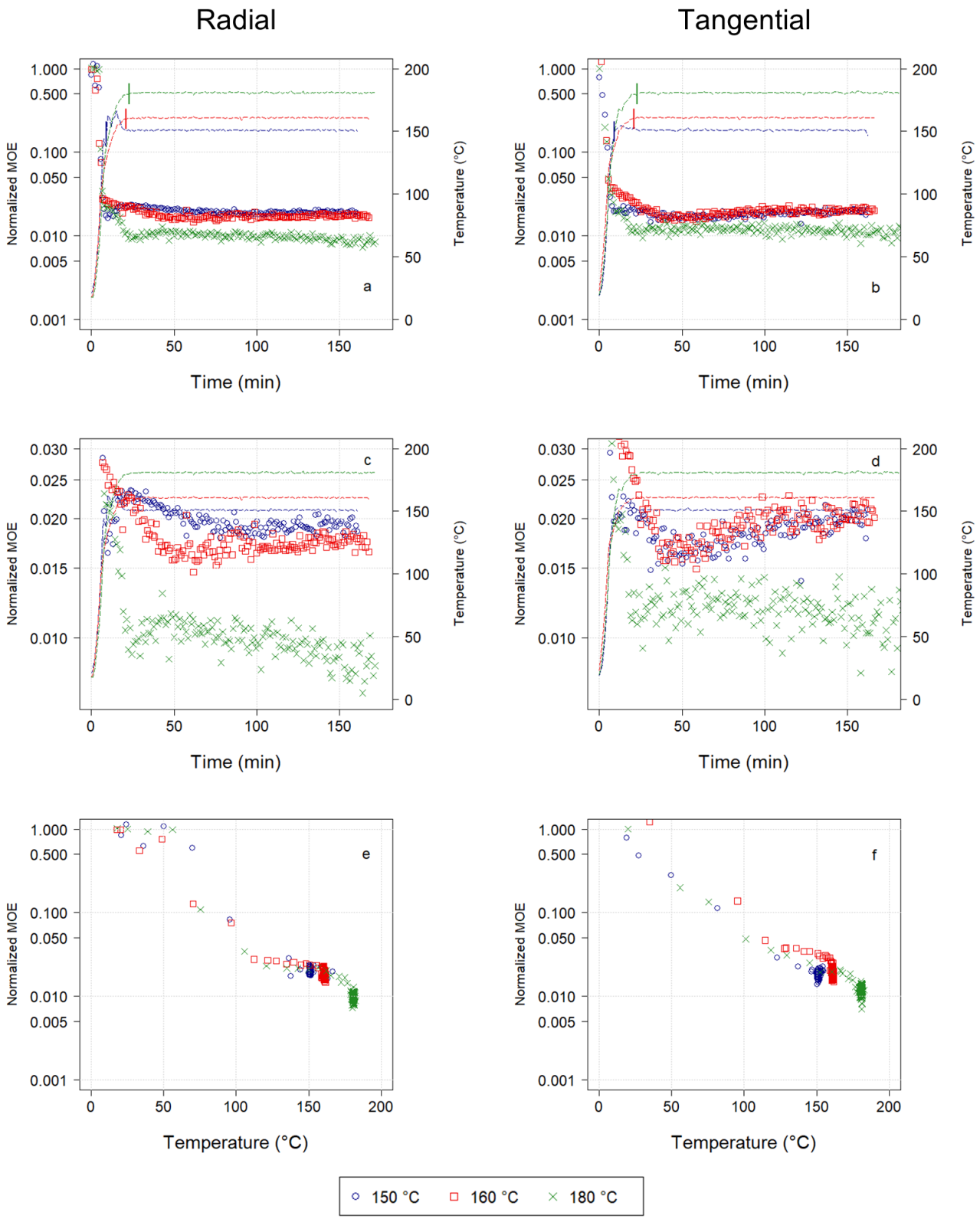

Figure 68. Modulus of elasticity of poplar as a function of time (a-d) and temperature (e-f) for different plateau temperatures. The left column (a, c, e) depicts radial tests and the right (b, d, f), tangential tests. Figures (c) and (d) are enlargements of the low values of MOE in figures (a) and (b). MOE measurements are represented by markers, while temperatures in the plot (a-d) are represented by dashed lines. Vertical solid lines highlight the beginning of the temperature plateau.

Once the plateau is reached—after 9, 21, and 23 minutes of treatment for a plateau temperature of 150, 160, and 180 °C, respectively—a second phase starts, during which changes occur at a constant temperature. In the radial direction (Figure 68c), whatever the duration of the plateau, a higher treatment temperature resulted in a lower MOE. At the beginning of the plateau, for example, the measured MOE represented only 0.028, 0.022, and 0.011 of its initial value for treatments at 150, 160, and 180 °C, respectively. At a given temperature, however, the evolution of the dimensionless MOE was not always monotonic. At 150 °C, the MOE decreased to a minimum of 0.018 after 97 minutes of treatment (88 minutes from the beginning of the plateau) and then slowly increased up to a maximum of 0.020 at the end of the treatment. The same behavior occurred faster for the treatment at 160 °C. The minimum value (0.016) was reached at approximately 50 minutes (29 minutes from the beginning of the plateau), after which values increased up to 0.018 at the end of the treatment. Finally, the treatment at 180 °C demonstrated even more complex behavior: the apparent MOE decreased quite rapidly down to 0.009 at minute 29, only 6 minutes after the beginning of the plateau. Then, it regained the same value as at the beginning of the plateau (0.011) at minute 50 (17 minutes from the beginning of the plateau). The remaining portion of the test depicts a slow and regular decrease until the end (minimum of 0.008). In the tangential direction (Figure 68d), dimensionless MOE values at the beginning of the plateau were 0.023, 0.022, and 0.012 at 150, 160, and 180 °C, respectively. Minimum values were reached earlier than in the radial direction. At 150 °C, the minimum dimensionless MOE (0.016) was reached after 48 minutes (39 minutes from the beginning of the plateau), whereas, at 160 °C, it required 45 minutes (24 minutes from the beginning of the plateau) to reach the same minimum. For the treatment at 180 °C, after the beginning of the temperature plateau, the MOE value increased to a stable value of approximately 0.012 between 50 and 100 minutes (between 27 and 77 minutes from the beginning of the plateau, respectively) and then decreased to a minimum of ca. 0.010 at the end of the treatment.

3.1.2. Effect of pre-soaking media

Figure 69 shows typical MOE results obtained from poplar samples in the radial direction during hydrothermal treatment at 160 °C (a, c, e) and 180 °C (b, d, f), in which the effects of four different pre-soaking liquids were compared: distilled water, NaOH (0.6 % m/m), and H_2SO_4 (0.3 and 0.6 % m/m). As in section 3.1.1, results are represented as dimensionless MOE, using the mean radial MOE values measured at room temperature in water-saturated conditions as the reference value. As in Figure 68, Figure 69 depicts the evolution of dimensionless MOE versus time (a-d) and temperature (e-f).

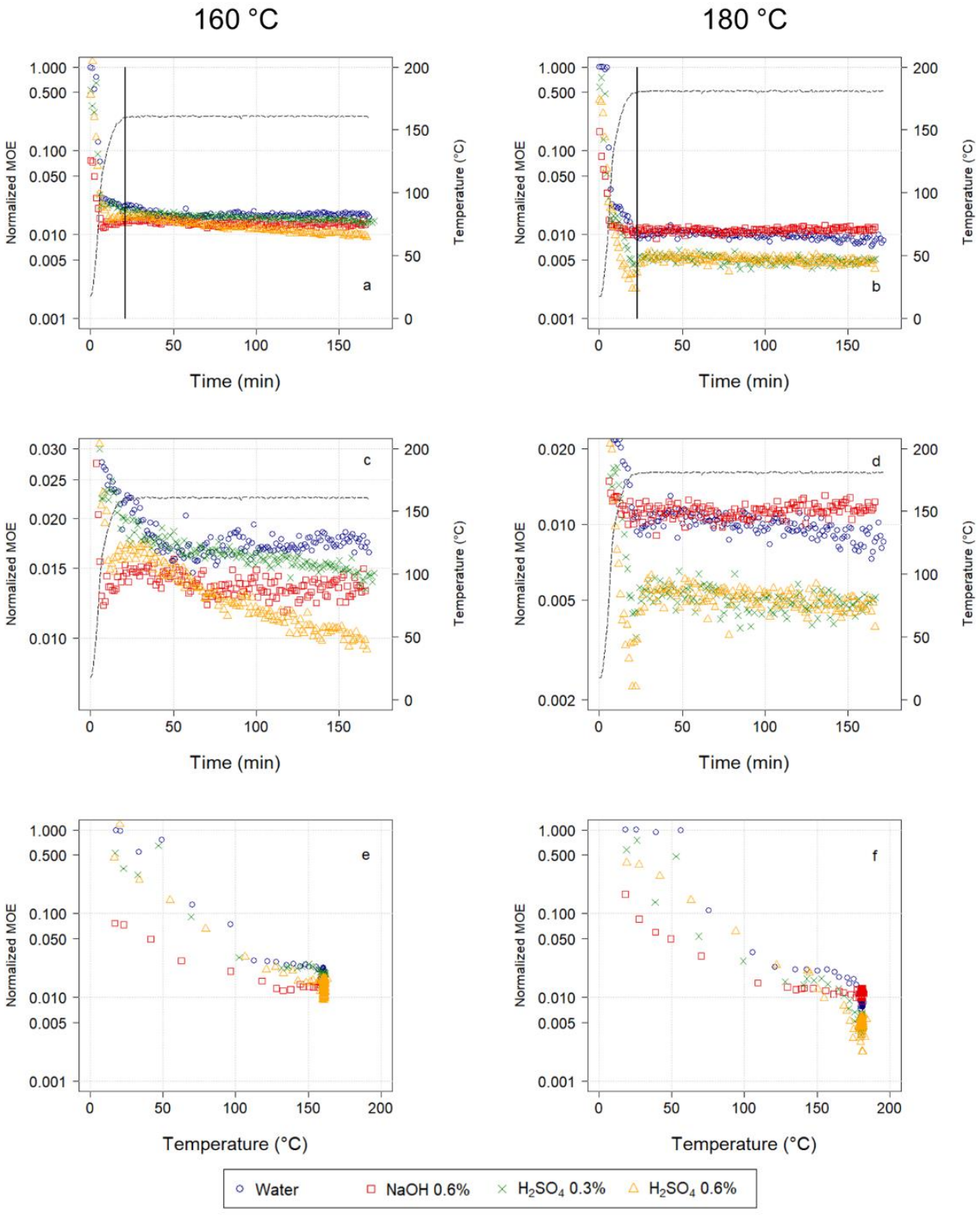

Figure 69. Modulus of elasticity as a function of time (a-d) and temperature (e,g) for two plateau temperatures: 160 °C (left column, a, c, e, g) and 180 °C (right column, b, d, f). In figures (c) and (d), the zoom scale of the y-axis is different as it was chosen to represent, at best, the notable trends.

Samples saturated with sodium hydroxide and sulfuric acid solutions presented lower MOE at room temperature than those saturated with distilled water (Figure 69e,f).

Sodium hydroxide yielded the lowest dimensionless MOE (approximately 0.1) at room temperature. These values further decreased to 0.015 and 0.011, respectively, at 160 and 180 °C when the plateau was attained. The behavior observed for NaOH-treated samples was then very different for treatments at 160 °C and 180 °C. Although at 180 °C MOE values seem to stagnate at 0.011, the behavior at 160 °C is similar to that of water-treated samples. MOE decreased to 0.012 and then increased again to almost the same value observed at the beginning of the plateau (0.015). The MOE of samples treated with NaOH remained the lowest until ca. 150 °C when they were reached in the 0.6 % H_2SO_4 treatments. Compared to samples treated with water, NaOH resulted in lower MOE values during the entire plateau for the 160 °C treatment. In contrast, at 180 °C, the MOE values were higher than those of the water treatment.

At 160 °C, the presence of H_2SO_4 caused a continuous reduction of MOE during the temperature plateau (Figure 69c-f), which was even more pronounced at higher H_2SO_4 concentration. At 180 °C, however, increasing the acid concentration caused almost no difference in the MOE. Indeed, both acid concentrations caused a loss of MOE with the same asymptotic value at 0.5 % for the dimensionless MOE, which represents a 200-fold division of the MOE at room temperature. Regardless of the temperature and the concentration, sulfuric acid resulted in lower MOE than water at the end of the treatment.

Finally, as expected, in all tested conditions, the use of a higher treatment temperature resulted in lower MOE. For samples treated with NaOH, however, only a slight difference was observed between the temperatures (160 and 180 °C).

3.2. Stress relaxation

After each linear loading, the stress relaxation of samples was monitored for 30 seconds. Figure 70 shows typical stress relaxation results of poplar samples during two different phases of the treatment: the heating-up phase (Figure 70a), for which results are expressed in terms of temperature, and the temperature plateau (Figure 70b), for which results are expressed in terms of treatment duration from the beginning of the plateau. The results shown in Figure 70 were obtained from a water-saturated sample treated at 160 °C and loaded in a radial direction. Experimental points are plotted as markers, and the best fit using Equation 12 is represented by dashed lines.

During the heating-up phase (Figure 70a), as the temperature increased from 17 °C to 54 °C, a significant increase in relaxation was observed. This trend is then inverted as the temperature continues to rise (curves at 77 °C and beyond). During this second period, the curves shifted upwards, revealing a reduction in viscoelasticity (results in green and yellow in Figure 70a). This trend continued once the temperature reached the plateau (curves evolving from yellow to pink in Figure 70b).

The parameters of Equation 12 were then used to calculate the normalized stress relaxation after 30 seconds (R_{30}), as described by Equation 13, to be explored in the following sections.

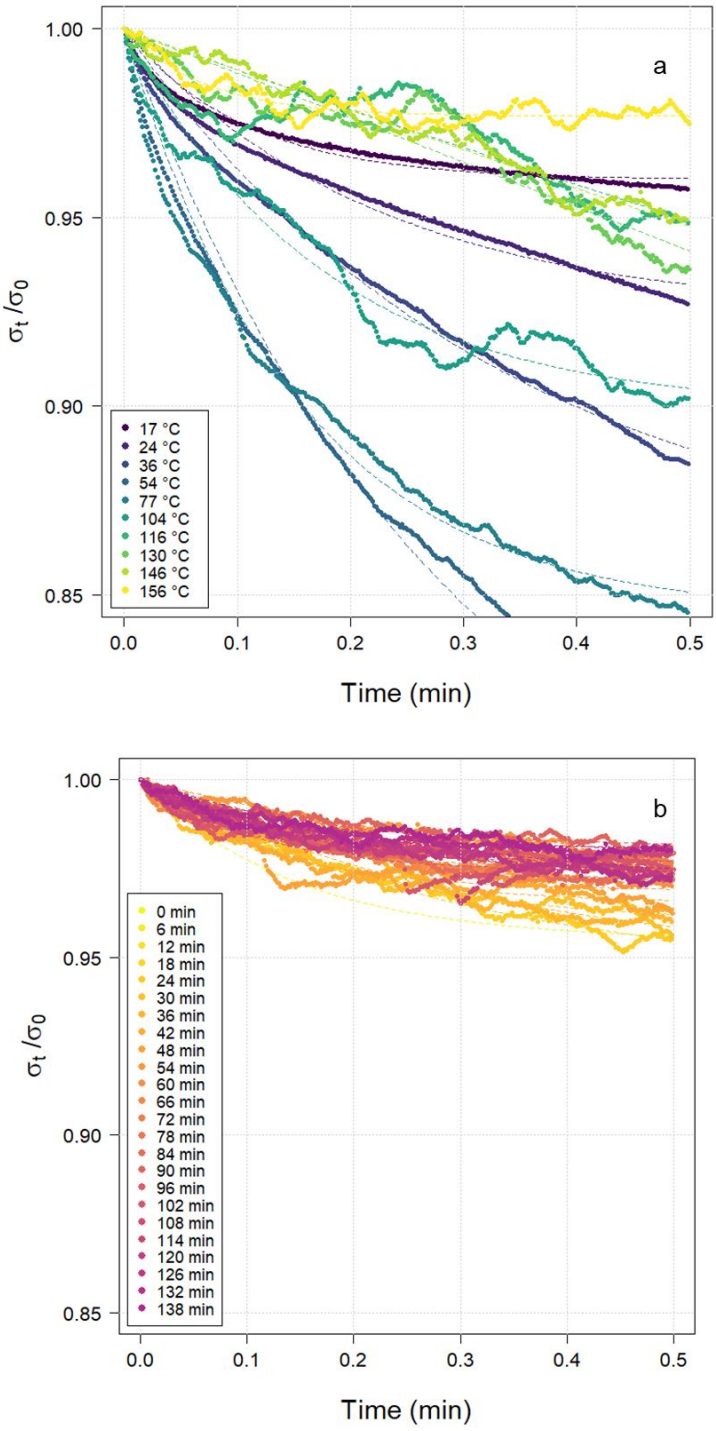

Figure 70. Typical stress relaxation results of water-saturated poplar in a radial direction (a) as a function of different temperatures during the heating-up phase and (b) as a function of time during the plateau at 160 °C. For the sake of clarity, only one result out of two and six are represented in (a) and (b), respectively.

3.2.1. Effect of temperature and wood direction

Figure 71 displays the evolution of R_{30} as a function of time (Figure 71a,b) and temperature (Figure 71c,d) for different temperatures (150, 160, and 180 °C) in radial (left column) and tangential (right column) directions. The dashed lines represent the temperature, and the vertical

lines indicate the beginning of the temperature plateau. For improved visualization of the results, results in Figure 71a,b were filtered using a 3-point sliding median.

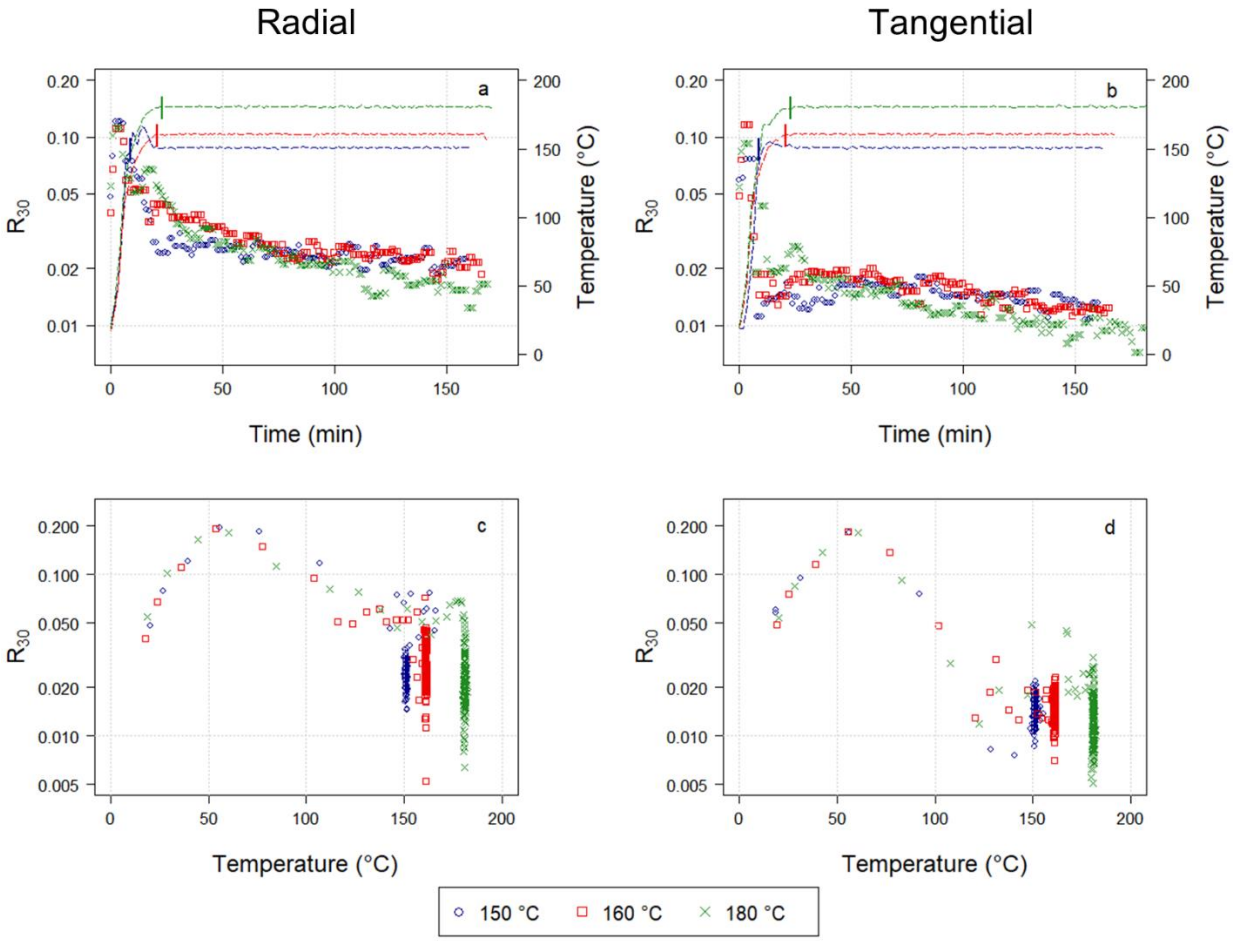

Figure 71. Relaxation ratio after 30 s of compression as a function of time (a, b) and temperature (c, d) for different plateau temperatures in the radial (left column) and tangential (right column) directions.

During the heating-up phase (Figure 71c,d), the evolution of R_{30} confirms the trend observed on the raw relaxation curves. When heated from room temperature to approximately 60 °C, R_{30} increases up to a maximum of 0.020 in the radial direction and 0.018 in the tangential direction. From this point, a continuous decrease is observed. The superposition of the results of different tests validates the repeatability, despite the extreme difficulty of such measurements. Once the temperature plateau was reached, R_{30} values were almost twice as high in a radial direction than those in a tangential direction. During this period, in a radial direction, the effect of temperature was noticeable, as the highest value was obtained at 180 °C, followed by 160 °C, and finally, 150 °C. At 150 °C, the relaxation was approximately 0.024, and almost no change was observed throughout the temperature plateau (Figure 71c). At 160 °C, the plateau started at 0.038 and was the same as the results of the 150 °C test (R_{30} = 0.024) after 75 minutes of treatment (54 minutes from the beginning of the plateau). During the 180 °C test, the R_{30} plateau started at 0.056 and regularly decreased to reach 0.015 at the end of the treatment. Similar trends were obtained in the tangential direction (Figure 71d), except for substantially smaller values of R_{30}.

3.2.2. Effect of pre-soaking liquid

The effect of different pre-soaking liquids on the viscoelastic properties of poplar during hydrothermal treatment was also assessed. Using the same protocol as in the previous section, tests were performed in a radial direction at 160 °C (Figure 72a,c) and 180 °C (Figure 72b,d). The identified R_{30} values are shown in Figure 72 as a function of time (a-b) and temperature (c-d). In Figure 72a-b, the beginning of the temperature plateau is highlighted by the vertical black line, while the temperature is plotted as dashed lines. As in Figure 71a-b, Figure 72a-b presents filtered results (3-point sliding median).

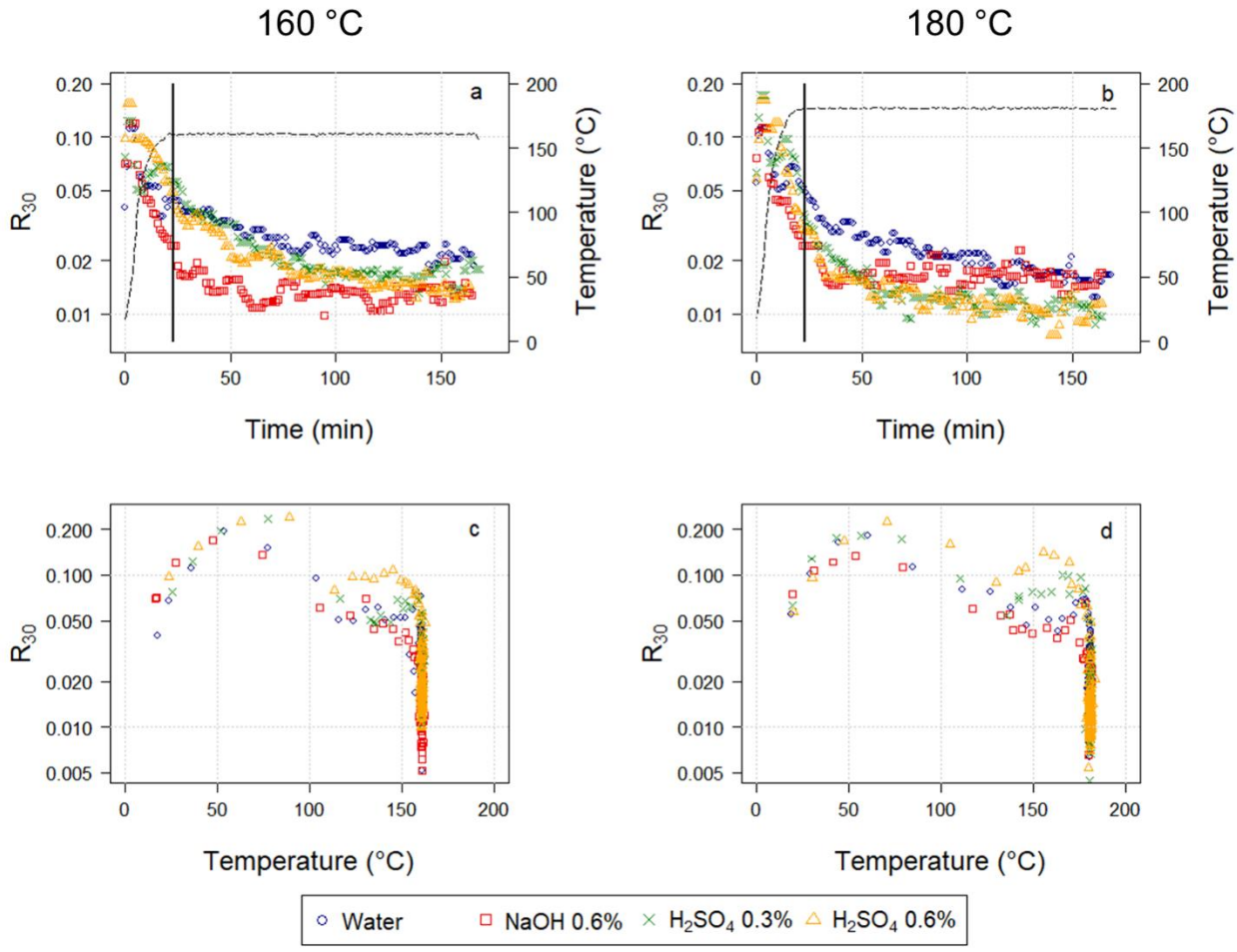

Figure 72. Dimensionless stress after 30 s of compression as a function of time (a, b) and temperature (c, d) for the tests at 160 °C (left column) and 180 °C (right column).

During the heating-up phase (observed in Figure 72c,d), different pre-soaking media appeared to have a similar effect on the R_{30} parameter, as previously observed for water-only treatment, i.e., an initial increase of R_{30} up to a maximum value at around 60 °C and followed by a decrease. Notably, during this phase, the test with acid allowed the highest R_{30} values to be obtained until the plateau temperature. Sodium hydroxide and water, in contrast, resulted in lower R_{30} values during the same period.

For H_2SO_4-soaked samples, regardless of the concentration and the temperature, R_{30} seemed to behave monotonously during the temperature plateau (Figure 72c-d), regularly decreasing with time. In both 160 and 180 °C treatments, water produced the highest R_{30} values throughout this phase. A slight reduction of R_{30} can be observed at the highest temperature (180 °C vs. 160 °C), regardless of the reaction liquid. An exception to this trend was found when using NaOH: samples treated with this soaking liquid caused almost no reduction in MOE during the temperature plateau, and little behavior difference can be observed between samples treated at 160 °C and 180 °C.

3.3. Qualitative results

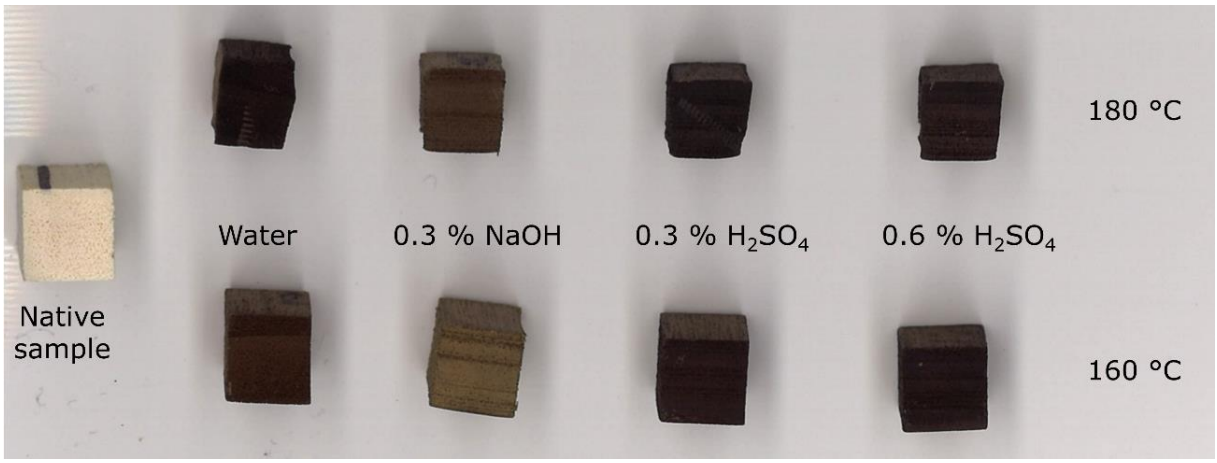

Figure 73. Poplar samples after 2.5 h of treatment under different temperatures and pre-soaking liquids.

Consistent with published studies, the sample color shifts from light to dark brown with increasing treatment severity, a cumulative effect of temperature level and acid concentration [24,206,207]. Furthermore, samples pre-soaked with sodium hydroxide maintained a light brown color, which may be seen as the opposite effect caused by acidity. Qualitative and morphological features can provide valuable information on biomass chemical modifications, as shown in previous studies [193,208].

4. Discussion

During hydrothermal treatment, two phenomena contribute to the changes observed on the mechanical properties of biomass: thermal activation and chemical degradation [34]. Thermal activation of the viscoelastic behavior occurs during the heating-up phase, when the temperature increase leads to greater mobility of macromolecules. The switch from a glassy state to a rubbery state is known for its great impact on the mechanical properties of polymers [147]. The transition is not as immediate for wood due to its complex mixture of multiple macromolecules. In the case of water-saturated wood, it is generally accepted that the temperature of glass transition ranges between 60 and 90 °C, which is mainly attributed to the glass transition of lignins [32,147,148].

This results in a substantial loss of rigidity, characterized by a decrease in the apparent MOE and higher relaxation [33,34,99,145,155,209].

Previous works have linked some of the chemical modifications that occur during hydrothermal treatment to the mechanical properties of biomass [33,34,107]. Lignin and, more precisely its glass transition, is usually singled out as the major factor responsible for the viscoelastic behavior of wood, especially with regard to thermal activation [32]. Nevertheless, some studies have found evidence of the importance of hemicelluloses on the mechanical behavior of wood [105,210]. Consistent with the present results, hemicellulose-free samples presented less viscoelasticity than native wood [107,210]. Furthermore, Mokdad et al. (2018) observed a reduction of stress relaxation during hydrothermal treatment and attributed it to the re-condensation of lignins. Hence, both hydrolysis and repolymerization should result in a decrease in stress relaxation with increased residence time.

An inverse relationship has been observed for rigidity. While hydrolysis reactions tend to reduce wood rigidity, the formation of condensed lignin linkages increases rigidity [33]. This observation is related to the degree of polymerization of molecules. Cleaved chains have a reduced mechanical role, which lowers the apparent rigidity [150].

The combination of our mechanical measurements (apparent MOE and relaxation) is consistent with the mechanisms described above. The water-soaked samples analyzed in a tangential direction, for example, showed a linear decrease of MOE with temperature during the heating-up phase (Figure 68b). In the radial direction (Figure 68a), a regular decrease was also observed, even though the trend is not linear. This is probably due to the presence of different morphological structures (fibers and rays) acting in radial direction and which are not activated in the same way. Regardless of the direction (Figure 68a-b), the results from all three treatments (150, 160, and 180 °C) merged into a single master curve. Similar observations made in previous studies were attributed to the thermal activation of the viscoelastic behavior of wood [34]. While thermal activation is undoubtedly one of the mechanisms involved in the reduction of rigidity during this phase, the evolution of relaxation (Figure 71a-b) implies that another phenomenon is occurring simultaneously. The first part of the heating-up period, with a concomitant decrease of MOE and an increase of relaxation, can be readily explained by thermal activation. This is not consistent once the maximum value of relaxation, at ca. 60 °C, has been reached. After this point, the apparent modulus continues to decrease while relaxation decreases instead of increasing. These facts indicate that, even at such low temperatures, there could be some chemical degradation, a phenomenon that would have been hidden if only stiffness had been measured. Evidence of chemical degradation at 80–90 °C has been previously revealed, and the importance of water as an activating agent of degradation reactions has been highlighted [145]. Considering the temperature level, the hydrolysis of hemicelluloses is the most probable mechanism [145,186].

During treatment at constant temperature (Figure 68a,b, and Figure 71a,b), the evolution of the mechanical behavior is solely related to chemical degradation, as mechanical and treatment times have been distinguished through cyclic loading. The monotonous decrease of relaxation (Figure 71c-d) can be attributed to both hydrolysis and condensation reactions, as their effects are additive [34]. On the contrary, hydrolysis reactions are likely to reduce MOE during the first minutes of the plateau, while condensation would be responsible for its subsequent increase [33]. The opposite effects of these two phenomena are likely to explain the trends observed in Figure

68c-d. For severe treatment (180 °C), however, a somewhat continuous decrease in the MOE was observed with residence time. A higher treatment temperature is likely to introduce a new phenomenon into the balance: cellulose depolymerization [34,115,120,211]. The results of Vila et al. [211], revisited by Mokdad et al. [34], showed a clear effect of treatment temperature on the reduction of the degree of polymerization (DP) of cellulose. While at 180 °C, the DP decreased by 75 % after 150 minutes of treatment (equivalent to the end of the plateau in our study), the loss was only by 25 % at 160 °C. The length of cellulose chains is, thus, a major factor influencing the MOE of samples treated at high temperature. To a lesser extent, increasing the severity of the treatment could favor depolymerization to the detriment of re-condensation. Indeed, the high water availability and the severe conditions to which biomass was subjected during this study are prone to promote the hydrolytic pathway of lignin degradation, leading to the formation of Hibbert ketones and limiting re-condensation of lignin [126,128].

Pre-soaking in specific liquids also affected the data trends. Soaking in sodium hydroxide at room temperature for 12 hours reduced the initial MOE by approximately a factor of ten (Figure 69a-b). Despite this considerable initial decrease, the module stagnates during the temperature plateau (Figure 69c-f). A similar observation can be made for relaxation. With sodium hydroxide, the relaxation reduced very rapidly as the temperature approached the plateau, as shown by an acceleration of the decrease of R_{30} (Figure 72c,d), but remained almost constant afterward, during the plateau (Figure 72a,b). The mechanisms involved in alkali pretreatments are different from those previously described for acid pretreatments. Sodium hydroxide has been proven to effectively promote the cleavage of ether and ester bonds of lignin-carbohydrate complexes (LCC) and of lignin C–C bonds [202], even at room temperature [212]. The pretreatment protocol used in this study, which includes an overnight pre-soaking step, could, therefore, promote early lignin and hemicellulose solubilization [202]. Furthermore, rather than producing acetic acid—such is the case for acid-catalyzed mechanisms—an alkali medium promotes saponification of acetyl and uronic ester groups of hemicelluloses, which limits autohydrolysis processes usually observed under acidic conditions or water [213]. Similar observations have been made by Chadni et al. [28] when evaluating the effect of the pH of the pre-soaking liquid on the steam explosion of spruce sawdust. The use of sodium hydroxide resulted in hemicelluloses with significantly higher molecular weights than those treated only with water. This fact is consistent with our results, in which almost no changes on the mechanical properties were observed during the temperature plateau for samples treated with sodium hydroxide. The light brown color of the samples after the treatment also supports this mechanism (Figure 73). Neutralization of sulfuric acid was also observed when using sodium carbonate as a tracer for residence-time distribution experiments in a pretreatment reactor [205]. Hydrothermally treated samples are usually expected to be darker, due to several mechanisms, such as the breakdown of lignin and wood extractives, tannin and flavonoid condensation induced by lignin condensation, and reactions with furfural and 5-hydroxymethylfurfural [24,206,207]. The lignin and hemicellulose extraction promoted by sodium hydroxide during sample saturation resulted in fewer degradation products and, consequently, a lighter color (Figure 73).

According to our measurements, the use of dilute acid as pre-soaking medium results in a monotonous decrease of both MOE and R_{30}. Following the above reasoning and given the fact that no module re-increase was observed during the plateau, it can be assumed that sulfuric acid favored cleavage rather than condensation of lignins. Furthermore, two different mechanisms

have been observed for the cleavage of β-O-4' aryl ether linkages: the homolytic and the heterolytic pathways. In acidic conditions, the acid-catalyzed hydrolytic route prevails, leading to the formation of Hibbert ketones [126]. For the same pretreatment conditions, dilute acid was found to enhance the depolymerization and solubilization of lignin into the liquid phase when compared to water-only pretreatments [214].

5. Conclusion

This study proposes a set of continuous rheologic measurements carried out during the hydrothermal treatment of poplar. Various treatment conditions were tested, including the temperature (150, 160, and 180 °C) and the soaking liquid (distilled water, acid solution, or alkaline solution). The two complementary mechanical properties measured in our protocol (stiffness and relaxation) allowed us to draw meaningful conclusions regarding the chemical mechanisms involved in hydrothermal treatment.

The concomitant evolution of stiffness and relaxation were analyzed in terms of thermal activation of viscoelasticity, cleavage of molecular linkages, and re-condensation.

According to our results, thermal activation solely occurs at the beginning of the heating period, when the temperature remains quite low. Concomitant thermal activation and chemical degradation were observed in relaxation tests at a relatively low temperature (60 °C). This effect, attributed to the hydrolysis of hemicelluloses, cannot be observed from rigidity tests because of its monotonous behavior during the heating phase.

Cleavage reactions (possibly affecting both hemicelluloses and lignins) were predominant at the beginning of the treatment plateau. The subsequent increase of the MOE highlighted the presence of the re-condensation of lignins.

Depending on the treatment severity, the dominance of either condensation or cleavage could be observed over long residence times, including the reduction of the DP of cellulose. Both higher temperature and the use of an acidic pre-soaking medium seemed to promote the hydrolysis of lignocellulosic biomass, whereas, the use of sodium hydroxide seemed to provoke lignin and hemicellulose extraction at low temperatures but limited further alterations during the temperature plateau.

6. Acknowledgments

This study was conducted in the Centre Européen de Biotechnologie et de Bioéconomie (CEBB), supported by Région Grand Est, Département de la Marne, Grand Reims, and the European Union. In particular, the authors would like to thank Département de la Marne for its financial support and the French Council for Poplar as well as Huberlant sawmill (Cormicy, France) for providing the wood used in this study.

CHAPTER V. A DAEM model based on *in-situ* shrinkage measurement of poplar wood during hydrothermal treatment as predictive indicator of chemical degradation

A. Preamble

Chapter IV has confirmed the ability of rheological properties to reflect the dynamics of chemical modifications during hydrothermal treatment. Stiffness and stress relaxation measurements have proven to provide complimentary information and, together, successfully highlighted the thermal activation of the viscoelastic behavior of biomass, cleavage reactions and lignin re-condensation. However, both of these properties presented a non-monotonous behavior at some point of the treatment: stress relaxation during the heating phase and stiffness during the temperature plateau.

To follow the additive effects of treatment on biomass deconstruction over time, an appropriate macroscopic indicator should have a monotonous behavior throughout the entire treatment, whatever the treatment severity. The same device used in Chapter IV to measure rheological properties is used in Chapter V to follow the evolution of sample size during treatment, which implies strain measurements at almost zero stress levels. These alterations are later related to the chemical alterations of biomass, evaluated either in the residual solid biomass — through mass loss and hygroscopicity — or in the treatment liquid — in terms of dissolved sugars and organic acids, production of inhibitors, and pH. Chemical analyses were performed at selected treatment times.

During preliminary tests, two (hydro)mechanical phenomena were showed to have an impact on samples dimensions and had to be considered during methodology development and data treatment: the hygrothermal recovery of cell wall's internal stress and changes of fiber saturation point.

Shrinkage monotonously increased with the increase of temperature and residence time. The obtained results were used to feed a Distributed Activation Energy Model (DAEM), whose parameters were identified using the data from all tests simultaneously.

Chemical results reflected the mechanisms typically described in literature. Water autoionization forms hydronium ions that act as catalysts for a series of hydrolysis reactions, to which hemicelluloses are the most susceptible components of the cell wall. The hydrolysis of the acetyl side groups resulted in the production of acetic acid — also observable by a decrease in the pH of the treatment liquid. The increasing extension of biomass degradation can be followed primarily by an increase in the quantity of dissolved oligosaccharides and, further, by their conversion into monosaccharides. The hydrolysis of biomass and, thus, the solubilization of its components in the liquid phase resulted in a mass loss of the solid fraction. The residual solid biomass was also altered. Sorption measurements revealed that the hygroscopicity of biomass decreased with the increase of treatment severity, which was attributed to the loss of the functional hydroxyl group itself, of acetyl groups or of entire osidic monomers.

Finally, the capacity of the identified DEAM model to predict the chemical properties of biomass as a function of treatment temperature and residence time was evaluated. The degree of conversion, as calculated by the DEAM model and fitted from the *in situ* shrinkage measurement, has proven to be a synthetic indicator of chemical alterations. This excellent result then served to the adjustment simple expressions to relate the physical and chemical measurements to the

identified model. Shrinkage therefore emerged as a good indicator of the chemical degradation of biomass during the pretreatment.

The conclusions of this chapter can be summarized by the figure below.

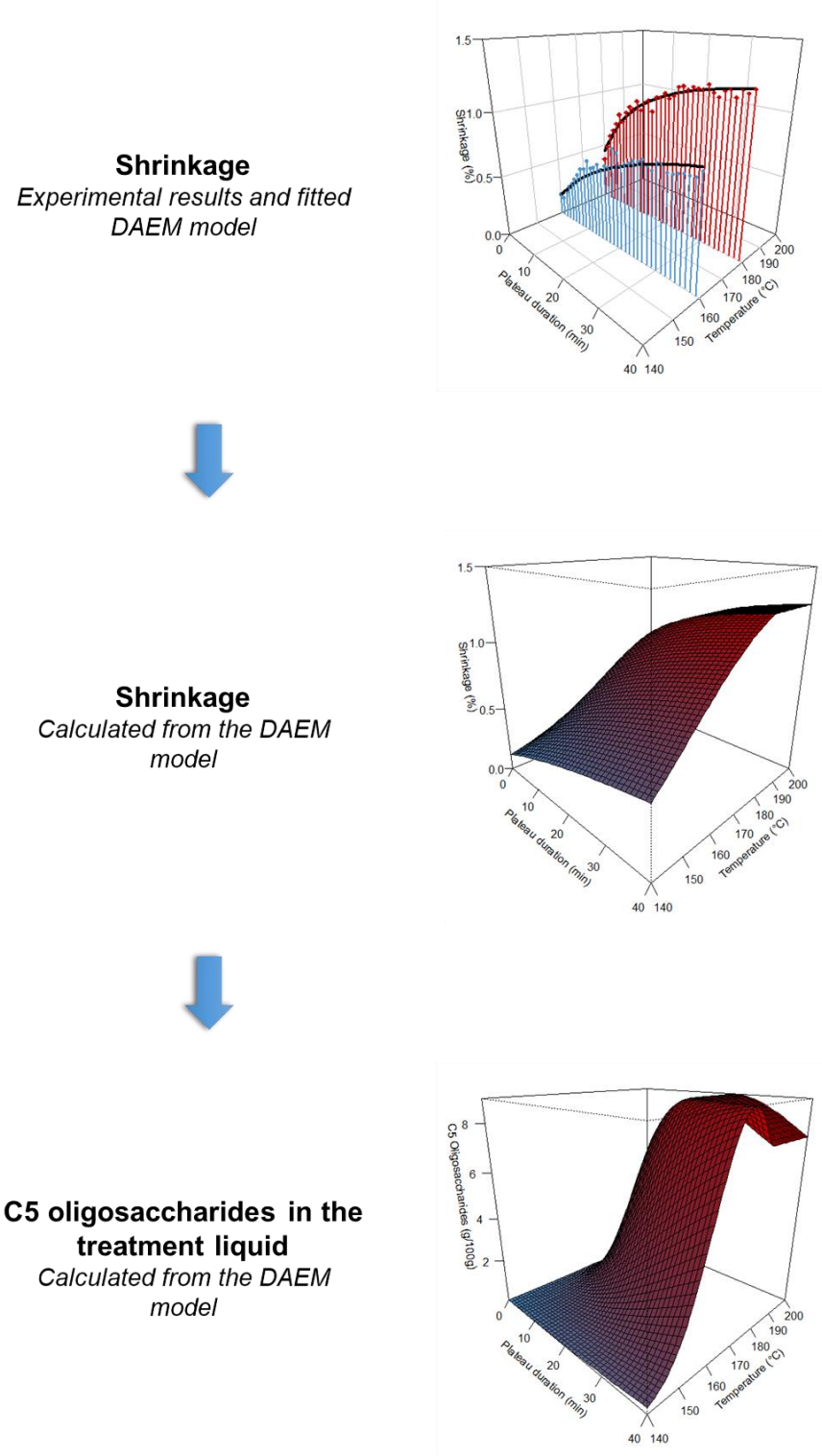

Figure 74. Graphical abstract of Chapter V

B. A DAEM model based on *in-situ* shrinkage measurement of poplar wood during hydrothermal treatment as predictive indicator of chemical degradation

Julia P. Lancha[1], Julien Colin[1,2], Giana Almeida[3], Joel Casalinho[2], Cédric Guerin[1], Patrick Perré[1,2]

[1] Université Paris-Saclay, CentraleSupélec, Laboratoire de Génie des Procédés et Matériaux, SFR Condorcet FR CNRS 3417, Centre Européen de Biotechnologie et de Bioéconomie (CEBB), 51110 Pomacle, France

[2] Université Paris-Saclay, CentraleSupélec, Laboratoire de Génie des Procédés et Matériaux, 8-10 rue Joliot-Curie, 91190 Gif-sur-Yvette, France

[3] Université Paris-Saclay, INRAE, AgroParisTech, UMR SayFood, 91300 Massy, France

To be submitted

Abstract

This study proposes the use of shrinkage as continuous indicator of biomass alterations during hydrothermal pretreatment. An original rheological monitoring tool developed recently [1] was used to perform shrinkage measurements during hydrothermal treatment. The originality of this device is its ability to perform continuously and accurately mechanical tests of biomass (various combinations of strain and stress) under water-saturated conditions up to 190 °C. By relating the alterations of chemical composition with continuous measurements of shrinkage, the ultimate goal of the work is to provide a macroscopic indicator likely to give rules to optimize the residence time and treatment temperature prior to the explosion step. To achieve this goal, chemical analyses were performed at selected treatment durations and the parameters of a DAEM model (Distributed Activation Energy Model) were identified on these measurements. This model allows the treatment severity and the chemical degradation of biomass to be predicted for various temperature-time pathways.

Keywords: Lignocellulosic biomass; Poplar; Steam explosion; Hydrothermal pretreatment; Shrinkage; DAEM model.

1. Introduction

The imperative to reduce greenhouse gas emissions and dependence on oil has led to an increased interest in the use of biomass for the production of biofuels and chemicals. Compared to the first generation, second-generation biofuels (2G) are likely to diversify the source of raw material by using lignocellulosic biomass, a largely available and relatively low-cost feedstock.

However, the production of 2G biofuels is more challenging than the first generation. Indeed, as lignocellulosic components play the role of support in plants, they are designed to last, for many decades in the case of trees, and withstand degradation. Their recalcitrant macromolecular structure is mainly composed of cellulose, hemicelluloses and lignins, interlinked in a complex matrix. Consequently, to produce bioethanol, a pretreatment is required to make carbohydrates sufficiently accessible for enzymatic hydrolysis before fermentation. There is a large range of pretreatments available: physical, chemical, mechanical, biological and combined [26]. Among them, steam explosion appears to be effective for a large variety of lignocellulosic biomasses, including softwood, hardwood and agricultural residues. It consists of two phases: (*i*) a hydrothermal treatment in which the biomass particles are heated under saturated steam conditions; (*ii*) and a rapid release of the pressure to atmospheric conditions [37,44]. Its performance has a double effect on the economic profitability of biofuels production, due to its own significant cost and its impact on the yield of subsequent processes – especially enzymatic hydrolysis and fermentation. The mechanical properties of biomass at the end of the hydrothermal treatment are also of interest because they highly influence the efficiency of the steam explosion stage. In order to optimize and monitor this pretreatment, the ultimate objective would be a model capable of predicting the kinetics of biomass alterations as a function of treatment conditions.

This study proposes the use of shrinkage as continuous indicator of biomass alterations during hydrothermal pretreatment. Previous studies have shown that chemical degradation can cause shrinkage in the case of heat treatment of wood [141], but, to the best of our knowledge, no study of shrinkage during hydrothermal pretreatment has been performed, probably due to the challenge to continuously measure shrinkage with accuracy in spite of these severe conditions. As a matter of fact, in industry, the acid pretreatment phase is carried out between 160 and 270 °C [44], which implies a saturated steam pressure of up to 55 bar.

To perform shrinkage measurements under conditions closer to those used during the steam explosion, a new rheological monitoring tool has recently been developed [34]. The originality of this device is its ability to perform continuous mechanical tests of biomass (various combinations of strain and stress) under water-saturated conditions up to 190 °C. In the present work, it was used to continuously assess the evolution of sample size during treatment (strain measurement at almost zero stress level).

By relating the alterations of chemical composition with continuous measurements of shrinkage, the objective of the present work is to provide a macroscopic indicator likely to give rules to optimize the residence time and treatment temperature prior to the explosion step. This optimization includes a good compromise between chemical degradation and the aptitude of the cell wall to break off, while limiting the amount of inhibition compounds. To achieve this goal, chemical analyses were performed at selected treatment durations and the parameters of a DAEM model (Distributed Activation Energy Model) were identified on the measurements. This model allows the treatment severity to be predicted for various temperature-time pathways.

2. Material and methods

2.1. Hydrothermal pretreatment

2.1.1. Experimental device

The hydrothermal pretreatments were performed in a device conceived in the laboratory [34]. It consists of two chambers: the bottom one, where the treatment takes place; and the top one, housing the instrumentation (Figure 75). In this device, the bottom chamber can reach up to 190 °C at the saturated water vapor pressure (more than 13 bars), while the top chamber should stay at ambient conditions, typically 30 °C and 50 % of relative humidity (RH), to preserve the accurate instrumentation. Maintaining such contrasted conditions in a single device is possible thanks to a patented system [156] that includes a controlled leakage. In the upper chamber, a counter pressure is applied (1.5 bar higher than saturated water vapor pressure) with a flow of cold dry air (T < 30 °C and RH < 50 %). Due to the huge water vapor gradient, water vapor diffuses from the lower chamber towards the top chamber. The controlled leakage, together with the successive fins, ensures a downwards convective flux that progressively limits the upwards convective-diffusion vapor flux in each volume between two successive fins, and eventually stops any flow to the upper chamber.

The mechanical system for deformation measurements consists of three main parts: an actuator (NEWPORT LTA-HL, 25 mm travel range, 120 N load capacity, 50 nm minimal increment), a charge rod and a load cell (MEASUREMENT SPECIALTIES XFTC 310, full range of 100 N). The actuator ensures both the rod displacement and the position measurement, while the load cell determines the force exerted on the rod. A relative humidity/temperature sensor is installed in the upper chamber to check if the air leakage is enough to ensure moderate conditions despite the severe conditions imposed in the lower chamber.

In the present work, this mechanical system was only used to assess the sample shrinkage during the hydrothermal test. In order to reduce the mechanical loading of the sample, likely to induce a deformation due to viscoelastic behavior, the contact of the rod with the sample was detected when the measured force reached a very low value (0.05 N) according to the following protocol:

1. Calibration of the load cell out in the absence of contact. This allows the sensor drift to be corrected during the test;
2. Slow displacement of the rod towards the sample (0.005 mm/min);
3. Contact detection when the measured force reaches 0.05 N. In order to reach this very low detection threshold (0.05 % of the full range of the load cell), a median filter was applied on-line on a sliding window of 200 measurements grabbed at a frequency of 300 measurements per second;
4. Backward translation to release the contact with the sample.

This protocol was repeated each 90 seconds. The size of the sample was obtained by the position of the actuator when the contact criterion was satisfied and corrected with a blank test to account for the thermal dilatation of the device. The sample dimensions were also verified before and after treatment, outside the chamber, using a laser sensor (BULLIER AUTOMATION M5L/4).

When performing mechanical tests, the device allows the study of one sample at a time, with maximum dimensions of 8 x 8 x 8 mm^3. For chemical analysis purposes, up to 3 samples of

8 x 8 x 40 mm^3 can fit into the sample holder. In this case, mechanical measurements are not possible.

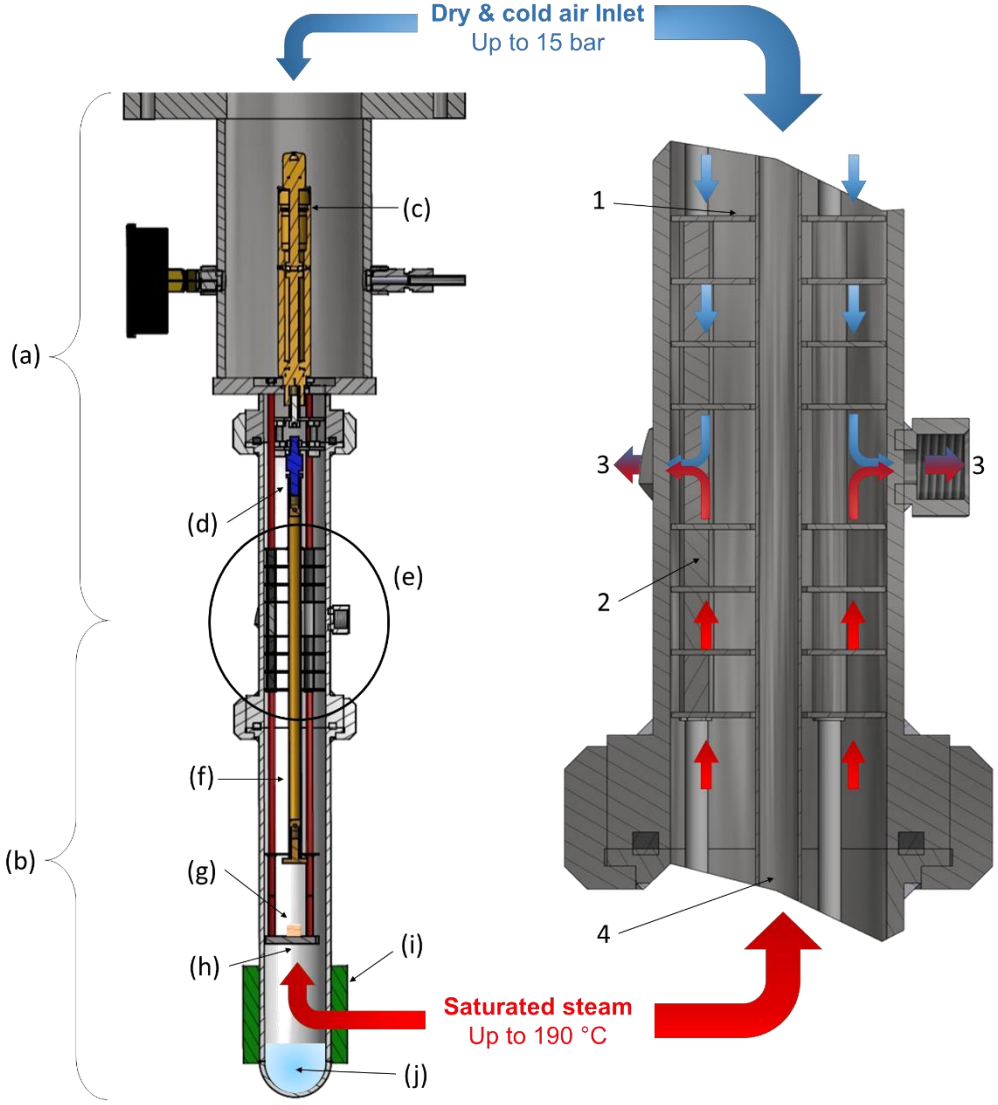

Figure 75. Up to scale CAD (Computer Aided Design) model of the device. Left: (a) instrumentation zone; (b) reaction chamber; (c) actuator (3 µm precision); (d) load cell (10^{-5} N precision); (e) frame for zoom; (f) compression rod; (g) sample; (h) sample holder; (i) electric heater; (j) liquid water. Zoom in the device (right): 1 - fin set (4 on each zone - cold/hot); 2 - fins and sample holder support rods; 3 - controlled leakage (3 symmetric outlets); 4 - compression rod.

An experimental test consists the following protocol:

1. Positioning the sample in the sample holder, closing the bottom chamber, opening the air leakage and launching the software for shrinkage determination;
2. Heating from room temperature at a rate of about 8 °C/min by two electric heating collars (370 W) placed at the outer surface of the chamber;
3. Maintaining the treatment temperature for the desired time;
4. Cooling to room temperature by two external fans at around 9 °C/min;
5. Plateau at room temperature for 90 minutes (optional).

This sequence can be repeated, allowing several plateaus to be performed one after the other. The temperature was measured by a K-thermocouple near the sample and controlled by a PID system (EUROTHERM 3216). At the bottom of the reactor, nearby the sample holder, 100 mL of distilled water ensured a vapor saturated atmosphere and, thus, a good heat transfer inside the chamber while avoiding drying. Treatments were performed at 160 and 180 °C. For this study, no acid was added to the water used to soak the samples before the test.

2.2. Chemical analysis

2.2.1. Sampling used for the whole chain of chemical analyses

Offline chemical analyses were performed to assess the biomass alteration due to the hydrothermal pretreatment. The flow chart of analysis is depicted in Figure 76. Unless otherwise specified, chemical analysis followed National Renewable Energy Laboratory's (NREL) analytical procedures [164,165,215]. The total process requires 5 g of biomass.

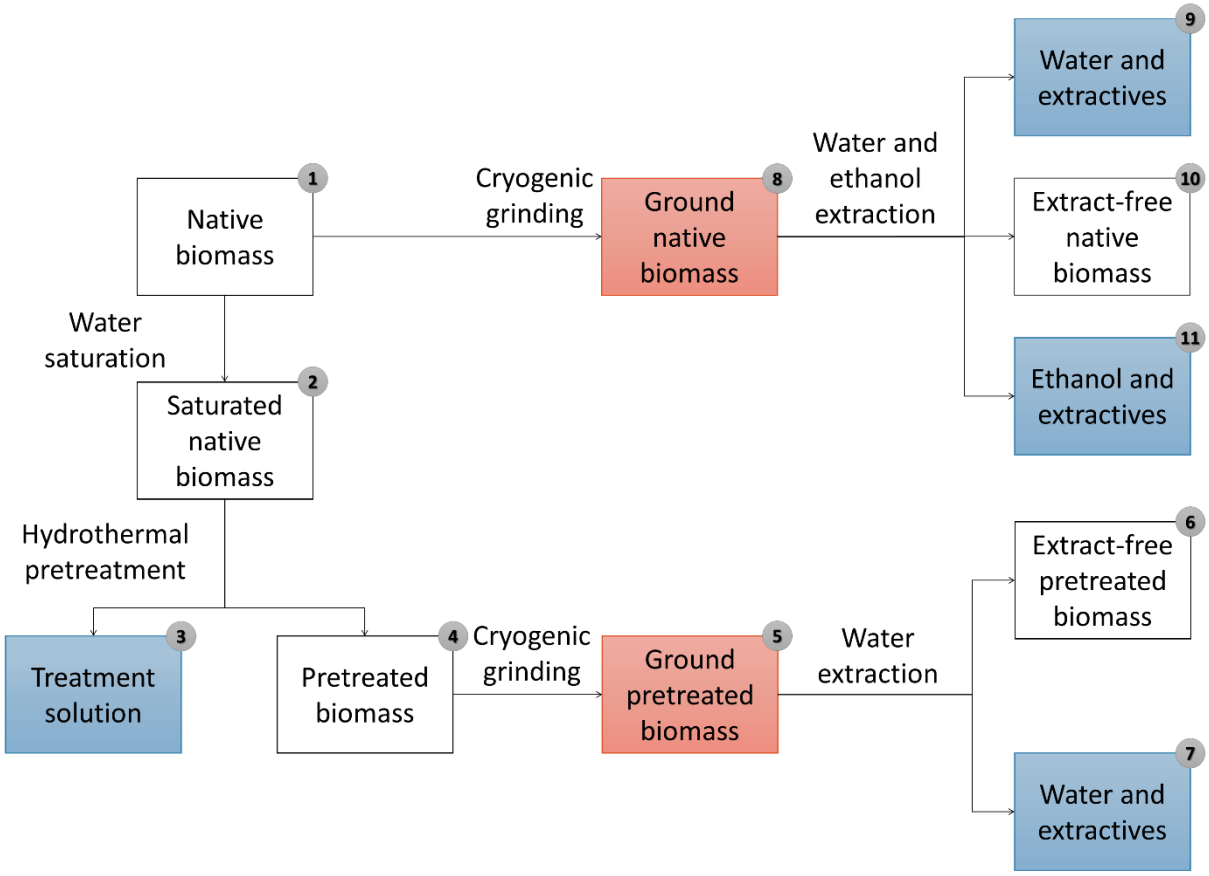

Figure 76. Flow chart of analysis. Fractions in blue were analyzed for monosaccharides, oligosaccharides, organic acids and degradation products; and fractions in red were analyzed for isotherm sorption

As shown in Figure 76, two fractions originate from hydrothermal pretreatment: the pretreated biomass (solid fraction) and the treatment solution (liquid fraction). Native and pretreated biomasses (fractions n°1 and 4) were ground prior to chemical analysis. This grinding was performed with a cryogenic ball mill (RETSCH CryoMill filled with liquid nitrogen) to avoid any

heat releases and thus any additional chemical degradation due to the heat released during grinding. Then, an aliquot of native and pretreated biomass (fractions in red in Figure 76) was analyzed for isotherm sorption. The remaining part went through extraction processes. The extractives as well as the hydrothermal process liquid (fractions in blue in Figure 76) were quantified for monosaccharides, oligosaccharides, organic acids, degradation products and pH. Extract-free native biomass (fraction n°10) had its content of structural carbohydrates and lignin determined according to the standard NREL protocol [215].

Four treatment durations were soundly chosen to determine the chemical modifications for each treatment temperature: 0, 10, 20 and 40 minutes. The treatment efficiency was evaluated by dosing the liquid fraction, which might contain hydrolyzed and partially degraded components of biomass.

2.2.2. Water and ethanol extractions

Native biomass was submitted to Soxhlet water and ethanol extractions according to NREL's protocol. For the pretreated biomass, however, an adaptation of the NREL method was made. Indeed, in this experimental set-up, biomass is not directly in contact with the hydrothermal process liquid. As a result, the liquid fraction present in the sample (n°4 in Figure 76) – attached to its surface or in the liquid phase of internal pores – may have significative quantities of hydrolyzed components (n°3 in Figure 76) and, thus, must not be neglected. Therefore, instead of just washing the treated biomass, as proposed by NREL method, a supplementary extraction step was performed and taken into account in the final result. To prevent any additional thermal degradation of chemical compounds, a three-step cold extraction was chosen. Distilled water was put in contact with an aliquot of the solid sample in a 20:1 (m/m) ratio. The mixture was submitted to an ultrasound bath for five minutes and then separated with a centrifuge. The supernatant was collected and the pellet was submitted to two additional extractions following the same protocol.

2.2.3. Chemical quantification

Monosaccharides and organic acids

Fractions presented in blue in Figure 76 were analyzed for monosaccharides and organic acids. Quantification was carried out on an Ultima 3000 HPLC (THERMO FISHER SCIENTIFIC) coupled with a Refractive Index Detector RI-101 (SHODEX). Separation was achieved on an Aminex HPX-87H column (300 x 7.8 mm) from Biorad at a temperature of 30 °C. A mobile phase of 2 mM of sulfuric acid (VWR) at a flow rate of 0.5 mL/min was used in isocratic mode and the injection volume was 10 µL. Total run analysis was 30 minutes. Components were identified by comparison of their retention time with standard solutions of glucose (ACROS ORGANICS), xylose (SIGMA-ALDRICH), arabinose (ACROS ORGANICS) and acetic acid (FISHER CHEMICAL). Quantification was achieved using the area of the peak in external calibration, the range of concentration was from 0.2 to 10 g/L.

Degradation products

In the same fractions, quantification of furfural and 5-(hydroxymethyl)furfural (HMF) were carried out on an Ultima 3000 HPLC (THERMO FISHER SCIENTIFIC) coupled with an UV Detector. Separation was achieved on an Acclaim Polar Advantage II C_{18} column (4.6 x 150 mm, 3 µm, 120 Å) from THERMO FISHER SCIENTIFIC. Column temperature was maintained at 30 °C. The mobile phase was a mixture of two solvents. Solvent A: Milli-Q water; and solvent B: Acetonitrile (SIGMA-ALDRICH) at a flow rate of 0.3 mL/min. Elution was achieved in gradient mode with an initial composition of 80 % of A and 20 % of B, held for 5 minutes. Proportion of B was then gradually increased to 99 % in 10 minutes and held at 99 % for 5 minutes, followed by going back to initial composition and stabilization of the column for 10 more minutes, summing a total run analysis of 30 minutes. Injection volume was 5 µL. Degradation products were identified by comparison of their retention time and of their UV spectra with standard solutions of HMF (SIGMA-ALDRICH) and furfural (SIGMA-ALDRICH). UV spectra were recorded from 200 to 380 nm, absorbance was recorded at 277.8, 285.5, quantification of HMF and furfural was done at 277.8 and 285.5 nm respectively, which corresponds to their maximum of absorption. Quantification was achieved using the area of the peaks in external calibration, the range of concentrations was from 0.1 to 30 mg/L.

Oligosaccharides

Oligosaccharides concentrations were determined in the liquid fractions represented in blue in the flow chart (Figure 76) from the difference of monomeric sugars concentrations measured before and after an analytical hydrolysis step [164]. To do so, we added 72 % H_2SO_4 to obtain an acid concentration of 4 %. The solution is then autoclaved at 121 °C for 1 hour.

2.2.4. Sorption measurements

Ground native and treated biomass (fractions represented in red in Figure 76) were analyzed. Sorption measurements were performed in a DVS device (SURFACE MEASUREMENT SYSTEMS, Intrinsic), equipped with an ultra-sensitive micro-balance (precision of 0.1 µg). Approximately 20 mg of ground biomass were put in the sample pan. A constant flow of nitrogen is mixed to water vapor to ensure the desired RH (accuracy of 0.5 %) at a constant temperature of 25 °C (accuracy of 0.1 °C). Sorption cycles started with a 0 % RH plateau, at the end of which dry mass was determined. Adsorption/desorption cycles of RH ranged from 0-90-0 % (with steps of 10 %). Samples were kept at a constant RH level until the mass change per minute (dm/dt) reached 0.002 %, as recommended in literature [216].

2.3. Material and sampling

The biomass used in this study comes from a 25-year poplar tree (*Populus euro-americana* 'Koster') that grew in a forest located in Auménancourt-le-Petit (Marne, North-East of France). It was chopped and cut in boards that were subsequently dried and stored before sample preparation.

The sample size was chosen to fulfil the protocols constraints (amount of biomass required for chemical tests, sample size for shrinkage determination). These constraints impose sample sizes of 8^3 mm^3 (radial - R, tangential - T, longitudinal - L) for deformation tests and 40 x 8 x 8 mm^3 (R x T x L) for chemical tests. The longitudinal direction was purposely chosen as the smallest dimension (8 mm) to ease mass transfer and thus ensure a good homogeneity of the hydrothermal treatment throughout the sample. Samples were obtained from a single defect-free board with a straight grain angle. Moreover, they were carefully cut along the longitudinal direction, along which the natural variability of wood is the lowest (Figure 77).

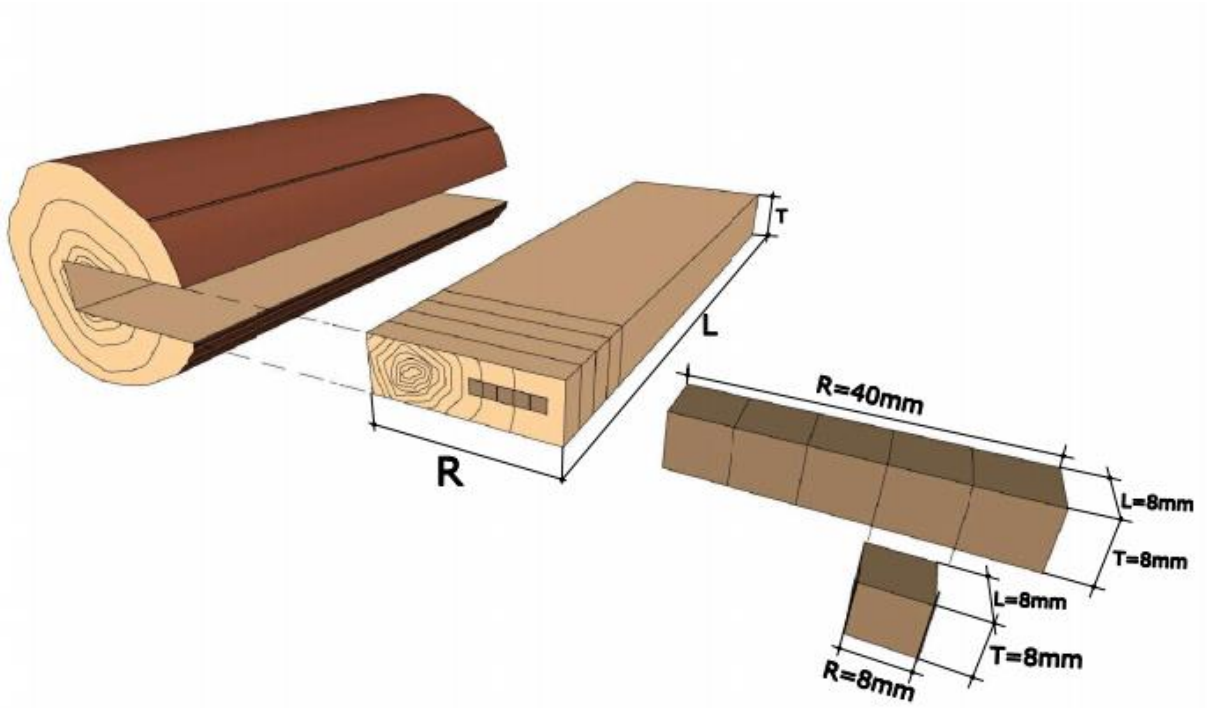

Figure 77. Schematic representation of the sampling process

2.3.1. Sample preparation before tests

The initial moisture content of the samples is required for calculating the anhydrous mass of wood, absolutely required to determine the mass loss due to the chemical degradation. The chemical analysis being incompatible with oven drying, the moisture content was determined from the mass of paired samples, before and after drying at 105 °C until reaching a stable mass. The initial moisture content was assumed similar in all samples as they had been stored together for a long period and as their mass was measured on the same day, one after the other.

Before hydrothermal pretreatment, the samples were saturated with water for three main reasons: (*i*) to reproduce the industrial process, where water vaporization during the explosion step is a crucial phenomenon; (*ii*) to ensure a good heat transfer; (*iii*) to avoid hydric swelling at the beginning of the test, that would disturb the shrinkage measurements. To do that, samples were immersed in distilled water and subjected to vacuum cycles until saturation. They remained

fully saturated throughout the pretreatment due to water condensation at their surface during the heating-up phase at the beginning of the test.

3. Results and discussion

3.1. Preliminary tests: hygrothermal recovery of cell wall's internal stress and change of fiber saturation point

Figure 78 depicts preliminary results obtained for deformation tests performed at 100 °C with poplar in radial and tangential directions. In both cases, two consecutive temperature plateaus were performed according to the protocol previously described (with plateaus of 90 minutes at room temperature between each one). Results in the radial direction of wood (Figure 78a) exhibit a rapid shrinkage increase during the heating-up phase. Then, the shrinkage remains stable during the 100 °C plateau (0.86 % of shrinkage) and decreases as the chamber cools down. However, it does not go back to its original value, with a residual value of ca. 0.21 % of shrinkage once a constant room temperature is reached. When this cycle is repeated, almost the same plateaus are obtained (0.85 % at 100 °C and 0.27 % at room temperature). For the tangential test, a lower shrinkage is observed at 100 °C (0.27 %), followed by a swelling of the sample at room temperature (in comparison with its initial value).

Chemical degradation of wood at this temperature level and for this duration might be considered as negligible [217,218]. Hence, it is likely that two well documented mechanical/hydromechanical phenomena concomitantly take place during these tests: (*i*) the hygrothermal recovery of the delayed strain field due to growth stress [219–222] and (*ii*) the changes in fiber saturation point (FSP) with temperature [87,223]. Indeed, due to the increase of thermal agitation with temperature, a smaller amount of water molecules are tied to the cell wall for a certain level of attraction forces [89,90]. This has the effect of reducing the fiber saturation point [85]. A part of the bound water then becomes free water, resulting in a partial shrinkage [141].

The two consecutive 100 °C plateaus allow us to distinguish the two phenomena, as the reduction fiber saturation point with temperature is supposed to be reversible. In the first plateau, shrinkage is possibly a result of both hygrothermal recovery and reduction of fiber saturation point. During this plateau, the last phenomenon increases the measured shrinkage in radial direction and partially masks the swelling phenomena due to growth stress release in tangential direction. At the end of the first plateau, fiber saturation point returns to its initial value (room temperature), but the growth stress release is irreversible. Thus, the sample does not return to its initial size.

These preliminary tests pointed out the importance of subjecting samples to a first plateau at 100 °C for 1 hour, followed by a plateau at room temperature, before the hydrothermal treatment. It is likely to cause a complete hygrothermal recovery. It allows the change of sample size during hydrothermal pretreatment to be strictly related to the cell wall alterations.

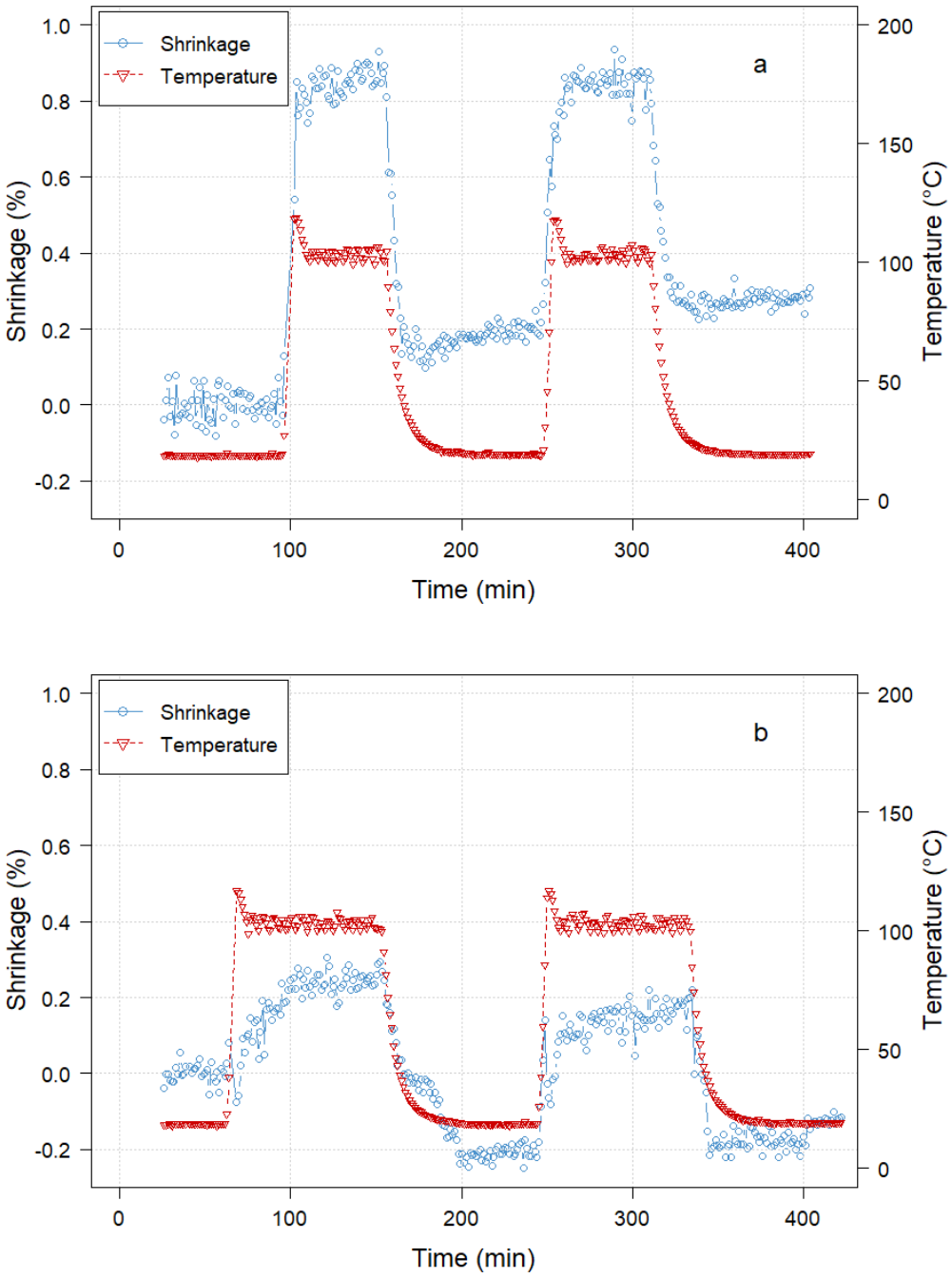

Figure 78. Preliminary shrinkage tests in radial (a) and tangential (b) directions

3.2. Shrinkage kinetics

Typical raw data of shrinkage tests at 160 and 180 °C for radial and tangential directions are presented in Figure 79 and shrinkage results at certain periods of the test are summarized in Table 8. At least two repetitions were performed for each condition and similar results were obtained. The shrinkage (S) is calculated using the formula:

$$S\,(\%) = \frac{(L_0 - L_t)}{L_0} \,.\, 100 \qquad (14)$$

Where L_0 is the averaged sample dimension during the first plateau and L_t its dimension at time t.

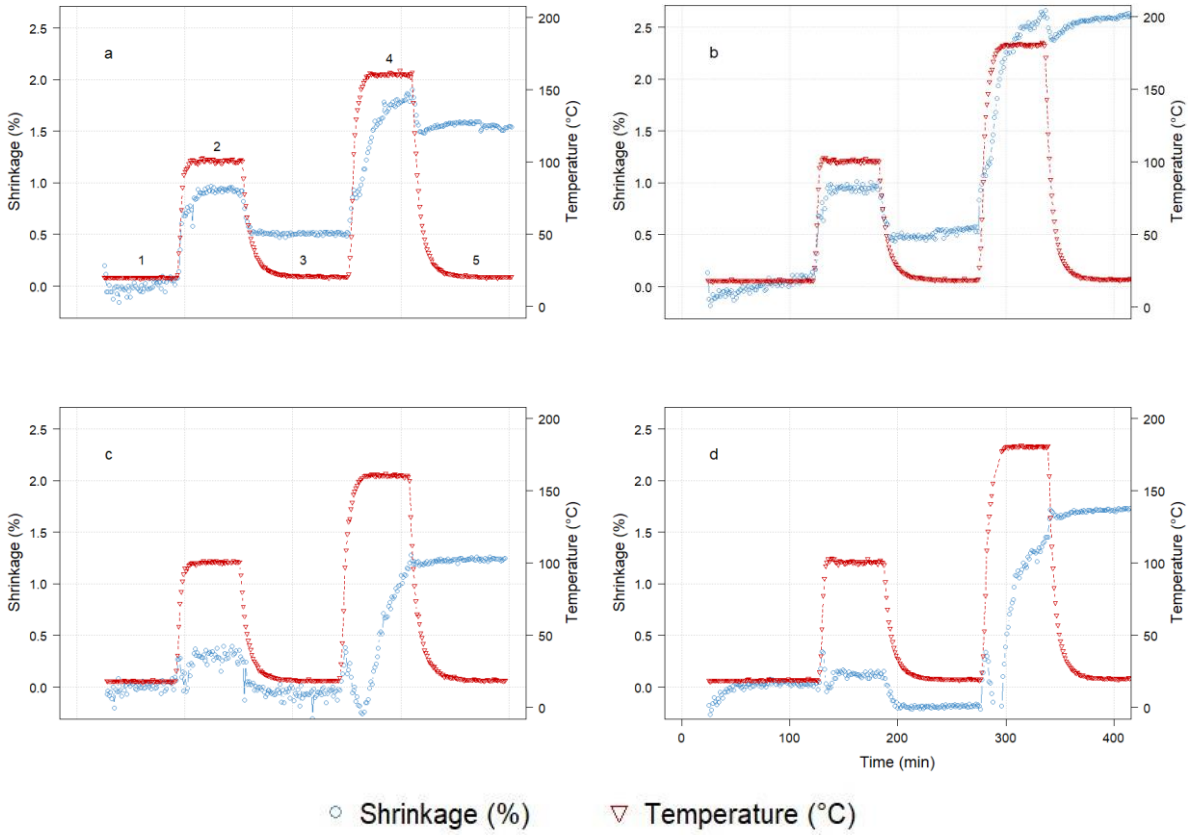

Figure 79. Typical shrinkage evolution for tests performed in radial (a, b) and tangential (c, d) directions (raw, uncorrected data) at 160 °C (a, c) and 180 °C (b, d). Plateaus 1, 3 and 5: room temperature; plateau 2: 100 °C, plateau 4: treatment temperature.

As previously stated, the first plateau at 100 °C (2) causes an initial shrinkage for all tested conditions, which reaches a stable value rapidly once the temperature is stabilized. For the radial tests, around 0.9 % of shrinkage is observed at this point, while no more than 0.3 % is observed for the tangential tests. At the end of the plateau 2 (1 hour at 100 °C), growth stresses are considered to be completely released [221,222,224]. The subsequent cooling phase (3) causes a shrinkage decrease of around 0.5 % in the radial direction but a swelling (-0.06 % and -0.19 %) in the tangential direction. However, whichever the direction, the sample swells when it is cooled down to the ambient temperature in comparison with the previous plateau. This is explained by the effect of temperature on FSP, hence on the sample dimension. Our protocol allows the two previously mentioned phenomena, relaxation of growth stresses and change of FSP, to be distinguished and quantified. The reversible and temperature dependent contribution of FSP can be estimated from the change of sample dimensions between the plateau at 100 °C (plateau n°2) and the plateau after cooling (plateau n°3). This represents 0.5 % in the radial direction and

around 0.3 % in the tangential direction. The irreversible deformation caused by hygrothermal recovery is the difference between plateaus 1 and 3 (the two plateaus at room temperature), a shrinkage in the radial direction and a swelling in the tangential direction. These contrasted behaviors are due to the anisotropic growth stress field in trees, which is in agreement with previous works [219,225].

Table 8. Shrinkage (%) measured in radial and tangential directions at various steps of tests performed at 160 and 180 °C : (1) mean value during plateau n°1 (room temperature); (2) mean value during plateau n°2 (100 °C); (3) mean value during plateau n°3 (room temperature); (4) maximum total shrinkage obtained during hydrothermal pretreatment; (4) mean value during the last plateau (room temperature).

Direction	Condition	1	2	3	4	5
Radial	160 °C	0.00 ± 0.06	0.90 ± 0.07	0.51 ± 0.01	1.91	1.56 ± 0.03
	180 °C	0.00 ± 0.07	0.93 ± 0.07	0.53 ± 0.03	2.51	2.45 ± 0.02
Tangential	160 °C	0.00 ± 0.05	0.30 ±0.06	-0.06 ± 0.06	1.17	1.24 ± 0.02
	180 °C	0.00 ± 0.07	0.12 ± 0.02	-0.19 ± 0.01	1.31	1.56 ± 0.02

During the plateau at the test temperature (n°4) the shrinkage increased with time, both for the tangential and radial tests. As a consequence of the higher thermal activation, the shrinkage curve is higher for the test at 180 °C. Considering the treatment conditions applied, the observed shrinkage is likely a combined effect of the change of fiber saturation point and degradation of wood cell wall. This is particularly evident in the radial test at 160 °C. At the end of hydrothermal pretreatment (4), the reversible component of shrinkage is cancelled, so the difference between plateau 3 and plateau 5 represents the shrinkage due to degradation. In the case of radial direction at 180 °C, the swelling observed during the last cooling is smaller. As a result, reversible shrinkage has a smaller contribution to the total shrinkage. Note also that during the last plateau at room temperature, the shrinkage continues to increase: we explain this phenomenon by a slight drying of the sample due to the temperature gradient inside the chamber: the cooling occurs through the chamber walls, cooler than the sample in this transient phase, likely to induce a condensation from the sample to the chamber walls.

The trends observed for tangential samples are quite different. In particular, a swelling is observed during the first cooling (phase 3) and shrinkage increased during the last cooling phase, namely after the plateau at 180 °C. This is probably a combination of growth stress relaxation (larger in tangential direction) for the first observation and due to a slight drying at the end of the test, together with the loss of cell wall rigidity, an effect of collapse for the second observation. The tangential direction of wood is indeed known to be prone to collapse [226,227].

As our purpose is to use shrinkage as continuous indicator of the effect of hydrothermal treatment, the raw data must be corrected to obtain the irreversible part only. The following procedure was applied:

- A blank test was performed with the same protocol, but without sample. This test allows therefore to correct the measurement for the non-uniform temperature level of the device (sample holder and rod to test the contact) during transient states,
- The differential of thermal dilatation of the stainless steel due to the sample length was computed using the actual temperature,
- The shrinkage due to the effect of temperature on FSP was corrected using the swelling measured during the first cooling (from phase 2 to phase 3) and assuming this effect to be linear with the temperature.

In this procedure, the sample dimension during phase 3 (after the first cooling) was considered as the initial length appearing in Equation (14). Figure 80 depicts the irreversible part of the shrinkage obtained according to this correction procedure for radial tests. After the correction procedure, the radial tests depicted a nice evolution during the treatment plateau (Figure 80), while the tests in the tangential direction present a strange behavior. This result is not consistent with the trends obtained for the dimensional changes of biomass during pyrolysis [143]. The combination of collapse, together with a growth stress strain which is maybe not completely relaxed at 100 °C could explain this strange behavior. The accuracy of the results in tangential direction is thus questionable. Therefore, for the analysis of the shrinkage evolution, we will only focus on the radial tests.

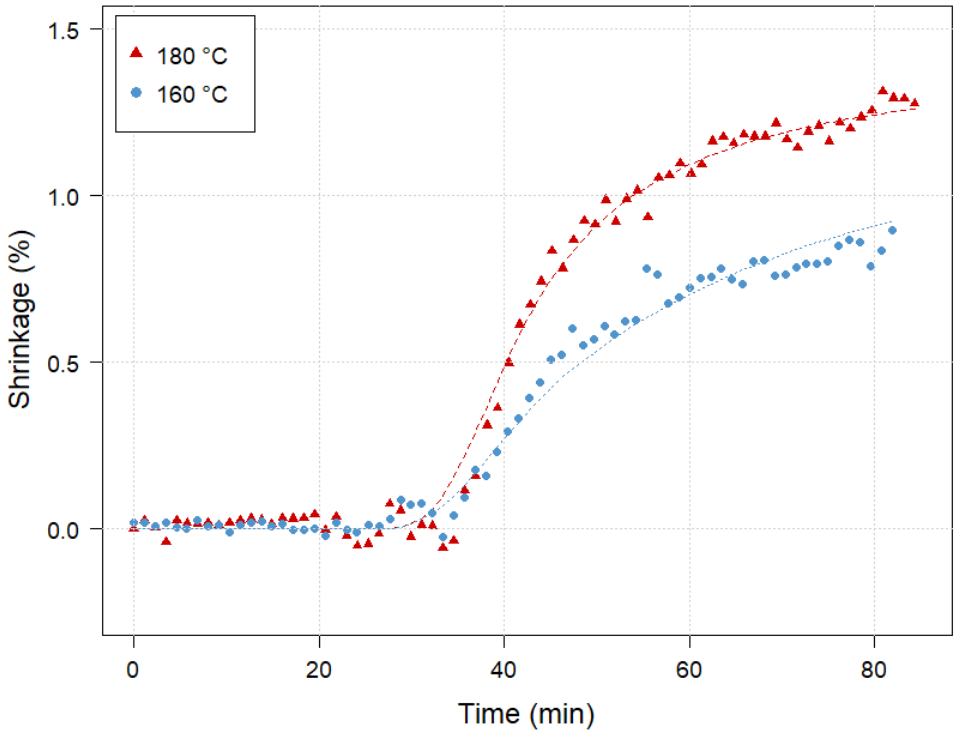

Figure 80. Radial shrinkage (%) of biomass samples subjected to hydrothermal pretreatment: experimental points and the corresponding DAEM model. These results reflect exclusively the irreversible component due to chemical degradation.

It is well known that hemicellulose is the first lignocellulosic component to be degraded during hydrothermal treatment [115]. Some lignin degradation could also occur and partly explain the dimensional changes of poplar since hardwood lignins are rich in syringyl units, the most susceptible to hydrothermal degradation [115]. In addition to hydrolysis, a rearrangement in the lignocellulosic matrix organization can also be at the origin of shrinkage. Previous works [135] have indeed showed that, once the lignin reaches its glass transition temperature, it becomes fluid and coalesces, being later forced out of the matrix by the collapse of microfibrils. Chemical changes leading to shrinkage are more deeply discussed in the next sections.

Due to this complex inherent structure and chemical nature, lignocellulosic biomass decomposes at different rates, through different mechanisms and pathways. It is thus impossible to describe the entire process with a single reaction. In order to face such complex situation, the DAEM model has been largely used to model the thermal degradation of materials, especially for the pyrolysis of lignocellulosic biomass [228,229]. We will then use such an approach to model the shrinkage kinetics. To the best of our knowledge, such a model has never been used for the hydrothermal pretreatment of biomass.

The model assumes that the decomposition mechanisms follow multiple parallel first-order reactions with different activation energies, represented by a continuous distribution function [230]. Each independent and irreversible reaction *i* contributes to the hydrolyzed mass fraction according to Equation (15).

$$\frac{d\left(\frac{V_i}{V_i^{\infty}}\right)}{dt} = k_i\left(\frac{V_i^{\infty} - V_i}{V_i^{\infty}}\right) = A\exp\left(-\frac{E_i}{RT(t)}\right)\left(\frac{V_i^{\infty} - V_i}{V_i^{\infty}}\right) \quad (15)$$

Where V_i is the hydrolyzed mass fraction of the reaction *i*, V_i^{∞} the total mass fraction that can be hydrolyzed, A the pre-exponential factor (assumed constant for all reactions), E_i the activation energy, *R* the universal gas constant, *T* the temperature and *t* the time.

Considering the complexity of the reactions involved in the degradation of lignocellulosic biomass, a continuous distribution of activation energies is assumed, representing the fraction released by reactions with an activation energy inferior to *E*. The derivative of this function with respect to the activation energy ($f(E)$) gives a distribution function of the product fraction concerned by each activation energy:

$$dV^{\infty} = V^{\infty} f(E)dE \quad (16)$$

From Equations (15) and (16):

$$\alpha = \frac{V}{V^{\infty}} = 1 - \int_0^{\infty} \exp\left[-\int_{t_0}^{t} A\exp\left(-\frac{E}{RT}\right)dt\right] f(E)dE \quad (17)$$

Where α is the degree of conversion, ranging between 0 and 1.

Without additional information, a Gaussian, hence symmetrical, distribution is often chosen as distribution function [230]. It involves two parameters, the mean activation energy E_0 and the standard deviation of the energy distribution σ:

$$f(E) = \frac{1}{\sigma\sqrt{2\pi}} \exp\left[-\frac{(E - E_0)^2}{2\sigma^2}\right] \quad (18)$$

For modelling purposes, this distribution was discretized into a finite set of N parallel reactions.

Finally, the shrinkage (S) is assumed to linearly depend on the extent of conversion α by a coefficient β.

$$S\ (\%) = \beta \cdot \alpha \quad (19)$$

The parameters of the DAEM model were identified using the two tests simultaneously (160 °C and 180 °C) for the radial test. The identified parameters are summarized in Table 9 and the model is plotted in Figure 80.

Table 9. Set of identified parameters for radial direction.

	A (min^{-1})	**E_0 (J/mol)**	**σ (J/mol)**	**β**
Radial	1.20×10^{18}	2.66×10^{5}	6.15×10^{3}	1.392

Values of activation energy of the same order of magnitude were found for eucalyptus during hydrothermal pretreatment [211]. Previous works have applied DAEM to the pyrolysis of each main component of lignocellulosic biomass separately [230]. They found that standard deviation (σ) increases with the increasing of the heterogeneity of the component, being higher for lignin, followed by hemicellulose and finally cellulose (divided by a factor of 10 each time). The standard deviation found in this study is between the ones attributed to lignin and hemicellulose in other studies. Given the high heterogeneity of these components, they should be responsible for the wide activation energy distribution found.

A deeper analysis on chemical degradation of biomass during hydrothermal pretreatment is important to understand the mechanisms leading to shrinkage and is presented in the next sections. We just have to keep in mind that in the following sections, a continuous measurement is not possible anymore. All analyses are therefore performed at certain treatment durations.

3.3. Mass loss

Mass loss (ML) is widely used as a macroscopic indicator of biomass degradation and of the treatment intensity [231,232]. Figure 81 presents the average ML for the two treatment temperatures (160 °C and 180 °C).

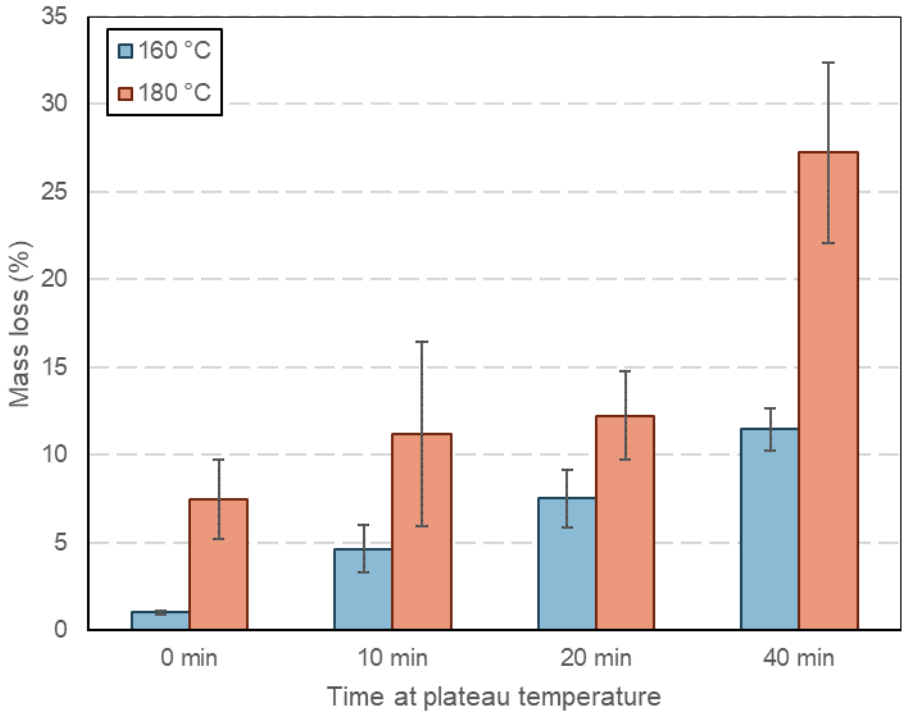

Figure 81. Mass loss (3 repetitions) for different durations of hydrothermal treatment at 160 °C and 180 °C.

As expected, ML increases with the treatment temperatures and treatment duration. At 40 minutes of treatment at 180 °C, ML is twice as high as at 20 minutes, reaching 27.3 %. Whereas after the same time (40 minutes) at 160 °C, only 11.5 % of ML is observed. It is important to notice that, as the heating-up phase takes a few minutes, the equivalent cooking time at the beginning of the plateau is around 10 minutes. That is the reason why a biomass degradation is already observed at 0 minutes (1.02 % and 7.49 % respectively for the tests at 160 °C and 180 °C).

These results are consistent with deformation measurements and suggest that more severe treatments cause a higher biomass degradation. They also agree with previous studies. For example, a mass loss of 30.2 % was found for *Eucalyptus globulus* biomass subjected to a hydrothermal treatment at 180 °C for 45 minutes [211]. Assor et al. [33] reported infradensity losses in oak and spruce subjected to hydrothermal treatment equivalent to the mass loss experienced by the samples and attributed those losses to the hydrolysis and the dissolution of cell wall polymers.

3.4. Sorption isotherms

The alteration of the cell wall was also assessed by the change of sorption isotherms compared to the native biomass (Figure 82).

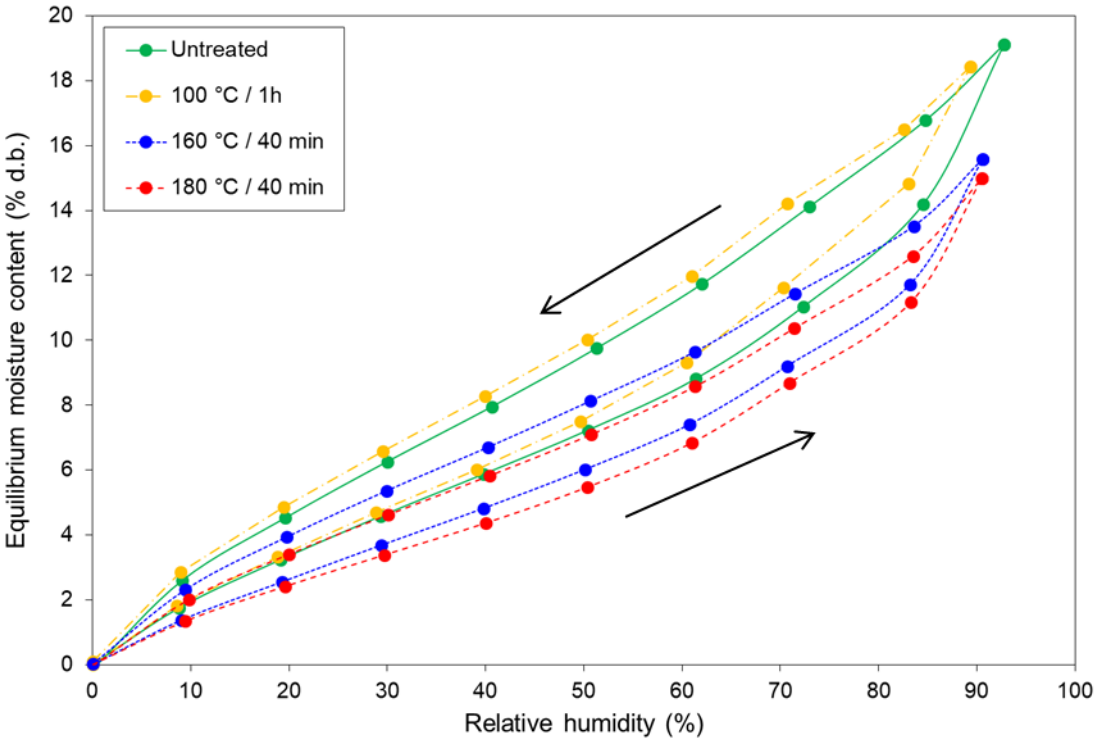

Figure 82. Experimental sorption and desorption curves (2 repetitions) at 25 °C for native and pretreated poplar biomass

A clear impact of the hydrothermal pretreatment on biomass hygroscopicity can be observed by the decrease of the equilibrium moisture content (EMC) – whatever the RH, during adsorption or desorption – with the increasing of treatment severity. At 50 % of RH during adsorption, the difference between native biomass and the treatment at 180 °C for 40 minutes is of 1.76 %. This value represents a relative decrease of the EMC by 24.3 %. These facts have already been reported in literature for both hydrothermally treated wood [142] and torrefied wood [141,233], and were attributed to the reduction of accessible hydroxyl groups [85,233]. In the case of hydrothermal pretreatment, this reduction can be explained by a loss of the functional hydroxyl group itself, of acetyl groups or of entire osidic monomers. It is consistent with shrinkage results presented in Figure 79. In the case of radial direction at 180 °C, the swelling observed during the last cooling (between plateaus 4 and 5) is smaller than the previous cooling (between plateaus 2 and 3). This fact could also be attributed to a higher degradation of OH groups, reducing the ability of biomass to bind water and, thus, reducing fiber saturation point [141] and its temperature dependency. Moreover, it is well illustrated by the increasing concentration of acetic acid in the liquid fraction (Figure 83b) and the loss of C5 units (Figure 84a-b), presented in the next sections. In either way, this gives an additional correlation between mass loss and alteration of cell wall properties. Thus, the decrease in bound water between microfibrils – that forces them apart, hence increases the cell wall volume [85] – may cause the shrinkage observed during the hydrothermal treatment.

Biomass submitted to 100 °C for 1 hour, however, has a very similar behavior to native biomass. This confirms that, for these conditions, biomass only suffered minor or no changes, since hydroxyl groups would be the first ones affected by the treatment. This observation validates the

method used for the hygrothermal recovery of growth stress, which assumed this absence of irreversible chemical effects after the plateau at 100 °C.

3.5. Chemical degradation

Mass loss only does not show how selective is the hydrothermal degradation, neither if the temperature level allows different kinds of reactions to be activated. The chemical characterization of the hydrolysates is therefore of great interest. Figure 83 presents the pH and the mass of acetic acid of the liquid fraction (sum of fractions n°3 and 7 in Figure 76) released during treatment.

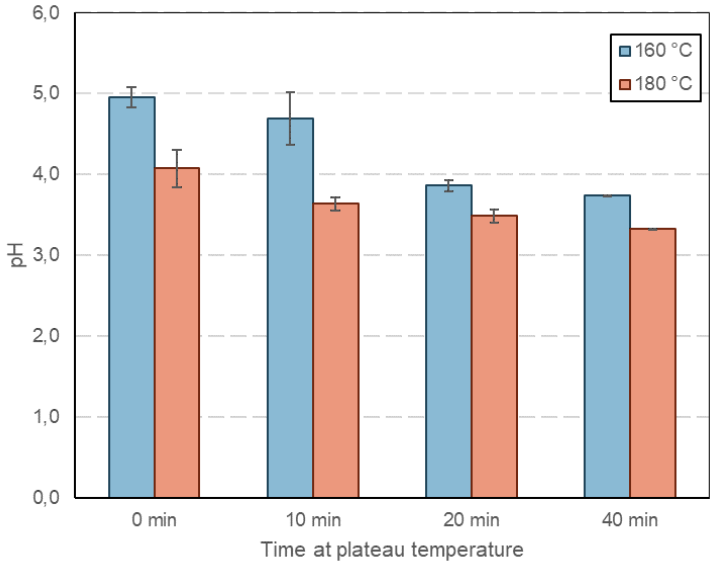

(a)

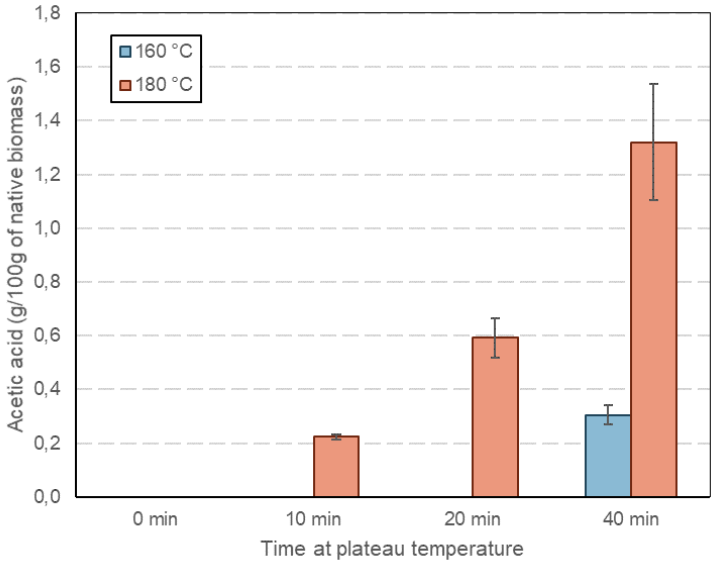

(b)

Figure 83. Effect of time at 160 °C and 180 °C on the pH (a) and acetic acid content (b) of the liquid fraction (3 repetitions)

In this work, only distilled water was used as hydrothermal process liquid. Nevertheless, it is possible to observe a decrease in pH during the treatment, from 4.96 and 4.08 at the beginning of treatment plateau (0 minute) to 3.74 and 3.33 after 40 minutes, for temperatures of 160 and 180 °C respectively. This decrease is mostly explained by the formation of acetic acid, up to 0.31 and 1.32 grams of acetic acid per gram of native biomass (for 160 °C and 180 °C, respectively) are formed and released in the liquid fraction. This is due to the hydrolysis of hemicellulose O-acetyl branching groups in the presence of hydronium ions from water autoionization. Acetic acid acts then as an autocatalysis agent itself, promoting hydrolysis [115]. Thus, the deacetylation represents an important fraction of the mass loss. For mild treatment conditions this phenomenon is mainly visualized by a decrease in pH rather than an increase in the acetic acid concentration, because its values probably range under the detection limit of the HPLC-RI method applied (0.2 g/L).

Figure 84 presents the effect of time and temperature on the composition of the liquid fraction. Fractions n°3 and 7 (Figure 76) are merged in terms of C5 and C6 sugars and their respective degradation products – furfural and HMF.

Results from chemical quantification as well as the degree of conversion (α) calculated with DAEM model for each temperature and plateau duration tested are summarized in Table 10.

These results allow an overview of the hydrolysis reactions taking place during hydrothermal pretreatment. Oligosaccharide quantity is the result of a balance involving their production by polysaccharides degradation and their consumption by hydrolysis into monosaccharides. For milder treatments, their production is greater than their consumption, which results in an increasing content of C5 and C6 oligosaccharides. For a treatment temperature of 160 °C, oligosaccharides represent from 2.5 % (0 minutes) to 30.9 % (40 minutes) of the C5 polysaccharides initially present (m/m) in native biomass and from 0.2 % (0 minutes) to 0.5 % (40 minutes) in the case of C6 sugars. At 180 °C these values range from 8.1 %, at the beginning of treatment plateau, up to a maximum of 51.5 % after 20 minutes for C5 sugars and from 0.3 % to around 0.9 % for C6 sugars. Between 20 and 40 minutes at 180 °C, however, the oligosaccharide content decreases. In this case, it is probably the consumption reaction that prevails, which is a consequence of the reduction in the solid matrix available for hydrolysis (illustrated by mass loss). Likewise, the monosaccharide content is a compromise between its production by hydrolysis and its degradation into smaller products such as furfural (for C5 sugars) and HMF (for C6 sugars). Unlike oligosaccharides, however, monosaccharides content increases steadily. It shows that, for the studied conditions, monosaccharide production is still higher than its degradation.

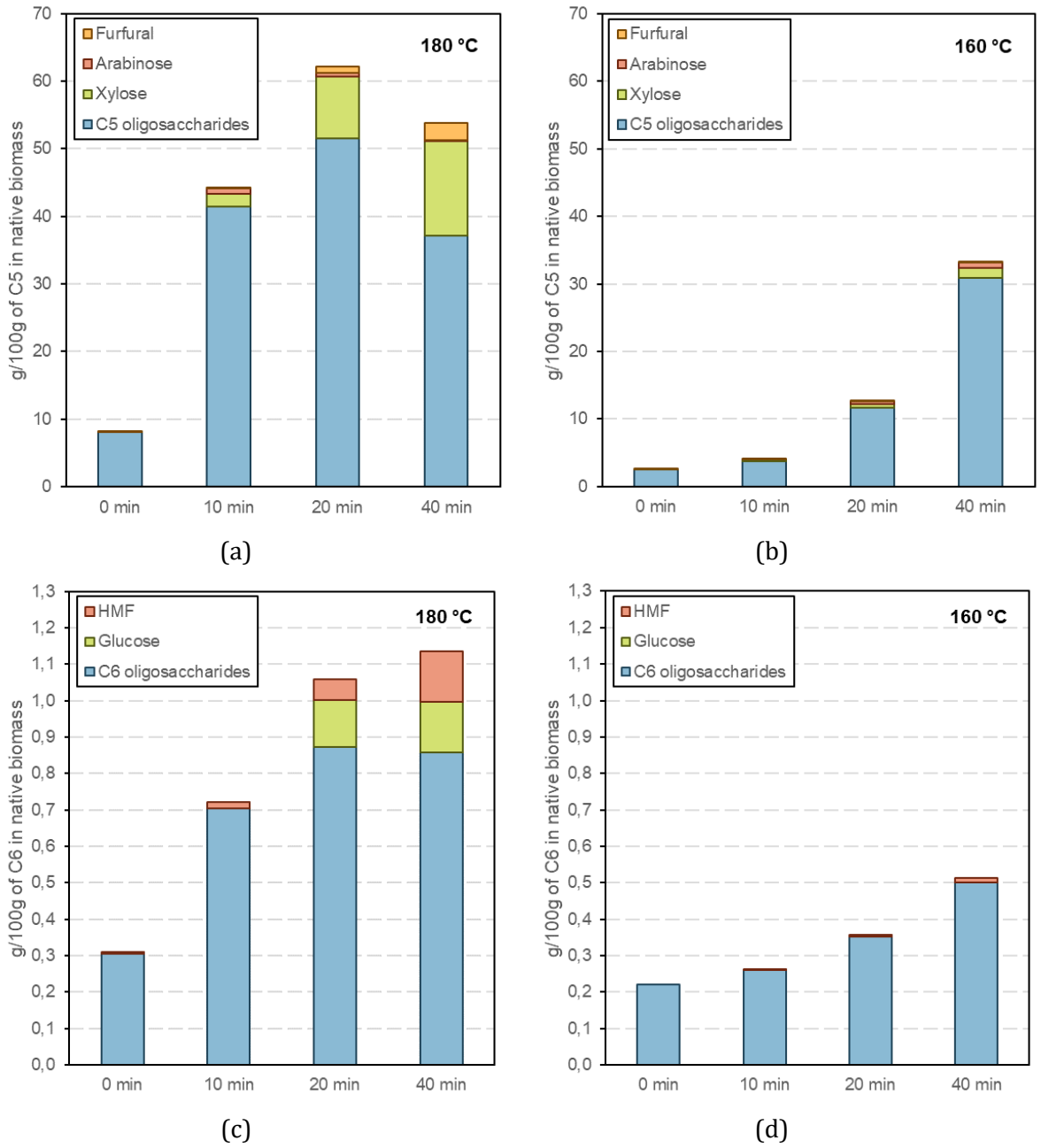

Figure 84. Effect of time at 160 °C (a) and 180 °C (b) on the composition of the liquid fraction in terms of C5 sugars and their respective degradation products. Effect of time at 160 °C (c) and 180 °C (d) on the composition of the liquid fraction in terms of C6 sugars and their respective degradation products.

Table 10. Experimental results of chemical quantification and calculated conversion degree for several hydrothermal pretreatment conditions (time and temperature)

	160 °C				180 °C			
Plateau duration (min)	0	10	20	40	0	10	20	40
α	0.237	0.411	0.524	0.663	0.514	0.722	0.820	0.906
ML *(%)*	1.0 *±0.1*	4.6 *±1.4*	7.5 *±1.7*	11.5 *±1.2*	7.5 *±2.3*	11.2 *±5.3*	12.2 *±2.5*	27.2 *±5.2*
pH	5.0 *±0.12*	4.7 *±0.33*	3.9 *±0.07*	3.7 *±0.01*	4.1 *±0.23*	3.6 *±0.08*	3.5 *±0.08*	3.3 *±0.01*
Acetic acid *(g/100g of native biomass)*	0.00 *±0.00*	0.00 *±0.00*	0.00 *±0.00*	0.31 *±0.04*	0.00 *±0.00*	0.22 *±0.01*	0.59 *±0.07*	1.32 *±0.22*
Xylose *(g/100g of native biomass)*	0.00 *±0.00*	0.06 *±0.00*	0.09 *±0.01*	0.23 *±0.00*	0.00 *±0.00*	0.30 *±0.01*	1.56 *±0.13*	2.34 *±0.05*
Arabinose *(g/100g of native biomass)*	0.00 *±0.00*	0.00 *±0.00*	0.07 *±0.01*	0.13 *±0.02*	0.00 *±0.00*	0.14 *±0.03*	0.08 *±0.00*	0.04 *±0.00*
Glucose *(g/100g of native biomass)*	0.00 *±0.00*	0.00 *±0.00*	0.00 *±0.00*	0.00 *±0.00*	0.00 *±0.00*	0.00 *±0.00*	0.05 *±0.00*	0.06 *±0.00*
Furfural *(g/100g of native biomass)*	0.00 *±0.00*	0.00 *±0.00*	0.00 *±0.00*	0.04 *±0.01*	0.01 *±0.00*	0.04 *±0.00*	0.15 *±0.03*	0.42 *±0.04*
HMF *(mg/100g of native biomass)*	0.0 *±0.0*	0.4 *±0.0*	1.5 *±0.2*	5.2 *±1.1*	2.1 *±1.1*	7.3 *±3.1*	24.0 *±1.4*	56.4 *±0.6*
Total dissolved sugars *(g/100g of native biomass)*	0.5 *±0.11*	0.8 *±0.02*	2.3 *±0.07*	5.8 *±0.31*	1.5 *±0.05*	7.8 *±0.31*	10.9 *±0.53*	9.5 *±0.50*
C5 oligosaccharides *(g/100g of native biomass)*	0.42 *±0.04*	0.63 *±0.00*	1.97 *±0.00*	5.22 *±0.19*	1.36 *±0.00*	7.01 *±0.13*	8.69 *±0.19*	7.48 *±0.05*
C6 oligosaccharides *(g/100g of native biomass)*	0.09 *±0.07*	0.11 *±0.01*	0.14 *±0.06*	0.20 *±0.07*	0.12 *±0.05*	0.29 *±0.16*	0.36 *±0.10*	0.35 *±0.14*

A total hydrolysis up to 62.1 % of C5 polysaccharides is observed after 20 minutes at 180 °C. However, the total amount of recovered C5 sugars (and its degradation products) decreases after 40 minutes at the same temperature. It is probably due to the severity of the treatment, which may cause a further degradation of furfural into other degradation products or the condensation of C5 and/or furfural with lignin forming insoluble products [115]. From this point of view, the

quantity of hydrolysis products measured for more severe conditions may be under-estimated. This trend is not observed for the mildest treatment (160 °C) at the durations studied.

From the data, it can also be seen that C5 sugars are much more hydrolyzed than C6 sugars. While the total amount of C5 (and its degradation products) present in the liquid fraction reaches 62.1 % (180 °C/20 minutes) of the amount initially present in the raw biomass, no more than 1.2 % of C6 are fractionated. These results are not surprising and have already been reported in previous works, who attributed it to the crystallinity of cellulose [115,234] – only composed of C6 – and the lower degree of polymerization [118] of hemicelluloses – mainly composed of C5. These results can be correlated to the shrinkage curbs previously presented, since they both follow the same trend. For the studied treatment durations, shrinkage seems to be mainly tied to a loss of cell wall volume or thickness due to the degradation of hemicellulose polymers into nonstructural components, such as soluble oligosaccharides. This is also consistent with the decrease in hygroscopicity, as the -OH groups available for binding to bound water belong mainly to hemicellulose.

In general terms, the destruction of the polymeric matrix of the cell wall leads to a mass loss, increases cell wall porosity [235] and could link the chemical degradation of the cell wall with the loss of its mechanical properties, resulting in shrinkage.

3.6. The degree of reaction as indicator of chemical changes

The goal of this work was to evaluate the pertinence of using biomass shrinkage as an indicator of its chemical degradation during hydrothermal pretreatment. Therefore, the measured properties of biomass subjected to different treatment temperatures and durations were plotted as a function of the calculated degree of conversion α (Figure 85). The degree of conversion, calculated using the DAEM model with the fitted parameters, allows the degradation arising during the heating phase to be considered. Consistently, the degree of conversion is higher than zero at the beginning of the plateau. By plotting the graphs, it appears that the two temperature levels are located on the same trajectories. The degree of conversion, as calculated by the DEAM model and fitted from the in-situ shrinkage measurement, is therefore a synthetic indicator of chemical alterations. The sole visible deviation is the mass loss, for which values measured after 10 and 20 minutes at 180 °C are smaller than the general trend. However, this result is excellent and encouraged us to adjust simple expressions to relate the physical and chemical measurements to the degree of conversion.

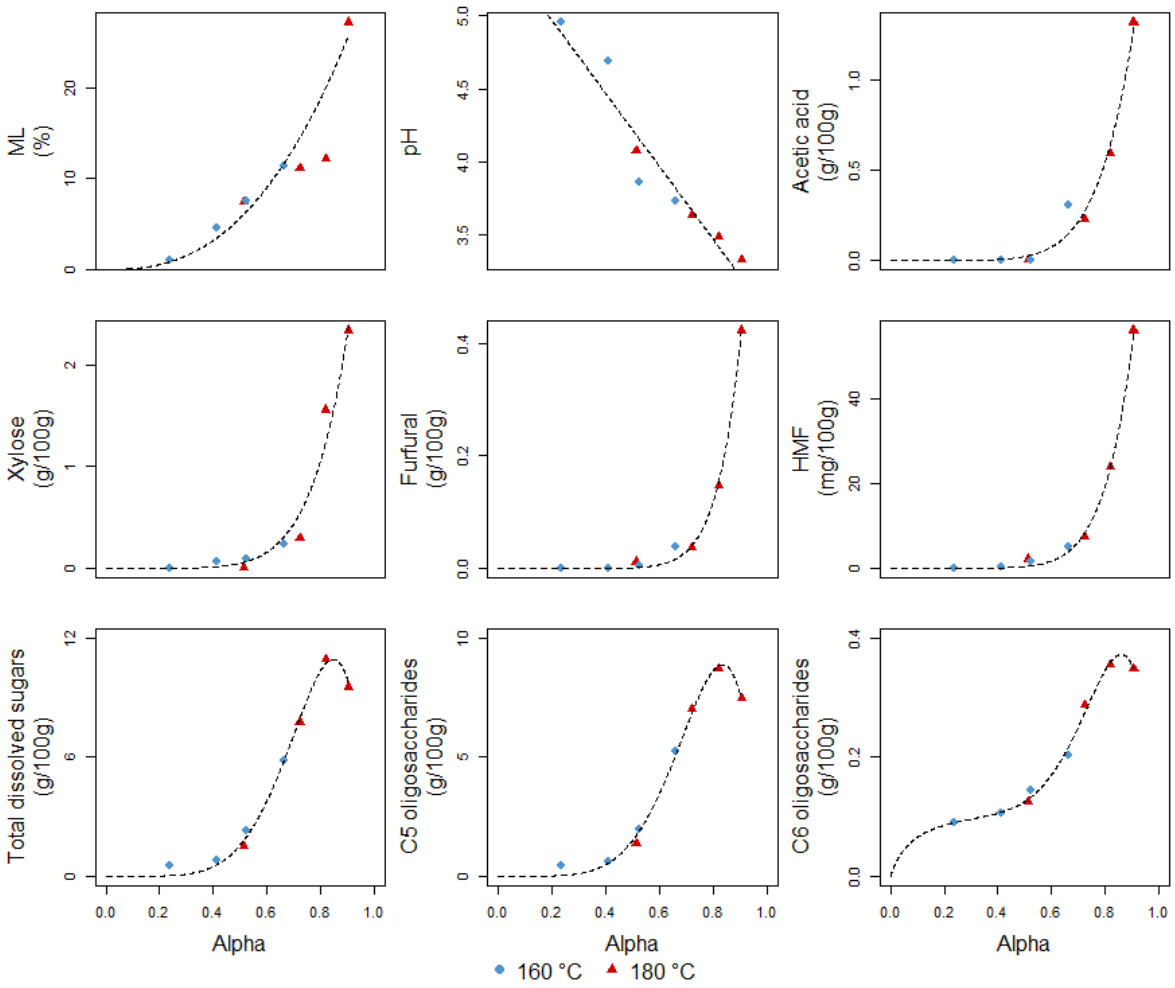

Figure 85. Biomass properties as a function of the degree of conversion (α).

The relationships found for both treatment temperatures simultaneously clearly confirm that shrinkage is a good indicator of the chemical degradation of biomass and of the pretreatment conditions (temperature duration). Table 11 summarizes the set of expressions allowing biomass properties to be predicted by the degree of conversion (α).

When biomass is used for the bioethanol production, the quantity of sugars and inhibition products released are extremely relevant parameters. The pretreatment step must maximize the sugar yield and the polysaccharides accessibility for enzymatic hydrolysis, while ensuring a low amount of inhibitors to be produced. The relationships found in this work could greatly assist in determining the ideal pretreatment conditions. For example, from Figure 84, we can see that after 20 minutes of treatment at 180 °C, oligosaccharides production is counterbalanced by its consumption. At the same time, furfural and HMF concentrations increase drastically. It means that intensifying the pretreatment severity would not be benefic if a further fermentation step is foreseen.

Table 11. Expressions proposed to express biomass properties as a function of the degree of conversion (α) caused by hydrothermal pretreatment

Properties	Expressions proposed to express properties as a function of the degree of conversion (α)
ML *(%)*	$ML = 33.47\ \alpha^{2.56}$
pH	$pH = 5.46 - 2.50\ \alpha$
Acetic acid (AA) *(g/100g of native biomass)*	$AA = 2.58\ \alpha^{6.94}$
Xylose (XYL) *(g/100g of native biomass)*	$XYL = 4.69\ \alpha^{6.63}$
Furfural (FUR) *(g/100g of native biomass)*	$FUR = 1.16\ \alpha^{10.26}$
HMF *(mg/100g of native biomass)*	$HMF = 129.91\ \alpha^{8.46}$
Total dissolved sugars (TDS) *(g/100g of native biomass)*	$TDS = 256.12\ \alpha^{6.22}(1-\alpha)^{1.13}$
C5 oligosaccharides (C5O) *(g/100g of native biomass)*	$C5O = 232.68\ \alpha^{6.08}(1-\alpha)^{1.20}$
C6 oligosaccharides (C6O) *(g/100g of native biomass)*	$C6O = \frac{0.12\ \alpha}{(0.09 + \alpha)} + 9.37\ \alpha^{7.54}(1-\alpha)^{1.24}$

4. Conclusion

An in-house developed device was used to characterize dimensional changes of poplar subjected to hydrothermal pretreatment at 160 and 180 °C. This device allowed the kinetics of sample shrinkage to be measured for the first time during this type of treatment.

Chemical characterization of the hydrolyzed fraction enabled a better understanding of the mechanisms leading to this deformation.

A DAEM model was identified from the shrinkage evolution. The degree of conversion of the biomass, as calculated from this model as a function of treatment conditions, is able to predict the change of physical and chemical characteristics. These excellent findings prove that shrinkage is an excellent indicator of the chemical degradation of lignocellulosic biomass during the hydrothermal treatment.

5. Acknowledgments

This study was carried out in the Centre Européen de Biotechnologie et de Bioéconomie (CEBB), supported by Région Grand Est, Département de la Marne, Grand Reims and the European Union. In particular, the authors would like to thank Département de la Marne for its financial support and the French Council for Poplar as well as Huberlant sawmill (Cormicy, France) for providing the wood used in this study.

General conclusion

This work addressed an explicit need of pretreatment optimization in a context of lignocellulosic biomass valorization for the production of biofuels and bio-based chemicals. Focus was given to the hydrothermal treatment prior to the explosion step, whose mechanisms leading to biomass deconstruction have not yet been fully elucidated. In particular, the objective of this research was to identify a macroscopic indicator of biomass deconstruction, likely to give rules to optimize the residence time and treatment temperature prior to the explosion step. Poplar was chosen as a biomass model for this study mainly because of its high growth rate, a highly desirable feedstock property.

Due to the complex structure of lignocellulosic biomass, such a goal can only be fulfilled through a multiscale approach.

As a first step, we explored the chemical and anatomical changes taking place at the cell wall and the tissue scales. This was accomplished by using the qualitative results obtained from different imaging techniques. In particular, the unique combination of confocal Raman microscopy and X-ray nano-tomography provided valuable information on topochemical and anatomical changes of the samples. Holocellulose hydrolysis and lignin migration were observed through confocal Raman microscopy. This migration was confirmed by scanning electronic microscopy, showing the formation of droplets. The composition of these droplets, however, is likely different depending on their location within the cell wall. From an anatomical point of view, samples shrank and had thinner cell walls. Subject to more severe pre-treatments, cells were disrupted and detached from adjacent cells. Imaging techniques provided, thus, an overall vision of the degradation of cell walls after hydrothermal treatment. These results can be a helpful tool when it comes to assessing the biomass susceptibility to the explosion step and its accessibility to enzymes.

As a second step, the modifications undergone by lignocellulosic biomass during hydrothermal treatment have been continuously assessed at a macroscopic scale. It was only possible thanks to a device developed in the laboratory, which allows reliable rheologic properties to be measured under high temperatures and relative humidity. A part of this thesis work consisted on developing a software able to control this equipment and to continuously acquire the data from the tests. A lot of effort has also been put on understanding the features of this device, which allowed the establishment of measurement protocols prioritizing the quality and reliability of the results. With this equipment, different rheological tests could be performed on solid biomass by numerous combinations of stress and strain. The assessment of biomass macroscopic changes was conducted in two stages.

Firstly, the evolution of stress relaxation and stiffness were studied under different treatment temperatures. These two rheological properties have proven to be complementary in highlighting the dynamics of chemical modifications during hydrothermal treatment. The main mechanisms revealed are thermal activation of the viscoelastic properties of lignocellulosic biomass, cleavage reactions and lignin re-condensation. Initially, thermal activation is observed solely (when treatment temperature remains quite low). Stress relaxation results provided evidence of concomitant thermal activation and chemical degradation in early stages of the treatment

(starting at 60 °C). This initial degradation was attributed to hydrolysis reactions of hemicelluloses, known as the most thermolabile component of lignocellulosic biomass. Once the plateau was reached, the predominance of either cleavage or re-condensation depended on the severity of the treatment. At the beginning of the temperature plateau, cleavage reactions were the most important ones regardless of the treatment temperature. For medium severity treatments (the second half of the plateau for low temperatures or half of the treatment time for the highest treatment temperature) a clear prevalence of lignin condensation has been identified through an increase in samples stiffness. For the most severe conditions tested in this study (180 °C and long residence time), a new loss of stiffness was observed, which was attributed the reduction of the degree of polymerization of cellulose. The same protocol was applied to samples pre-soaked in different liquids. As classically applied in biomass pretreatment, the effect of sulfuric acid concentration was evaluated (0.6 %, 0.3 % and distilled water). As an alternative to the traditional acidic media, an alkali pre-soaking liquid (NaOH 0.6 %) was also studied. Our results demonstrated that acidic media favored cleavage reactions. Contrastingly, the alkali pre-soaking provoked lignin and hemicellulose extraction at low temperatures but limited further alterations during the temperature plateau.

These results showed that, combined, stress relaxation and stiffness can successfully draw a profile of the mechanisms involved in biomass deconstruction during hydrothermal treatment. However, both present a non-monotonous behavior at some point of the treatment. This feature is undesirable when seeking for an indicator of the additive degradation caused during pretreatment.

Secondly, we therefore decided to explore another macroscopic measurement: the evolution of samples dimensions over time. Parallelly, biomass chemical changes were evaluated through classical chemical analyses for selected treatment durations and supported the results typically found in literature. Carrying out these analyses has highlighted the interest of a continuous indicator of biomass degradation. Indeed, scanning different treatment conditions quickly turns into a heavy task, due to the complexity of the standard chemical protocol.

After data processing, the results have demonstrated that samples continuously shrank during hydrothermal treatment and that shrinkage increased with the increase of temperature and residence time. Based on the obtained results, the parameters of a Distributed Activation Energy Model (DAEM) were identified by fitting the *in situ* shrinkage measurements. From this model, the degree of conversion can be calculated as a function of treatment temperature and residence time, and used as a synthetic indicator of chemical alterations. This excellent result then served to the adjustment simple expressions to relate the physical and chemical measurements to the identified model. Shrinkage therefore proved to be a good indicator of the chemical degradation of biomass during the pretreatment. It can be used as a valuable tool to choose the optimal conditions of hydrothermal treatment or can be applied in simulations of steam explosion.

Perspectives

A variety of perspectives and opportunities for further research and applications emerge from this work. They can be summarized as follows:

- A lot has been discussed in this thesis work about lignin chemical changes, especially regarding lignin re-condensation. A parallel chemical investigation of these changes using analytical chemistry methods could greatly enrich this work. It would provide both a better understanding of the modifications to which the lignin remaining in the solid phase is subjected, such as condensation, and the identification of molecules of interest solubilized in the liquid phase.
- The DAEM model developed during this study should be validated with other types of lignocellulosic biomass. It would also be interesting to include the acid concentration as a parameter in the model.
- Confocal Raman spectroscopy has proven its interest on the investigation of concomitant chemical and anatomical changes. However, many challenges were met during this study, which limited the analyses to mild treatment temperatures. Much work remains to be done to overcome the limitations imposed by laser induced florescence. Exploring other topochemistry techniques may be an answer to the encountered problems. One of the options is to somehow take advantage of this characteristic rather than trying to overcome it, as some studies have demonstrated that laser induced fluorescence is related to the type of bonds present in lignin structure.
- The explosion phase that follows hydrothermal treatment is an important step in the steam explosion process. This phase, which benefits from the high saturated steam pressure, is responsible for the fragmentation of the particles and, thus, the accessibility of the cell wall for subsequent enzymatic attack. It would be therefore interesting to improve the prediction of TransPore – a comprehensive computational model simulating the heat and mass transfer in porous media – for biomass fragmentation during the explosion, by taking into account the effect of both the average shape of a cell and the cell wall thickness on the modulus of rupture. The present work provides valuables insights on how these three characteristics change during the hydrothermal phase. The reduction of cell wall thickness has successfully been demonstrated by X-ray nano-tomography and quantified by image analysis. The same technique illustrated changes on the shape of the cells, resulting in a reduction of the mean cell circularity. Furthermore, the identified DAEM model was able to predict chemical changes on biomass for different temperatures and treatment durations. These outcomes could be combined in a new study that also includes the explosion stage.
- From a broader perspective, and in terms of further applications, our results show two opposed approaches. The pretreated biomass can either be used in fermentation processes—in which case a minimum modification of the composing polysaccharides is required—or in the obtention of platform molecules resulting from sugar degradation. The first approach calls for milder treatments, whilst the second implies an increased treatment severity.

- If applied to fermentation processes, the studies on biomass pretreatment should be further analyzed through the perspective of enzymatic hydrolysis. This is, indeed, the only mean to validate the possible outcomes of pretreatment optimization.
- Finally, the economic and environmental aspects of this process should be taken into account during process optimization to find the right balance between the increase in efficiency and the pretreatment energy consumption. It would also allow to validate the interests of this technology as an alternative for fossil fuels and chemicals.

References

[1] V. Masson-Delmotte, P. Zhai, H.-O. Pörtner, D. Roberts, J. Skea, P.R. Shukla, A. Pirani, W. Moufouma-Okia, C. Péan, R. Pidcock, S. Connors, J.B.R. Matthews, Y. Chen, X. Zhou, M.I. Gomis, E. Lonnoy, T. Maycock, M. Tignor, T. Waterfield, Global Warming of 1.5°C: An IPCC Special Report on the impacts of global warming of 1.5°C above pre-industrial levels and related global greenhouse gas emission pathways, in the context of strengthening the global response to the threat of climate change, 2019. https://doi.org/10.1002/9780470996621.ch50.

[2] Y.H.P. Zhang, Reviving the carbohydrate economy via multi-product lignocellulose biorefineries, J. Ind. Microbiol. Biotechnol. 35 (2008) 367–375. https://doi.org/10.1007/s10295-007-0293-6.

[3] P. Varanasi, P. Singh, M. Auer, P.D. Adams, B. a Simmons, S. Singh, Survey of renewable chemicals produced from lignocellulosic biomass during ionic liquid pretreatment., Biotechnol. Biofuels. 6 (2013) 14. https://doi.org/10.1186/1754-6834-6-14.

[4] G. De Bhowmick, A.K. Sarmah, R. Sen, Lignocellulosic biorefinery as a model for sustainable development of biofuels and value added products, Bioresour. Technol. 247 (2018) 1144–1154. https://doi.org/10.1016/j.biortech.2017.09.163.

[5] EUROSTAT, Greenhouse gas emission statistics - emission inventories, (2019). https://ec.europa.eu/eurostat/statistics-explained/pdfscache/1180.pdf.

[6] REN21, Renewables 2019 Global Status Report, Paris, 2019.

[7] B. Kamm, P.R. Gruber, M. Kamm, Biorefineries - Industrial Processes and Products, in: Ullman's Encycl. Ind. Chem., Wiley, Weinheim, 2015: p. 38. https://doi.org/10.1016/s1351-4180(10)70462-1.

[8] W.-Y. Chen, J. Seiner, T. Suzuki, M. Lackner, Handbook of Climate Change Mitigation, Second edi, Springer Science+Business Media, New York, 2012. https://doi.org/10.1007/978-3-319-14409-2_39.

[9] F.H. Isikgor, C.R. Becer, Lignocellulosic biomass: a sustainable platform for the production of bio-based chemicals and polymers, Polym. Chem. 6 (2015) 4497–4559. https://doi.org/10.1039/c5py00263j.

[10] M. Pelckmans, T. Renders, S. Van De Vyver, B.F. Sels, Bio-based amines through sustainable heterogeneous catalysis, Green Chem. 19 (2017) 5303–5331. https://doi.org/10.1039/c7gc02299a.

[11] P. Gallezot, Conversion of biomass to selected chemical products., Chem. Soc. Rev. 41 (2012) 1538–58. https://doi.org/10.1039/c1cs15147a.

[12] M.C. Rulli, D. Bellomi, A. Cazzoli, G. De Carolis, P. D'Odorico, The water-land-food nexus of first-generation biofuels, Sci. Rep. 6 (2016) 1–10. https://doi.org/10.1038/srep22521.

[13] OECD/IEA, From 1st to 2nd generation biofuel technologies - An overview of current industry and RD&D activities, Paris, 2008. https://doi.org/10.1007/978-3-642-34519-7.

[14] T.D. Foust, A. Aden, A. Dutta, S. Phillips, An economic and environmental comparison of a biochemical and a thermochemical lignocellulosic ethanol conversion processes, Cellulose. 16 (2009) 547–565. https://doi.org/10.1007/s10570-009-9317-x.

[15] W.H. Smith, F.C. Helwig, Liquor the Servant of Man, Little Brown & Co., Boston, 1940.

[16] C.R. Soccol, V. Faraco, S.G. Karp, L.P.S. Vandenberghe, V. Thomaz-soccol, A.L. Woiciechowski,

A. Pandey, Lignocellulosic Bioethanol : Current Status and Future Perspectives, 2nd ed., Elsevier Inc., 2019. https://doi.org/10.1016/B978-0-12-816856-1.00014-2.

[17] M.R. Ladish, N.S. Mosier, Y. Kim, E. Ximenes, D. Hogdett, Converting cellulose to biofuels, Chem Eng Prog. 106 (2010) 56–63.

[18] K.D. Mojsov, Aspergillus Enzymes for Food Industries, in: New Futur. Dev. Microb. Biotechnol. Bioeng. Aspergillus Syst. Prop. Appl., Elsevier B.V., 2016: pp. 215–222. https://doi.org/10.1016/B978-0-444-63505-1.00033-6.

[19] J. Baruah, B.K. Nath, R. Sharma, S. Kumar, R.C. Deka, D.C. Baruah, E. Kalita, Recent trends in the pretreatment of lignocellulosic biomass for value-added products, Front. Energy Res. 6 (2018) 1–19. https://doi.org/10.3389/fenrg.2018.00141.

[20] P. D. Muley, D. Boldor, Advances in Biomass Pretreatment and Cellulosic Bioethanol Production Using Microwave Heating, in: Proc. SEEP2017, Bled, 2017: pp. 173–180. https://doi.org/10.18690/978-961-286-048-6.18.

[21] G.W. Huber, S. Iborra, A. Corma, Synthesis of transportation fuels from biomass: Chemistry, catalysts, and engineering, Chem. Rev. 106 (2006) 4044–4098. https://doi.org/10.1021/cr068360d.

[22] C.K. Nitsos, K.A. Matis, K.S. Triantafyllidis, Optimization of hydrothermal pretreatment of lignocellulosic biomass in the bioethanol production process, ChemSusChem. 6 (2013) 110–122. https://doi.org/10.1002/cssc.201200546.

[23] E. Ximenes, C.S. Farinas, Y. Kim, M.R. Ladisch, Hydrothermal Pretreatment of Lignocellulosic Biomass for Bioethanol Production, in: H. Ruiz, M. Hedegaard Thomsen, H. Trajano (Eds.), Hydrothermal Process. Biorefineries, Springer, Cham, 2017: pp. 181–205. https://doi.org/10.1007/978-3-319-56457-9.

[24] S. Ewanick, R. Bura, Hydrothermal pretreatment of lignocellulosic biomass, in: K. Waldron (Ed.), Bioalcohol Prod. Biochem. Convers. Lignocellul. Biomass, Woodhead Publishing, New Delhi, 2010: pp. 3–23. https://doi.org/10.1533/9781845699611.1.3.

[25] M.J. Negro, P. Manzanares, I. Ballesteros, J.M. Oliva, A. Cabañas, M. Ballesteros, Hydrothermal pretreatment conditions to enhance ethanol production from poplar biomass, Appl. Biochem. Biotechnol. - Part A Enzym. Eng. Biotechnol. 108 (2003) 87–100. https://doi.org/10.1385/ABAB:105:1-3:87.

[26] P. Alvira, E. Tomás-Pejó, M. Ballesteros, M.J. Negro, Pretreatment technologies for an efficient bioethanol production process based on enzymatic hydrolysis: A review, Bioresour. Technol. 101 (2010) 4851–4861. https://doi.org/10.1016/j.biortech.2009.11.093.

[27] N. Mosier, C. Wyman, B. Dale, R. Elander, Y.Y. Lee, M. Holtzapple, M. Ladisch, Features of promising technologies for pretreatment of lignocellulosic biomass, Bioresour. Technol. 96 (2005) 673–686. https://doi.org/10.1016/j.biortech.2004.06.025.

[28] M. Chadni, N. Grimi, O. Bals, I. Ziegler-devin, N. Brosse, Steam explosion process for the selective extraction of hemicelluloses polymers from spruce sawdust, Ind. Crop. Prod. 141 (2019) 111757. https://doi.org/10.1016/j.indcrop.2019.111757.

[29] A.T.W.M. Hendriks, G. Zeeman, Pretreatments to enhance the digestibility of lignocellulosic biomass, Bioresour. Technol. 100 (2009) 10–18. https://doi.org/10.1016/j.biortech.2008.05.027.

[30] H.H. Brownell, E.K.C. Yu, J.N. Saddler, Steam-explosion pretreatment of wood: Effect of chip size, acid, moisture content and pressure drop, Biotechnol. Bioeng. 28 (1986) 792–801. https://doi.org/10.1002/bit.260280604.

[31] J.M. Martínez, J. Reguant, M.Á. Montero, D. Montané, J. Salvadó, X. Farriol, Hydrolytic Pretreatment of Softwood and Almond Shells. Degree of Polymerization and Enzymatic Digestibility of the Cellulose Fraction, Ind. Eng. Chem. Res. 36 (1997) 688–696. https://doi.org/10.1021/ie960048e.

[32] G.M. Irvine, The significance of the glass transition of lignin in thermomechanical pulping, Wood Sci. Technol. 19 (1985) 139–149. https://doi.org/10.1007/BF00353074.

[33] C. Assor, V. Placet, B. Chabbert, A. Habrant, C. Lapierre, B. Pollet, P. Perré, Concomitant changes in viscoelastic properties and amorphous polymers during the hydrothermal treatment of hardwood and softwood, J. Agric. Food Chem. 57 (2009) 6830–6837. https://doi.org/10.1021/jf901373s.

[34] S. Mokdad, J. Casalinho, G. Almeida, P. Perré, Assessment of biomass alterations during hydrothermal pretreatment by in- situ dynamic mechanical analysis, Biomass and Bioenergy. 108 (2018) 330–337. https://doi.org/10.1016/j.biombioe.2017.11.014.

[35] W. Sui, H. Chen, Water transfer in steam explosion process of corn stalk, Ind. Crops Prod. 76 (2015) 977–986. https://doi.org/10.1016/j.indcrop.2015.08.001.

[36] W. Sui, H. Chen, Effects of water states on steam explosion of lignocellulosic biomass, Bioresour. Technol. 199 (2016) 155–163. https://doi.org/10.1016/j.biortech.2015.09.001.

[37] A. Limayem, S.C. Ricke, Lignocellulosic biomass for bioethanol production: current perspectives, potential issues and future prospects, Prog. Energy Combust. Sci. 38 (2012) 449–467. https://doi.org/10.1016/j.pecs.2012.03.002.

[38] A. Rafsanjani, D. Derome, F.K. Wittel, J. Carmeliet, Computational up-scaling of anisotropic swelling and mechanical behavior of hierarchical cellular materials, Compos. Sci. Technol. 72 (2012) 744–751. https://doi.org/10.1016/j.compscitech.2012.02.001.

[39] V. Placet, Conception et exploitation d'un dispositif expérimental innovant pour la caractérisation du comportement viscoélastique et de la dégradation thermique du bois dans des conditions sévères, Université Henri Poincaré, Nancy-I, 2006.

[40] F.H. Isikgor, C.R. Becer, Lignocellulosic biomass: a sustainable platform for the production of bio-based chemicals and polymers, Polym. Chem. 6 (2015) 4497–4559. https://doi.org/10.1039/c5py00263j.

[41] C. Chen, L. Hu, Nanocellulose toward Advanced Energy Storage Devices : Structure and Electrochemistry, Acc. Chem. Res. 51 (2018) 3154–3165. https://doi.org/10.1021/acs.accounts.8b00391.

[42] R.M. Rowell, Handbook of Wood Chemistry and Wood Composites, CRC Press, Boca Raton, 2005. https://doi.org/10.1201/9780203492437.

[43] J.G.F. Walker, Primary Wood Processing : Principles and practice, Chapman & Hall, London, 1993.

[44] S. Haghighi Mood, A. Hossein Golfeshan, M. Tabatabaei, G. Salehi Jouzani, G.H. Najafi, M. Gholami, M. Ardjmand, Lignocellulosic biomass to bioethanol, a comprehensive review with a focus on pretreatment, Renew. Sustain. Energy Rev. 27 (2013) 77–93. https://doi.org/10.1016/j.rser.2013.06.033.

[45] A. Geitmann, J. Gril, Plant Biomechanics: From Structure to Function at Multiple Scales, Springer Nature, Cham, 2018. https://doi.org/10.1007/978-3-319-79099-2.

[46] M.T. Holtzapple, Hemicelluloses, in: Encycl. Food Sci. Food Technol. Nutr., 2nd ed., Academic Press, Amsterdam, 2003: pp. 3060–3070.

[47] E. Sjöström, Wood chemistry - Fundamentals and Applications, Academic Press, New York, 1993.

[48] J. Walker, Primary Wood Processing: Principles and Practice, 2st Ed., Springer, Dordrecht, Netherlands, 1993.

[49] J.-P. HALUK, Compostion chimique du bois, in: P. Jodin (Ed.), Le Bois Matériau d'Ingéniérie, Nancy, 1994: pp. 53–89.

[50] X. Lu, K. Yamauchi, N. Phaiboonsilpa, S. Saka, Two-step hydrolysis of Japanese beech as treated by semi-flow hot-compressed water, J. Wood Sci. 55 (2009) 367–375. https://doi.org/10.1007/s10086-009-1040-6.

[51] A. Sakakibara, Y. Sano, Chemistry of Lignin, in: D. Hon, N. Shiraishi (Eds.), Wood Cellul. Chem., 2nd ed., Marcel Dekker Inc, New York, 2001: pp. 109–174.

[52] C. Li, X. Zhao, A. Wang, G.W. Huber, T. Zhang, Catalytic Transformation of Lignin for the Production of Chemicals and Fuels, Chem. Rev. 115 (2015) 11559–11624. https://doi.org/10.1021/acs.chemrev.5b00155.

[53] R.B. Santos, E.A. Capanema, M.Y. Balakshin, H. Chang, H. Jameel, Lignin Structural Variation in Hardwood Species, J. Agric. Food Chem. 60 (2012) 4923–4930. https://doi.org/10.1021/jf301276a.

[54] X. Tian, Z. Fang, J. Richard L. Smith, Z. Wu, M. Liu, Properties, Chemical Characteristics and Application of Lignin and Its Derivatives, in: Z. Fang, J. Richard L. Smith (Eds.), Prod. Biofuels Chem. from Lignin, Springer Singapore, 2016: pp. 3–33. https://doi.org/10.1007/978-981-10-1965-4.

[55] J.S. Lupoi, E. Gjersing, M.F. Davis, Evaluating lignocellulosic biomass , its derivatives , and downstream products with Raman spectroscopy, Front. Bioeng. Biotechnol. 3 (2015) 1–18. https://doi.org/10.3389/fbioe.2015.00050.

[56] S.D. Mansfield, H. Kim, F. Lu, J. Ralph, Whole plant cell wall characterization using solution-state 2D NMR, Nat. Protoc. 7 (2012) 1579–1589. https://doi.org/10.1038/nprot.2012.064.

[57] Y. Lu, Y. Lu, H. Hu, F. Xie, X. Wei, X. Fan, Structural Characterization of Lignin and Its Degradation Products with Spectroscopic Methods, J. Spectrosc. 2017 (2017) 15. https://doi.org/https://doi.org/10.1155/2017/8951658.

[58] J.S. Lupoi, S. Singh, R. Parthasarathi, B.A. Simmons, R.J. Henry, Recent innovations in analytical methods for the qualitative and quantitative assessment of lignin, Renew. Sustain. Energy Rev. 49 (2015) 871–906. https://doi.org/10.1016/j.rser.2015.04.091.

[59] H. Nishimura, A. Kamiya, T. Nagata, M. Katahira, T. Watanabe, Direct evidence for α ether linkage between lignin and carbohydrates in wood cell walls, Sci. Rep. 8 (2018) 1–11. https://doi.org/10.1038/s41598-018-24328-9.

[60] D. Tarasov, M. Leitch, P. Fatehi, Lignin-carbohydrate complexes: Properties, applications, analyses, and methods of extraction: A review, Biotechnol. Biofuels. 11 (2018) 1–28. https://doi.org/10.1186/s13068-018-1262-1.

[61] M. Ek, G. Gellerstedt, G. Henriksson, Pulp and Paper Chemistry and Technology, Walter de Gruyter, Berlin, 2009.

[62] A. Déjardin, F. Laurans, D. Arnaud, C. Breton, G. Pilate, J.C. Leplé, Wood formation in Angiosperms, Comptes Rendus - Biol. 333 (2010) 325–334. https://doi.org/10.1016/j.crvi.2010.01.010.

[63] J.P. Joseleau, T. Imai, K. Kuroda, K. Ruel, Detection in situ and characterization of lignin in the G-layer of tension wood fibres of Populus deltoides, Planta. 219 (2004) 338–345.

https://doi.org/10.1007/s00425-004-1226-5.

[64] N. Gierlinger, New insights into plant cell walls by vibrational microspectroscopy, Appl. Spectrosc. Rev. 53 (2018) 517–551. https://doi.org/10.1080/05704928.2017.1363052.

[65] M. Fujita, H. Harada, Ultrastructure and Formation of Wood Cell Wall, in: D.N.S. Hon, N. Shiraishi (Eds.), Wood Cellul. Chem., 2nd ed., Marcel Dekker Inc, New York, 2001: pp. 1–49.

[66] L.A. Donaldson, Lignification and lignin topochemistry — an ultrastructural view, Phytochemistry. 57 (2001) 859–873.

[67] J. Fahlén, The cell wall ultrastructure of wood fibres – effects of the chemical pulp fibre line, 2005.

[68] R. Keller, La constitution du bois, in: P. Jodin (Ed.), Le Bois Matériau d'Ingéniérie, ARBOLOR, Nancy, 1994: pp. 13–52.

[69] U.P. Agarwal, Raman imaging to investigate ultrastructure and composition of plant cell walls: Distribution of lignin and cellulose in black spruce wood (Picea mariana), Planta. 224 (2006) 1141–1153. https://doi.org/10.1007/s00425-006-0295-z.

[70] A. Fahn, Plant anatomy, 4th ed., Pergamon Press, 1990.

[71] A. Marie Eriksen, D. John Gregory, C. Villa, N. Lynnerup, K. Bo Botfeldt, A. Redsted Rasmussen, The effects of wood anisotropy on the mode of attack by the woodborer Teredo navalis and the implications for underwater cultural heritage, (2015). https://doi.org/10.1016/j.ibiod.2015.11.018.

[72] R.A. PARHAM, R.L. GRAY, Formation and Structure of Wood, (1984) 3–56. https://doi.org/10.1021/ba-1984-0207.ch001.

[73] B. Franke, P. Quenneville, Numerical Modeling of the Failure Behavior of Dowel Connections in Wood, J. Eng. Mech. 137 (2011) 186–195. https://doi.org/10.1061/(ASCE)EM.1943-7889.0000217.

[74] U.P. Agarwal, R.H. Atalla, In-situ Raman microprobe studies of plant cell walls: Macromolecular organization and compositional variability in the secondary wall of Picea mariana (Mill.) B.S.P., Planta. 169 (1986) 325–332. https://doi.org/10.1007/BF00392127.

[75] R.H. Atalla, U.P. Agarwal, Raman microprobe evidence for lignin orientation in the cell walls of native woody tissue, Science (80-.). 227 (1985) 636–638. https://doi.org/10.1126/science.227.4687.636.

[76] R.H. Atalla, U.P. Agarwal, Recording Raman spectra from plant cell walls, J. Raman Spectrosc. 17 (1986) 229–231. https://doi.org/10.1002/jrs.1250170213.

[77] N. Gierlinger, Raman imaging of plant cell walls, in: T. Dieing, O. Hollricher, J. Toporski (Eds.), Confocal Raman Microsc., Springer, Ulm, 2010: pp. 225–236.

[78] U.P. Agarwal, Analysis of cellulose and lignocellulose materials by raman spectroscopy: A review of the current status, Molecules. 24 (2019). https://doi.org/10.3390/molecules24091659.

[79] U.P. Agarwal, S.A. Ralph, FT-Raman Spectroscopy of Wood : Identifying Contributions of Lignin and Carbohydrate Polymers in the Spectrum of Black Spruce (Picea mariana), Appl. Spectrosc. 51 (1997) 1648–1655.

[80] J.H. Wiley, R.H. Atalla, Band assignments in the Raman spectra of celluloses, Carbohydr. Res. 160 (1987) 113–129. https://doi.org/0008-6215(87)80306-3.

[81] N. Gierlinger, M. Schwanninger, Chemical Imaging of Poplar Wood Cell Walls by Confocal Raman Microscopy, Plant Physiol. 140 (2006) 1246–1254. https://doi.org/10.1104/pp.105.066993.1246.

[82] P. Cabrolier, Caractérisation des propriétés structurales et mécaniques des composantes pariétales du bois à l ' échelle du tissu, AgroParisTech ENGREF/INRA, 2012.

[83] D.D. Stokke, Q. Wu, G. Han, Introduction to wood and natural fiber composites, 2014.

[84] D. Derome, A. Rafsanjani, S. Hering, M. Dressler, A. Patera, C. Lanvermann, M. Sedighi-Gilani, F.K. Wittel, P. Niemz, J. Carmeliet, The role of water in the behavior of wood, J. Build. Phys. 36 (2013) 398–421. https://doi.org/10.1177/1744259112473926.

[85] E.T. Engelund, L.G. Thygesen, S. Svensson, C.A.S. Hill, A critical discussion of the physics of wood-water interactions, Wood Sci. Technol. 47 (2013) 141–161. https://doi.org/10.1007/s00226-012-0514-7.

[86] G. Almeida, Influence de la structure du bois sur ses propriétés physico-mécaniques à des teneurs en humidité élevées, Département Des Sci. Du Bois La Forêt. (2006) 232.

[87] C. Skaar, Wood-Water Relations, Springer Berlin Heidelberg, Berlin, Heidelberg, 1988. https://doi.org/10.1007/978-3-642-73683-4.

[88] G. Almeida, R. Rémond, P. Perré, Hygroscopic behaviour of lignocellulosic materials: Dataset at oscillating relative humidity variations, J. Build. Eng. 19 (2018) 320–333. https://doi.org/10.1016/j.jobe.2018.05.005.

[89] C.P. McLaughlin, T.R.A. Magee, The determination of sorption isotherms and the isosteric heats of sorption for potatoes, J. Food Eng. 35 (1998) 267–280. https://doi.org/10.1016/S0260-8774(98)00025-9.

[90] N.D. Mrad, C. Bonazzi, F. Courtois, N. Kechaou, N.B. Mihoubi, Moisture desorption isotherms and glass transition temperatures of osmo-dehydrated apple and pear, Food Bioprod. Process. 91 (2013) 121–128. https://doi.org/10.1016/j.fbp.2012.09.006.

[91] DOE FUNDAMENTALS HANDBOOK - MATERIAL SCIENCE, U. S. Dep. Energy. 1 (1993). https://www.standards.doe.gov/standards-documents/1000/1017-BHdbk-1993-v1/@@images/file (accessed January 3, 2020).

[92] E.P. Popov, Engineering Mechanics of Solids, Second edi, Pearson, 1998.

[93] T. Ozyhar, S. Hering, P. Niemz, Viscoelastic characterization of wood: Time dependence of the orthotropic compliance in tension and compression, J. Rheol. (N. Y. N. Y). 57 (2013) 699–717. https://doi.org/10.1122/1.4790170.

[94] J.A. Nairn, Numerical simulations of transverse compression and densification in wood, Wood Fiber Sci. 38 (2006) 576–591.

[95] J.M. Dinwoodie, Timber: Its nature and behaviour, Second Edi, E & FN Spon, London, 2000.

[96] D.W. Green, J.E. Winnandy, D.E. Kretschmann, Mechanical Properties of Wood, in: Wood Handb. — Wood as an Eng. Mater., U.S. Department of Agriculture, Forest Service, Forest Products Laboratory, Madison, 1999: pp. 1–45. https://doi.org/10.1557/proc-546-213.

[97] R.K. Roeder, Mechanical Characterization of Biomaterials, in: A. Bandyopadhyay, S. Bose (Eds.), Charact. Biomater., Elsevier, Oxford, 2013: pp. 49–104. https://doi.org/10.1016/B978-0-12-415800-9.00003-6.

[98] D. Guitard, M. Fournier, Comportement mécanique du bois, in: P. Jodin (Ed.), Le Bois Matériau d'Ingéniérie, ARBOLOR, Nancy, 1994: pp. 91–125.

[99] J.E. Winandy, R.M. Rowell, The chemistry of wood strength. The chemistry of solid wood. Advances in chemistry, (1984).

[100] J.F. Steffe, Rheological Methods in Food Process Engineering, 2nd ed., Freeman Press, East Lansing, 1996.

[101] L. Salmén, Micromechanical understanding of the cell-wall structure, Comptes Rendus - Biol. 327 (2004) 873–880. https://doi.org/10.1016/j.crvi.2004.03.010.

[102] T.A. Tabet, F.A. Aziz, Cellulose Microfibril Angle in Wood and Its Dynamic Mechanical Significance, in: T. van de Ven, L. Godbout (Eds.), Cellul. - Fundam. Asp., IntechOpen, 2013: pp. 114–142. https://doi.org/10.5772/51105.

[103] M. Özparpucu, N. Gierlinger, I. Cesarino, I. Burgert, W. Boerjan, M. Rüggeberg, Significant influence of lignin on axial elastic modulus of poplar wood at low microfibril angles under wet conditions, J. Exp. Bot. 70 (2019) 4039–4047. https://doi.org/10.1093/jxb/erz180.

[104] M. Åkerholm, L. Salmén, The oriented structure of lignin and its viscoelastic properties studied by static and dynamic FT-IR spectroscopy, Holzforschung. 57 (2003) 459–465. https://doi.org/10.1515/HF.2003.069.

[105] A. Bergander, L. Salmén, Cell wall properties and their effects on the mechanical properties of fibers, J. Mater. Sci. 37 (2002) 151–156. https://doi.org/10.1023/A:1013115925679.

[106] L. Salmén, I. Burgert, Cell wall features with regard to mechanical performance. A review. COST Action E35 2004-2008: Wood machining - Micromechanics and fracture, Holzforschung. 63 (2009) 121–129. https://doi.org/10.1515/HF.2009.011.

[107] P. Navi, S. Stanzl-Tschegg, Micromechanics of creep and relaxation of wood. A review. COST Action E35 2004-2008: Wood machining - Micromechanics and fracture, Holzforschung. 63 (2009) 186–195. https://doi.org/10.1515/HF.2009.013.

[108] L. Goswami, M. Eder, N. Gierlinger, I. Burgert, Inducing large deformation in wood cell walls by enzymatic modification, J. Mater. Sci. 43 (2008) 1286–1291. https://doi.org/10.1007/s10853-007-2162-0.

[109] A. Bergander, L. Salmén, Variations in transverse fibre wall properties: Relations between elastic properties and structure, Holzforschung. 54 (2000) 654–660. https://doi.org/10.1515/HF.2000.110.

[110] T. Tabarsa, Y.H. Chui, Characterizing microscopic behavior of wood under transverse compression. Part II. Effect of species and loading direction, Wood Fiber Sci. 33 (2001) 223–232.

[111] N.R. Jadhav, V.L. Gaikwad, K.J. Nair, H.M. Kadam, Glass transition temperature: Basics and application in pharmaceutical sector, Asian J. Pharm. 3 (2009) 82–89. https://doi.org/10.4103/0973-8398.55043.

[112] Anne-Mari Olsson, L. Salmén, The effect of lignin composition on the viscoelastic properties of wood, Nord. Pulp Pap. Res. J. 12 (1997) 140–144.

[113] E.L. Back, N.L. Salmén, Glass transitions of wood components hold implications for molding and pulping processes, Tappi. 65 (1982) 107–110.

[114] E. Obataya, M. Norimoto, J. Gril, The effects of adsorbed water on dynamic mechanical properties of wood, Polymer (Guildf). 39 (1998) 3059–3064. https://doi.org/10.1016/S0032-3861(97)10040-4.

[115] G. Garrote, H. Dominguez, J.C. Parajo, Hydrothermal processing of lignocellulosic materials, Holz Als Roh- Und Werkst. 57 (1999) 191–202. https://doi.org/10.1007/s001070050039.

[116] P. Sannigrahi, D.H. Kim, S. Jung, A. Ragauskas, Pseudo-lignin and pretreatment chemistry, Energy Environ. Sci. 4 (2011) 1306–1310. https://doi.org/10.1039/c0ee00378f.

[117] C. Asada, C. Sasaki, T. Hirano, Y. Nakamura, Chemical characteristics and enzymatic saccharification of lignocellulosic biomass treated using high-temperature saturated steam:

Comparison of softwood and hardwood, Bioresour. Technol. 182 (2015) 245–250. https://doi.org/10.1016/j.biortech.2015.02.005.

[118] S. Liu, H. Lu, R. Hu, A. Shupe, L. Lin, B. Liang, A sustainable woody biomass biorefinery, Biotechnol. Adv. 30 (2012) 785–810. https://doi.org/10.1016/j.biotechadv.2012.01.013.

[119] J. Ma, Z. Ji, J.C. Chen, X. Zhou, Y.S. Kim, F. Xu, The mechanism of xylans removal during hydrothermal pretreatment of poplar fibers investigated by immunogold labeling, Planta. 242 (2015) 327–337. https://doi.org/10.1007/s00425-015-2313-5.

[120] N. Jacquet, N. Quiévy, C. Vanderghem, S. Janas, C. Blecker, B. Wathelet, J. Devaux, M. Paquot, Influence of steam explosion on the thermal stability of cellulose fibres, Polym. Degrad. Stab. 96 (2011) 1582–1588. https://doi.org/10.1016/j.polymdegradstab.2011.05.021.

[121] Y. Yu, H. Wu, Significant differences in the hydrolysis behavior of amorphous and crystalline portions within microcrystalline cellulose in hot-compressed water, Ind. Eng. Chem. Res. 49 (2010) 3902–3909. https://doi.org/10.1021/ie901925g.

[122] H.L. Trajano, C.E. Wyman, Fundamentals of biomass pretreatment at low pH, in: Aqueous Pretreat. Plant Biomass Biol. Chem. Convers. to Fuels Chem., First Edit, 2013: pp. 103–128. https://doi.org/10.1002/9780470975831.ch6.

[123] P.N. Ciesielski, W. Wang, X. Chen, T.B. Vinzant, M.P. Tucker, S.R. Decker, M.E. Himmel, D.K. Johnson, B.S. Donohoe, Effect of mechanical disruption on the effectiveness of three reactors used for dilute acid pretreatment of corn stover Part 2: morphological and structural substrate analysis., Biotechnol. Biofuels. 7 (2014) 47. https://doi.org/10.1186/1754-6834-7-57.

[124] H. Inouye, Y. Zhang, L. Yang, N. Venugopalan, R.F. Fischetti, S.C. Gleber, S. Vogt, W. Fowle, B. Makowski, M. Tucker, P. Ciesielski, B. Donohoe, J. Matthews, M.E. Himmel, L. Makowski, Multiscale deconstruction of molecular architecture in corn stover., Sci. Rep. 4 (2014) 3756. https://doi.org/10.1038/srep03756.

[125] S.D. Shinde, X. Meng, R. Kumar, A.J. Ragauskas, Recent advances in understanding the pseudo-lignin formation in a lignocellulosic biorefinery, Green Chem. 20 (2018) 2192–2205. https://doi.org/10.1039/c8gc00353j.

[126] S.N. Obame, I. Ziegler-Devin, R. Safou-Tchima, N. Brosse, Homolytic and Heterolytic Cleavage of β-Ether Linkages in Hardwood Lignin by Steam Explosion, J. Agric. Food Chem. 67 (2019) 5989–5996. https://doi.org/10.1021/acs.jafc.9b01744.

[127] J. Li, G. Henriksson, G. Gellerstedt, Lignin depolymerization / repolymerization and its critical role for delignification of aspen wood by steam explosion, Bioresour. Technol. 98 (2007) 3061–3068. https://doi.org/10.1016/j.biortech.2006.10.018.

[128] R. Samuel, S. Cao, B.K. Das, F. Hu, Y. Pu, A.J. Ragauskas, Investigation of the fate of poplar lignin during autohydrolysis pretreatment to understand the biomass recalcitrance, RSC Adv. 3 (2013) 5305–5309. https://doi.org/10.1039/c3ra40578h.

[129] T. Auxenfans, C. Terryn, G. Paës, Seeing biomass recalcitrance through fluorescence, (2017) 1–8. https://doi.org/10.1038/s41598-017-08740-1.

[130] K. Saito, Y. Horikawa, J. Sugiyama, T. Watanabe, Effect of thermochemical pretreatment on lignin alteration and cell wall microstructural degradation in Eucalyptus globulus : comparison of acid , alkali , and water pretreatments, J. Wood Sci. 62 (2016) 276–284. https://doi.org/10.1007/s10086-016-1543-x.

[131] T. Auxenfans, D. Crônier, B. Chabbert, G. Paës, Understanding the structural and chemical changes of plant biomass following steam explosion pretreatment, Biotechnol. Biofuels. 10 (2017) 36. https://doi.org/10.1186/s13068-017-0718-z.

[132] C. Wang, H. Li, M. Li, J. Bian, R. Sun, Revealing the structure and distribution changes of Eucalyptus lignin during the hydrothermal and alkaline pretreatments, Sci. Rep. 7 (2017) 1–10. https://doi.org/10.1038/s41598-017-00711-w.

[133] M.H. Studer, J.D. DeMartini, M.F. Davis, R.W. Sykes, B. Davison, M. Keller, G.A. Tuskan, C.E. Wyman, Lignin content in natural populus variants affects sugar release, Proc. Natl. Acad. Sci. U. S. A. 108 (2011) 6300–6305. https://doi.org/10.1073/pnas.1009252108.

[134] Q. Zhao, H. Wang, Y. Yin, Y. Xu, F. Chen, R.A. Dixon, Syringyl lignin biosynthesis is directly regulated by a secondary cell wall master switch, Proc. Natl. Acad. Sci. (2010). https://doi.org/10.1073/pnas.1009170107.

[135] B.S. Donohoe, S.R. Decker, M.P. Tucker, M.E. Himmel, T.B. Vinzant, Visualizing lignin coalescence and migration through maize cell walls following thermochemical pretreatment, Biotechnol. Bioeng. 101 (2008) 913–925. https://doi.org/10.1002/bit.21959.

[136] M.J. Selig, S. Viamajala, S.R. Decker, M.P. Tucker, M.E. Himmel, T.B. Vinzant, Deposition of Lignin Droplets Produced During Dilute Acid Pretreatment of Maize Stems Retards Enzymatic Hydrolysis of Cellulose, Biotechnol. Prog. 23 (2007) 1333–1339. https://doi.org/10.1021/bp0702018.

[137] Y. Zeng, S. Zhao, H. Wei, M.P. Tucker, M.E. Himmel, N.S. Mosier, R. Meilan, S.Y. Ding, In situ micro-spectroscopic investigation of lignin in poplar cell walls pretreated by maleic acid, Biotechnol. Biofuels. 8 (2015). https://doi.org/10.1186/s13068-015-0312-1.

[138] N. Banerjee, R. Bhatnagar, L. Viswanathan, Inhibition of glycolysis by furfural in Saccharomyces cerevisiae, Eur. J. Appl. Microbiol. Biotechnol. 11 (1981) 226–228. https://doi.org/10.1007/BF00505872.

[139] S.D. Shinde, X. Meng, R. Kumar, A.J. Ragauskas, Recent advances in understanding the pseudo-lignin formation in a lignocellulosic biorefinery, Green Chem. 20 (2018) 2192–2205. https://doi.org/10.1039/c8gc00353j.

[140] R. Kumar, F. Hu, P. Sannigrahi, S. Jung, A.J. Ragauskas, C.E. Wyman, Carbohydrate derived-pseudo-lignin can retard cellulose biological conversion, Biotechnol. Bioeng. 110 (2013) 737–753. https://doi.org/10.1002/bit.24744.

[141] G. Almeida, J.O. Brito, P. Perré, Changes in wood-water relationship due to heat treatment assessed on micro-samples of three Eucalyptus species, Holzforschung. 63 (2009) 80–88. https://doi.org/10.1515/HF.2009.026.

[142] Y. Yin, L. Berglund, L. Salmén, Effect of steam treatment on the properties of wood cell walls, Biomacromolecules. 12 (2011) 194–202. https://doi.org/https://doi.org/10.1021/bm101144m.

[143] G. Almeida, D.V.B. Santos, P. Perré, Mild pyrolysis of fast-growing wood species (Caribbean pine and Rose gum): Dimensional changes predicted by the global mass loss, Biomass and Bioenergy. 70 (2014) 407–415. https://doi.org/10.1016/j.biombioe.2014.07.028.

[144] K. Jungnikl, O. Paris, P. Fratzl, I. Burgert, The implication of chemical extraction treatments on the cell wall nanostructure of softwood, Cellulose. 15 (2008) 407–418. https://doi.org/10.1007/s10570-007-9181-5.

[145] V. Placet, J. Passard, P. Perré, Viscoelastic properties of wood across the grain measured under water-saturated conditions up to 135 °c: Evidence of thermal degradation, J. Mater. Sci. 43 (2008) 3210–3217. https://doi.org/10.1007/s10853-008-2546-9.

[146] J. Passard, P. Perré, Viscoelastic behaviour of green wood across the grain . Part II: A temperature dependent constitutive model defined by inverse method, 62 (2005) 823–830. https://doi.org/10.1051/forest.

[147] A.-M. Olsson, L. Salmén, Viscoelasticity of In Situ Lignin as Affected by Structure, in: Viscoelasticity Biomater., 1992: pp. 133–143. https://doi.org/10.1021/bk-1992-0489.ch009.

[148] L. Salmén, Viscoelastic properties of in situ lignin under water-saturated conditions, J. Mater. Sci. 19 (1984) 3090–3096. https://doi.org/10.1007/BF01026988.

[149] W. Dwianto, T. Morooka, M. Norimoto, Method for measuring viscoelastic properties of wood under high temperature and high pressure steam conditions, J. Wood Sci. 45 (1999) 373–377. https://doi.org/10.1007/BF01177908.

[150] W. Dwianto, T. Morooka, M. Norimoto, T. Kitajima, Stress relaxation of sugi (cryptomeria japonica d.don) wood in radial compression under high temperature steam, Holzforschung. 53 (1999) 541–546. https://doi.org/10.1515/HF.1999.089.

[151] L. Salmén, J.S. Stevanic, A.M. Olsson, Contribution of lignin to the strength properties in wood fibres studied by dynamic FTIR spectroscopy and dynamic mechanical analysis (DMA), Holzforschung. 70 (2016) 1155–1163. https://doi.org/10.1515/hf-2016-0050.

[152] P. Sannigrahi, A.J. Ragauskas, G.A. Tuskan, Poplar as a feedstock for biofuels: A review of compositional characteristics, Biofuels, Bioprod. Biorefining. 4 (2010) 209–226. https://doi.org/10.1002/bbb.206.

[153] JGI - Joint Genome Institute, Populus trichocarpa v1.1, (n.d.). https://mycocosm.jgi.doe.gov/Poptr1_1/Poptr1_1.home.html (accessed April 2, 2020).

[154] P.A. Townsend, S.P. Kar, R.O. Miller, Poplar (Populus spp.) Trees for Biofuel Production, (2019). https://farm-energy.extension.org/poplar-populus-spp-trees-for-biofuel-production/#Current and Potential Use as a Biofuel (accessed April 2, 2020).

[155] V. Placet, J. Passard, P. Perré, Viscoelastic properties of green wood across the grain measured by harmonic tests in the range 0-95°C: Hardwood vs. softwood and normal wood vs. reaction wood, Holzforschung. 61 (2007) 548–557. https://doi.org/10.1515/HF.2007.093.

[156] V. Placet, P. Perré, Chambre d'essai bi-climatique. Ref: BFF 06P0432, Ref: BFF 06P0432, 2006.

[157] Y.S. Touloukian, C.Y. Ho, Thermophysical properties of matter, Plenum Press, New York, 1972.

[158] International Organization for Standardization, ISO 527 - Plastics — Determination of tensile properties, (2019). https://www.iso.org/obp/ui/fr/#iso:std:iso:527:-1:ed-3:v1:fr (accessed February 14, 2020).

[159] International Organization for Standardization, ISO 604 - Plastiques — Détermination des propriétés en compression, (2002). https://www.iso.org/obp/ui/#iso:std:iso:604:ed-3:v1:fr (accessed February 14, 2020).

[160] ASTM International, ASTM D638 - 14 - Standard Test Method for Tensile Properties of Plastics, (2014). https://www.astm.org/Standards/D638 (accessed February 14, 2020).

[161] R.K. Korhonen, S. Saarakkal, Biomechanics and Modeling of Skeletal Soft Tissues, in: V. Klika (Ed.), Theor. Biomech., IntechOpen, 2011. https://doi.org/10.5772/19975.

[162] Instron, Are you experiencing variation or unexpected calculation results?, (2020). https://www.instron.fr/fr-fr/our-company/press-room/newsletters/plastics-news/plastics3 (accessed February 14, 2020).

[163] S. Zhao, M. Arnold, R.L. Abel, J.P. Cobb, S. Ma, U. Hansen, O. Boughton, Standardizing Compression Testing for Measuring the Stiffness of Human Bone, Bone Jt. Res. 7 (2018) 524–538. https://doi.org/10.1302/2046-3758.78.BJR-2018-0025.R1.

[164] A. Sluiter, B. Hames, R. Ruiz, C. Scarlata, J. Sluiter, D. Templeton, Determination of sugars, byproducts, and degradation products in liquid fraction process samples, 2008.

https://doi.org/NREL/TP-510-42623.

[165] A. Sluiter, A. Ruiz, C. Scarlata, J. Sluiter, D. Templeton, Determination of Extractives in Biomass, 2008. https://doi.org/NREL/TP-510-42621.

[166] A. Sluiter, B. Hames, R.O. Ruiz, C. Scarlata, J. Sluiter, D. Templeton, Determination of Structural Carbohydrates and Lignin in Biomass, 2011. https://doi.org/NREL/TP-510-42618.

[167] N. Gierlinger, T. Keplinger, M. Harrington, Imaging of plant cell walls by confocal Raman microscopy, Nat. Protoc. 7 (2012) 1694–1708. https://doi.org/10.1038/nprot.2012.092.

[168] B. Prats-mateu, M. Felhofer, A. De Juan, N. Gierlinger, Multivariate unmixing approaches on Raman images of plant cell walls : new insights or overinterpretation of results ?, Plant Methods. (2018). https://doi.org/10.1186/s13007-018-0320-9.

[169] R.M. El-abassy, B. Von Der Kammer, A. Materny, UV Raman spectroscopy for the characterization of strongly fluorescing beverages, LWT - Food Sci. Technol. 64 (2015) 56–60. https://doi.org/10.1016/j.lwt.2015.05.026.

[170] R.C.E. Dias, C. Yeretzian, Investigating Coffee Samples by Raman Spectroscopy for Quality Control - Preliminary Study, Int. J. Exp. Spectrosc. Tech. 1 (2016) 1–5.

[171] J. Schleusener, J. Lademann, M.E. Darvin, Depth-dependent autofluorescence photobleaching using 325, 473, 633, and 785 nm of porcine ear skin ex vivo , J. Biomed. Opt. 22 (2017) 091503. https://doi.org/10.1117/1.jbo.22.9.091503.

[172] H. Wang, J. Zhao, A.M.D. Lee, H. Lui, H. Zeng, Improving skin Raman spectral quality by fluorescence photobleaching, Photodiagnosis Photodyn. Ther. 9 (2012) 299–302. https://doi.org/10.1016/j.pdpdt.2012.02.001.

[173] A.M. Macdonald, P. Wyeth, On the use of photobleaching to reduce fluorescence background in Raman spectroscopy to improve the reliability of pigment identification on painted textiles, (2006) 830–835. https://doi.org/10.1002/jrs.1510.

[174] M.E. Darvin, N.N. Brandt, J. Lademann, Photobleaching as a Method of Increasing the Accuracy in Measuring Carotenoid Concentration in Human Skin by Raman Spectroscopy, Biomed. Opt. Spectrosc. 109 (2010) 235–240. https://doi.org/10.1134/S0030400X10080096.

[175] W.-C. Shih, K.L. Bechtel, M. V. Rebec, Noninvasive glucose sensing by transcutaneous Raman spectroscopy, J. Biomed. Opt. 20 (2015) 051036. https://doi.org/10.1117/1.jbo.20.5.051036.

[176] K.B. Ferreira, A.G.G. Oliveira, J.A. Gomes, Raman spectroscopy of automotive paints: Forensic analysis of variability and spectral quality, Spectrosc. Lett. 50 (2017) 102–110. https://doi.org/10.1080/00387010.2017.1288635.

[177] K. Golcuk, G.S. Mandair, A.F. Callender, N. Sahar, D.H. Kohn, M.D. Morris, Is photobleaching necessary for Raman imaging of bone tissue using a green laser?, Biochim. Biophys. Acta - Biomembr. 1758 (2006) 868–873. https://doi.org/10.1016/j.bbamem.2006.02.022.

[178] D. Tuschel, Selecting an excitation wavelength for raman spectroscopy, (2016). https://www.horiba.com/fileadmin/uploads/Scientific/Documents/Raman/Specy_Workbench_Selecting_Excitation_Wavelength_for_Raman.pdf.

[179] B. Prats-mateu, P. Bock, M. Schroffenegger, J.L. Toca-herrera, N. Gierlinger, Following laser induced changes of plant phenylpropanoids by Raman microscopy, Sci. Rep. 8 (2018) 1–12. https://doi.org/10.1038/s41598-018-30096-3.

[180] T. Dieing, O. Hollricher, J. Toporski, Confocal Raman microscopy, Springer, Ulm, 2010.

[181] T. Saito, J.-I. Toriwaki, New algorithms for euclidean distance transformation of an n-dimensional digitized picture with applications, Pattern Recognit. 27 (1994) 1551–1565.

https://doi.org/10.1016/0031-3203(94)90133-3.

[182] T. Hildebrand, P. Rüegsegger, A new method for the model-independent assessment of thickness in three-dimensional images, J. Microsc. 185 (1997) 67–75. https://doi.org/10.1046/j.1365-2818.1997.1340694.x.

[183] W. Schutyser, T. Renders, G. Van den Bossche, S. Van den Bosch, S.-F. Koelewijn, T. Ennaert, B.F. Sels, Catalysis in Lignocellulosic Biorefineries: The Case of Lignin Conversion, in: M. Van de Voorde, B. Sels (Eds.), Nanotechnol. Catal., Wiley, 2017: pp. 537–584. https://doi.org/10.1002/9783527699827.ch23.

[184] N. Gierlinger, M. Schwanninger, The potential of Raman microscopy and Raman imaging in plant research, Spectroscopy. 21 (2007) 69–89.

[185] J.P. Lancha, J. Colin, G. Almeida, P. Perré, In situ measurements of viscoelastic properties of biomass during hydrothermal treatment to assess the kinetics of chemical alterations, Bioresour. Technol. 315 (2020) 123819. https://doi.org/10.1016/j.biortech.2020.123819.

[186] J.P. Lancha, J. Colin, G. Almeida, J. Casalinho, C. Guerin, P. Perré, A DAEM model based on in-situ shrinkage measurement of poplar wood during hydrothermal treatment as predictive indicator of chemical degradation, Manuscr. Submitt. Publ. (2020).

[187] X. Zhou, J. Ma, Z. Ji, X. Zhang, S. Ramaswamy, F. Xu, R. Sun, Dilute acid pretreatment differentially affects the compositional and architectural features of Pinus bungeana Zucc . compression and opposite wood tracheid walls, Ind. Crop. Prod. 62 (2014) 196–203. https://doi.org/10.1016/j.indcrop.2014.08.035.

[188] Y. Zeng, S. Zhao, H. Wei, M.P. Tucker, M.E. Himmel, N.S. Mosier, In situ micro - spectroscopic investigation of lignin in poplar cell walls pretreated by maleic acid, Biotechnol. Biofuels. 8 (2015) 126. https://doi.org/10.1186/s13068-015-0312-1.

[189] L.A. Donaldson, K.K.Y. Wong, K.L. Mackie, Ultrastructure of steam-exploded wood, Wood Sci. Technol. 22 (1988) 103–114. https://doi.org/10.1007/BF00355846.

[190] A. Lähdetie, P. Nousiainen, J. Sipilä, T. Tamminen, A.S. Jääskeläinen, Laser-induced fluorescence (LIF) of lignin and lignin model compounds in Raman spectroscopy, Holzforschung. 67 (2013) 531–538. https://doi.org/10.1515/hf-2012-0177.

[191] Z. Ji, Z. Ling, X. Zhang, G.-H. Yang, F. Xu, Impact of Alkali Pretreatment on the Chemical Component Distribution and Ultrastructure of Poplar Cell Walls, BioResources. 9 (2014) 4159–4172.

[192] R. Kumar, G. Mago, V. Balan, C.E. Wyman, Physical and chemical characterizations of corn stover and poplar solids resulting from leading pretreatment technologies, Bioresour. Technol. 100 (2009) 3948–3962. https://doi.org/10.1016/j.biortech.2009.01.075.

[193] A. Zoghlami, Y. Refahi, C. Terryn, G. Païs, Multimodal characterization of acid-pretreated poplar reveals spectral and structural parameters strongly correlate with saccharification, Bioresour. Technol. 293 (2019) 122015. https://doi.org/10.1016/j.biortech.2019.122015.

[194] Q. Sun, Y. Pu, X. Meng, T. Wells, A.J. Ragauskas, Structural Transformation of Isolated Poplar and Switchgrass Lignins during Dilute Acid Treatment, ACS Sustain. Chem. Eng. 3 (2015) 2203–2210. https://doi.org/10.1021/acssuschemeng.5b00426.

[195] S. Liu, H. Lu, R. Hu, A. Shupe, L. Lin, B. Liang, A sustainable woody biomass biorefinery, Biotechnol. Adv. 30 (2012) 785–810. https://doi.org/10.1016/j.biotechadv.2012.01.013.

[196] J. Barros, H. Serk, I. Granlund, E. Pesquet, The cell biology of lignification in higher plants, Ann. Bot. 115 (2015) 1053–1074. https://doi.org/10.1093/aob/mcv046.

[197] C. Lapierre, B. Pollet, C. Rolando, New insights into the molecular architecture of hardwood lignins by chemical degradative methods, Res. Chem. Intermed. 21 (1995) 397–412. https://doi.org/10.1007/BF03052266.

[198] C. Lapierre, Application of New Methods for the Investigation of Lignin Structure, in: H.G. Jung, D.R. Buxton, R.D. Hatfield, J. Ralph (Eds.), Forage Cell Wall Struct. Dig., American Society of Agronomy, Madison, 1993: pp. 133–166. https://doi.org/10.2134/1993.foragecellwall.c6.

[199] L.-P. Xiao, Z. Lin, W.-X. Peng, T.-Q. Yuan, F. Xu, N.-C. Li, Q.-S. Tao, H. Xiang, R.-C. Sun, Unraveling the structural characteristics of lignin in hydrothermal pretreated fibers and manufactured binderless boards from Eucalyptus grandis, Sustain. Chem. Process. 2 (2014) 9. https://doi.org/10.1186/2043-7129-2-9.

[200] K. Waldron, Bioalcohol production: Biochemical conversion of lignocellulosic biomass, Woodhead Publishing, New Delhi, 2010.

[201] L.J. Jönsson, C. Martín, Pretreatment of lignocellulose: Formation of inhibitory by-products and strategies for minimizing their effects, Bioresour. Technol. 199 (2016) 103–112. https://doi.org/10.1016/j.biortech.2015.10.009.

[202] J.S. Kim, Y.Y. Lee, T.H. Kim, A review on alkaline pretreatment technology for bioconversion of lignocellulosic biomass, Bioresour. Technol. 199 (2016) 42–48. https://doi.org/10.1016/j.biortech.2015.08.085.

[203] G. Wypych, The Effect of Fillers on the Mechanical Properties of Filled Materials, in: G. Wypych (Ed.), Handb. Fill., Fourth ed., ChemTec Publishing, Toronto, 2016: pp. 467–531. https://doi.org/10.1016/b978-1-895198-91-1.50010-5.

[204] J. Passard, P. Perré, Viscoelastic behaviour of green wood across the grain. Part II. A temperature dependent constitutive model defined by inverse method, Ann. For. Sci. 62 (2005) 823–830. https://doi.org/10.1051/forest:2005088.

[205] Z. Youssef, F. Ducept, H. Bennaceur, B. Malinowska, G. Almeida, P. Perre, D. Flick, Residence time distribution in a biomass pretreatment reactor: Experimentation and modeling, Chem. Eng. Res. Des. 125 (2017) 233–244. https://doi.org/10.1016/j.cherd.2017.07.015.

[206] M.J. Negro, P. Manzanares, J.M. Oliva, I. Ballesteros, M. Ballesteros, Changes in various physical/chemical parameters of Pinus pinaster wood after steam explosion pretreatment, Biomass and Bioenergy. 25 (2003) 301–308. https://doi.org/10.1016/S0961-9534(03)00017-5.

[207] X.F. Sun, F. Xu, R.C. Sun, P. Fowler, M.S. Baird, Characteristics of degraded cellulose obtained from steam-exploded wheat straw, Carbohydr. Res. 340 (2005) 97–106. https://doi.org/10.1016/j.carres.2004.10.022.

[208] J.P. Lancha, G. Almeida, J. Colin, N. Ruscassier, P. Lv, P. Perré, Multiscale investigation on the chemical and anatomical changes of lignocellulosic biomass submitted to hydrothermal pre-treatment, Manuscr. Submitt. Publ. (2020).

[209] J. Fahlén, L. Salmén, Cross-sectional structure of the secondary wall of wood fibers as affected by processing, J. Mater. Sci. 38 (2003) 119–126. https://doi.org/10.1023/A:1021174118468.

[210] S.Y. Zhang, B.H. Fei, C.G. Wang, Effects of chemical extraction treatments on nano-scale mechanical properties of the wood cell wall, BioResources. 11 (2016) 7365–7376. https://doi.org/10.15376/biores.11.3.7365-7376.

[211] C. Vila, J.L. Francisco, V. Santos, J.C. Parajó, Effects of hydrothermal processing on the cellulosic fraction of Eucalyptus globulus wood, Holzforschung. 67 (2013) 33–40. https://doi.org/10.1515/hf-2012-0046.

[212] L. Wu, M. Arakane, M. Ike, M. Wada, T. Takai, M. Gau, K. Tokuyasu, Low temperature alkali

pretreatment for improving enzymatic digestibility of sweet sorghum bagasse for ethanol production, Bioresour. Technol. 102 (2011) 4793–4799. https://doi.org/10.1016/j.biortech.2011.01.023.

[213] Y. Chen, M.A. Stevens, Y. Zhu, J. Holmes, H. Xu, Understanding of alkaline pretreatment parameters for corn stover enzymatic saccharification, Biotechnol. Biofuels. 6 (2013) 1. https://doi.org/10.1186/1754-6834-6-8.

[214] L. Zhang, L. Yan, Z. Wang, D.D. Laskar, M.S. Swita, J.R. Cort, Characterization of lignin derived from water - only and dilute acid flowthrough pretreatment of poplar wood at elevated temperatures, Biotechnol. Biofuels. 8 (2015) 1–14. https://doi.org/10.1186/s13068-015-0377-x.

[215] A. Sluiter, B. Hames, R. Ruiz, C. Scarlata, J. Sluiter, D. Templeton, D.C. Nrel, Determination of Structural Carbohydrates and Lignin in Biomass Determination of Structural Carbohydrates and Lignin in Biomass, Golden, 2011.

[216] C.A.S. Hill, A. Norton, G. Newman, The water vapor sorption behavior of natural fibers, J. Appl. Polym. Sci. 112 (2009) 1524–1537.

[217] Z.H. Liu, L. Qin, F. Pang, M.J. Jin, B.Z. Li, Y. Kang, B.E. Dale, Y.J. Yuan, Effects of biomass particle size on steam explosion pretreatment performance for improving the enzyme digestibility of corn stover, Ind. Crops Prod. 44 (2013) 176–184. https://doi.org/10.1016/j.indcrop.2012.11.009.

[218] M.E. Vallejos, F.E. Felissia, M.C. Area, Hydrothermal Treatments Applied to Agro-and Forest-Industrial Waste to Produce High Added-Value Compounds, BioResources. 12 (2017) 2058–2080.

[219] J. Gril, B. Thibaut, E. Berrada, G. Martin, Recouvrance hygrothermique du bois vert. I. Influence de la température. Cas du jujubier (Ziziphus lotus (L) Lam), Ann. Des Sci. For. 50 (1993) 57–70. https://doi.org/http://dx.doi.org/10.1051/forest:19930104.

[220] L. Salmén, Thermal Expansion of Water-saturated Wood, Holzforschung. 44 (1990) 17–19. https://doi.org/https://doi.org/10.1515/hfsg.1990.44.1.17.

[221] K.C. Sujan, H. Yamamoto, M. Matsuo, M. Yoshida, K. Naito, T. Shirai, Continuum contraction of tension wood fiber induced by repetitive hygrothermal treatment, Wood Sci. Technol. 49 (2015) 1157–1169. https://doi.org/10.1007/s00226-015-0762-4.

[222] M. Ueda Matsuo, G. Niimi, K.C. Sujan, M. Yoshida, H. Yamamoto, Hygrothermal recovery of compression wood in relation to elastic growth stress and its physicochemical characteristics, J. Mater. Sci. 51 (2016) 7956–7965. https://doi.org/10.1007/s10853-016-0065-7.

[223] J.F. Siau, Transport Processes in Wood, Springer Berlin Heidelberg, Berlin, Heidelberg, 1984. https://doi.org/10.1007/978-3-642-69213-0.

[224] D. Jullien, Analyse expérimentale et numérique des contraintes résiduelles dans un matériau élastique orthotrope élaboré par couches successives. Cas d'un disque de bois vert, Université Montpellier 2 - Sciences et techniques du Languedoc, 1995.

[225] S. Bardet, J. Gril, K. Kojiro, S. Bardet, J. Gril, K. Kojiro, T. Strain, H. Wood, Ó.Ö.Ñ.Ø. Óò, Thermal Strain of Green Hinoki Wood : Separating the Hygrothermal Recovery and the Reversible Deformation To cite this version : HAL Id : hal-00789662 Deformation , in : Mechanics , Models and Methods in Civil Engineering , (2013).

[226] P. Perré, Experimental device for the accurate determination of wood-water relations on micro-samples, Holzforschung. 61 (2007) 419–429. https://doi.org/10.1515/HF.2007.075.

[227] V. Placet, J. Passard, P. Perré, Viscoelastic properties of wood across the grain measured under

water-saturated conditions up to 135 °C: Evidence of thermal degradation, J. Mater. Sci. 43 (2008) 3210–3217. https://doi.org/10.1007/s10853-008-2546-9.

[228] J. Cai, W. Wu, R. Liu, An overview of distributed activation energy model and its application in the pyrolysis of lignocellulosic biomass, Renew. Sustain. Energy Rev. 36 (2014) 236–246. https://doi.org/10.1016/j.rser.2014.04.052.

[229] S. Cavagnol, J.F. Roesler, E. Sanz, W. Nastoll, P. Lu, P. Perré, Exothermicity in wood torrefaction and its impact on product mass yields: From micro to pilot scale, Can. J. Chem. Eng. 93 (2015) 331–339. https://doi.org/10.1002/cjce.22128.

[230] J. Cai, W. Wu, R. Liu, An overview of distributed activation energy model and its application in the pyrolysis of lignocellulosic biomass, Renew. Sustain. Energy Rev. 36 (2014) 236–246. https://doi.org/10.1016/j.rser.2014.04.052.

[231] G. Almeida, J.O. Brito, P. Perré, Alterations in energy properties of eucalyptus wood and bark subjected to torrefaction : The potential of mass loss as a synthetic indicator, Bioresour. Technol. 101 (2010) 9778–9784. https://doi.org/10.1016/j.biortech.2010.07.026.

[232] J. Pachón-Morales, J. Colin, F. Pierre, F. Puel, P. Perré, Effect of torrefaction intensity on the flow properties of lignocellulosic biomass powders, Biomass and Bioenergy. 120 (2019) 301–312. https://doi.org/10.1016/j.biombioe.2018.11.017.

[233] L.X. Phuong, M. Takayama, S. Shida, Y. Matsumoto, T. Aoyagi, Determination of the accessible hydroxyl groups in heat-treated Styrax tonkinensis (Pierre) Craib ex Hartwich wood by hydrogen-deuterium exchange and2H NMR spectroscopy, Holzforschung. 61 (2007) 488–491. https://doi.org/10.1515/HF.2007.086.

[234] M.F. Li, C.Z. Chen, R.C. Sun, Effect of pretreatment severity on the enzymatic hydrolysis of bamboo in hydrothermal deconstruction, Cellulose. 21 (2014) 4105–4117. https://doi.org/10.1007/s10570-014-0451-8.

[235] S. Viamajala, B.S. Donohoe, S.R. Decker, T.B. Vinzant, M.J. Selig, M.E. Himmel, M.P. Tucker, Heat and Mass Transport in Processing of Lignocellulosic Biomass for Fuels and Chemicals, in: Sustain. Biotechnol. Sources Renew. Energy, Springer Netherlands, 2010: pp. 1–18. https://doi.org/10.1007/978-90-481-3295-9.

université PARIS-SACLAY

ECOLE DOCTORALE N°579
Sciences mécaniques et énergétiques, matériaux et géosciences (SMEMAG)

Titre : Une approche multi-échelle pour comprendre et prévoir les effets de la cuisson acide sur la biomasse lignocellulosique
Mots clés : Biomasse lignocellulosique ; Cuisson acide ; Bioéthanol ; Modèle à énergie d'activation distribuée ; Imagerie

Résumé : La biomasse lignocellulosique est une matière première prometteuse pour la production de biocarburants et de produits chimiques renouvelables. Cependant, en raison de la structure macromoléculaire récalcitrante des tiges de plantes, un prétraitement est nécessaire pour rendre les glucides suffisamment accessibles pour l'hydrolyse enzymatique. Parmi la vaste gamme de prétraitements disponibles, l'explosion à la vapeur se distingue car elle ne nécessite pas de solvant et peut être appliquée à diverses matières premières. Elle se déroule en deux étapes : une cuisson acide suivie d'une décompression brutale.

Les modifications subies par la biomasse lors de la cuisson acide ont un impact important sur la phase explosive et les étapes ultérieures de la production de bioéthanol. Elles affectent ainsi largement la rentabilité de l'ensemble de la chaîne de production. Ayant pour origine des altérations chimiques, ces modifications sont observables à de multiples échelles.

C'est pourquoi une approche multi-échelle est proposée dans ce travail, avec pour objectif ultime de fournir des indicateurs mécaniques macroscopiques de la cinétique du traitement, susceptibles de donner des règles pour optimiser le temps de séjour et la température de la cuisson acide. Pour comprendre comment le comportement mécanique à l'échelle macroscopique est affecté par les changements de propriétés à l'échelle moléculaire et microscopique au cours du traitement, trois disciplines – mécanique, chimie et imagerie – ont été combinées. En raison de sa croissance rapide et de son faible besoin en engrais, le peuplier (*Populus euro-americana* 'Koster') a été utilisé comme biomasse modèle pour cette étude.

Au niveau microscopique, la microscopie confocale Raman a révélé que les altérations chimiques dépendent de l'organisation des différents composants à l'intérieur de la paroi cellulaire et de leurs interactions entre eux. La combinaison unique de cette technique avec la nano-tomographie à rayons X a permis d'obtenir une vision globale de la dégradation de la paroi cellulaire après la cuisson acide, avec des informations précieuses sur les modifications topochimiques et anatomiques des échantillons. Des analyses chimiques complémentaires ont permis la quantification de l'hydrolyse concomitante de la biomasse.

Au niveau macroscopique, un dispositif développé préalablement au sein du laboratoire a été amélioré pour effectuer avec précision des essais mécaniques continus de la biomasse (diverses combinaisons de contraintes et de déformations) dans des conditions de saturation en eau jusqu'à 190 °C. L'effet du temps de séjour est donc suivi en continu. Grâce à des mesures d'élasticité et de relaxation, les propriétés viscoélastiques ont été utilisées pour comparer différentes conditions de traitement (température et acidité). Enfin, ce dispositif a permis de mesurer pour la première fois la cinétique du retrait de l'échantillon lors de ce type de traitement, à partir de laquelle un modèle DAEM a été identifié. Le degré de conversion de la biomasse, calculé à partir de ce modèle, est capable de prédire l'évolution des caractéristiques physiques et chimiques en fonction des conditions de traitement. Ces résultats prouvent que le retrait est un excellent indicateur de la dégradation chimique de la biomasse lignocellulosique lors de la cuisson acide.

Title: A multiscale approach to understand and predict the effects of hydrothermal treatment on lignocellulosic biomass
Keywords: Lignocellulosic biomass; Hydrothermal treatment; Bioethanol; Distributed Activation Energy Model; Imaging techniques

Abstract: Lignocellulosic biomass is a promising feedstock for the production of renewable fuels and bio-based chemicals. However, due to the recalcitrant macromolecular structure of plant stems, a pretreatment is required to make carbohydrates sufficiently accessible for enzymatic hydrolysis. Among the large range of available processes, steam explosion stands out, as it requires no additional solvent and can be applied to a variety of raw materials. It consists of two steps: a hydrothermal treatment followed by a sudden decompression.

Biomass alterations during hydrothermal treatment have a great impact on the explosion and the subsequent steps of bioethanol production. Caused by chemical alterations, these modifications are reflected at multiple spatial levels. For this reason, a multiscale approach is proposed in the present work, with the ultimate goal of providing macroscopic mechanical indicators of the treatment kinetics likely to give rules to optimize the residence time and treatment temperature during hydrothermal treatment. To understand how the mechanical behavior at the macroscopic scale is affected by the changes in the properties at molecular and microscopic scales during treatment, three disciplines – mechanics, chemistry and imaging techniques – were combined. Because of its fast growth and low need of fertilizers, poplar (*Populus euro-americana* 'Koster') was used as model biomass for this study.

At the microscopic level, the use of Raman confocal microscopy revealed that chemical alterations depend on the organization of the different components within the cell wall and their interactions with each other. The unique combination of this technique with X-ray nano-tomography provided a global vision of the degradation of the cell wall after hydrothermal treatment, with valuable information on both topochemical and anatomical changes of the samples. Complimentary wet chemistry analysis allowed to quantify the concomitant hydrolysis and degradation of biomass.

At a macroscopic level, an in-house developed device was improved to accurately perform continuous mechanical tests on macroscopic solid samples (various combinations of strain and stress) under water-saturated conditions up to 190 °C. The effect of residence time is therefore continuously monitored. Through elasticity and stress relaxation measurements, viscoelastic properties were used to compare different treatment conditions (temperature levels and acidity). Finally, this device allowed the kinetics of sample shrinkage to be measured. From these results a DAEM model was identified. The degree of conversion of the biomass, as calculated from this model, is able to predict the change of physical and chemical characteristics for any time-temperature pathway. These findings prove that shrinkage is an excellent indicator of the chemical degradation of lignocellulosic biomass during the hydrothermal treatment.

Université Paris-Saclay
Espace Technologique / Immeuble Discovery
Route de l'Orme aux Merisiers RD 128 / 91190 Saint-Aubin, France